UNIVERSIDAD NACIONAL AUTÓNOMA DE MEXICO

PROGRAMA DE MAESTRÍA Y DOCTORADO EN CIENCIAS QUÍMICAS

Síntesis, química redox y reactividad de complejos de formazán y formazanato de Re(I)

TESIS

PARA OPTAR POR EL GRADO DE

DOCTORA EN CIENCIAS

M. en C. Liliana Capulin Flores

Dr. Noé Zúñiga Villarreal
Instituto de Química, UNAM

Dr. Edwin Otten
Stratingh Institute for Chemistry, University of Groningen

CDMX, México, Marzo 2024

UNIVERSIDAD NACIONAL AUTÓNOMA DE MÉXICO

PROGRAMA DE MAESTRÍA Y DOCTORADO EN CIENCIAS QUÍMICAS

Síntesis, química redox y reactividad de complejos de formazán y formazanato de Re(I)

T E S I S
PARA OPTAR POR EL GRADO DE

DOCTORA EN CIENCIAS

P R E S E N T A

M. en C. Liliana Capulin Flores

Dr. Noé Zúñiga Villarreal
Instituto de Química, UNAM

Dr. Edwin Otten
Stratingh Institute for Chemistry, University of Groningen

Ciudad de México, Marzo de 2024.

Comité tutor

Dra. María Ángeles Paz Sandoval   CINVESTAV, IPN

Dra. Itzel Guerrero Ríos   Facultad de Química, UNAM

Comité Evaluador

Presidente   Dra. Noráh Yolanda Barba Behrens, Facultad de Química, UNAM

Vocal   Dra. Verónica García Montalvo, Instituto de Química, UNAM

Vocal   Dr. Francisco Javier Zuno Cruz, Universidad Autónoma del Estado de Hidalgo

Vocal   Dra. Ma. del Carmen Virginia Ortega Alfaro, Inst. de Ciencias Nucleares, UNAM

Secretario   Dra. Itzel Guerrero Ríos Facultad de Química, UNAM

_____
Tutor: Dr. Noé Zúñiga Villarreal

_____
Tutor: Dr. Edwin Otten

Synthesis, redox chemistry and reactivity of formazan and formazanate Re(I) complexes

PhD thesis

to obtain the degree of PhD at the
University of Groningen
on the authority of the
Rector Magnificus Prof. J.M.A. Scherpen
and in accordance with
the decision by the College of Deans.

and

to obtain the degree of PhD at the
Universidad Nacional Autónoma de México
on the authority of the
Rector Dr. L. Lomelí Vanegas
and in accordance with
the decision by the Assessment Committee of the Master and Doctoral Program in
Chemical Sciences.

Double PhD degree

This thesis will be defended in public on

Tuesday 13 February 2024 at 16.15 hours

by

Liliana Capulin Flores

born on 26 January 1989

Supervisors

Prof. E. Otten
Prof. W.R. Browne
Prof. N. Zúñiga-Villarreal

Assessment Committee

Prof. A.J. Minnaard
Prof. D.G.H. Hetterscheid
Prof. B. Royo
Prof. I. Guerrero Rios

Cover design by: Liliana Capulin Flores

Printed by:Proefschrift AIO

In memoriam

David Martínez Velázquez (1990-2023)

Acknowledgements

Firstly, I want to express my gratitude to my hosting institutions: the University of Groningen (Strantingh Institute for Chemistry) and Universidad Nacional Autónoma de México (Instituto de Química). To CONACyT (Consejo Nacional de Ciencia y Tecnología, CVU 512 521) and the University of Groningen for financing my doctoral studies. To the analytical staff at the University of Groningen: Johan Hekelaar, Renze Sneep, Peter van de Meulen, Johan Kemmink, and Léon Rohrbach; and, at Instituto de Química, UNAM: E. Huerta-Salazar, B. Quiroz-García, and F.J. Pérez-Flores, for their technical assistance.

Secondly, but not least in importance, I want to thank my supervisors *Prof. Dr. Noé Zúñiga* Villarreal and Prof. Dr. Edwin Otten; without them, none of these could turn out as it is today. Dr. Noé, nos conocemos por tanto tiempo que no sé por dónde empezar. Gracias por haberme dado la oportunidad de trabajar con usted desde licenciatura hasta Doctorado. Por todo lo que nos ha enseñado dentro y fuera del laboratorio, por ser un ejemplo para sus alumnos. Por creer en mí y alentarme a continuar a pesar de los tropiezos en el camino, que ahora en la distancia, han sido necesarios para llegar hasta aquí. Tuvo razón cuando me dijo: ya verás Lili que nos reiremos de esto algún día.

Edwin, first of all, thank you for trusting us and accepting a collaboration with, until then, unknown people. I hope this experience has been as rewarding for you as it has been for me. I am infinitely grateful for allowing me to be part of your group and for showing me a different research approach. For everything you patiently and kindly taught me and the feedback I received throughout this journey. I really appreciate your advice, as it has helped me recognize the areas where I can improve. I have learned from you to visualize my results differently and accept that not everything turns out as expected, but it is still okay. Thank you for motivating me to develop new skills and allowing me to present our work at national and international conferences and visit other institutions to receive training. I am also grateful for the freedom you gave me throughout this time. Two years passed very quickly, and they were not enough for me; I will always be thinking about new experiments to try!

I also want to acknowledge our collaborators. *Prof. Dr. Inke Siewert*, for the fruitful discussions and suggestions. Thank you for hosting me in Göttingen for one week. *Philip Rohatschek* and *Thorben Kuessner*, many thanks for helping me record some of the electrochemical measurements presented in this work. Thanks, *Lucas Paul*, for helping me with the luminescence experiments in *Chapter 2* and *3*. *Remco Havenith*, I appreciate your suggestions and feedback regarding the calculations performed in this thesis and your contributions in *Chapter 2*.

Thanks to the reading committee in Groningen: Prof. A.J. Minnaard, Prof. D.G.H. Hetterscheid, and Prof. B. Royo, and in México: Prof. Noráh Yolanda Barba Behrens, Prof. Verónica García Montalvo, Prof. Francisco Javier Zuno Cruz and Prof. Ma. Del Carmen

Virginia Ortega Alfaro. Your comments and suggestions have helped me to enrich this work.

Prof. Angeles Paz and Prof. Itzel Guerrero Ríos, I had the pleasure of having you on my doctoral committee. I will always be grateful for your feedback during our online meetings, curiosity about my work, and commitment to my professional development. Thanks, Prof. Itzel, for accepting to be part of the reading committee in Groningen and México.

Johannes Klein, I appreciate your insightful comments and questions during the group meetings that allowed me to improve this work. I am excited to collaborate with you as a postdoctoral fellow. It has been a pleasure to meet Laura and little Maria.

Wesley Browne, I am thankful to you for allowing me to use the technical facilities in your lab and for the support received as part of the MOLAN cluster.

Silène Engbers, you have become one of my closest friends here in Groningen. Thank you for being there and listening to me whenever I was down. Your kindness and empathy made a difference to me. I have found in you a very generous, genuine, and thoughtful person. I have enjoyed our cooking nights so much, so having dinner at your place and spending time with Derek and Marie, they are lovely! Thanks for all the trips and conferences together. As I said to you, you are a great scientist and person. I am delighted to have you as my paranymph.

Yaroslava Lopatina, thank you for accepting being my paranymph as well. It is really nice to be surrounded by successful women as you are. I have enjoyed sharing with you Saturday nights, tasting Ukrainian delicacies, and chatting with a cup of tea! I am happy you will stay longer, so we will have more time to strengthen our friendship!

Isaac Leach, you have also been such a good friend! I am grateful for your unconditional support; it has meant a lot to me. You are one of the kindest and most cheerful people I have ever met. Thanks for everything, the conferences and outside lab gatherings. I will miss you! I wish you all the best and great success in your new endeavors.

I want to thank my lab colleagues, *Jelte Steen* and *Folkert de Vries*, for always being willing to help others (including me), which I really appreciate. Thanks for showing me the lab and surroundings and creating a pleasant working atmosphere. *Wenlong Tang* and *Fionn Ferreira*, thanks for being such friendly colleagues. I also want to thank the former members of the Otten group, *Basile Roufosse*, *Preslav Smits*, and *Sietse Dijt*. I enjoyed sharing the office and the lab with you!

To the former and current members of the Klein group, *Taegeun Jo*, *Kristopher Hessling*, *Hangyul Lee*, *Lisa Wijtenhorst* and *Kevin Harreither*, it has been a great pleasure to have you as colleagues. *Kristo*, I will always be grateful for your help when I arrived in

Groningen for the first time! *Hangyul*, I am thrilled I got to know you better; you are genuinely kind and diligent. I wish you all the best for the near future.

Thanks to the Kudernac crew, *Baptiste Vial*, *Jacopo Martinelli*, *Julien Smith*, *Luis Pantaleone*, and *Victor Verduijn*, for all the scientific/social gatherings and for making me part of your gang. You have made everything funnier!

Johan, thanks for the small chats in the morning. It is an excellent way to start every day!

I hope you all have enjoyed the Mexican candy testing sessions!

También quiero agradecer a la banda mexicana en Groningen, aunque no pude convivir tanto con ustedes como lo hubiera deseado, me divertí todas las veces que salimos juntos.

A mis compañeros y amigos del Lab 3-C. *David Martínez Velázquez*, me es difícil creer que ya no estás, me hubiera gustado verte a mi regreso. Fue un honor compartir el laboratorio contigo y reír con tus ocurrencias. Fuiste un gran compañero y amigo, siempre te recordaré. *Gabriela Morales Salas*, aunque físicamente estamos lejos, no hemos perdido contacto. Gracias por los mensajes y videollamadas, ya pronto nos veremos por acá, te deseo todo el éxito. *Josué Solís Huitrón* muchas gracias por los consejos y palabras de aliento, he aprendido de ti a ver las situaciones desde una diferente perspectiva. *Angela Hernández Licona*, siempre sonriente y positiva, el claro ejemplo de motivación y perseverancia, gracias por todos estos años de amistad. *Obdulia Sánchez Guadarrama*, gracias por haberme permitido conocerte y por las buenas vibras que siempre me mandas. *Karla Salas Martin*, *Ingrid Espinosa López*, *Alexia Molina Garduño*, *Edgar Flores Juárez* y *Bárbara Lerate Rosales* (miembro honorario), ha sido un placer convivir con ustedes, gracias por los buenos deseos. *Azucena Beltrán Ramírez*, gracias infinitas, por estar ahí siempre que lo necesito. Tu visita me trajo un poco de casa, me siento afortunada de tenerte como amiga.

Othoniel Reyes Camacho, también fuiste una parte importante durante este tiempo, agradezco por haber tenido tu apoyo. Aunque nuestras vidas tomaron rumbos diferentes, siempre te tendré presente.

A mi *madre*, Silvia Flores Velázquez, mis hermanos *Elizabeth* Capulín Flores y *Eduardo Morelos Flores*, y a mis niños *Leonel Reyes Capulín* y *Julia Vera Capulín*, ha sido un reto estar lejos, pero siempre fue un aliciente saber que ustedes me esperan y se alegran de mis triunfos. ¡Los quiero mucho!

Table of Contents

List of abbreviations

CPE Controlled Potential Electrolysis

Co(Cp*)$_2$ Decamethylcobaltocene

Co(Cp*)$_2$$^+$ Decamethylcobaltocenium

CV Cyclic voltammetry

DABCO (1,4-diazobicyclo[2.2.2]octane)

DFT Density Functional Theory

Fc Ferrocene

Fc$^+$ Ferrocenium

GC Gas Chromatography

ILCT Intra-Ligand Charge Transfer

LLCT Ligand to Ligand Charge Transfer

LMCT Ligand to Metal Charge Transfer

MLCT Metal to Ligand Charge Transfer

NHE Normal Hydrogen Electrode

OTTLE cell Optically Transparent Thin-Layer Electrochemical cell

PCM Polarizable Continuum Model

PPN$^+$ Bis(triphenylphosphine)iminium

PPh$_4$$^+$ Tetraphenylphosphonium

SPEC Spectroelectrochemistry

TDDFT Time Dependent Density Functional Theory

List of synthesized complexes
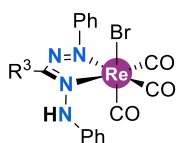
H1^{Br} (R^3 = Ph)
H2^{Br} (R^3 = *p*-MeC$_6$H$_4$)
H3^{Br} (R^3 = *p*-OMeC$_6$H$_4$)
H4^{Br} (R^3 = *p*-FC$_6$H$_4$)
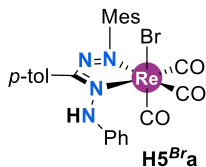
H5^{Br}a
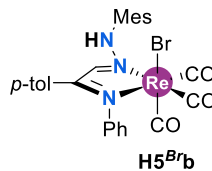
H5^{Br}b
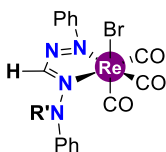
H6^{Br} (R' = H)
Me6^{Br} (R' = Me)
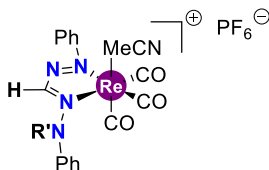
[Me6^{Br}][PF$_6$] (R' = Me)
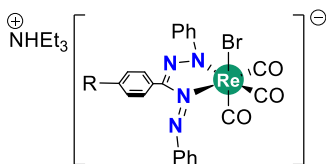
[1^{Br}]⁻ (R = H)
[2^{Br}]⁻ (R = Me)
[3^{Br}]⁻ (R = OMe)
[4^{Br}]⁻ (R = F)
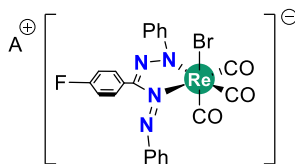
[A][4^{Br}]

A$^⊕$ = [Co(Cp*)$_2$]$^+$, [PPN]$^+$, [PPh$_4$]$^+$
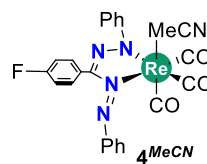
4^{MeCN}

Chapter 1

Introduction

The activation of small molecules represents a growing area in Chemistry. Molecules, such as N_2, O_2, CO_2, NO_x, CH_4, are abundant in our atmosphere.[1] Ideal starting materials given their vastness, availability, and renewability, although difficult to transform by applying *traditional chemistry* methods. Given their high thermodynamic stability and kinetic inertness, finding chemical strategies to activate such inert substrates through an efficient conversion is a subject of continuous research, since they can serve as synthons for the preparation of more complex molecules.

Besides the synthetic perspective, other interests are involved in utilizing air pollutants, such as CO_2[2] and NO_x,[3] which could also represent a viable strategy to mitigate their atmospheric accumulation.[4,5] Equally crucial in the current global energy crisis, converting H_2O or CO_2 into fuels could represent a feasible alternative for energy storage.[6]

Chemical reactions in nature are driven efficiently, mediated by a piece of sophisticated machinery that activates even the most inert substrates. For instance, during photosynthesis, water is oxidized in the presence of light. The products of this reaction (protons and electrons) are transferred to [NiFeS]-metalloenzyme catalytic center, where CO_2 is reduced into carbohydrates.[7] In these bio-transformations, metalloenzymes are the key components, complex structures that catalytically promote chemical transformations. Constituted by a metal cofactor bound to a protein unit, they can be conceived as super-active inorganic catalysts. Thus, taking inspiration from nature, the most reasonable starting point in small molecule activation research is exploring the reactivity of such molecules with metal complexes. In this regard, a considerable amount of work has been devoted to investigate the activation and subsequent transformation of small molecules using metal catalysts, where it has been demonstrated that the high tunability and redox capabilities of these species could effectively mediate substrate transformation.[8,9]

1. Carbon dioxide

Carbon dioxide is a relatively simple compound produced naturally by mammals' respiration, biomass degradation, and geochemical phenomena. Being the main greenhouse gas generated by the combustion of fossil fuels, its overproduction since the Industrial Revolution has caused a dramatic effect on atmosphere dynamics.[10] Recent reports indicate CO_2 emissions will rapidly rise if no actions are taken, causing an increase of the global temperature of 5°C by 2100.[11]

CO_2 capture and sequestration by adsorbing the gas on porous materials' surfaces to store it underground could be a potential strategy to decrease CO_2 atmospheric concentration. However, it represents a temporary solution since it does not seek a practical purpose for CO_2 other than confinement. Therefore, CO_2 capture, and sequestration combined with its conversion are attractive because they aim to convert it into valuable chemicals which would turn CO_2 into a renewable C_1 building block for synthesis.[12] As mentioned above, extensive research has focused on CO_2 conversion mediated by transition metal complexes similar to what nature does. However, before entering in-depth into the reactivity of metal complexes towards CO_2, a brief introduction to the chemical properties of CO_2 as a substrate is developed in the next section.

1.1 Electronic structure and reactivity

In its ground state, carbon dioxide is a triatomic linear molecule composed of a central carbon bound to two side-on oxygens. The highest-occupied molecular orbital $1\pi_g$ is doubly degenerate and primarily localized on the oxygens. While the lowest-unoccupied molecular orbital $2\pi_u$ is also doubly degenerate, this possesses mainly carbon character (Figure 1).[13]

Disruption of the linearity by bending the O-C-O angle alters the energy and the extent of the degeneracy of π-symmetry frontier orbitals. Notably, the LUMO ($2\pi_u$) is stabilized ($6a_1$ orbital), while HOMO ($1\pi_g$) rises in energy ($4b_2$;$1a_2$), *see* Figure 1.[13,14] This bending is induced when electrons are placed on the LUMO as happens when CO_2 interacts with a nucleophile –such as late-transition metals in low oxidation states– or when it is reduced.[14]
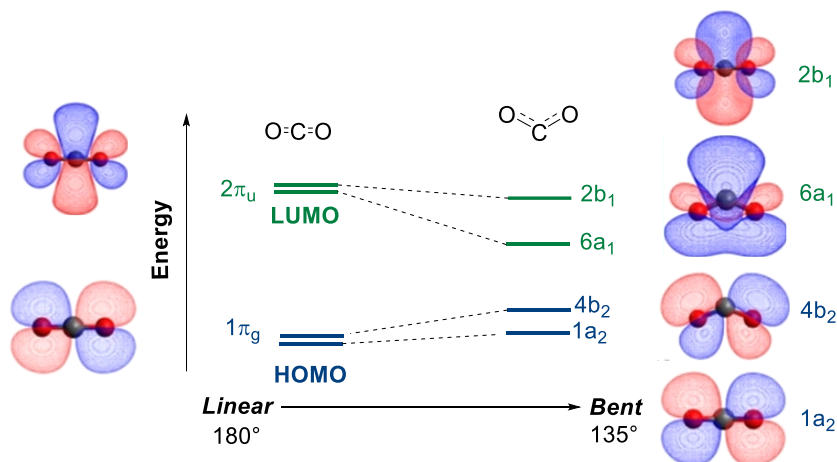
Figure 1. Simplified Walsh diagram for CO_2 bending. Modified figure taken from *ChemPhysChem*, 18(22), **2017**, 3135–3141.

Due to the polarized $C^{\partial+}$-$O^{\partial-}$ bonds, CO_2 may undergo both nucleophilic and electrophilic attacks. However, the terminal oxygens are weakly basic, so the molecule is more likely to undergo nucleophilic additions to the central carbon.

In organic synthesis, the most typical reaction of CO_2 is indeed nucleophilic addition. Carbanions, phenolates, alkoxides, and amines are the common nucleophiles that, in the presence of CO_2 and auxiliary reagents, produce carboxylic acids, carbonates, and urea derivatives. However, the need for either the generation of the nucleophile or the requirement of strong bases, makes their application at the industrial level not very practical (Scheme 1).[15]
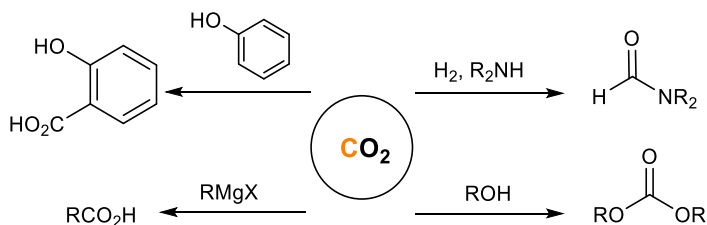
Scheme 1. Uses of CO_2 for organic syntheses.

Metal complexes have shown more versatile reactivity towards CO_2, and reports on its coordination chemistry are known since 1975.[16] Overall, CO_2 exhibits at least four coordination modes involving monodentate (η^1 = *I*, *III*) or bidentate coordination (η^2 = *II*, *IV*), that may differ if upon coordination, charge transfer from the metal to the ligand could occur, forming the respective carbonite species (CO_2^{2-}).[17,18] This is observed in modes *III* and *IV*, or radical anion-type complexes ($CO_2^{\bullet-}$),[19] as depicted in *I* (**Chart 1**). [14,20]

Aresta and coworkers studied the reactivity of Ni(0) phosphine-based complexes in the presence of CO_2 and isolated compound Ni(PCy$_3$)$_2$(CO$_2$)]. In this species, the CO_2 ligand coordinates Ni through the C=O bond, similar to the metal-olefin interaction.[16] Upon coordination, the O-C-O angle is reduced, and the coordinated C-O bond is elongated compared to the free C-O arm. Interestingly, in the presence of early transition metals in a low oxidation state, the metal undergoes oxidative addition of CO_2, yielding a metallocarboxylate species [18]
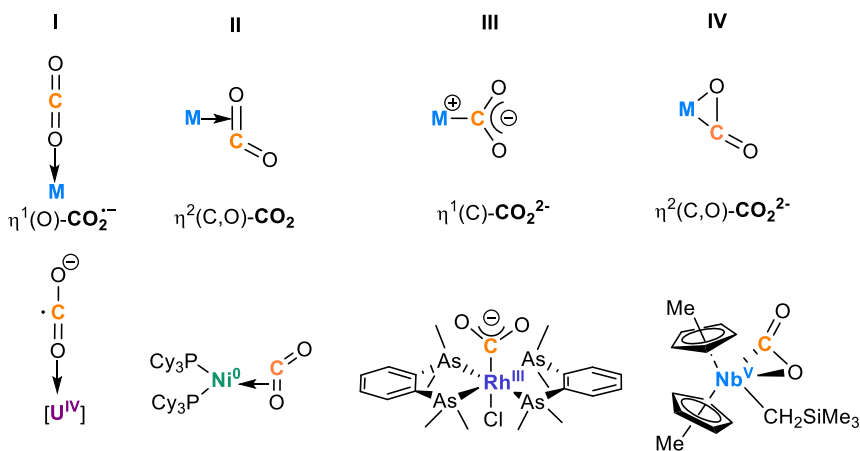
Chart 1. CO_2 coordination complexes.

1.2 Reduction of carbon dioxide

Carbon dioxide can also be activated under reductive conditions. One-electron reduction of CO_2 generates the corresponding radical anion $CO_2^{\bullet-}$. However, the high thermodynamic stability of the molecule and sluggish electron transfer hinders this process. It requires nearly 46 kcal/mol to proceed, partly due to the significant reorganization energy needed to bend the molecule.[21] This is one of the main challenges in CO_2 conversion because any value-added product we could synthesize from multiple direct reductions of CO_2 has the radical anion formation as the first elementary step. The standard redox potentials ($E°$) of the most common redox pairs CO_2/C^{red} are shown in Scheme 2. These values also manifest the difficulty of forming the radical anion, a process that occurs at the most negative reduction potential of -1.90 V vs NHE. Proton-coupled electron-transfers, on the other hand, are more facile, as can be seen from the redox potentials in Scheme 2. Although the direct reduction to carbon monoxide and formic acid are theoretically the most favorable conversions (they do not require quite negative potentials, and only 2e$^-$/2H$^+$ are needed), the slow kinetics of the outer-sphere electron transfer shifts the thermodynamic redox potentials to even more negative values. Therefore, to trigger the reaction at a reasonable rate, an additional driving force is required, called *overpotential* (η).[22]

$E° = -1.90$ V

$CO_2{}^{\bullet-}$

| CH$_4$ + H$_2$O | e$^-$ | CO + H$_2$O |

$E° = -0.24$ V   8 e$^-$ 2 e$^-$ $E° = -0.53$ V

8H$^+$ 2H$^+$

CO$_2$

6 e$^-$ 2 e$^-$

6H$^+$ 2H$^+$

CH$_3$OH + H$_2$O   4 e$^-$ | 4H$^+$ H$_2$COH

$E° = -0.38$ V $E° = -0.61$ V

HCOH + H$_2$O

$E° = -0.48$ V
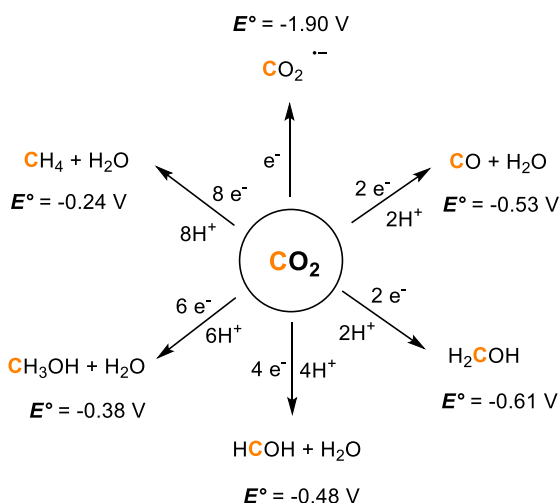
Scheme 2. Cell-half reactions vs. NHE at pH =7 for the reduction of CO₂.

2. The electrocatalysis of CO$_2$ reduction: the molecular approach

Since both kinetic and thermodynamic restraints govern the activation and reduction of CO₂, different approaches to facilitate the conversion have been considered. In this regard, transition metal complexes are a promising alternative because they can intervene in the conversion as substrate activators and catalysts. Because the radical anion CO₂$^{\bullet-}$ is the critical intermediate in any electron transfer implicated in the reduction of CO₂, one way to stabilize it is *via* coordination with a metal complex. Thus, the formation of a CO₂-adduct can potentially decrease the kinetic barriers allowing the reduction to occur faster through an inner-sphere mechanism (Figure 2a).[23]

Upon CO₂ activation, the metal complex catalyzes the reduction. It serves as a bridge between the electron source and the substrate, enabling electron transfer. The electrons can be generated either electrochemically by applying a potential on a working electrode, or photochemically by using a sacrificial electron donor. In this case, one of the advantages of electrochemical reduction is that the applied potential can be easily controlled to match the target reaction's potential. Moreover, green sources like wind and solar energy can generate the electricity required to drive such transformations.[15]
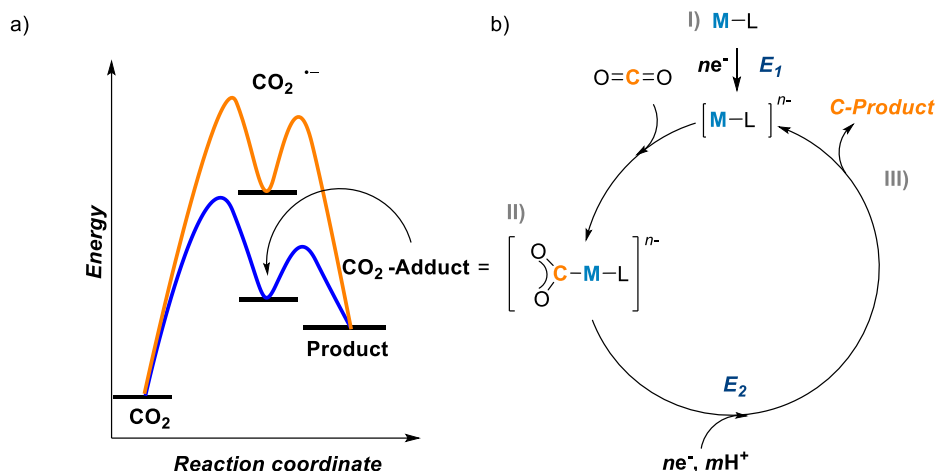
Figure 2. a) Energy profile for one-electron reduction of CO_2 in the absence and presence of a catalyst. b) General catalytic cycle for CO_2 reduction mediated by metal complexes Modified figures taken from *Dalton Trans*. 2022, 6993–7010.

Overall, the electrocatalytic cycle can be divided into three stages: i) *in situ* generation of the active catalyst, ii) formation of the CO_2-catalyst adduct, and iii) further reduction and product release. During the first stage, the complex is reduced on the surface of the electrode with a potential E_1. Subsequently, the reduced catalyst coordinates the substrate, and by supplying electrons and protons, the product is formed and released with a potential E_2 (Figure 2b).[23]

Therefore, structural changes in the metal complex may influence the catalytic activity because both E_1 and substrate/product affinity depend on the intrinsic properties of the catalyst. In this respect, one of the benefits of using molecular catalysts is their precise tunability through ligand modifications.

3. Redox-active ligands in small molecule activation and catalysis

The properties of a metal complex are the consequence of metal-ligand interactions, wherein ancillary ligands modulate complex reactivity through electronic and steric effects. The traditional view about the passive role of ligands has changed over the last decades since the discovery of ligands capable of participating actively in chemical reactions.

The term *non-innocent* is a descriptor applied to ligands that can engage in electron transfer processes or bond cleavage/formation.[24] Redox-active ligands are non-innocent fragments that can be reversibly oxidized or reduced when coordinated to a metal center. Since they can participate in ligand-based reductions, redox-active ligands can act as electron reservoirs, storing and releasing electrons whenever needed, an

important feature for redox catalysis. Consequently, these backbones adopt different resonance structures upon changing redox states, which could also provide an additional venue for reactivity. The Lewis acidity/basicity of the metal is also influenced when switching from one redox state to another; thus, having redox-active fragments could provide another strategy to modulate metal nucleophilicity.

Substrate activation can be achieved *via* metal-ligand cooperativity if the metal is also redox-active. For instance, the catalyst can participate in two-electron reductions by delivering two electrons (one offered by the metal and the other by the ligand). This aspect is desirable when using abundant base metals due to their tendency to undergo one-electron reductions and, with that, the formation of highly reactive radical intermediates. Therefore, by combining a base metal with a redox-active ligand, we can induce noble metal-like reactivity to the catalyst so that it can carry out two-electron processes.[25]

3.1   Redox-active ligands in the electrochemical catalytic reductions

Electrochemical conversion of small molecules is challenging because it involves, besides substrate activation, multielectron redox reactions that are kinetically hindered.[26] In this respect, Queyriaux[27] recently summarized the implications of using a metal catalyst with a redox-active ligand in the electrocatalytic reduction of CO_2 and H^+. Although molecular electrocatalysts with redox-active ligands are usually shown to be i) selective, ii) efficient (work at low overpotentials with high turnover frequencies, and iii) stable, there are also potential disadvantages related to having such reactive fragments.

3.1.1   Selectivity

As mentioned above, the most efficient pathway for CO_2 reduction is the proton-coupled electron transfer. This means that upon supplying CO_2 and protons, the active species must selectively catalyze CO_2 reduction and no other competing transformations, *e.g.*, hydrogen evolution reaction. However, proton reduction is thermodynamically favored ($E°$ [H^+/H_2] = -0.41 V *vs* NHE) compared to the proton-assisted reductions of CO_2 to carbon monoxide and formic acid ($E°$ [CO_2/CO] = -0.53 V; $E°$ [$CO_2/HCOOH$] = -0.61 V *vs* NHE, respectively). Consequently, it is commonly found to have a mixture of products during electrocatalytic tests. In these cases, it has been reported that redox-active ligands may influence product distribution and can thereby lead to higher faradaic efficiency towards the desired reduction product. In contrast, when the catalyst supports an innocent ligand, upon reduction, the negative charge most likely will be located at the metal, increasing its nucleophilicity. This effect has been found to favor protonation, forming a metal-hydride species, the intermediate that is often responsible for the competing hydrogen evolution reaction.

Therefore, we should expect that control of nucleophilicity may be relevant for selectivity in electrocatalytic reduction of CO_2. In fact, it has been hypothesized that having a redox-active motif frees the metal from excess charge lowering its nucleophilicity and, therefore, increasing its selectivity towards CO_2. Of note, a balanced distribution of the electron density is desirable; otherwise, with a poor nucleophilic center, CO_2 activation would not be achieved.

Jurss and coworkers studied the influence of the extent of redox non-innocence character in nickel bipyridyl-*N*-heterocyclic carbene donors in the electrocatalytic CO_2 reduction. They found better faradaic efficiencies for CO production in catalyst **III** with a more rigid and planar framework (Figure 3). DFT calculations showed the correlation between the electronic structure of the active double reduced form and its selectivity towards CO_2. In catalyst **III,** with the more rigid and planar ligand, the electron density resides on the ligand framework, decreasing metal nucleophilicity and, thereby, discouraging metal-hydride formation. In contrast, disruption of the macrocyclic structure, as observed in the *N*-methyl substituted catalyst **I**, reduces the ligand's redox-active character. With that, metal nucleophilicity is enhanced, favoring H⁺ binding, thus the catalytic hydrogen evolution reaction.[28]

With its cobalt analog, the influence of the metal was investigated. Interestingly, catalyst **III** with cobalt also exhibited the highest selectivity toward CO_2 among the three complexes, although in this case, the electronic density is evenly distributed between the ligand and metal. As expected, having a poor nucleophilic metal and a double-reduced ligand gives a 1:1 ratio of CO/H_2 when the catalyst used is **I**.[29]
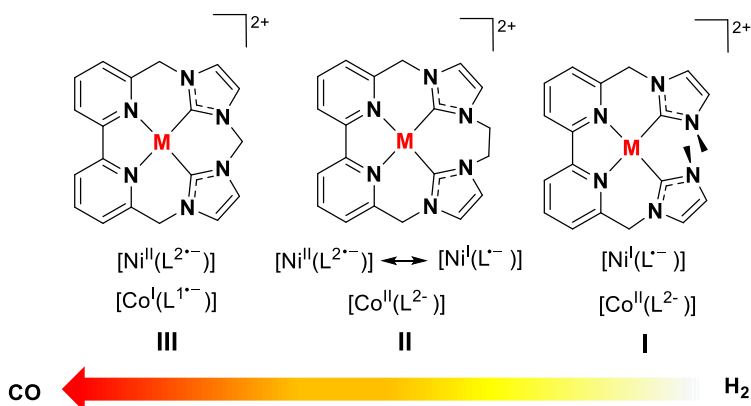
Figure 3. Cobalt complexes with bipyridine *N*-heterocyclic carbenes for CO_2 reduction.

3.1.2   Overpotential requirements

Previously introduced, overpotential (η) refers to the additional amount of energy needed to observe catalysis. This value compares the potential at which the catalysis occurs against the thermodynamic potential ($E°$) of the reaction to catalyze. Therefore, it is preferable that the potential of the active catalyst E_1 should be close enough to $E°(CO_2/CO)$. In this case, modulation of E_1 through systematic changes in the ligand framework is a relevant tool for decreasing overpotential requirements. However, this may also negatively impact the catalytic rate since with low η, metal nucleophilicity falls, hampering CO_2 activation.[23]

In this regard, McCrory discussed the influence of incorporating groups on the ligand backbone to stabilize the CO_2-adduct, avoiding losing catalytic performance while decreasing overpotential. For instance, adding positively charged functional groups can aid in stabilizing the adduct *via* attractive electrostatic forces, as shown for iron tetraphenylporphyrin complexes decorated with trimethylanilium groups (Figure 4a). These catalysts exhibit higher activity at relatively low overpotentials.[30] A similar effect is observed when the ligand contains proton-responsive groups that stabilize the CO_2 adduct through secondary interactions.[23] On this matter, Hess and coworkers recently reported the catalytic activity of Fe and Co complexes supporting the redox non-innocent dihydropyrrole-bisquinazoline ligand [Mabiq] (Figure 4b). Their outcomes indicated that ligand-based reductions in the Fe species positively influence overpotential requirements and selectivity. In the presence of protons, the redox-active ligand undergoes protonation, preventing metal-hydride formation. [31,32]
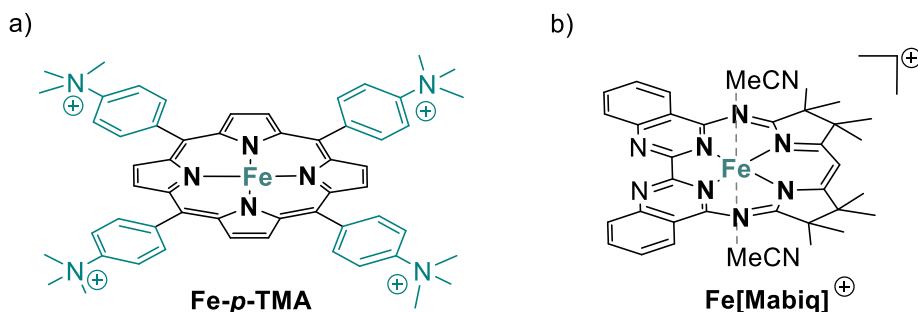
Figure 4. a) Porphyrin and b) bisquinazoline iron-based catalysts for the proton-coupled CO_2 reduction.

3.1.3   Stability and new venues for reactivity

Since the catalyst is active in its reduced state, having a redox non-innocent ligand could improve its stability. Waymouth and coworkers investigated experimentally and computationally the impact of redox-active ligands in the electrochemical behavior of [MnBr(CO)$_3$(L,L).

They discovered that exchanging the bipyridine ligand with the redox-active phenylazopyridine moiety enhances the stability of the first reduced state, avoiding bromide elimination upon one-electron reduction. In this family of catalysts, bromide elimination is followed by complex dimerization, a known deactivation pathway in the catalysis of CO_2 reduction (Scheme 3). [33]
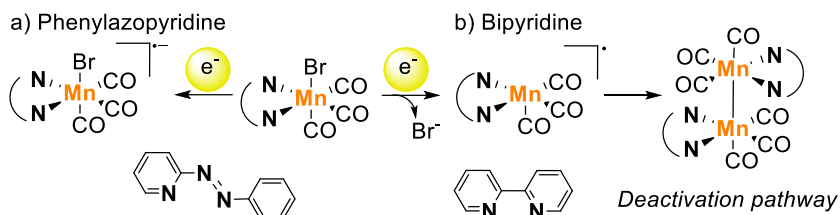
Scheme 3. One-electron reduction of Mn catalysts supporting nitrogen-based ligands.

Accumulation of reducing equivalents in the ligand scaffold may trigger new reactivity patterns otherwise absent in innocent ligands. The Grapperhaus group explored the activity of a Zn(II) catalyst supported by a nitrogen-based macrocycle (thiosemicarbazonate-pyridinehydrozonato). Such catalyst fixes, activates and reduces CO_2 through metal-ligand cooperativity interactions yielding formate (HCO_2^-). It was found that the redox-active macrocyclic ligand featuring a frustrated Lewis pair interaction with Zn(II) promotes CO_2 reduction (Scheme 4).[34]
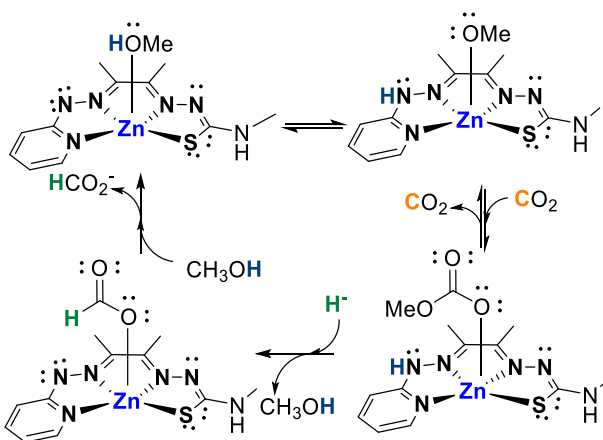
Scheme 4. CO_2 capture and reduction by a Zn(II) macrocyclic complex.

Since redox events may take place on the ligand, these fragments tend to be reactive. Thus, a ligand-based adduct is sometimes preferred over CO_2 addition on the metal center. The ligand-CO_2 interaction might be quite strong in these cases, rendering C-C, C-N, or C-O covalent bonds that inactivate the catalyst. For instance, Kubiak and coworkers observed the formation of a strong C-C coupling between CO_2 and the pyridine monoimine (PMI) ligand when studying the electrocatalytic properties of

[[Ar]PMI)Mo(CO)3] complexes for CO_2 reduction. Although the presence of a redox-active moiety anodically shifts the redox potentials, the stability of the resulting ligand-CO_2 adduct prevents catalysis from taking place (Scheme 5a).[35]

   Redox-active ligands supporting proton-responsive groups have also shown side reactivity. Fujita and coworkers designed a bipyridine ligand with hydroxy functions as proton-responsive groups aiming to enhance the catalytic performance of the benchmark Lehn's catalyst ReCl(CO)3 (L,L) (L,L = bipyridine). They found the catalyst is unstable under reductive conditions and deprotonates with concomitant hydrogen evolution upon adding reducing equivalents. Electrochemical studies with the deprotonated species under catalytic conditions (CO_2, H^+) indicated reprotonation of the proton-responsive groups might be a potential deactivation pathway (Scheme 5b).[36]
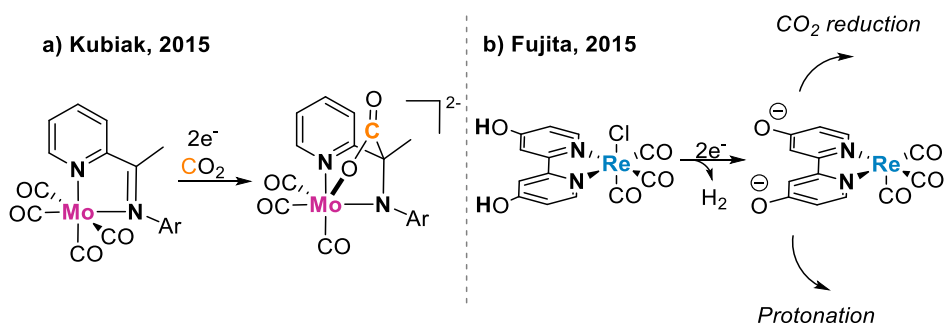
Scheme 5. a) CO_2 activation mediated by a Mo(PMI) complex. b) Reductive deprotonation of a based- bipyridine Re(I) catalyst with proton-responsive groups.

4. Group 7 catalysts for CO_2 reduction

   Extensive research has been focused on developing metal complexes as molecular catalysts for CO_2 reduction. Iron-based catalysts with porphyrins and ruthenium and osmium carbonyl complexes with bipyridine ligands have been studied for this purpose. Moreover, group 9 catalysts supporting N-macrocyclic and pincer-type ligands have also been reported. A feature in common in all these cases is the presumable non-innocent role of the ligand.[22] For group 7, tricarbonyl complexes with α-diimines are the family of catalyst that have been extensively exploited for the electrocatalytic CO_2 reduction.

   In 1984, Lehn and coworkers reported the activity of the *fac*-ReCl(CO)3(bipy) (bipy = bipyrdine) complex for the electrochemical reduction of CO_2. This was a following study inspired by their previous work with Ru(bipy)3(Cl)2 and ReCl(CO)3((bipy), for the photochemically induced reduction. Lehn's catalyst has endured up to now because it is a quite simple complex that selectively produces CO *via* a proton-coupled two-electron pathway with current efficiencies up to 98%.[37]

Lehn's catalyst has been investigated in-depth to understand the fundamentals of its exceptional reactivity, aiming to develop more efficient systems. Computational studies supported by spectroscopic data indicate that the redox non-innocent nature of the bipyridine fragment is responsible for such high selectivity. This is mainly due to the better orbital interaction of the substrate with the catalyst that, in its active state, delocalized electron density on both the metal and the ligand.[38] Although the complex is highly active, the catalysis occurs at somewhat high overpotentials (η = 1.57 V) (**Chart 2a**).

Several Re(I) complexes containing functionalized bipyridines have been studied. For instance, introducing electron-donating groups on the ligand framework enhanced catalytic activity, albeit at the cost of a higher overpotential (η = 1.74 V) (**Chart 2b**).[39] Moreover, the incorporation of hydrogen bond donors at the proximity of the metal center accelerated the catalysis but with increased overpotential (**Chart 2c**).[40]

a) **Lehn's catalyst**
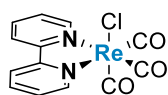
η (V) = 1.57
TOFmax (s-1) = 47.5

b) **Kubiak**, **2010**
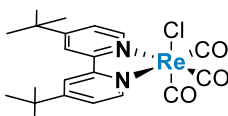
η (V) = 1.74
TOF (s^{-1}) = NR

c) **Jurss**, **2020**
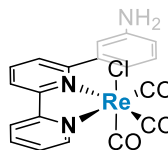
η (V) = 1.44
TOF$_{max}$ (s^{-1}) = 239

d) **Kubiak**, **2016**
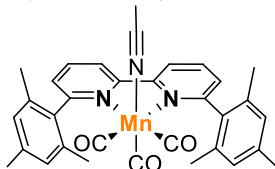
η^{HO} (V) = 1.46
TOF$_{max}$ (s^{-1}) =2000

η^{LO} (V) = 1.06
TOF$_{max}$ (s^{-1}) =3.7

η^{LO}(V) = 0.3-0.45^b
TOF$_{max}$ (s^{-1}) =2.8

e) **Daasbjerg**, **2020**
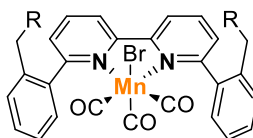
R = OH η (V) = 1.43
TOF$_{max}$ (s^{-1}) = 840

R = NEt$_2$ η (V) = 1.49
TOF$_{max}$ (s^{-1}) = 5500

f) **Duan**, **2020**

η (V) = 1.59
TOF$_{max}$ (s^{-1}) = 3180

Chart 2.Re and Mn catalysts for CO_2 reduction. The overpotentials were calculated using the expression $\eta = E°_{CO_2/CO(MeCN)} - E°_{cat/2}$ were $E°_{cat/2}$ = -0.541 V *vs* Fc$^{+/0}$ when no explicit proton source is present.[30] HO and LO correspond to high and low overpotential catalysis, respectively.^{b} The low overpotential catalysis reported in the presence of Mg^{2+} as Lewis acid.

For group 7 catalysts, two pathways have been elucidated for generating the active complex, the double reduced species. In the two-electron mechanism, the catalyst is formed upon two consecutive one-electron reductions and subsequent halide loss (Scheme 6a). On the other hand, if the halide is released after the first reduction, a 17-electron radical intermediate is formed. Then, dimerization may take place, associated with an increase in overpotential and thus detrimental to catalyst performance (Scheme 6b).[41]
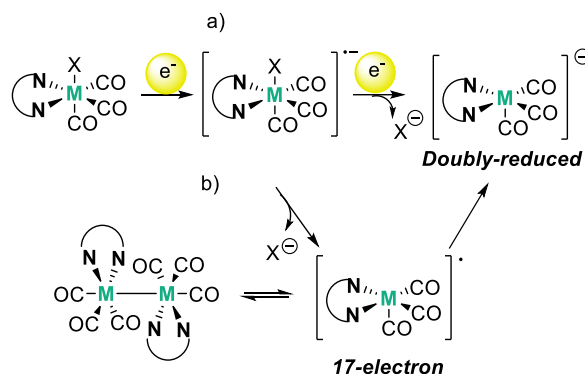
Scheme 6. Reaction mechanism for the formation of the active catalyst for group 7 catalysts.

Complexes with its earth-abundant congener, Mn, have also been studied. In these species, the rate of dimerization is higher. Modification of the ligand steric and electronics can help to hinder dimerization. As previously mentioned, using a redox-active fragment has been shown to prevent halide dissociation.[33] On the other side, including the sterically demanding mesityl groups on the bipyridine does not avoid halide elimination but can block radical dimerization. With this strategy, Kubiak and coworkers achieved catalysis at relatively lower overpotentials when Mg^{2+} is added as a Lewis acid (**Chart 2d**).[42] It was found Mg^{2+} aided in weakening the C-O bond in the CO_2 adduct with the formation of $MgCO_3$ as a driving force. In this case, the addition of trifluoroethanol –commonly used as proton source for the proton-coupled CO_2 reduction– did not improve catalytic response at low overpotentials. Since the thermodynamic redox potential for the proton-coupled reduction ($E°(CO_2/CO) = -0.541$ V *vs* $Fc^{+/0}$) is more positive than the redox potential of the reduction under reductive disproportionation conditions ($E°(CO_2/CO) = -1.15$ V *vs* $Fc^{+/0}$ when $MgCO_3$ is formed) the overpotential found for $MnBr(CO)_3(mesbpy)$ in the absence of protons is lower.

The incorporation of different proton-donor groups on the bipyridine moiety also influenced product selectivity. Daasbjerg and coworkers found that the presence of a hydroxy substituent at the benzylic position of the 2,2-benzyl-bipyridine ligand promotes CO formation, while its substitution by an amine group catalyzes formic acid production (**Chart 2e**).[43] Finally, the groups of Lloret-Fillol and Royo investigated the activity of bulky substituents in N-heterocyclic carbenes and reported enhanced catalytic activity but with high overpotentials (**Chart 2f**). [44]

5. The formazan/ate scaffold, a promising redox-active ligand in catalysis

Throughout this chapter, the reactivity of non-innocent ligands in small molecule activation and catalysis was clearly emphasized. The bipyridine ligand and analogs (α-diimine motifs) have demonstrated their capabilities to support redox transformations, in which their non-innocent nature plays an essential role in selectivity. In this matter, a wide variety of conjugated nitrogen-based backbones with redox non-innocent character are available to be assessed for the electrochemical reduction of CO_2.

5.1 General features

Within this library of compounds, the formazan/ate ligand attracted our attention. Formazans are a large family of molecules containing the skeleton {–N=N–C(R)=N–NH–} (Figure 5a). First synthesized and characterized by von Pechmann and Bamberger,[45] formazans are colorful compounds that exhibit well-defined redox states, widely used in clinical assays to quantify cell metabolism.[46]

In coordination chemistry, their deprotonated form, the formazanate anion {–N=N–C(R)=N–N–}⁻, has been used as a chelating ligand (Figure 5a). Although, structurally, it resembles the β-diketiminate ligand, its properties might differ. For instance, β-diketiminate ligands are less stable once they undergo redox changes.[47] This contrasts to what is observed in formazanate ligands, in which case, having a nitrogen-rich conjugated scaffold with low-lying frontier orbitals give rise to complexes with particular electrochemical and photophysical properties that are not accessible in the β-diketiminate analogs.[48] An additional advantage is its straightforward derivatization –as long as the starting materials are available– that makes possible to functionalize the backbone and thereby, systematically tuning the electronic structure of the metal complex.[45,49]

Four donor sites enable different coordination modes, making the formazanate ligand a flexible backbone. Complexes with the main group and transition elements have been described,[50] exhibiting three characteristic coordination modes: *closed*, *open,* and *linear*. (Figure 5b).[51–53]

a)

Formazan → **Formazanate** + H⁺

- -

b)

closed   *open*   *linear*
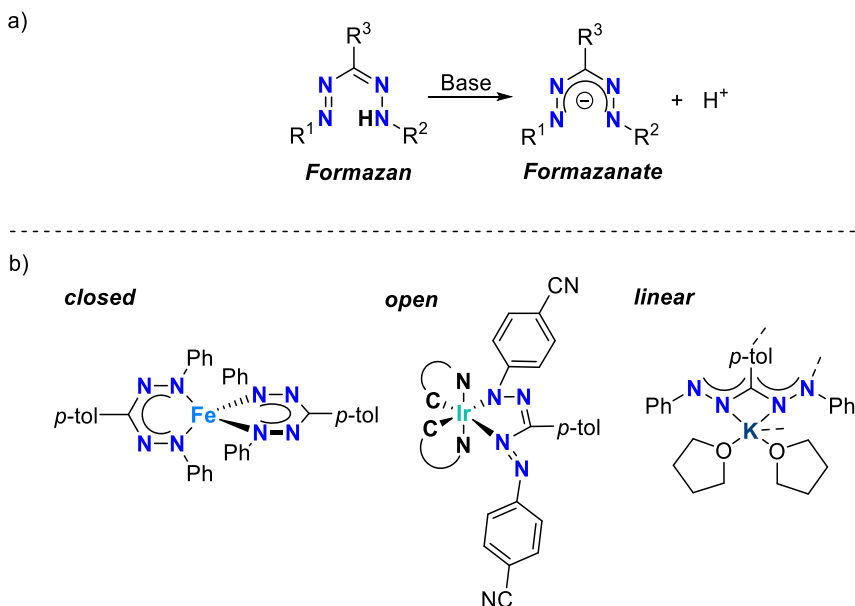
Figure 5. a) Structure of the formazan and formazanate ligand and b) different coordination modes for formazanate complexes.

The most common binding fashion is the *closed* form that renders six-membered rings with full π-delocalization within the metallacycle. Few examples have been reported for the *open* coordination, that gives access to five-membered chelates, wherein charge delocalization is less pronounced. It has been suggested that the steric hindrance of the substituents on the terminal N-atoms may influence the coordination pattern, and, usually, such species are in equilibrium with their corresponding *closed* forms (Scheme 7).[54]
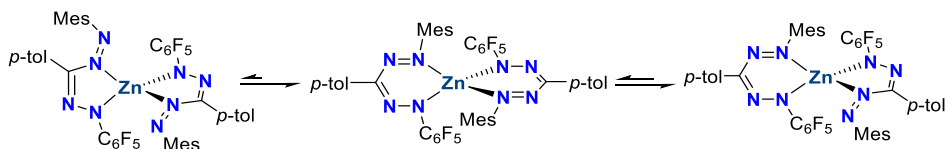
Scheme 7. Equilibrium between the *open*- and *closed*-form in Zn(II) formazanates.

Formazanate ligands are strong π-acceptors and their π-acidity can be systematically tuned by changing the nature of the substituents. Since the frontier orbitals in formazanate complexes are mainly localized on the formazanate fragment, changes in the substitution pattern also alter the energy of the HOMO and LUMO levels and, with that, influence other properties such as redox potentials.[50]

5.2   Formazanate ligands as electron reservoirs

Formazanate complexes display a characteristic redox behavior, typically defined by ligand-centered reversible redox events. In 2014, our research group described the electrochemical properties of bis(formazanate) Zn(II) complexes and reported their isolation in three redox states: neutral, anionic, and dianionic. One- and two-electron reductions were identified as ligand-centered processes yielding the anionic and dianionic metalloverdazyl radicals, respectively, wherein each ligand unit accepts one electron (Scheme 8).[55]

Zinc
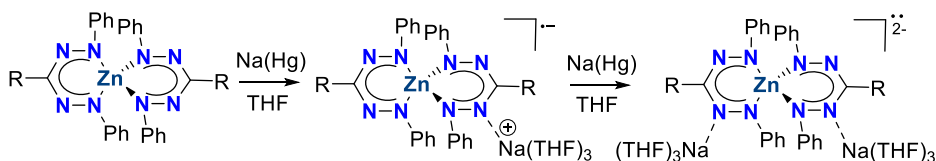
Scheme 8. Reduction of bis-formazanate Zn(II) complexes, R = ^{t}Bu, p-tol;

More interestingly, the ability of the formazanate moiety to perform its role as an electron sink was exemplified with monoformazanate boron species. Such complexes can afford the addition of up to two reducing equivalents, rendering a dianionic formazanate complex. This study showed that steric constraints may have an impact on the reversibility of the second reduction event (Scheme 9).[56] Similar outcomes were reported by Gilroy and coworkers for monoformazanate boron difluoride complexes, in which case the formazanate serves as a two-electron reservoir, although the double-reduced species is less stable.[57]

Electron storage capabilities have also been described for formazanate complexes with Al,[58] Fe[59], Ir[60], Pt[61]. In complexes with the main group and transition elements, the redox potentials are significantly influenced by the nature of the substituents attached to the nitrogen atoms. With electron withdrawing groups, reduction potentials are shifted anodically, facilitating reduction processes.

Boron
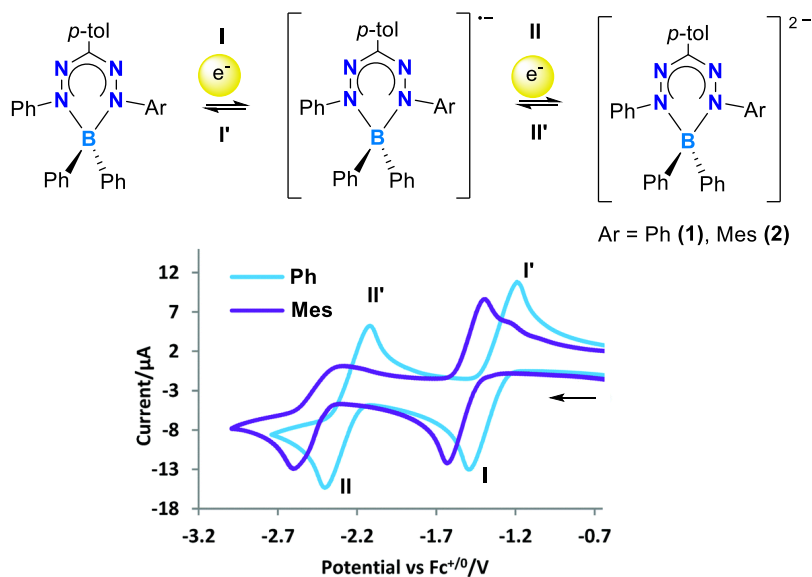
Scheme 9. Mono(formazanate) boron species: neutral, monoanionic and dianionic; and the cyclic voltammogram of B(PhNNC(p-tol)NNAr)(Ph)$_2$recorded in THF at 100 mV/s. Modified figure taken from *Chem. Commum.*,**2017**, *53*(3), 513–516.

5.3   Reactivity of the reduced formazanate fragment

Reduced formazanate species have shown promising reactivity in bond activation and catalysis. For instance, the electrons stored in the two-electron reduced boron compound 1 (Scheme 9) are used to promote nucleophilic attacks on molecules of the type E-X (E$^+$ = Bn$^+$, H$^+$) that generate the corresponding leucoverdazyl-type compounds. The N-E interaction in these species is shown to be weak as the addition of one equivalent of TEMPO yields the stable borataverdazyl radical anion and the corresponding oxypiperidine species (Scheme 10).[62]
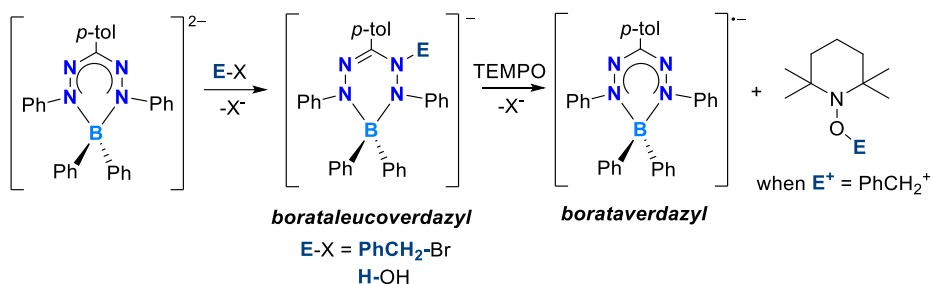
Scheme 10. Electrophilic addition on the two-electron reduced boron species 1.

Switchable catalysis stands for the use of external stimuli to control reactivity. Functional groups embedded in the catalyst's structure can respond reversibly to light, metal ion-coordination, changes in pH or redox state and thus promote one or more chemical events during catalysis.[63] On this subject, redox-active units can play a role as triggers depending on their redox states.[64] Recently, our group explored the activity of a dinuclear formazanate Zn(II) species as a catalyst for switchable ring opening polymerization (ROP). It was found the catalyst is only active in its reduced state with 94% conversion of the starting monomer (lactide), while oxidation of the ligand turns off the polymerization.

Further investigation into the catalyst's electronic structure indicates it exists as a radical mononuclear complex that coordinates the substrate. The flexible six-membered formazanate species, then, is converted into the five-membered isomer, leaving a nucleophilic pendant N-arm that attacks the coordinated lactide monomer. At this step, the polymerization process starts with the incorporation of lactide units *via* the macrocycle radical-type intermediate. By nucleophilic attack of the zinc-coordinated oxygen to the Zn-bound carbonyl group, the catalyst is regenerated, and cyclic polylactide release as product (Scheme 11). The addition of an oxidant stops the catalytic activity. [65] This study showed that the redox activity and hemilability of the formazanate ligands are promising properties that one may take advantage of in other catalytic systems.
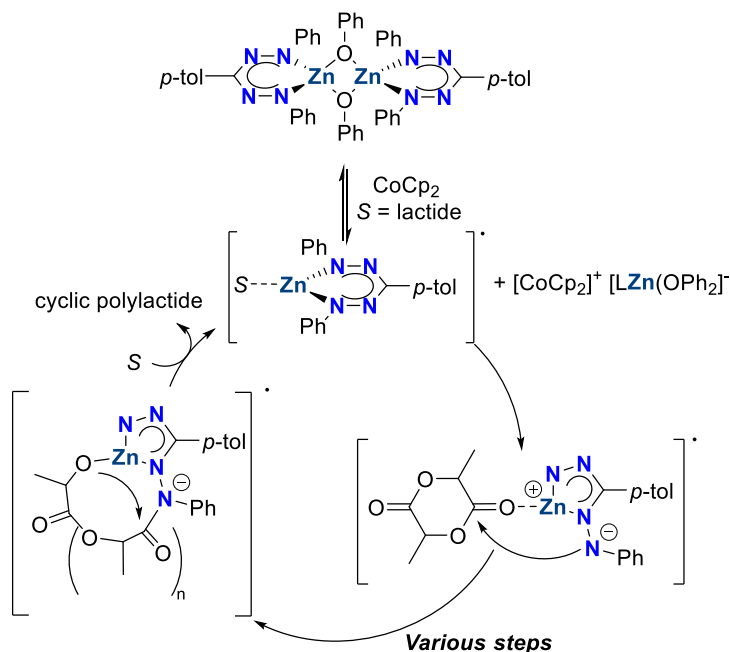
Scheme 11. Proposed catalytic cycle for switching ROP by a formazanate Zn(II) catalyst. Scheme taken from *ACS Catal.*, **2022**, *12*, 4125–4130.

5.4   Reactivity of formazanate complexes with CO_2

So far, there are few examples of the reactivity of formazanate complexes toward carbon dioxide. The group of Holland reported in 2018 that low-coordinate formazanate silylamide iron(II) complexes react with CO_2 to yield trimethylsilyl isocyanate (TMSNCO) and the corresponding formazanate siloxide iron compound. The mechanism suggests that CO_2 reversibly coordinates to the metal center in a $\eta^1(O)$ fashion upon solvent dissociation. By nucleophilic attack of the silylamide on the coordinated CO_2 and subsequent $SiMe_3$ migration, a silylamide carbamate iron intermediate is generated. Upon reaction with another carbamate molecule, a dinuclear species is afforded with concomitant release of TMSNCO. It was concluded that the presence of solvent molecules encourages additional pathways that also lead to the formation of TMSNCO. In this case, the formazanate behaves as a traditional 'innocent' ligand (Scheme 12a).[66]

Similarly, our group informed in 2019 the catalytic studies of monoformazanate ferrate(II) dihalide complexes for selective conversion of CO_2 into cyclic carbonates in the presence of epoxide.[67] Ligand exchange of the labile halides by epoxide and subsequent nucleophilic attack of the free X- onto the coordinated oxirane enables ring opening.

Then, CO_2 insertion into the Fe–O bond followed by ring closure regenerates the catalyst. Again, the metal drives the reaction in this example, while the formazanate acts as an ancillary ligand (Scheme 12b).
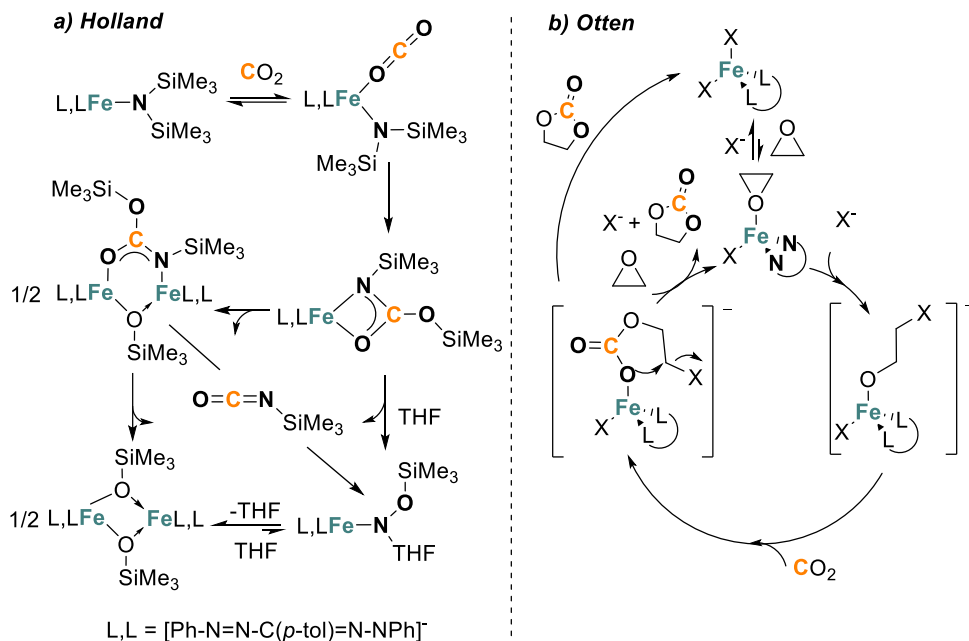
Scheme 12. Carbon dioxide activation by iron formazanate complexes. Schemes taken from. *Angew. Chem. Int. Ed.*, **2018** *130*, 6617–6621 and. *ChemSusChem*, **2019**, *12*, 3635–3641.

Very recently, a report from the Roesky group describes the insertion of CO_2 into a bis(formazanate) magnesium complex as a precedent of substrate activation achieved through metal-ligand cooperativity. The reaction was carried out with an excess of dry ice in toluene with immediate color change, a highly indicative of ligand-based reactivity. Isolation of crystalline material along with spectroscopic characterization, evidences CO_2 insertion into the Mg–N bond, rendering a trimeric species. The insertion was proven to be reversible as heating the reaction mixture regenerates the starting material. It was proposed magnesium coordinates CO_2 in a $\eta^1(O)$ fashion; then, by nucleophilic attack of the terminal formazanate nitrogen to the electrophilic carbon and further rearrangement, a five-membered formazan chelate fused to a five-membered carbamate-like ring is afforded. It subsequently assembles into a trinuclear compound (Scheme 13).[68]
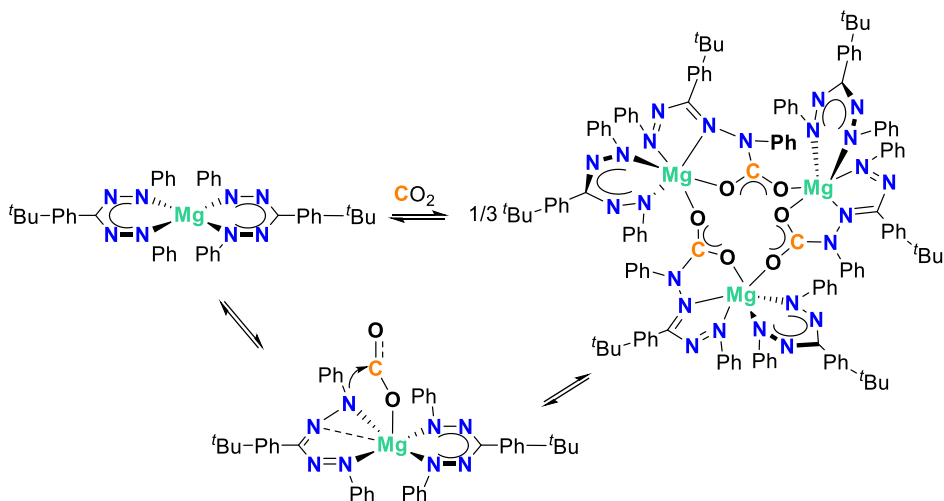
Scheme 13. Reversible insertion of CO_2 into a bis(formazanate)magnesium complex.

6. Motivation

Although the coordination chemistry of the formazanate ligand has been described since 1941 for various transition elements,[50,69] for d[7] metals, it has been scarcely explored. Brown and coworkers reported the reaction of Mn(acac)$_3$ with an excess of the neutral benzothiazolylformazan ligand in refluxing ethanol that yielded the bis(benzothiazolylformazanate) Mn(II) complex, wherein the formazan served both as ligand and reducing agent.[70] Apart from this, examples of coordination complexes with its heavier Re congener are still unknown to the best of our knowledge. Furthermore, inspired by the precedents on chemical reactivity driven by complexes with redox-active ligands in small molecule activation, we developed in this project a fundamental study on the coordination chemistry of formazan/ate ligands towards carbonyl Re(I) species, aiming to evaluate the catalytic properties of the resulting complexes for the electrochemical reduction of CO_2 (Scheme 14).

We envisioned replacing the redox non-innocent bipyridine moiety with the redox-active formazan/ate ligand in ReX(CO)$_3$(bpy) catalyst could enhance its stability, preventing the detrimental dimerization pathway that takes place as a consequence of the poor ability of the catalyst to distribute the electronic equivalents upon reduction (Scheme 6). Moreover, by synthesizing Re(I) complexes with the neutral formazan ligand, we sought to design a catalyst that could act as a two-electron/one-proton reservoir aiming to facilitate substrate activation and reduction *via* secondary interactions. Finally, with the preparation of the formazanate Re(I) analogs, we pursued to compare the influence of the proton relay.

Our findings indicate that careful considerations must be taken in designing catalysts with redox non-innocent ligands, as an enhanced redox activity can be translated into poor reactivity of the metal center. On the other hand, our outcomes also represent another example of the key role of redox-active ligands to drive small molecule activation.
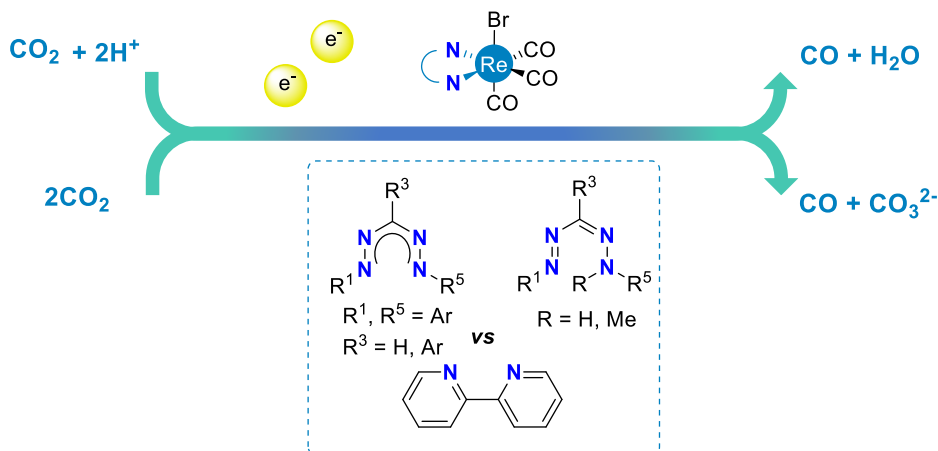
Scheme 14. Proposed project.

7.   Thesis outline

In this chapter, we have revised the fundamentals of CO_2 conversion and discussed the previous literature on electrocatalysis mediated by metal complexes. *Chapter 2* describes the synthetic studies of Re(I) complexes supporting the neutral formazan ligand. The complete characterization of five complexes with different triarylformazan ligands is presented, and their electronic properties are studied by spectroscopic and computational methods. In *Chapter 3*, the preparation of formazanate Re(I) derivatives is described, and their electronic properties are compared against their formazan analogs by spectroscopic and computational studies.

Chapter 4 is devoted to an extensive study of the (spectro)electrochemical properties of formazan and formazanate Re(I) species and the electronic structure of their reduced forms elucidated by computational methods. Finally, in *Chapter* 5, the evaluation of the electrocatalytic activity of the complexes herein investigated is presented. In this chapter, we discussed the correlation between the electronic structure of the reduced forms and their reactivity towards CO_2.

References

(1)   National Oceanic and Atmospheric Administration U.S. Department of Commerce. *Atmosphere*.

(2)   Ali, K. A.; Ahmad, M. I.; Yusup, Y. Issues, Impacts, and Mitigations of Carbon Dioxide Emissions in the Building Sector. *Sustain.* **2020**, *12* (7247), 1–11. https://doi.org/10.3390/SU12187427.

(3)   Gómez-García, M. A.; Pitchon, V.; Kiennemann, A. Pollution by Nitrogen Oxides: An Approach to NOx Abatement by Using Sorbing Catalytic Materials. *Environ. Int.* **2005**, *31*, 445–467. https://doi.org/10.1016/j.envint.2004.09.006.

(4)   Valluri, S.; Claremboux, V.; Kawatra, S. Opportunities and Challenges in CO_2 Utilization. *J. Environ. Sci.* **2022**, *113*, 322–344. https://doi.org/10.1016/j.jes.2021.05.043.

(5)   Timmons, A. J.; Symes, M. D. Converting between the Oxides of Nitrogen Using Metal-Ligand Coordination Complexes. *Chem. Soc. Rev.* **2015**, *44* (19), 6708–6722. https://doi.org/10.1039/c5cs00269a.

(6)   Yamamura, T.; Nakanishi, T.; Lee, J.; Yamate, S.; Otomo, J. Design and Evaluation of Hydrogen Energy Storage Systems Using Metal Oxides. *Energy & Fuels* **2022**, *36* (17), 9745–9756. https://doi.org/10.1021/acs.energyfuels.2c00910.

(7)   Wu, H. L.; Li, X. B.; Tung, C. H.; Wu, L. Z. Bioinspired Metal Complexes for Energy-Related Photocatalytic Small Molecule Transformation. *Chem. Commun.* **2020**, *56* (99), 15496–15512. https://doi.org/10.1039/d0cc05870j.

(8)   Ghosh, A. C.; Duboc, C.; Gennari, M. Synergy between Metals for Small Molecule Activation: Enzymes and Bio-Inspired Complexes. *Coor. Chem. Rev*, **2021**, *428*, 213606–213628. https://doi.org/10.1016/j.ccr.2020.213606.

(9)   Macyk, W.; Franke, A.; Stochel, G. Metal Compounds and Small Molecules Activation - Case Studies. *Coord. Chem. Rev.* **2005**, *249* (21–22), 2437–2457. https://doi.org/10.1016/j.ccr.2005.06.018.

(10)   United States Environmental Protection Agency. *Overview of Greenhouse Gases*.

(11)   Tollefson, J. How Hot Will Earth Get by 2100? *Nature* **2020**, *580*, 444–446.

(12)   Modak, A.; Bhanja, P.; Dutta, S.; Chowdhury, B.; Bhaumik, A. Catalytic Reduction of CO_2 into Fuels and Fine Chemicals. *Green Chem.* **2020**, *22* (13), 4002–4033. https://doi.org/10.1039/d0gc01092h.

(13)   Aresta, M.; Dibenedetto, A.; Quaranta, E. *Reaction Mechanisms in Carbon Dioxide Conversion*; Springer, **2016**, 221. https://doi.org/10.1007/978-3-662-46831-9.

(14)   Paparo, A.; Okuda, J. Carbon Dioxide Complexes: Bonding Modes and Synthetic Methods. *Coord. Chem. Rev.* **2017**, *334*, 136–149. https://doi.org/10.1016/j.ccr.2016.06.005.

(15)   Federsel, C.; Jackstell, R.; Beller, M. State-of-the-Art Catalysts for Hydrogenation of Carbon Dioxide. *Angew. Chem. Inter. Ed.* **2010**, *49* (36), 6254–6257. https://doi.org/10.1002/anie.201000533.

(16)   Michele Aresta, B.; Francesco Nobile, C.; Albano, V. G.; Forni, E.; Manassero, M. New Nickel-Carbon Dioxide Complex: Synthesis, Properties, and Crystallographic Characterization of (Carbon Dioxide)-Bis(Tricyclohexylphosphine)Nickel. *J. Chem. Soc. Chem. Comm.* **1975,** 636-636. https://doi.org/10.1039/C39750000636.

(17)   Herskovitz, T.; Department, D.; Pont, I.; Station, E.; November, R. Carbon Dioxide Coordination Chemistry. 5. The Preparation and Structure of $Rh(N1-CO_2)(Cl)(Diars)_2$. *J. Am. Chem. Soc.* **1983**, *105*, 5914–5915.

(18)   Bristow, G. S.; Hitchcock, P. B.; Lappert, M. F. A Novel Carbon Dioxide Complex: Synthesis and Crystal Structure of $[Nb(n-C_5H_4Me)_2(CH_2SiMe_3)(n^2 =CO_2)]$. *J. Chem. Soc. Comm. Chemm.* **1981**, 1145–1146. https://doi.org/10.1039/C39810001145.

(19)   Castro-Rodriguez, I.; Nakai, H.; Zakharov, L. N. A Linear, O-Coordinated n^1-CO_2 Bound to Uranium. *Science,* **2004**, *305*, 1757–1760. https://10.1126/science.1102602.

(20)   Yin, X.; Moss, J. R. Recent Developments in the Activation of Carbon Dioxide by Metal Complexes. *Coord. Chem. Rev.* **1999**, *181* (1), 27–59. https://doi.org/10.1016/S0010-8545(98)00171-4.

(21)   Schneider, J.; Jia, H.; Muckerman, J. T.; Fujita, E. Thermodynamics and Kinetics of CO_2, CO, and H^+ binding to the Metal Centre of CO_2 reduction catalysts. *Chem. Soc. Rev.* **2012**, *41* (6), 2036–2051. https://doi.org/10.1039/c1cs15278e.

(22)   Francke, R.; Schille, B.; Roemelt, M. Homogeneously Catalyzed Electroreduction of Carbon Dioxide - Methods, Mechanisms, and Catalysts. *Chem. Rev.* **2018**, *118* (9), 4631–4701. https://doi.org/10.1021/acs.chemrev.7b00459.

(23)   Nie, W.; McCrory, C. C. L. Strategies for Breaking Molecular Scaling Relationships for the Electrochemical CO_2 Reduction Reaction. *Dalton Trans.* **2022**, *51*, 6993–7010. https://doi.org/10.1039/d2dt00333c.

(24)   Berben, L. A.; De Bruin, B.; Heyduk, A. F. Non-Innocent Ligands. *Chem. Commun.* **2015**, *51* (9), 1553–1554. https://doi.org/10.1039/c4cc90480j.

(25)   Chirik, P. J.; Wieghardt, K. Radical Ligands Confer Nobility on Base-Metal Catalysts. *Science* **2010**, *327* (5967), 794–795. https://doi.org/10.1126/science.1183281.

(26)   Collman, J. P.; Wagenknecht, P. S.; Hutchison, J. E. Molecular Catalyst for Multielectron Redox Reactions of Small Molecules: The "Cofacial Metallodiporphyrin" Approach. *Angew. Chem., Inter. Ed.* **1994**, *33*, 1537–1554. https://doi.org/10.1002/anie.199415371.

(27)   Queyriaux, N. Redox-Active Ligands in Electro-assisted Catalytic H^+ and CO_2 Reductions: Benefits and Risks. *ACS Catal.* **2021**, 4024–4035. https://doi.org/10.1021/acscatal.1c00237.

(28)   Su, X.; McCardle, K. M.; Panetier, J. A.; Jurss, J. W. Electrocatalytic CO_2 Reduction with Nickel Complexes Supported by Tunable Bipyridyl-N-Heterocyclic Carbene Donors: Understanding Redox-Active Macrocycles. *Chem. Commun.* **2018**, *54* (27), 3351–3354. https://doi.org/10.1039/c8cc00266e.

(29)   Su, X.; McCardle, K. M.; Chen, L.; Panetier, J. A.; Jurss, J. W. Robust and Selective Cobalt Catalysts Bearing Redox-Active Bipyridyl- N-Heterocyclic Carbene Frameworks for Electrochemical CO_2 Reduction in Aqueous Solutions. *ACS Catal.* **2019**, *9*, 7398–7408. https://doi.org/10.1021/acscatal.9b00708.

(30)   Azcarate, l.; Costentin, C.; Robert, M.; Savéant, J. M. Through-Space Charge Interaction Substituent Effects in Molecular Catalysis Leading to the Design of the Most Efficient Catalyst of CO_2 to CO Electrochemical Conversion. *J. Am. Chem. Soc.* **2016**, *138* (51), 16639–16644. https://doi.org/10.1021/jacs.6b07014.

(31)   Rickmeyer, K.; Niederegger, L.; Keilwerth, M.; Hess, C. R. Multifaceted Role of the Non-innocent Mabiq Ligand in Promoting Selective Reduction of CO_2 to CO. *ACS Catal.* **2022**, *12* (5), 3046–3057. https://doi.org/10.1021/acscatal.1c04636.

(32)   Kaspar, M.; Altmann, P. J.; Pöthig, A.; Sproules, S.; Hess, C. R. A Macrocyclic "Co0" Complex: The Relevance of Ligand Non-Innocence to Reactivity. *Chem. Comm.* **2017**, *53* (53), 7282–7285. https://doi.org/10.1039/c7cc02239e.

(33)   Matson, B. D.; McLoughlin, E. A.; Armstrong, K. C.; Waymouth, R. M.; Sarangi, R. Effect of Redox Active Ligands on the Electrochemical Properties of Manganese Tricarbonyl Complexes. *Inorg. Chem.* **2019**, *58*, 7453–7465. https://doi.org/10.1021/acs.inorgchem.9b00652.

(34)   Cronin, S. P.; Strain, J. M.; Mashuta, M. S.; Spurgeon, J. M.; Buchanan, R. M.; Grapperhaus, C. A. Exploiting Metal-Ligand Cooperativity to Sequester, Activate, and Reduce Atmospheric Carbon Dioxide with a Neutral Zinc Complex. *Inorg. Chem.* **2020**, *59* (7), 4835–4841. https://doi.org/10.1021/acs.inorgchem.0c00121.

(35)   Sieh, D.; Lacy, D. C.; Peters, J. C.; Kubiak, C. P. Reduction of CO_2 by Pyridine Monoimine Molybdenum Carbonyl Complexes: Cooperative Metal-Ligand Binding of CO_2. *Chem. Eur. J.* **2015**, *21* (23), 8497–8503. https://doi.org/10.1002/chem.201500463.

(36)   Manbeck, G. F.; Muckerman, J. T.; Szalda, D. J.; Himeda, Y.; Fujita, E. Push or Pull? Proton Responsive Ligand Effects in Rhenium Tricarbonyl CO_2 Reduction Catalysts. *J. Phys. Chem. B* **2015**, *119* (24), 7457–7466. https://doi.org/10.1021/jp511131x.

(37)   Hawecke, J.; Lehn, J. M. Electrocatalytic Reduction of Carbon Dioxide Mediated by Re(Bipy)(CO)$_3$Cl. *J. Chem. Soc. Dalton Trans.* **1984**, 717–718. https://doi.org/10.1016/j.chempr.2017.09.018.

(38)   Benson, E. E.; Sampson, M. D.; Grice, K. A.; Smieja, J. M.; Froehlich, J. D.; Friebel, D.; Keith, J. A.; Carter, E. A.; Nilsson, A.; Kubiak, C. P. The Electronic States of Rhenium Bipyridyl Electrocatalysts for CO$_2$ Reduction as Revealed by X-Ray Absorption Spectroscopy and Computational Quantum Chemistry. *Angew. Chem. Inter. Ed.* **2013**, *52*, 4841–4844. https://doi.org/10.1002/anie.201209911.

(39)   Smieja, J. M.; Kubiak, C. P. Re(Bipy-tBu)(CO)$_3$Cl-Improved Catalytic Activity for Reduction of Carbon Dioxide: IR-Spectroelectrochemical and Mechanistic Studies. *Inorg. Chem.* **2010**, *49*, 9283–9289. https://doi.org/10.1021/ic1008363.

(40)   Talukdar, K.; Sinha Roy, S.; Amatya, E.; Sleeper, E. A.; Le Magueres, P.; Jurss, J. W. Enhanced Electrochemical CO$_2$ Reduction by a Series of Molecular Rhenium Catalysts Decorated with Second-Sphere Hydrogen-Bond Donors. *Inorg. Chem.* **2020**, *59* (9), 6087–6099. https://doi.org/10.1021/acs.inorgchem.0c00154.

(41)   Sinopoli, A.; La, N. T.; Martinez, J. F.; Wasielewski, M. R.; Sohail, M. Manganese Carbonyl Complexes for CO$_2$ Reduction. *Coord. Chem. Rev.* **2018**, *365*, 60–74. https://doi.org/10.1016/j.ccr.2018.03.011.

(42)   Sampson, M. D.; Kubiak, C. P. Manganese Electrocatalysts with Bulky Bipyridine Ligands: Utilizing Lewis Acids to Promote Carbon Dioxide Reduction at Low Overpotentials. *J. Am. Chem. Soc.* **2016**, *138* (4), 1386–1393. https://doi.org/10.1021/jacs.5b12215.

(43)   Rønne, M. H.; Cho, D.; Madsen, M. R.; Jakobsen, J. B.; Eom, S.; Escoudé, É.; Hammershøj, H. C. D.; Nielsen, D. U.; Pedersen, S. U.; Baik, M. H.; Skrydstrup, T.; Daasbjerg, K. Ligand-Controlled Product Selectivity in Electrochemical Carbon Dioxide Reduction Using Manganese Bipyridine Catalysts. *J. Am. Chem. Soc.* **2020**, *142* (9), 4265–4275. https://doi.org/10.1021/jacs.9b11806.

(44)   Franco, F.; Pinto, M. F.; Royo, B.; Lloret-Fillol, J. A Highly Active N-Heterocyclic Carbene Manganese(I) Complex for Selective Electrocatalytic CO$_2$ Reduction to CO. *Angew. Chem. Int. Ed.* **2018**, *57*, 4603–4606. https://doi.org/10.1002/anie.201800705.

(45)   Nineham, A. W. The Chemistry of Formazans and Tetrazolium Salts. *Chem. Rev.* **1955**, *55* (2), 355–483. https://doi.org/10.1021/cr50002a004.

(46)   Ghasemi, M.; Turnbull, T.; Sebastian, S.; Kempson, I. The Mtt Assay: Utility, Limitations, Pitfalls, and Interpretation in Bulk and Single-Cell Analysis. *Int. J. Mol. Sci.* **2021**, *22* (23). https://doi.org/10.3390/ijms222312827.

(47)   Khusniyarov, M. M.; Bill, E.; Weyhermüller, T.; Bothe, E.; Wieghardt, K. Hidden Noninnocence: Theoretical and Experimental Evidence for Redox Activity of a β-Diketiminate(1-) Ligand. *Angew. Chem. Int. Ed.* **2011**, *50* (7), 1652–1655. https://doi.org/10.1002/anie.201005953.

(48)   Camp, C.; Arnold, J. On the Non-Innocence of "Nacnacs": Ligand-Based Reactivity in β-Diketiminate Supported Coordination Compounds. *Dalton Trans.* **2016**, *45* (37), 14462–14498. https://doi.org/10.1039/c6dt02013e.

(49)   Katrizky, A.; Belyakov, S.; Cheng, D.; Durst, D. Syntheses of Formazans under Phase-Transfer Conditions. *Synth.* **1995**, *5*, 577–581. https://doi.org/10.1055/s-1995-3958.

(50)   Gilroy, J. B.; Otten, E. Formazanate Coordination Compounds: Synthesis, Reactivity, and Applications. *Chem. Soc. Rev.* **2020**, *49* (1), 85–113. https://doi.org/10.1039/c9cs00676a.

(51)   Milocco, F.; De Vries, F.; Bartels, I. M. A.; Havenith, R. W. A.; Cirera, J.; Demeshko, S.; Meyer, F.; Otten, E. Electronic Control of Spin-Crossover Properties in Four-Coordinate Bis(Formazanate) Iron(II) Complexes. *J. Am. Chem. Soc.* **2020**, *142* (47), 20170–20181. https://doi.org/10.1021/jacs.0c10010.

(52)   Kabir, E.; Patel, D.; Clark, K.; Teets, T. S. Spectroscopic and Electrochemical Properties of Electronically. *Inorg. Chem.* **2018**, *57*, 10906–10917. https://doi.org/10.1021/acs.inorgchem.8b01543.

(53)   Travieso-Puente, R.; Chang, M.; Otten, E. Alkali Metal Salts of Formazanate Ligands: Diverse Coordination Modes as a Result of the Nitrogen Rich [NNCNN]. *Dalton Trans.* **2014**, *43*, 18035–18041. https://doi.org/10.1039/c4dt02578d.

(54)   Chang, M. C.; Roewen, P.; Travieso-Puente, R.; Lutz, M.; Otten, E. Formazanate Ligands as Structurally Versatile, Redox-Active Analogues of β-Diketiminates in Zinc Chemistry. *Inorg. Chem.* **2015**, *54* (1), 379–388. https://doi.org/10.1021/ic5025873.

(55)   Chang, M. C.; Dann, T.; Day, D. P.; Lutz, M.; Wildgoose, G. G.; Otten, E. The Formazanate Ligand as an Electron Reservoir: Bis(Formazanate) Zinc Complexes Isolated in Three Redox States. *Angew. Chem. Inter. Ed.* **2014**, *53* (16), 4118–4122. https://doi.org/10.1002/anie.201309948.

(56)   Mondol, R.; Snoeken, D. A.; Chang, M. C.; Otten, E. Stable, Crystalline Boron Complexes with Mono-, Di- and Trianionic Formazanate Ligands. *Chem. Commun.* **2017**, *53* (3), 513–516. https://doi.org/10.1039/C6CC08166E.

(57)   Barbon, S. M.; Price, J. T.; Reinkeluers, P. A.; Gilroy, J. B. Substituent-Dependent Optical and Electrochemical Properties of Triarylformazanate Boron Difluoride Complexes. *Inorg. Chem.* **2014**, *53* (19), 10585–10593. https://doi.org/10.1021/ic5016912.

(58)   Mondol, R.; Otten, E. Aluminum Complexes with Redox-Active Formazanate Ligand: Synthesis, Characterization, and Reduction Chemistry. *Inorg. Chem* **2019**, *58* (9), 6344–6355. https://doi.org/10.1021/acs.inorgchem.9b00553.

(59)   Broere, D. L. J.; Mercado, B. Q.; Lukens, J. T.; Vilbert, A. C.; Banerjee, G.; Lant, H. M. C.; Lee, S. H.; Bill, E.; Sproules, S.; Lancaster, K. M.; Holland, P. L. Reversible Ligand-Centered Reduction in Low-Coordinate Iron Formazanate Complexes. *Chem. Eur. J.* **2018**, *24* (37), 9417–9425. https://doi.org/10.1002/chem.201801298.

(60)   Kabir, E.; Mu, G.; Momtaz, D. A.; Bryce, N. A.; Teets, T. S. Formazanate Complexes of Bis-Cyclometalated Iridium. *Inorg. Chem.* **2019**, *58*, 11672–11683. https://doi.org/10.1021/acs.inorgchem.9b01657.

(61)   Kabir, E.; Patel, D.; Clark, K.; Teets, T. S. Spectroscopic and Electrochemical Properties of Electronically Modified Cycloplatinated Formazanate Complexes. *Inorg. Chem.* **2018**, *57*, 10906–10917. https://doi.org/10.1021/acs.inorgchem.8b01543.

(62)   Mondol, R.; Otten, E. Reactivity of Two-Electron-Reduced Boron Formazanate Compounds with Electrophiles: Facile N–H/N–C Bond Homolysis Due to the Formation of Stable Ligand Radicals. *Inorg. Chem.* **2018**, *57*, 9720–9727. https://doi.org/10.1021/acs.inorgchem.8b00079.

(63)   Choudhury, J. Recent Developments on Artificial Switchable Catalysis. *Tetrahedron Lett.* **2018**, *59* (6), 487–495. https://doi.org/10.1016/j.tetlet.2017.12.070.

(64)   Wei, J.; Diaconescu, P. L. Redox-Switchable Ring-Opening Polymerization with Ferrocene Derivatives. *Acc. Chem. Res.* **2019**, *52* (2), 415–424. https://doi.org/10.1021/acs.accounts.8b00523.

(65)   de Vries, F.; Otten, E. Reversible On/Off Switching of Lactide Cyclopolymerization with a Redox-Active Formazanate Ligand. *ACS Catal.* **2022**, *12* (7), 4125–4130. https://doi.org/10.1021/acscatal.1c05689.

(66)   Broere, D. L.; Mercado, B. Q.; Holland, P. L. Selective Conversion of CO_2 into Isocyanate by Low-Coordinate Iron Complexes. *Angew. Chem. Int. Ed.* **2018**, *130*, 6617–6621.

(67)   Kamphuis, A. J.; Milocco, F.; Koiter, L.; Pescarmona, P. P. Highly Selective Single-Component Formazanate Ferrate (II) Catalysts for the Conversion of CO_2 into Cyclic Carbonates. *ChemSusChem* **2019**, 3635–3641. https://doi.org/10.1002/cssc.201900740.

(68)   Jin, D.; Sun, X.; Hinz, A.; Roesky, P. W. Reversible Insertion of CO_2 into a Bis(Formazanate) Magnesium Complex. *CCS Chemistry* **2023**, 1–8. https://doi.org/10.31635/ccschem.023.202202614.

(69)   Hunter, L.; Roberts, C. B. The Azo-Group as a Chelating Group. Part V. Metallic Derivatives of Arylazo-Oximes and of Formazyl Compounds. *J. Chem. Soc.* **1941**, 823–826. https://doi.org/10.1039/JR9410000823

(70)   Brown, D. A.; Bögge, H.; Lipunova, G. N.; Müller, A.; Plass, W.; Walsh, K. G. Iron and Manganese Complexes of Benzothiazolylformazans. *Inorganica Chim. Acta* **1998**, *280* (1), 30–38. https://doi.org/10.1016/s0020-1693(98)00050-4.

Neutral Formazan Ligands Bound to the *fac*-(CO)₃Re(I) fragment: Structural, Spectroscopic and Computational Studies

Metal complexes with ligands that coordinate *via* the nitrogen atom of azo (N=N) or imino (C=N) groups are of interest due to their π-acceptor properties and redox-active nature, which leads to interesting (opto)electronic properties and reactivity. Here we describe the synthesis and characterization of rhenium(I) tricarbonyl complexes with neutral N,N bidentate formazans, which possess both N=N and C=N fragments within the ligand backbone (Ar^1-N=N-C(R^3)=N-NH-Ar^5). The compounds were synthesized by reacting equimolar amounts of [ReBr(CO)$_5$] and the corresponding neutral formazan. X-Ray crystallographic and spectroscopic (IR, NMR) characterization confirmed the generation of formazan-type species with the structure *fac*-[ReBr(CO)$_3$(κ^2-*N^2*,*N^5*(Ph-N^{1}H-N^2=C(R^3)-N^4=N^5-Ph))]. The formazan ligand coordinates the metal center in the '*open*' form, generating a five-membered chelate ring with a pendant NH arm. The electronic absorption and emission properties of these complexes are governed by the presence of low-lying π*-orbitals on the ligand as shown by DFT calculations. The high orbital mixing between the metal and ligand results in photophysical properties that contrast to those observed in *fac*-[ReBr(CO)$_3$(L,L) species with α-diimine ligands.

1.   Introduction

Formazans are a large family of compounds containing the R^1-N=N-C(R^3)=N-NH-R^5 backbone, known for their use as analytical reagents for metal detection,[1] and as cellular[2] and textile dyes.[3] These applications are the consequence of its well-defined redox chemistry[4] and its ability to chelate metal centers in its deprotonated form, i.e., the delocalized formazanate anion (R^1-N=N-C(R^3)=N-N-R^5)⁻. Although formazanate coordination chemistry was first described in 1941,[5] it was not until the last decade that its study has reemerged due to its electrochemical and optical properties.[6] In addition to taking advantage of the unique optoelectronic properties imparted by formazanate ligands, recent reports show that their redox-active nature can also be used to obtain new catalytic reactivity.[8] A wide variety of formazanate complexes with both main group and transition metal elements have been reported, wherein the (anionic) ligand usually coordinates through the terminal donor sites to form 6-membered chelates.[7] In contrast to complexes with anionic formazanates, reports on coordination of the neutral formazan fragment remain scarce to date. In 2015, our group described the first example of a formazan-type complex,[9] in which the neutral ligand binds Zn(C_6F_5)₂ through one terminal and one internal nitrogen atoms yielding a five-membered chelate (Scheme 1), also described as the '*open*' coordination mode. It was hypothesized that the poor basicity of the Zn-C_6F_5 group in the precursor allowed the isolation of the Zn-formazan compound, as the more basic reagent ZnMe₂ does result in rapid deprotonation of the formazan NH group.[9]

Scheme 1. Synthesis of Zn formazan species.

Metal complexes with ligands containing the NH functionality have gained importance in catalysis since the NH arm can serve as an anchor for substrate recognition, thus enhancing catalyst selective and activity.[10] A proton source located at the proximity of the metal center has been widely investigated in the proton-coupled electron transfer reduction of small molecules relevant in energy conversion reactions such as hydrogen evolution[11,12] and CO_2 reduction[13-15] It was proposed to modulate the redox properties, aid in the stabilization of intermediates or impact the kinetics due to the increased local proton concentration. Furthermore, deprotonation of the NH group is known to modify the electronic and geometric structure of such complexes.[16-18]

Extensive research has focused on the properties and potential applications of *fac*-[L,LReX(CO)₃] (L = α-diimine) compounds in medicinal inorganic chemistry,[19,20] material science, [21,22], and catalysis.[23,24] Particularly, these compounds have shown to be good candidates for electrochemical CO_2 reduction, in which a proton source is required either for enhancing or triggering the catalytic process.[25,26] Mainly, Re-based bipyridine systems have been reported as catalysts for CO_2 electroreduction, wherein the presence of XH (X = O, N, C)[18,27,28] functionalizations boosts the catalytic effect or induces other reactivity patterns (**Chart 1**).[29–31] Key to the catalytic conversion of CO_2 to CO by the well-studied bipyridine Re and Mn complexes is the involvement of the supporting ('redox-active') ligand in the reduction chemistry.[28,32-34] We hypothesize that replacing the bipyridine ligand (an aromatic **α**-diimine) for a redox-active formazan ligand (formally an amino-substituted **α**-azoimine) could provide an avenue to influence the potential at which reduction of the catalyst occurs.[35,36] In addition, such ligands provide access to flexible coordination modes (hemilability)[37] due to the presence of four nitrogen atoms in the backbone, as well as proton-responsivity *via* the NH moiety that is in close proximity to the metal center, features that are key to the activity/selectivity of metalloenzymes but challenging to emulate in synthetic catalysts.[38] Herein, we report the synthesis of a series of *fac*-Re(CO)₃(formazan) complexes and investigate their (electronic) structures and photophysical properties.
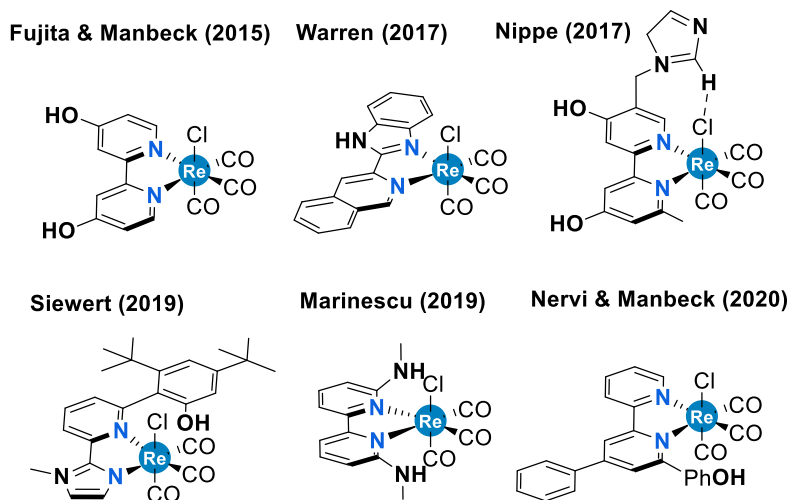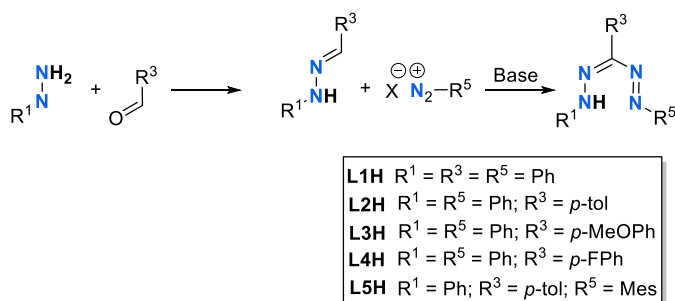

Chart 1.Representative examples of Re complexes bearing an XH functionality.

2. Results & discussion

2.1 Ligand synthesis

Formazan ligands **L1H-L4H** were synthesized according to the procedure reported by Hicks and coworkers, *via* aldehyde condensation with phenylhydrazine followed by a coupling reaction with phenyldiazonium chloride in a biphasic reaction medium (CH$_2$Cl$_2$/water) under mild basic conditions.[4] Similarly, **L5H** was prepared using the methodology previously described by our group, in which the coupling step is carried out in acetone/water with NaOH as base (Scheme 2).[9] In all cases, the compounds were obtained in moderate yields after purification (27-54%).

L1H R^1 = R^3 = R^5 = Ph
L2H R^1 = R^5 = Ph; R^3 = *p*-tol
L3H R^1 = R^5 = Ph; R^3 = *p*-MeOPh
L4H R^1 = R^5 = Ph; R^3 = *p*-FPh
L5H R^1 = Ph; R^3 = *p*-tol; R^5 = Mes

Scheme 2. Synthesis of formazan ligands.

2.2 Complex synthesis

Equimolar amounts of ReBr(CO)$_5$ and the corresponding formazan, **L1H-L4H**, reacted in refluxing toluene for 1 h to afford complexes **H1^{Br}-H4^{Br}** in moderate to good yields (28-67%) (Scheme 3a). In all cases complete conversion of the starting material was confirmed by ^{1}H NMR and infrared spectroscopy. The compounds are air-stable solids with dark red color and are soluble in low to medium polarity solvents. Complexes **H2^{Br}-H4^{Br}** were isolated as pure materials by either recrystallization or rinsing with pentane. A minor impurity was invariably present (^{1}H NMR spectroscopy) in the isolated material of **H1^{Br}**. Attempts to further purify the material by crystallization were unsuccessful. The reaction of the asymmetric formazan **L5H** with ReBr(CO)$_5$ in refluxing toluene gave a mixture of two complexes (**H5^{Br}a** and **H5^{Br}b**) based on ^{1}H NMR spectroscopy (Scheme 3b), which differ in the substituent at the NH position (Mes or Ph). Unsurprisingly, complexes **H5^{Br}a/b** present similar physical properties –dark red solids soluble in low polarity solvents–that we were unable to separate, and solution characterization data are reported below for the mixture.
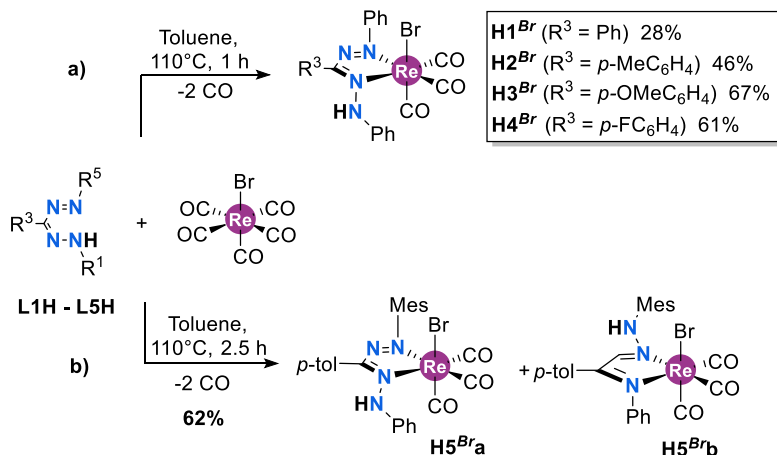
Scheme 3. General synthesis of compounds a) H1^{Br}-H4^{Br}, and b) the mixture of isomers H5^{Br}a, and H5^{Br}b.

2.3 Characterization

2.3.1 FT-IR spectroscopy

The infrared spectra of complexes **H1^{Br}-H4^{Br}** and the mixture **H5^{Br}a/b** feature the characteristic pattern for *fac*-tricarbonyl species: three intense bands in the ν(CO) carbonyl region arising from the IR-active 3A normal vibration modes for complexes with a C*1* symmetry (Figure 1). The CO stretching frequencies for compound **H1^{Br}** are observed at 2035, 1959 and 1923 cm^{-1} in CH$_2$Cl$_2$ solution. The effect of the *para*-substituent on the aromatic ring (R^3) is minimal, and compounds **H2^{Br}-H5^{Br}** show virtually identical IR spectra.
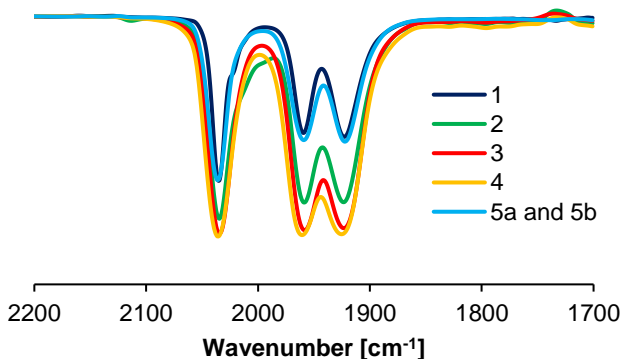
Figure 1. CO stretching bands (ν(CO)) in the FT-IR spectra of complexes H1^{Br}-H4^{Br}, and the mixture H5^{Br}a-H5^{Br}b in CH$_2$Cl$_2$ solution at rt.

2.3.2   NMR studies

^{1}H NMR spectra of **H1^{Br}-H4^{Br}** show a singlet *ca*. 8.5 ppm assigned to the hydrazo proton, consistent with the presence of a neutral formazan ligand (*see* Figure S1 in the supporting information section). In agreement with the presence of an asymmetric, protonated formazan ligand, the ^{13}C NMR spectrum shows three distinct carbonyl resonances between 185 and 192 ppm indicative of C_1 symmetry for these Re complexes (Figure S2). In ^{13}C NMR spectroscopy, the *N*-Ph *ipso*-carbon atoms attached to the formazan backbone display distinctive chemical shifts. Unequivocal assignment of these was possible based on an HSQC experiment where coupling between the hydrazo NH group and one of the Ph *ipso*-C resonances was observed. The resonance of the *ipso*-C bound to the azo group appears at 157 ppm, which is downfield from both the *ipso*-C linked to the NH function located ca. 141 ppm, and the *ipso*-C of the *C*-Ar group (120-125 ppm). Similarly, the N-Ph groups are inequivalent in the ^{1}H NMR spectrum also at elevated temperature (80 °C in toluene-d_8), suggesting that chemical exchange by proton transfer between the azo (C-N=N-Ph) and hydrazo (C=N-NH-Ph) fragments does not readily occur. This was further corroborated by the absence of exchange crosspeaks in the 2D EXSY spectrum (60 °C, mixing time of 0.5 s, Figure S4).

^{1}H NMR analysis of the reaction mixture of complexes **H5^{Br}a/b** indicates the generation of two main products in ratio of 0.7:1.0 with both compounds exhibiting the characteristic NH proton signal of the neutral formazan ligand at 8.15 and 7.60 ppm, respectively (Figure 2a). Minor signals for another species were observed (< 5%), but not investigated further. For the two major products, the observation of eight unique resonances in the aliphatic region of the ^{1}H and ^{13}C NMR spectra indicates that all CH₃ groups are inequivalent: each of the two products features four signals due to the CH₃ substituents at the *p*-tolyl (1) and mesityl (3) rings. Thus, at room temperature the rotation around the *N*-Mes bond is slow on the NMR timescale. In the most downfield part of the ^{13}C{^{1}H} NMR spectrum, i.e., between 180 and 200 ppm, there are six resonances which can be attributed to carbonyl ligands, which corroborates that both **H5^{Br}a** and **H5^{Br}b** are tricarbonyl rhenium complexes (Figure S3). Based on the spectroscopic data, we assign **H5^{Br}a** and **H5^{Br}b** as two different isomers with the composition [(**L5H**)Re(CO)₃Br] which differ in the nature of the 'pendant' (non-coordinating) *N*-Ar group of the formazan (*see* Scheme 3b). Heating an NMR tube containing the mixture of complexes **H5^{Br}a/b** to 80 °C inside the NMR spectrometer did not significantly change their molar ratio. Inspection of 2D NMR experiments allowed the assignment of ^{1}H and ^{13}C spectra (*see* Figure S3). Unequivocal identification of the *m*-CH (Mes), and the *m*- and *o*-CH (*p*-tolyl) protons allowed to establish the connectivity in both of the isomeric compounds present in solution. The ^{1}H,^{13}C correlations in the HMBC spectrum between the NH fragment and the carbon atoms that are two and three bonds away indicate that in the major isomer (**H5^{Br}b**) the NH group is bound to a mesityl group, whereas in **H5^{Br}a** it is connected to a phenyl group.

The greater shielding effect of mesityl compared to the phenyl group causes the NH proton of the former to appear at higher field (δ = 7.61 ppm in **H5^{Br}b**, and 8.22 ppm in **H5^{Br}a**).

To investigate the dynamics of isomers **H5^{Br}a/b** in solution, we collected a ^{1}H EXSY NMR spectrum at 80 °C in toluene-d_8 (Figure 2b). Crosspeaks are observed between the Mes *ortho*-CH$_3$ groups within each isomer due to rotation around the *N*-Mes bond, but not between isomers **H5^{Br}a** and **H5^{Br}b**. Whereas free formazans undergo intramolecular proton exchange rapidly ('tautomerization'), [39,40] the lack of exchange between **H5^{Br}a/b** indicates that the Re-N bonds are non-labile and coordination to the Re center effectively blocks exchange. This is in agreement with the data for the symmetrical derivative **H4^{Br}**, which also does not show exchange between the azo and hydrazo fragments (*vide supra*). It should be noted that, however, the EXSY spectrum does evidence exchange between the NH groups in **H5^{Br}a/b**; we believe it occurs by an intermolecular pathway instead. This is further corroborated by the observation of exchange crosspeaks between the NH protons in **H5^{Br}a/b** and residual H$_2$O when the NMR solvent is not fully anhydrous (Figure S5).

a)
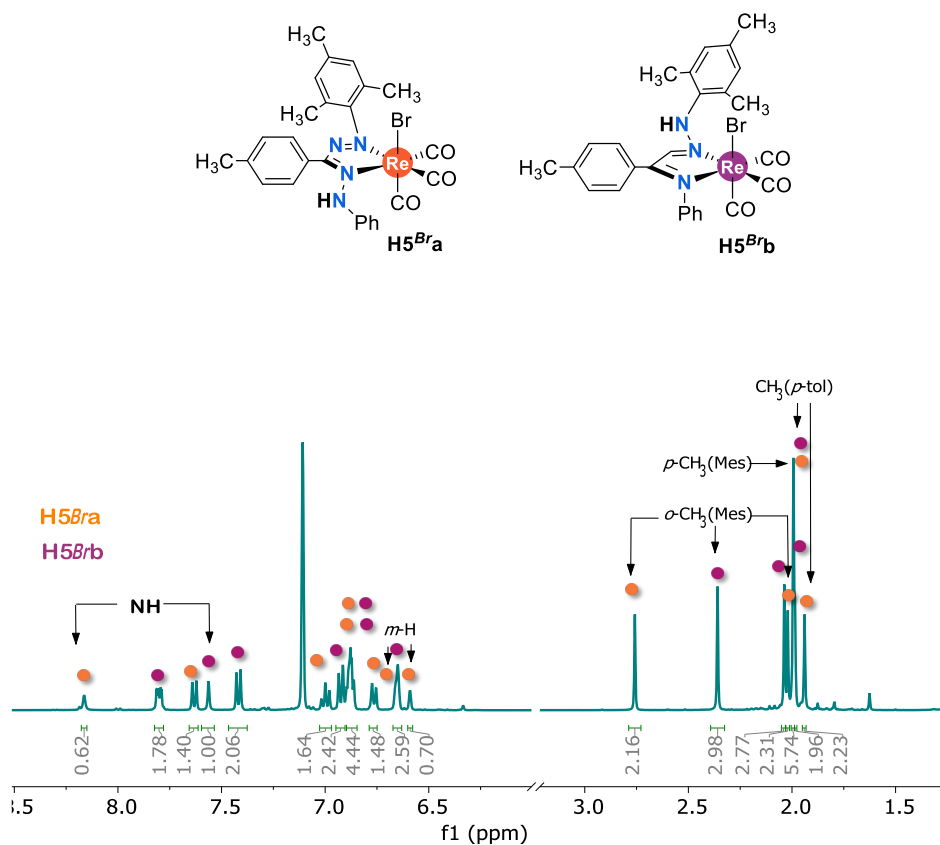
b)
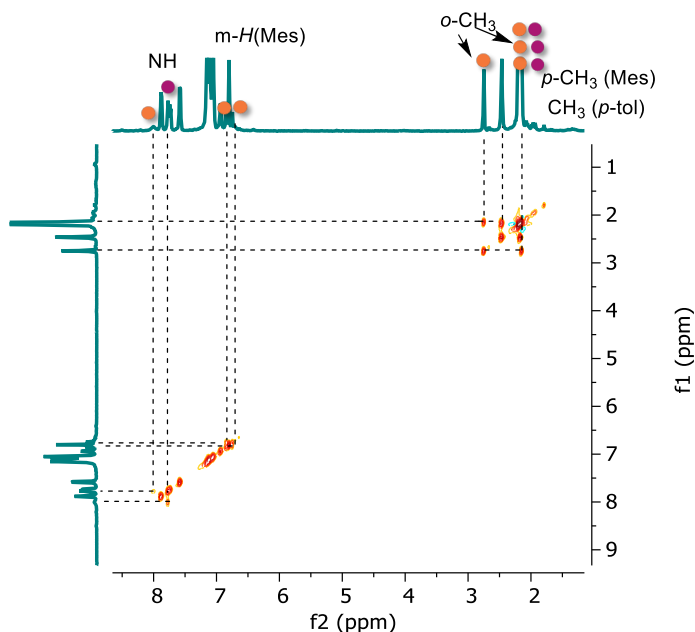
Figure 2.a) ¹H NMR spectrum of the mixture H5^{Br}a/b at room temperature in benzene-d_6. b) EXSY experiment at 80°C in toluene-d_8.

Additional experiments were conducted to determine whether intermolecular proton interchange processes also place in the complexes containing a symmetric formazan ligand. Partial H/D exchange of the NH proton in complex **H4**^{Br} was achieved by mixing a CDCl₃ solution of the aforementioned complex with D₂O. ¹H NMR analysis of the resulting mixture indicated that it was composed of 60% **D4**^{Br} (deuterated product) and 40% the non-deuterated species **H4**^{Br}. Remaining D₂O was subsequently removed by stirring over MgSO₄. The **H4**^{Br}/**4D**^{Br} mixture was isolated and then reacted with an equivalent of **H2**^{Br} in C₆D₆. We chose a different formazan complex to corroborate the intermolecular proton exchange, and in our case **H2**^{Br} was available. Monitoring the composition by ¹H NMR spectroscopy showed that the intensity of the NH resonance of **H4**^{Br} increased (to 72%) in the course of 30 min with a concomitant decrease of that in **H2**^{Br}, confirming that intermolecular proton exchange is taking place (*see* Figure S6).

2.3.3   Structural studies

Crystals suitable for single-crystal X-ray diffraction were obtained from slow diffusion of pentane into a CHCl₃ solution of compounds **H3**^{Br} and **H4**^{Br}, respectively. The mixture of **H5**^{Br}a/b did not crystallize using the same method, but we were able to obtain a microcrystalline sample from hot hexane that contained some small needles that were suitable for X-ray crystallographic characterization. This was identified as isomer **H5**^{Br}b,

in which the sterically most demanding Mes group is situated at the non-coordinated N atom of the ligand; the structure observed for this material is consistent with the major species in solution by NMR spectroscopy. Analysis of the molecular structures of **H3^{Br}**, **H4^{Br}**, and **H5^{Br}b** shows that the three compounds are isostructural (*see* Figure 3 and Table 1 for pertinent bond lengths and angles). The geometry around the metal center is pseudo-octahedral with the carbonyl ligands in a *facial* arrangement. The formazan fragment coordinates in a bidentate fashion through atoms N1 and N3, generating a five-membered chelate. Coordination of the neutral formazan is scarce, only observed in the complex [**L2H**]Zn(C$_6$F$_5$)$_2$ previously reported by our group.[9] The formazan bite angles are virtually identical in the three complexes (**H3^{Br}** = 73.04(9)°, **H4^{Br}** = 73.0(2)°, **H5^{Br}b** = 72.9(1)°), and somewhat smaller than the bite angle reported for the [**L2H**]Zn(C$_6$F$_5$)$_2$ complex (74.23(13)°). The C7-N2 and C7-N3 bond lengths are different from each other, the magnitude of C7-N3 bond lies in between the typical values for C-N single and double bonds (–C(sp^2) -N– = 1.355Å; –C(sp^2)=N– = 1.279 Å), while the C7-N2 bond length indicates a single bond character. The N1-N2 bond length is longer than a N=N double bond (–N=N– = 1.240 Å), and smaller than a N-N single bond (–N-N– = 1.454 Å).[41] The metallacycle is not fully planar as the Re atom is displaced out of the ligand plane (N1-N2-C7-N3) by 0.213-0.393 Å. The dihedral angle between the ligand plane and a phenyl group in the R^1 position is similar in complexes **H3^{Br}** (50.67°) and **H4^{Br}** (51.12°). Changing the R^1 substituent for the bulkier mesityl group (**H5^{Br}b**) causes a rotation out of the ligand plane by almost 30° resulting in a dihedral angle of 79.52° that prevents steric interactions between the Mes substituent and the equatorial CO ligand. The structure indicates that rotation around the *N*-Mes bond cannot occur freely due to these steric interactions, which is in agreement with the solution NMR data discussed above. The Re1-N1 bond length to the azo moiety is virtually the same in the three complexes (2.099- 2.126 Å) but it is shorter than the Re-N(azo) bond length reported for a related [ReBr(CO)$_3$(azopyridine)][42] complex (2.156(3) Å). The Re1-N3 bond lengths are in accordance with the typical Re-N(imine) bond distances (2.173-2.185 Å in compounds **H3^{Br}**-**H5^{Br}** *vs.* 2.173(3) Å in [ReBr(CO)$_3$(6-methoxipyridine-2-yl)-*N*-(2-methylthiophenyl)methanimine]), respectively).[43] The unusually short Re-N1(azo) bond length reflects that π-backdonation from the Re center to the azo group is more pronounced in the formazan species than in azopyridine complexes.[44] The π-acceptor capabilities of the azo ligand are also reflected in the Re-carbonyl bond lengths. The Re-C20 bond length, *trans* to the azo group, is longer than the Re-C21 bond length. This is consistent with the considerable π-acidity of the azo group,[45,46] which appears to be more significant in our formazan complexes than in the corresponding azopyridine analogues.[42] These complexes are not isomorphic in the solid state as their crystalline parameters differ from each other.
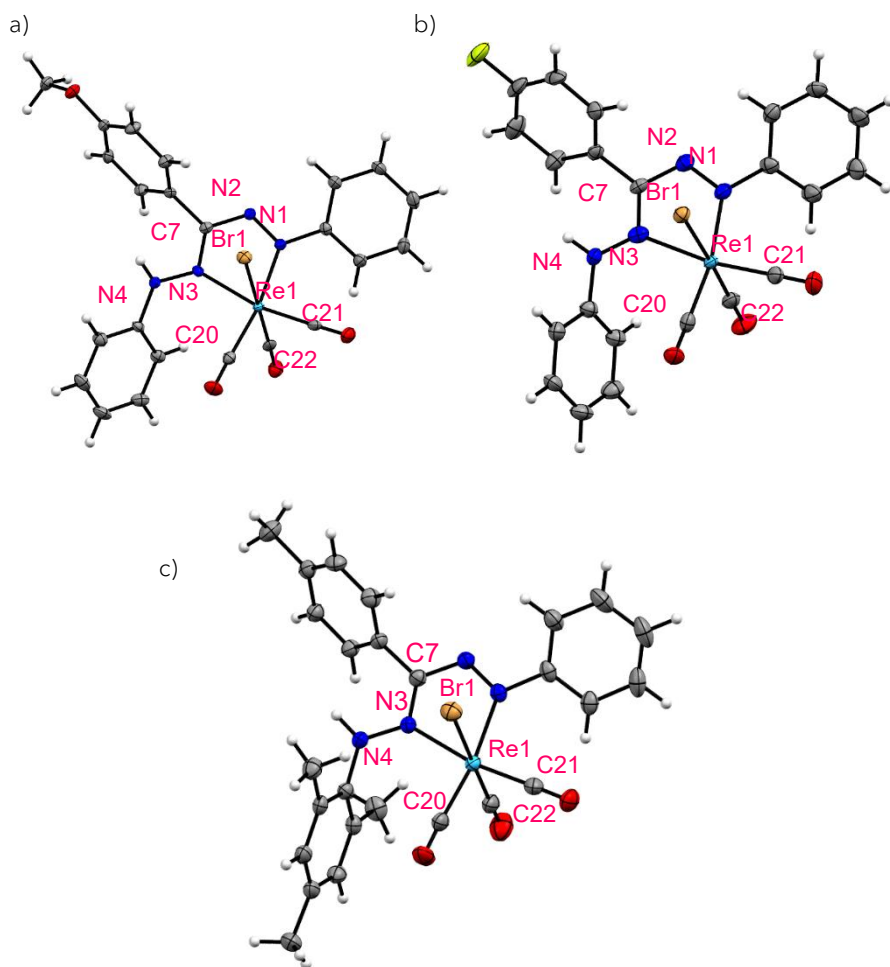
Figure 3.ORTEP representation of the molecular structures of a) H3^{Br}, b) H4^{Br}, and c) H5^{Br}b showing 50% of ellipsoids.

Table 1.Selected metrical parameters for H3^{Br}, H4^{Br}, and H5^{Br}b (bond lengths in Å, angles in °).

	H3^{Br}	H4^{Br}	H5^{Br}b
Re1-Br1	2.5977(3)	2.6236(7)	2.5946(6)
Re1-N1	2.126(2)	2.099(6)	2.122(3)
Re1-N3	2.173(3)	2.185(5)	2.174(4)
Re1-C20	1.955(3)	1.955(6)	1.957(5)
Re1-C21	1.921(3)	1.919(5)	1.916(6)
Re1-C22	1.941(2)	1.918(6)	1.964(4)
N1-N2	1.298(3)	1.291(7)	1.293(5)
C7-N2	1.363(4)	1.382(7)	1.364(8)
C7-N3	1.330(4)	1.319(8)	1.326(5)
N3-N4	1.343(4)	1.324(8)	1.343(7)
Br1-Re1-C22	178.02(9)	176.8(2)	178.6(2)
N1-Re1-C20	170.3(1)	168.7(2)	170.2(2)
N3-Re1-C21	166.5(1)	169.7(2)	170.3(2)
N1-Re1-N3	73.04(9)	73.0(2)	72.9(1)

2.3.4   UV-vis spectroscopy

The electronic spectra of complexes **H1^{Br}-H4^{Br}** and the mixture of complexes **H5^{Br}a/b** were measured at 25°C in toluene ($c \approx 10^{-5}$ M), Figure 4. Their corresponding data are summarized in **Table 2**. Compounds **H1^{Br}-H4^{Br}** show similar features: an intense band in the range of 490-510 nm with maximum molar absorptivities from 18 000 to 28 000 M^{-1}cm^{-1}. DFT calculations and comparison to literature data allows us to assign this band to electronic excitations that are Re(d$_\pi$)→azo(π*)[42] MLCT and formazan π→π* in nature.[9] A band of lower intensity in the range of 330-400 nm (ε =15 000-16 500 M^{-1}cm^{-1}) is observed in all compounds. While bands at similar energies are typically assigned to metal-to-ligand charge transfer in related compounds,[47,48] time-dependent DFT calculations for **H4^{Br}** instead indicate little involvement of the Re d-orbitals in this transition (*vide infra*). In this case, the calculations suggest, this band arises from intra-ligand and ligand to metal charge transfers. Overall, the **λ**$_{max}$ values of **H1^{Br}**, **H2^{Br}**, and **H4^{Br}** do not differ significantly, suggesting that the substituent at the *para*-position of the *N*-Ar rings has little influence on the energy of the electronic transitions, which is in line with the notion that the acceptor orbital in these transitions is a formazan π*-orbital that is relatively insensitive to the *para*-substituent. In the case of complex **H3^{Br}**, **λ**$_{max}$ is slightly red-shifted (509 nm) compared to complex **H1^{Br}** (490 nm), indicating that the involvement of the π-donating OMe group on the conjugated system is noticeable. When the spectrum of **H4^{Br}** was recorded in acetonitrile, a modest hypsochromic shift was observed (λ_{max}^{AcCN} = 483 nm (Figure S18); $\lambda_{max}^{Toluene}$ = 495 nm), showing that these species manifest a small, negative solvatochromism (Figure S7). Comparing **λ**$_{max}$ values to those reported for complexes with anionic formazanate ligands,[9,49,50] the absorption

maxima in **H1^{Br}**-**H4^{Br}** are blue-shifted due to a smaller extent of π-conjugation within the backbone of the neutral ligands compared to the fully delocalized anions. The mixture of complexes **H5^{Br}a/b** features two intense bands at 520 and 452 nm derived from the MLCT and π-π* formazan electronic transitions and a shoulder at 350 nm. Overall, the influence of the substituents on the lowest energy band is more pronounced when they are located at the N=N and NH formazan positions, similar to what was observed in complexes with anionic formazanate ligands.[6] Clearly, the nature of electronic absorptions for the two isomers **H5^{Br}a/b** is quite distinctive, as is manifested by the significant shift in λ$_{max}$.
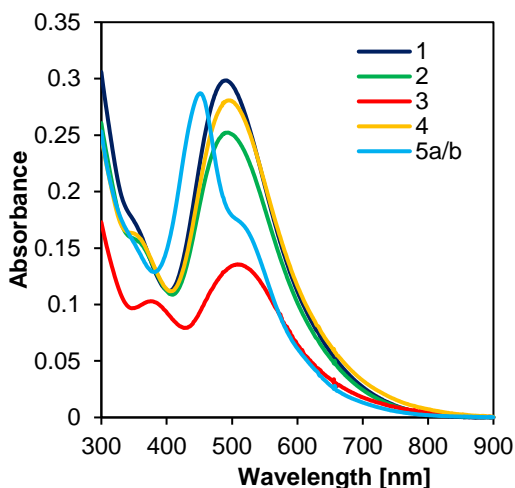
Figure 4. Absorption spectra for compounds H1^{Br}-H4^{Br} and H5^{Br}a/b in toluene solution.

Table 2. UV-vis absorption data.

Compound	λ$_{max}$(nm)	ε(M^{-1}·cm^{-1})	λ$_{max}$ (nm)	ε(M^{-1}·cm^{-1})
H1^{Br}	356	16 500	490	18 100
H2^{Br}	353	15 300	485	19 400
H3^{Br}	375	10 500	509	14 100
H4^{Br}	353	15 300	495	27 000
H5^{Br}a/b			452	
			~520^a	

^{a} approximate band position due to its appearance as a shoulder on the more intense absorption of the other isomer.

2.4 Density Functional Theory (DFT) calculations

For representative complexes **H4^{Br}** and **H5^{Br}a/b**, geometry optimizations were carried out in the ground state using density functional theory (DFT; MN15L[51] functional and def2-TZVP[52] basis set) using the crystallographic coordinates as a starting point. The geometries were confirmed to be minima on the potential energy surface by frequency calculations (no imaginary frequencies); the resulting structures are in good agreement with the metrical parameters obtained from X-Ray diffraction (complexes **H4^{Br}** and **H5^{Br}b)**, albeit that the Re-Br and hydrazo N-N bonds are slightly overestimated (Tables S2-3). Analysis of the frontier orbitals at the optimized geometry of **H4^{Br}** showed that the HOMO is mainly localized on the *fac*-[ReBr(CO)$_3$] core, and is composed of a Re d$_\pi$ orbital that is antibonding with a bromine *p* orbital and π-bonding with the CO ligand located *trans* to Br. The HOMO level also contains some ligand character (the hydrazo-phenyl fragment). On the other hand, the LUMO is primarily a π*-orbital of the formazan framework, with minor Re 5d character (Figure 5).

HOMO   **LUMO**
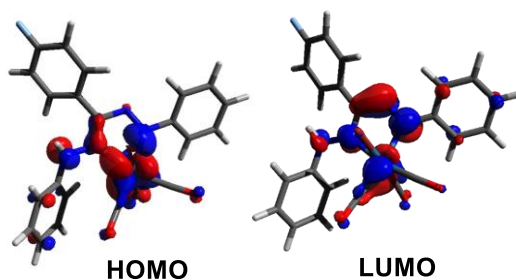
Figure 5. Frontier orbitals for H4^{Br} (isovalue = 0.05).

The optimized structures of **H5^{Br}a** and **H5^{Br}b** are overall similar, but the variation in the position of the Mes group (on the *azo* or *hydrazo N*-atom, respectively) leads to somewhat different frontier orbitals. While those of **H5^{Br}b** are similar to **H4^{Br}**, the HOMO of **H5^{Br}a** has noticeably smaller formazan contribution (Figure 6). The relative stability between the isomeric forms **H5^{Br}a** and **H5^{Br}b** was also evaluated based on these DFT calculations. Using the gas phase geometries, the Gibbs free energy difference between both compounds was computed in toluene solution using the solvation energies from SMD calculations and found to be 1.6 kcal/mol at room temperature, with **H5^{Br}b** being the most stable isomer. Qualitatively, the trend in relative stability is consistent with our empirical data since compound **H5^{Br}b** is the predominant species in the reaction mixture according to the NMR integration. It should be noted that it is also possible that the **H5^{Br}a/b** ratio found experimentally is kinetically controlled, as no interconversion between both isomers was observed.

Figure 6. Frontier orbitals for the isomers H5^{Br}a/b (isovalue = 0.05).

Time-dependent Density Functional Theory (TDDFT) calculations were carried out on complex **H4^{Br}** as a representative example. Relevant excitations were analyzed in more detail using natural transition orbital calculations (NTOs) to provide insight into their nature (Table S4). According to the calculations, the three lowest-energy transitions in **H4$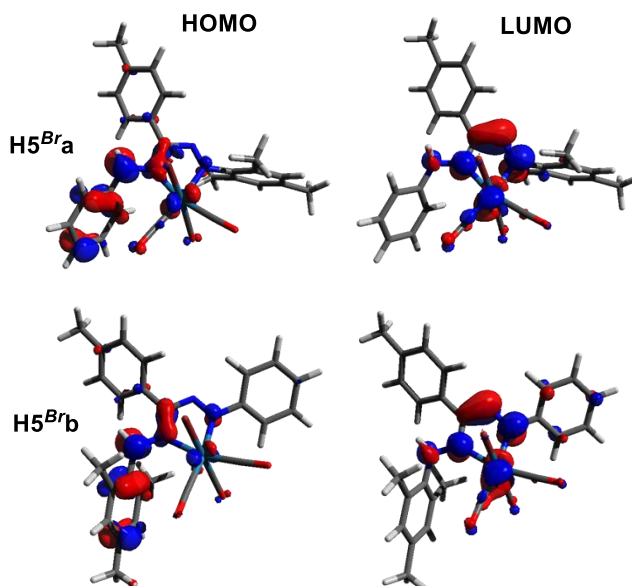^{Br}$** ($\lambda_{calc}$ = 645, 539 and 526 nm) all have small oscillator strength, and involve transitions from orbitals centered on the [ReBr(CO)₃] fragment (π^*(Re-Br) and (π(Re-CO)) into the formazan π^*-orbital. The fourth excited state with the highest oscillator strength in the visible range (λ_{calc} = 487 nm; $\lambda_{max,exp}$ = 495 nm, Figure S8) has more pronounced formazan (intraligand) π-π^* character, involving an occupied azo π-orbital as the donor (*see* Table S4 for the corresponding NTO), but also here the contribution of metal-based orbitals is still noticeable. Thus, in all excitations in the visible range, there is extensive mixing between the metal and ligand orbitals in the ground and excited states which results in electronic transitions of mixed nature: all show contributions from MLCT Re(dπ)→formazan(π^*), LLCT Br(p)→formazan(π^*) and ILCT azo(π)→formazan(π^*) excitations. The strong metal-ligand orbital mixing results in reduced charge transfer character in the MLCT bands, which is reflected in the minor influence of solvent polarity (toluene vs. acetonitrile) on the empirical electronic absorption spectrum (*vide supra*).[53] Similar to the absorptions in the visible range, analysis of the NTOs of the higher energy transitions shows that these involve the formazan π^*-orbital as the acceptor, and are also highly mixed in character.

TDDFT calculations were performed on the optimized structures of complexes **H5^{Br}a/b** to understand the impact of the pendant R^1/R^5 arms on the electronic transitions. The intense low-energy absorption is computed to be shifted to higher energy for **H5^{Br}a** (444 nm) compared to **H5^{Br}b** (489 nm), *see* Figure S9, Table S5-6. This is in agreement with the empirical UV/vis spectrum, which shows two distinct bands at 452 and 520 nm for the **H5^{Br}a/b** mixture. As in **H4^{Br}**, the natural transition orbital pair for the main low-energy excitation in **H5^{Br}b** consists of a 'hole' NTO on the [ReBr(CO)$_3$] core, whereas the excited electron ('particle' NTO) consists primarily of the π* formazan orbital. A comparison of the NTOs for **H5^{Br}a** and **H5^{Br}b** shows that the main difference between the two isomers is found in the hole NTO (Figure 7), which has a higher formazan contribution in **H5^{Br}a**. Based on the optimized geometries, the orientation of the azo-NAr ring changes upon swapping the aryl groups on the nitrogen atoms (Ph/Mes): the angle between the plane defined by the five-membered chelate ring and the Mes-substituent is 73.77° in **H5^{Br}a**, whereas the corresponding angle with the Ph-substituent in **H5^{Br}b** is only 39.28°.

To test our hypothesis that the orientation of the azo-NAr group has a major impact on the spectral properties, we took the geometry of **H5^{Br}b** and rotated the *N*-Ph group out of the ligand plane to be in the same orientation as the *N*-Mes group in **H5^{Br}a**. This structure is labeled **H5^{Br}b_rot**. The main visible band in the TDDFT spectrum calculated at the **H5^{Br}b_rot** geometry is blue-shifted by 30 nm (1342 cm^{-1}) compared to **H5^{Br}b**, but the other transitions remain at similar energies (Figure S10). An analysis of the orbital mixing between the azo-NAr ring and the rest of the ligand π-system confirms that rotating the Ar ring out of the plane disrupts conjugation (Table S7), and thus we conclude that this is responsible for the spectral shift observed.
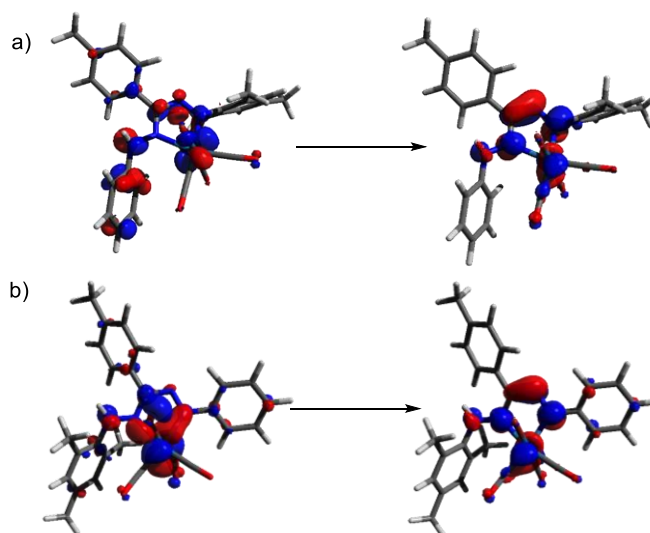
Figure 7.Natural transition orbitals for the highest-intensity excitation in the visible (isovalue = 0.05) for a) H5^{Br}a and b) H5^{Br}b represented as a hole → electron.

2.5   Luminescence spectroscopy

The emission spectrum of **H4^{Br}** measured at room temperature in acetonitrile using an excitation wavelength of 320 nm shows a broad featureless emission band at 380 nm (Figure 8). The excited state showed a monoexponential decay (λ_{ex} = 370 nm) with a lifetime (τ) of 3.69 ns under N₂ atmosphere, which does not appreciably change under O₂ (τ = 3.60 ns) (*see* Figure S12). Furthermore, the excitation spectrum (λ_{em} = 380 nm) exhibits a broad band centered at 310 nm (Figure 8). In contrast to the majority of *fac*-[ReX(CO)₃(L,L)] complexes with bidentate *N*-donor ligands (e.g., **α**-diimines), which typically show emission at higher wavelengths (400-600 nm),[54,55] this data shows that the triplet (metal-ligand or ligand-centered)[56] excited states typical for the photoluminescence of *fac*-[ReX(CO)₃(L,L)] compounds[57] are non-emissive in formazan Re(I) species. This also stands in contrast to complexes with anionic formazanate ligands, which show highly tunable emission with large Stokes shifts at much lower energies.[58-60]
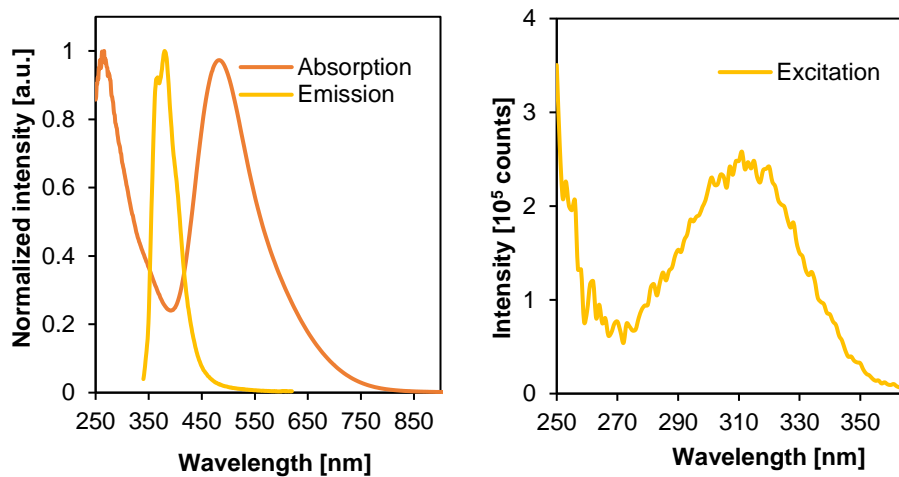
Figure 8. Normalized absorption and emission spectra of H4*Br* in MeCN recorded at λexc = 320 nm (left). Excitation spectrum of H4*Br* in MeCN. The data were collected at room temperature (right).

3.   Conclusions

We described the straightforward synthesis of the first complexes bearing the neutral formazan ligand towards a group 7 metal. The *fac*-(CO)₃ReBr(formazan) complexes obtained contain a five-membered chelate ring, in which ligand binds via the nitrogen atoms of the azo (N=*N*-Ar) and hydrazo (C=*N*-NHAr) groups which leaves a pendant acidic (exchangeable) NH moiety in close proximity to the metal center. Structural and spectroscopic data demonstrate that the formazan ligand is tightly bound to the metal center which is due to the strong π-acceptor character of the ligand. The effect of ligand substituents on the properties of the complexes is only minor, but the preparation of an asymmetric derivative with a *N*-Mes substituent demonstrates that changes in the sterics shifts the electronic absorption spectrum due to changes in the conjugation within the ligand. Computational studies at the DFT level confirm a high degree of covalency in the metal-formazan interaction and highly mixed metal-ligand character of the frontier orbitals, which is sensitive to the degree of conjugation within the ligand as demonstrated by sterically switching 'off' π-interactions in the derivative with a *N*-Mes group (compound **H5^{Br}a**). Unlike many *fac*-[ReX(CO)₃(L,L)] compounds (L,L = α-diimine ligands) reported in the literature, our formazan complexes are only weakly luminescent in the near-UV (λ_{em} = 380 nm), and emission from the lower-energy excited states is not observed. In ongoing work, we are investigating the possibility of using the proton-responsive nature of the NH group (i.e., formazan/formazanate interconversion) in 'cooperative' reactivity of this type of complexes.

4.   Experimental section

General considerations. All work —except ligand synthesis —was conducted under nitrogen atmosphere using conventional Schlenk and vacuum-line techniques. Pentane and toluene (Aldrich, anhydrous. 99.8%) were passed over columns of Al₂O₃ (Fluka) and BASF R3-11-supported Cu oxygen scavenger. [ReBr(CO)₅] was prepared according to the published procedures[61] from [Re₂(CO)₁₀] (Aldrich, 98%) and Br₂ (Aldrich, 98%). The ligands: 1,5-diphenyl-3-*p*-tolylformazan (**L2H**), 1,5-diphenyl-3-*p*-methoxyphenylformazan (**L3H**) and 1,5-diphenyl-3-*p*-flourophenylformazan (**L4H**) were synthesized using the methodology reported by Hicks and coworkers.[4] Particularly, 5-mesityl-1-phenyl-3-*p*-tolylformazan (**L5H**) was prepared using a modified procedure published by our group.[9] 1,3,5-triphenylformazan (**L1H**, TCI, 92%), *p*-tolualdehyde (Aldrich 97%), 4-methoxybenzaldehyde (Aldrich, 98%), 4-fluorobenzaldehyde (Aldrich, 98%), phenylhydrazine (Aldrich, 99%), aniline (Aldrich 99%), sodium nitrite (Aldrich, 99%), sodium carbonate (Aldrich, 99.5%), and [NBu₄]Br were used as received. CHCl₃ (Aldrich, 99%) and CDCl₃ (Aldrich, 99.8 atom %D) were used without further purification. NMR spectra were measured on Mercury 400, Varian Inova 500 or Bruker 600 MHz spectrometers. Residual solvent signals were used as internal reference for ¹H and ¹³C spectra and reported in ppm relative to TMS (0 ppm). Complete assignments were

based on two-dimensional experiments (COSY, HSQC, HMBC) using standard pulse sequences. FT-IR spectra were collected in DCM solution on a JASCO 4600 series FT-IR spectrometer in transmission mode using a liquid cell with CaF_2 windows. UV-vis spectra were recorded in toluene solution on an Agilent Technologies 8453 UV-vis spectrophotometer. Luminescence spectroscopy were measured on a Fluorolog®-3 spectrometer from HORIBA Jobin Yvon. X-ray diffraction data were collected at 100 K on a Bruker D8 Venture diffractometer with Mo Kα (λ = 0.71073 Å) (compounds 3 and 4) or Cu Kα (λ = 1.54178 Å) (compound 5b) radiation source. Crystal structures were refined using the SHELXL62 software. Non-hydrogen atoms were refined anisotropically.

Table 3.Crystallographic data for H3[Br], H4[Br] and H5[Br]b.

	H3[Br]	H4[Br]	H5[Br]b
chemical formula	$C_{23}H_{18}BrN_4O_4Re$	$C_{22}H_{15}BrFN_4O_3Re$	$C_{26}H_{24}BrN_4O_3Re$
M_r	680.52	668.49	706.6
cryst syst	triclinic	monoclinic	Triclinic
color, habit	Purple, needle	Purple, needle	Purple, block
size (nm)	0.42×0.13×0.04	0.70 ×0.170×0.060	0.40×0.33×0.20
space group	$P\bar{1}$ (No.2)	P 21/n (No.14)	$P\bar{1}$ (No.2)
a (Å)	9.0463(6)	10.095(2)	9.9235(12)
b (Å)	11.0459(7)	18.586(6)	10.9196(13)
c (Å)	12.7033(8)	12.219(4)	13.0134(15)
α (deg)	107.379(2)	90	77.085(4)
β (deg)	94.935(3)	107.191(8)	72.218(4)
γ (deg)	103.227(2)	90	75.163(4)
V (Å^3)	1162.89(13)	2190.1(11)	1281.7(3)
Z	2	4	2
ρ_{calc} (g · cm^{-3})	2.302	2.027	1.831
radiation, λ (Å)	Mo, Kα, 0.71073	Mo, Kα, 0.71073	Cu, Kα, 1.54178
μ(Mo, Kα) (mm^{-1})	8.777	7.413	11.384
F(000)	750	1272	684
temp (K)	100(2)	100(2)	100(2)
θ range (deg)	3.028-27.191	3.044-27.200	3.612-70.304
data collected (h, k, l)	−11:11, −14:14, −16:16	−12:12, −23:23, −15:15	−12:12, −13:13, −15:15
no. of reflns collected	45523	27390	21942
no. of indep reflns	5166	4818	4526
obsd reflns $F_o \geq 2.0\sigma(F_o)$	4966	4288	4396
R(F) [obsd reflns] (%)	1.78	2.81	2.19
Rw(F^2) [all reflns] (%)	5.24	6.13	5.51
GOF	1.051	1.192	1.119
weighing a, b	0.03300, 1.26140	0.0000, 12.4515	0.0000, 2.9889
params refined	303	293	324
min, max residual densities	−1.04, 1.32	−1.61, 1.82	-0.83, 0.85

Procedure for the synthesis of complexes H1^{Br}-H4^{Br}. Equimolar amounts of [ReBr(CO)₅] and the corresponding ligand were poured into a two-necked round bottom flask and dissolved in 20 mL of toluene. The reaction was heated up at reflux for 1 h observing that the mixture darkened upon completion. The solvent was evaporated to dryness. Specific details for the purification of the entitled complexes are mentioned below.

H1^{Br} (C₂₂H₁₆BrN₄O₃Re). [ReBr(CO)₅] (0.0934g, 0.230 mmol), **L1H** (0.06938 g, 0.230 mmol). Work-up. 5 mL of pentane were added to the mixture and the crude was stirred for 30 min allowing the formation of a dark-crimson solid material. The compound was filtered out and rinsed with pentane (3 x 5 mL). (41.8 mg, 27.9 %). ¹H NMR (CDCl₃, 25 °C, 400 MHz) δ/ppm: 7.30 (d, 2 H, ^3J = 8 Hz, Ph-NH *o*-H), 7.39 (t, 1 H, ^3J = 8 Hz, Ph-NH *p*-H), 7.45-7.57 (m, 5H, Ph-NH *m*-H, Ph-N=N *m*-H, Ph-NC *p*-H), 7.64 (m, 3H, Ph-NC *m*-H, Ph-N=N *p*-H,) 7.84 (d, 2 H, ^3J= 8 Hz, Ph-NC *o*-H), 7.89 (d, 2 H, ^3J = 8 Hz, Ph-N=N *o*-H), 8.58 (s, 1 H, NH). ¹³C{¹H} NMR (CDCl₃, 25 °C, 150 MHz) δ/ppm: 123.21 (Ph-NH *o*-CH), 123.95 (Ph-N=N o-CH), 127.90 (Ph-NH p-CH), 128.48 (Ph-CN ipso-C), 128.93 (Ph-CN o-CH), 129.31 (Ph-N=N m-CH), 129.39 (Ph-NH m-CH), 130.10 (Ph-CN m-CH), 131.69 (Ph-N=N p-CH), 131.86 (Ph-CN *p*-CH), 140.83 (Ph-NH *ipso*-C), 157.20 (Ph-N=N *ipso*-C), 164.65 (NCN C), 185.33 (CO *trans* Br C), 192.35 (CO *trans* Ph-NH-N C), 192.89 (CO *trans* Ph-N=N C). IR(CH₂Cl₂) ν(CO)/cm⁻¹: 2035(s), 1959(s), 1923(s). MS (FAB⁺) (m/z): [MH+2]⁺ = 653, [MH]⁺ = 651, [MH-CO]⁺ = 623, [MH-3CO]⁺ = 567. HRMS (ESI +) (m/z): Calcd. for [MH]⁺ = 651.004167. Found = 651.00337. [MH-3CO]⁺ = 567.01942. Found = 567.01817.

H2^{Br} (C₂₃H₁₈BrN₄O₃Re). [ReBr(CO)₅] (0.1235 g, 0.304 mmol), **L2H** (0.0959g 0.305 mmol). Work-up: Similar to the procedure described above. (93.3 mg, 46.0%). ¹H NMR (CDCl₃, 25 °C, 600MHz) δ/ppm: 2.47 (s, 1 H, CH₃), 7.29 (d, 2 H, ^3J= 8 Hz, Ph-NH *o*-H), 7.38 (t, 1 H, ^3J= 7 Hz, Ph-NH *p*-H), 7.43-7.56 (m, 7H, Ph-NH m-H, Ph-N=N m-H, *p*-tol m-H, Ph-N=N *p*-H), 7.74 (d, 2 H, ^3J= 8 Hz, *p*-tol *o*-H), 7.88 (d, 2 H, ^3J= 7 Hz, Ph-N=N *o*-H), 8.56 (s, 1 H, NH). ¹³C{¹H} NMR (CDCl₃, 25 °C, 150 MHz) δ/ppm: 21.71 (CH₃), 123.11 (Ph-NH *o*-CH), 123.97 (Ph-N=N *o*-CH), 125.58 (*p*-tol *ipso*-C), 127.75 (Ph-NH *p*-CH), 128.85 (*p*-tol *o*-CH), 129.29 (Ph-NH *m*-CH), 129.40 (Ph-N=N *m*-CH), 130.72 (*p*-tol *m*-CH), 131.65 (Ph-N=N *p*-CH), 140.96 (Ph-NH *ipso*-C), 142.49 (*p*-tol *p*-C), 157.24 (Ph-N=N *ipso*-C), 165.02 (NCN C), 185.37 (CO *trans* Br C), 192.40 (CO *trans* Ph-NH-N C), 192.88 (CO *trans* Ph-N=N C). IR(CH₂Cl₂) ν(CO)/cm⁻¹: 2035(s), 1959(s), 1924(s). MS (DART+) (m/z): [MH+2]⁺ = 667, [MH]⁺ = 665, [MH-CO]⁺ = 637, [MH-2CO]⁺ = 609, [MH-3CO]⁺ = 581. HRMS (ESI+) (m/z): Calcd. for [MH]⁺ = 665.01982. Found = 665.01917 [MH-3CO]⁺ = 581.035072. Found = 581.03365.

H3^{Br} (C₂₃H₁₈BrN₄O₄Re). [ReBr(CO)₅] (0.0930 g, 0.229 mmol), **L3H** (0.0758 g, 0.229 mmol). Work-up. The compound was recrystallized by slow diffusion of 15 mL of pentane into 5 mL of a DCM solution of **H3^{Br}**. The system was kept in the freezer for one day allowing the formation of crystalline material. The solid was washed with 3x5 mL of pentane. (105 mg, 67.07%). ¹H NMR (CDCl₃, 25 °C, 600MHz) δ/ppm: 3.88 (s, 1 H, CH₃O H), 7.10 (d, 2 H, ^3J= 8 Hz, *p*-CH₃OPh *m*-H), 7.27 (d, 2 H, ^3J= 8 Hz, Ph-NH *o*-H), 7.35 (t, 1

H, ^3J= 8 Hz, Ph-NH *p*-H), 7.45 (t, 2H, ^3J= 8 Hz, Ph-N=N *m*-H), 7.49 (t, 2H, ^3J= 8 Hz, Ph-NH *m*-H), 7.53 (t, 1H, ^3J= 7 Hz, Ph-N=N *p*-H), 7.81 (d, 2 H, ^3J= 6 Hz, *p*-CH₃OPh *o*-H), 7.88 (d, 2 H, ^3J= 8 Hz, Ph-N=N *o*-H), 8.47 (s, 1 H, NH). ^{13}C{^{1}H} NMR (CDCl₃, 25 °C, 150 MHz) δ/ppm: 55.64 (CH₃O, C), 115.39 (*p*-CH₃OPh *m*-CH), 120.64 (*p*-CH₃OPh *ipso*-C), 122.80 (Ph-NH *o*-CH), 123.96 (Ph-N=N *o*-CH), 127.52 (Ph-NH *p*-CH), 129.29 (Ph-NH *m*-CH), 129.41 (Ph-N=N *m*-CH), 130.82 (*p*-CH₃OPh *o*-CH), 131.68 (Ph-N=N *p*-CH), 141.14 (Ph-NH *ipso*-CH), 157.26 (Ph-N=N *ipso*-C), 162.17 (*p*-CH₃OPh *p*-C), 165.25 (NCN C), 185.38 (CO *trans* Br C), 192.40 (CO *trans* Ph-NH-N C), 192.92 (CO *trans* Ph-N=C C). IR(CH₂Cl₂) ν(CO)/cm⁻¹: 2034(s), 1958(m), 1923(s). MS (DART+) (m/z): [MH+2]⁺= 683, [MH]⁺= 681, [MH-CO]⁺= 653, [MH-2CO]⁺=625, [MH-3CO]⁺=597. Anal. Calcd. For (C₂₃H₁₈BrN₄O₄Re): C 40.59, H 2.67, N 8.23; found C 39.81, H 2.59, N 7.90.

H4^{Br} (C₂₂H₁₅BrFN₄O₃Re). [ReBr(CO)₅] (0.0951 g, 0.234 mmol), **L4H** (0.0745 g, 0.234 mmol). Work-up. After solvent evaporation, the crude was recrystallized by diffusion of pentane into a CHCl₃ solution at -30 °C. The crystalline material was filtered out and rinsed with 3x5 mL of pentane. (96 mg, 61.3%). ^{1}H NMR (CDCl₃, 25 °C, 600MHz) δ/ppm: 7.32 (d, 2H, ^3J = 8 Hz, Ph-NH *o*-H), 7.35 (t, 2H, $^3J_{H-H}$ = 8 Hz, $^3J_{H-F}$ = 8 Hz, *p*-FPh *m*-H), 7.41 (t, 1H, ^3J = 7 Hz, Ph-NH *p*-H), 7.49 (t, 2H, , ^3J = 8 Hz, Ph-NH *m*-H), 7.54 (t, 2H, ^3J = 8 Hz, Ph-N=N *m*-H), 7.58 (t, 1H, ^3J = 7 Hz, Ph-N=N *p*-H), 7.90 (m, 4H, Ph-N=N *o*-H, *p*-FPh *o*-H), 8.42 (s, 1H, NH). ^{19}F NMR (CDCl₃, 25 °C, 565MHz) δ/ppm: -105.92 (m, *p*-FPh F). ^{13}C{^{1}H} NMR (CDCl₃, 25 °C, 150 MHz) δ/ppm: 117.38 ($^2J_{C-F}$ = 22 Hz , *p*-FPh *m*-CH), 122.88 (Ph-NH *o*-CH), 123.94 (Ph-N=N *o*-CH), 124.74 ($^4J_{C-F}$ = 3 Hz, *p*-FPh *ipso*-C), 127.85 (Ph-NH *p*-CH), 129.36 (Ph-N=N *m*-CH), 129.47 (Ph-NH *m*-CH), 131.51 ($^3J_{C-F}$ = 9 Hz, *p*-FPh *o*-CH), 131.80 (Ph-N=N *p*-CH), 140.92 (Ph-NH *ipso*-C), 157.30 (Ph-N=N *ipso*-C), 164.39 (J_{C-F} = 253.5 Hz, *p*-FPh *p*-C), 164.26 (NCN C), 185.25 (CO *trans* Br C), 192.14 (CO *trans* Ph-NH-N C), 192.63 (CO *trans* Ph-N=C C). IR(CH₂Cl₂) ν(CO)/cm⁻¹: 2036(s), 1961(s), 1925(s). MS (DART +) (m/z): [MH]⁺ = 669, [M-CO]⁺ = 641, [M-3CO] = 585. Anal. Calcd. For (C₂₂H₁₅BrFN₄O₃Re): C 39.53, H 2.26, N 8.38; found C 39.12, H 2.04, N 8.29.

H5^{Br}a and **H5^{Br}b** (C₂₆H₂₄BrN₄O₃Re). [ReBr(CO)₅] (0.0886 g, 0.22 mmol) and **L5H** (0.0778 g, 0.022 mmol) were dissolved in 20 mL of toluene and heated in refluxing toluene for 2.5 h. An oily material was afforded after removal of the volatiles; then, the crude was triturated with 5 mL of pentane, yielding a dark solid. (95 mg, 61.5%). ^{1}H NMR (CDCl₃, 25 °C, 600MHz) δ/ppm: (**H5^{Br}a**) 1.99 (s, 3H, *p*-tol *p*-CH₃), 2.05 (s, 3H, Mes-N=N *p*-CH₃), 2.07 (s, 3H, Mes-N=N *o*-CH₃), 2.81 (s, 3H, Mes-N=N *o*-CH₃), 6.64 (s, 1H, Mes-N=N *m*-H), 6.71 (s, 1H, Mes-N=N *m*-H), 6.82 (d, 2H, , ^3J= 6 Hz, Ph-NH *o*-H), 6.93 (m, 3H, Ph-NH p-H, *p*-tol *m*-H), 7.05 (t, 2H, ^3J= 6 Hz, Ph-NH *m*-H), 7.68 (d, 2H, ^3J= 6 Hz, *p*-tol *o*-H), 8.22 (s, 1H, NH). (5b) 2.05 (s, 3H, Mes-NH *p*-CH₃), 2.05 (s, 3H, Mes-NH *o*-CH₃), 2.09 (s, 3H, *p*-tol *p*-CH₃), 2.41 (s, 3H, Mes-NH *o*-CH₃), 6.70 (s, 2H, Mes-NH *m*-H), 6.93 (m, 3H, Ph-N=N *p*-H, m-H), 6.99 (d, 2H, ^3J= 6 Hz, *p*-tol *m*-H), 7.47 (d, 2H, ^3J= 6 Hz, *p*-tol *o*-H), 7.61 (s, 1H, NH). 7.85 (m, 2H, Ph-N=N *o*-H). ^{13}C{^{1}H} NMR (CDCl₃, 25 °C, 150 MHz) δ/ppm: (5a) 17.80 (Mes *o*-CH₃), 20.42 (Mes *o*-CH₃), 20.80 (Mes *p*-CH₃), 21.37 (*p*-tol *p*-CH₃) , 121.53 (Ph *o*-CH), 126.68(*p*-tol *p*-C), 126.94 (Ph *m*-CH), 128.6 (Mes *m*-C), 129.24 (*p*-tol *o*-CH), 129.47 17

(Mes *o*-C), 130.17 (Mes *m*-C), 130.48 (*p*-tol *m*-CH), 131.17 (Mes *o*-C), 138.18 (Mes *p*-C), 142.20 (Ph *ipso*-C), 142.20 (*p*-tol *ipso*-C) , 155.20 (Mes *ipso*-C), 167.11 (NNCN C), 186.34 (CO *trans* Br C), 192.25 (CO *trans* Mes-N=N C), 193.04 (CO *trans* PhN-NH C). (**H5^{Br}b**) 18.61 (Mes *p*-CH₃), 19.56 (Mes *o*-CH₃), 21.14 (Mes *o*-CH₃), 21.33 (*p*-tol *p*-CH₃), 124.09 (Ph *o*-CH), 129.14 (*p*-tol *p*-C), 129.43 (*p*-tol *o*-CH), 129.49 (Mes *m*-C), 129.93 (Mes m-C), 130.94 (p-tol m-CH), 131.23 (Ph m-CH), 136.53 (Mes ipso-C), 137.70 (Mes *o*-C), 137.89 (Mes *o*-C), 140.68 (Mes *p*-C), 141.79 (*p*-tol *ipso*-C), 157.15 (Ph *ipso*-C), 161.04 (NNCN C), 184.77 (CO *trans* Br C), 192.29 (CO *trans* Mes-NH C), 194.16 (CO *trans* Ph-N=N C). IR(CH₂Cl₂) ν(CO)/cm⁻¹: 2036(s), 1959(s), 1922(s). MS (DART+) (m/z): [MH+2]⁺ = 709, [MH]⁺ = 707, [MH-CO]⁺ = 678, [MH-3CO]⁺ = 623. HRMS (ESI+) (m/z): Calcd. for [MH]⁺ = 707.06677. Found = 707.06667. [MH-2CO]⁺ = 651.07684. Found = 651.07610. [MH-3CO]⁺ = 623.08193. Found = 623.08092.

5. Supporting information

5.1 NMR

a) ¹H
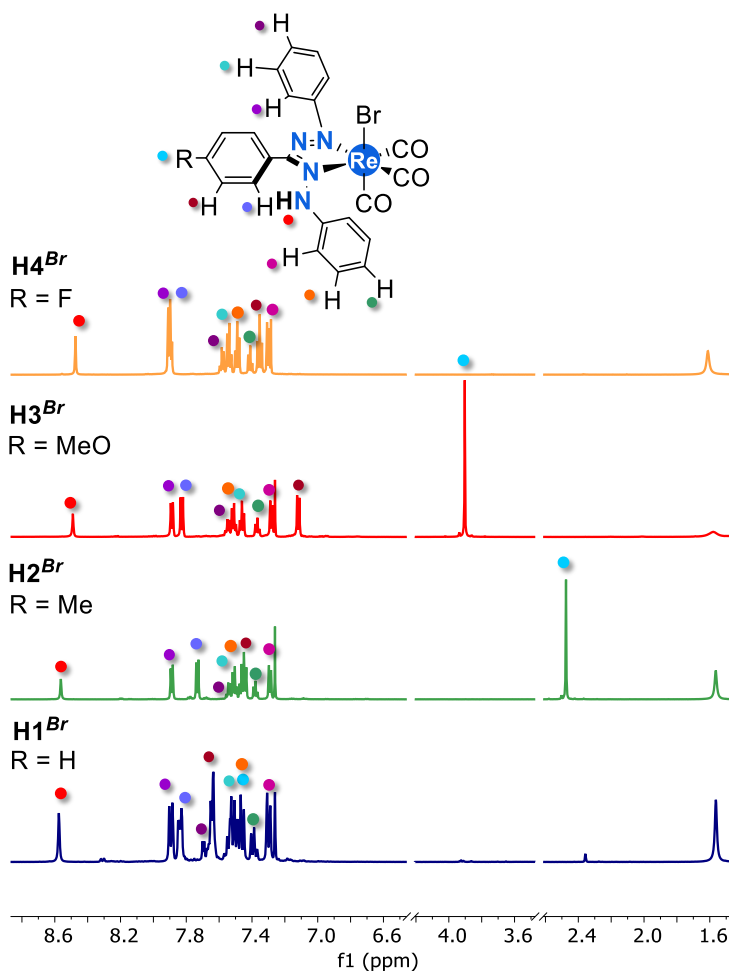
Figure S1. Proton NMR spectra in CDCl₃.

b) ^{13}C{^{1}H}
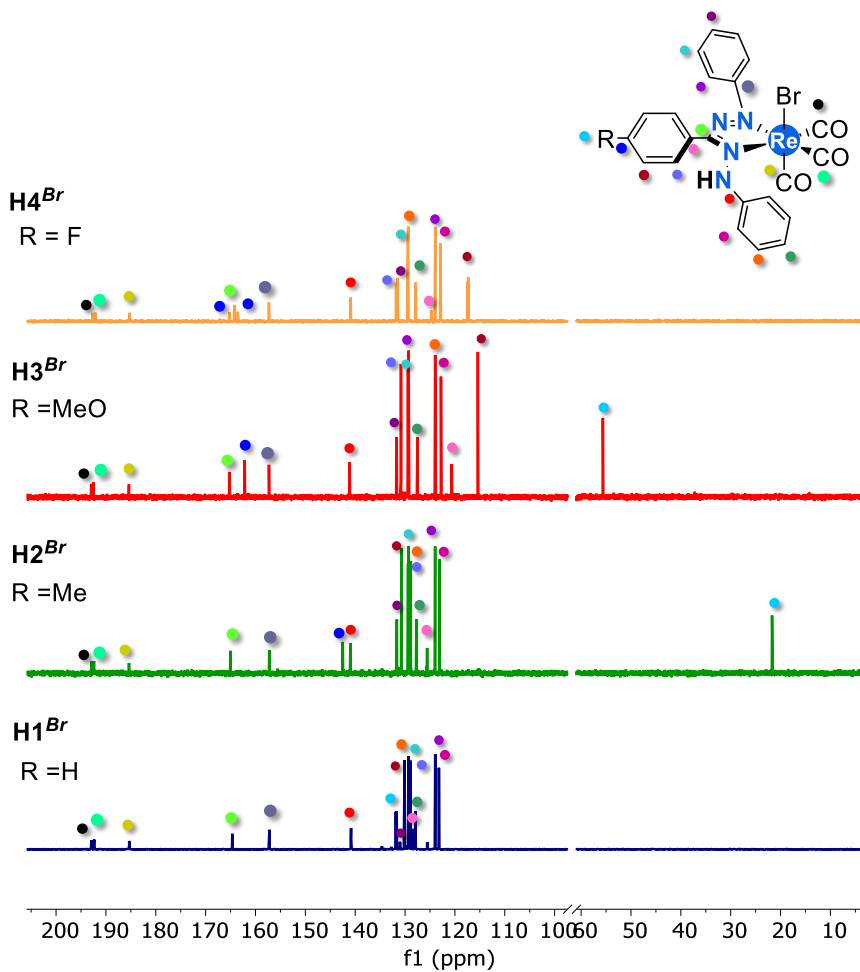
Figure S2. Carbon NMR spectra in CDCl₃.

a) ^{1}H
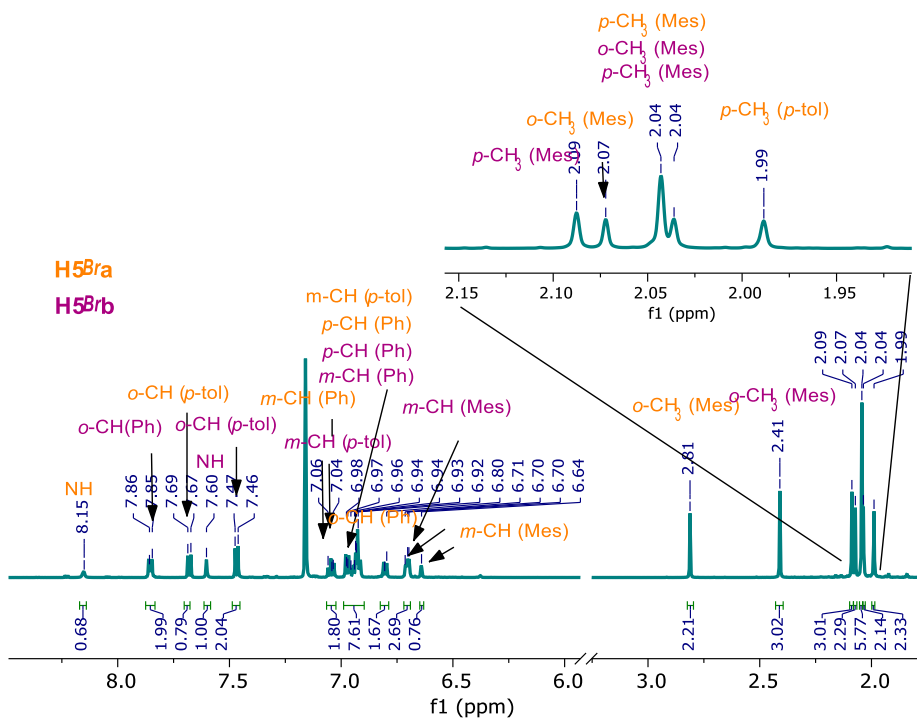
b) ^{13}C{^{1}H}
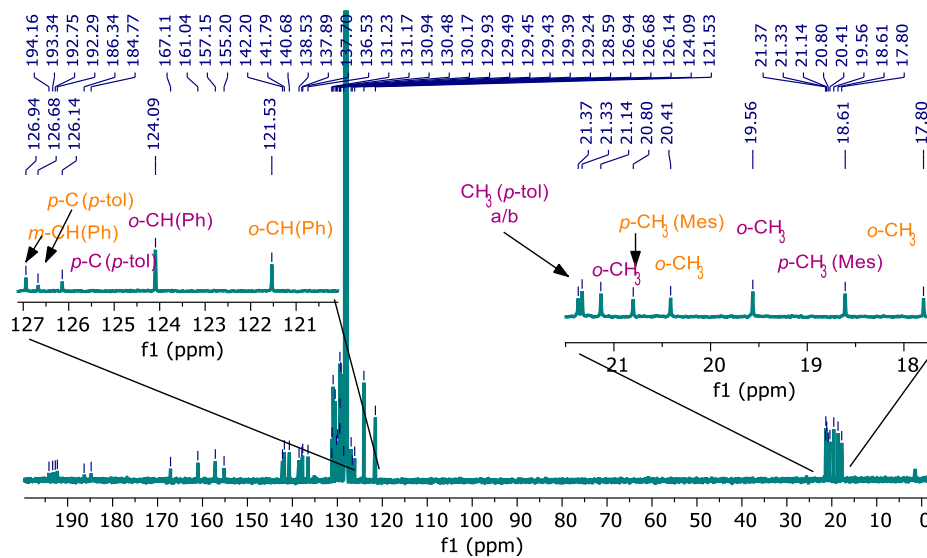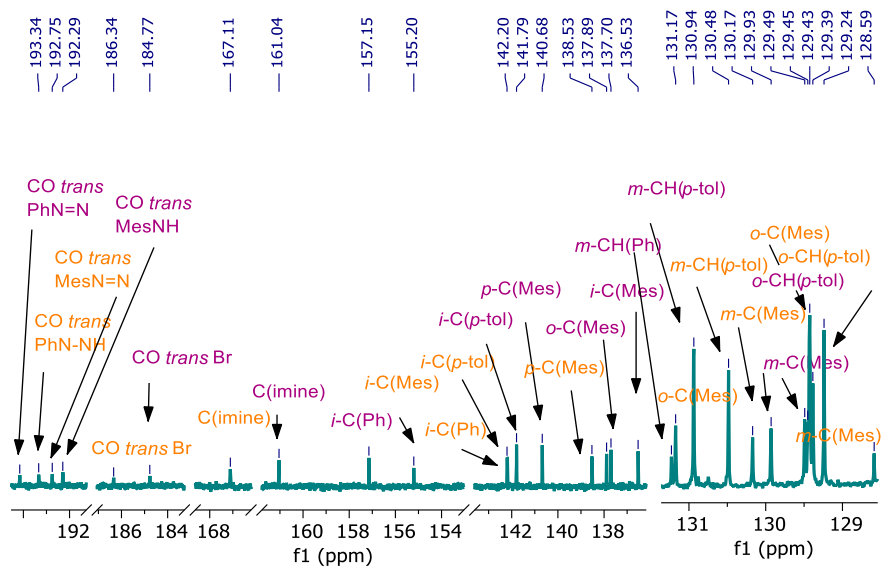
Figure S3. NMR spectra of the mixture of isomers $H5^{Br}a/b$. a) ^1H and b) $^{13}C\{^1H\}$ in benzene-d_6.
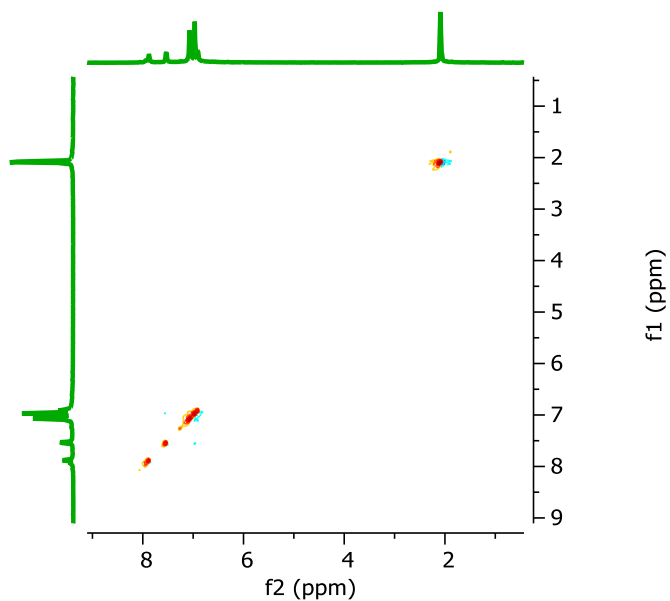
Figure S4. ^1H EXSY of $H2^{Br}$ at 60°C in benzene-d_6.
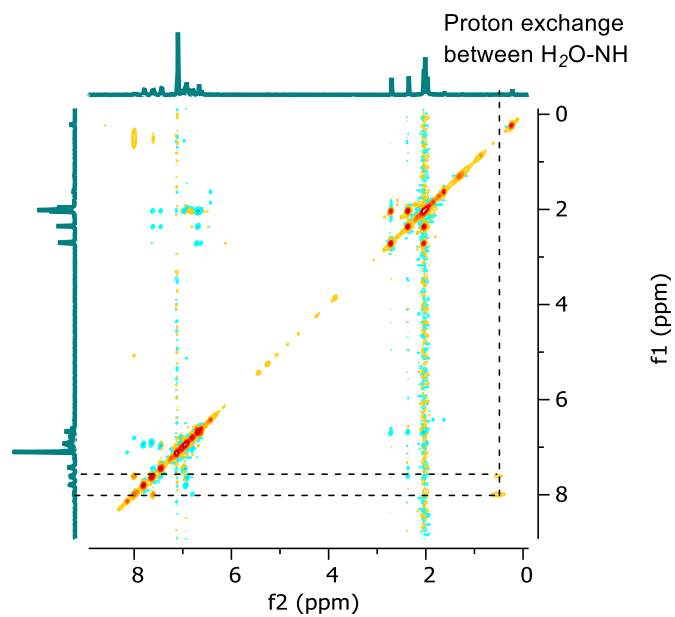
Figure S5. ^{1}H EXSY experiment of the mixture H5^{Br}a/b at 60°C in benzene-d_6.

a)

b)

$$D4^{Br} + H2^{Br} \rightleftharpoons H4^{Br} + D2^{Br}$$

28%   72%

NH   NH
(H2^{Br})   (H4^{Br})

Figure S6. ¹H NMR spectra of H/D exchange reactions: a) in H4^{Br} and b) between H/D4^{Br} and H2^{Br}.

5.2   UV-vis

Figure S7. UV-vis of H4^{Br} in MeCN.
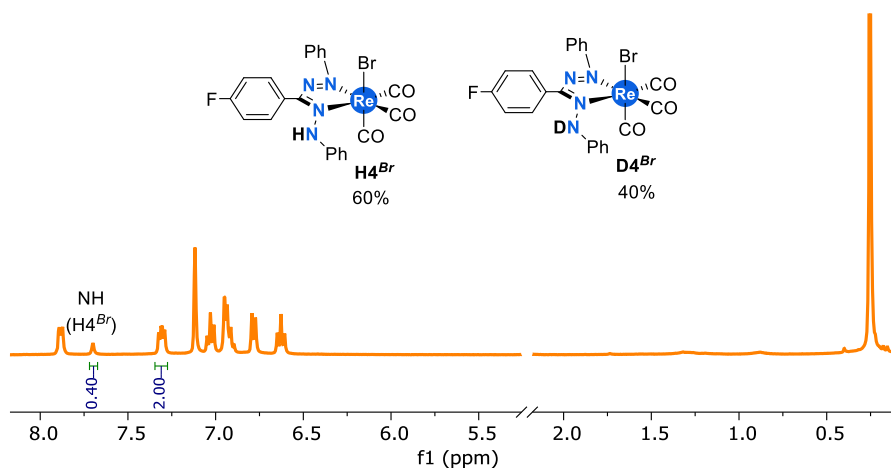
5.3   Computational studies

Density Functional Theory (DFT) calculations were carried out in Gaussian 16 Revision C.02[63] software, and visualized using Gaussview 6[64] or Avogadro.[65] Geometry optimizations in the ground state were performed in the gas phase at a MN15L[51] level of theory combined with a triple ζ–basis set: def2tzvp.[52] The carbonyl frequency values were scaled using a factor of 0.9578[66] (*see* Table S1). TDDFT calculations were performed on the optimized structures at the CAM-B3LYP/def2tzvp level of theory. Solvent effect was simulated using the continuum polarized model (CPM).[67]

Table S1.Comparison between experimental and theoretical carbonyl frequencies (scaled by a factor of 0.9578).

Compound ν(CO)/ cm^{-1}

H4^{Br}		H5^{Br}a		H5^{Br}b	
Exp.	Theor.	Exp	Theor.	Exp.	Theor.
2036	2025	2036	2026	2036	2021
1961	1965	1959	1965	1959	1960
1925	1930	1922	1933	1922	1926

Table S2. Comparison between the bond lengths obtained from X-ray diffraction vs theoretical values for H4^{Br}.[a]

Bond length	Experimental (Å)	Theoretical (Å)	Difference (Å)[a]
Re1-Br1	2.6236(7)	2.65547	0.03187
Re1-N1	2.099(6)	2.10272	0.00372
Re1-N3	2.185(5)	2.19551	0.01051
Re1-C20	1.955(6)	1.97518	0.02018
Re1-C21	1.919(5)	1.92875	0.00975
Re1-C22	1.918(6)	1.92473	0.00673
N1-N2	1.291(7)	1.2997	0.0087
C7-N2	1.382(7)	1.3701	0.0119
C7-N3	1.319(8)	1.32976	0.01076
N3-N4	1.324(8)	1.37402	0.05002

Table S3. Comparison between bond lenghts obtained from X-ray diffraction vs theoretical values for H5^{Br}b.[a]
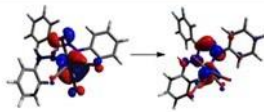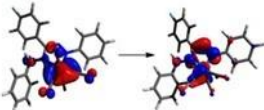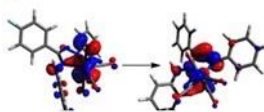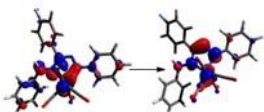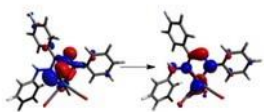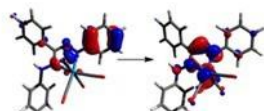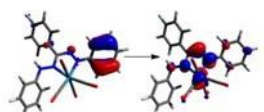
Bond length	Experimental (Å)	Theoretical (Å)	Difference (Å)[a]
Re1-Br1	2.5946(6)	2.64731	**0.05271**
Re1-N1	2.122(3)	2.11241	**-0.00959**
Re1-N3	2.174(4)	2.18773	**0.01373**
Re1-C20	1.957(5)	1.96716	0.01016
Re1-C21	1.916(6)	1.93083	0.01483
Re1-C22	1.964(4)	1.92394	**-0.04006**
N1-N2	1.293(5)	1.29652	0.00352
C7-N2	1.364(8)	1.3711	0.0071
C7-N3	1.326(5)	1.32938	0.00338
N3-N4	1.343(7)	1.37085	**0.02785**

[a] Values in bold indicate that the difference is statistically significant. Underestimated bond lengths are reported as negative values.

5.3.1   Time-dependent DFT
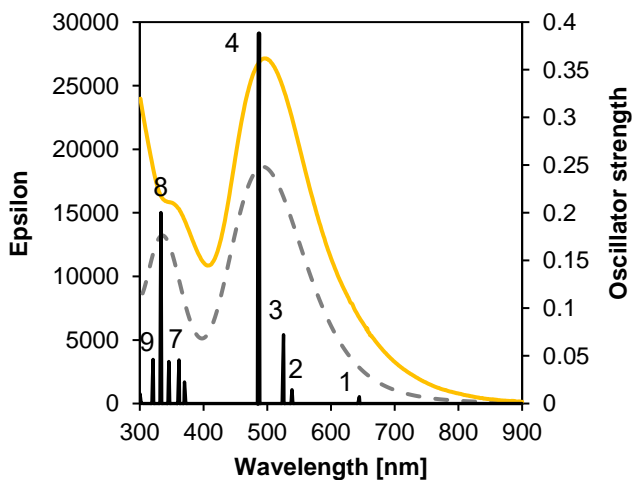
Figure S8. Comparison between experimental (yellow trace) and theoretical (dash line) spectra in H4^{Br}.

Table S4. Natural transitions orbitals (isovalue = 0.05) for the main electronic transitions in H4^{Br}.
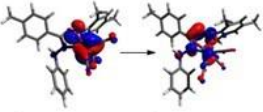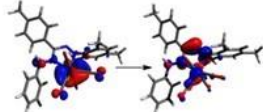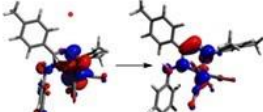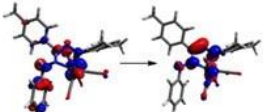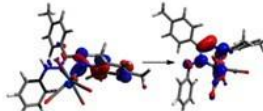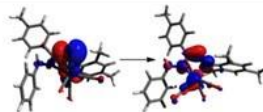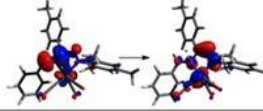
Excited state	Electronic transitions	TD-DFT λ_{theo}(nm)/ Energy (eV)	λ_{exp}(nm)	Oscillator strength	NTO Hole → Electron	Occupation number
1	H-1→L H→ L	644.54/1.9236		0.0072		0.99892
2	H-3→L H-2→L H-1→ L H→ L	538.83/2.3010	495 nm	0.0145		0.99618
3	H-3→ L H-2→L H-1→L H→L	525.58/2.3590		0.0722		0.99368
4	H-2→ L H-1→ L H → L	487.04/2.5457		0.3878		0.98807
7	H-12→L H-9→L H-3→L H-6→L H-5→L H-4→L	345.57/3.5878		0.0441		0.98121
8	H-12→L H-10→L H-9→L H-8→L H-6→L H-5→L	333.14/3.7217	353	0.2003		0.97748
9	H-12→L H-8→L H-7→L H-6→L H-5→L	320.80/3.8648		0.0463		0.97670
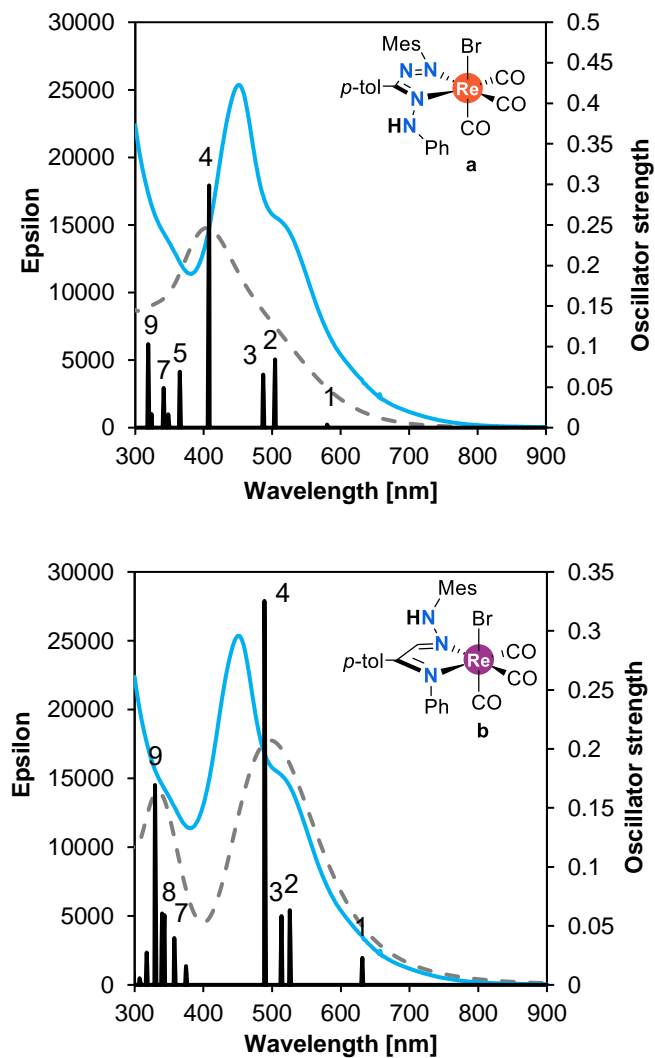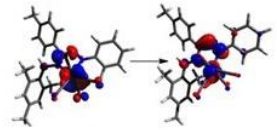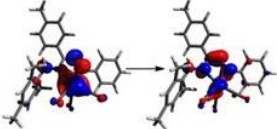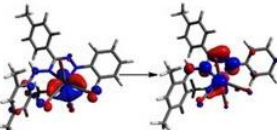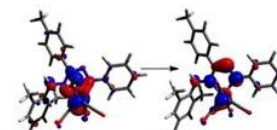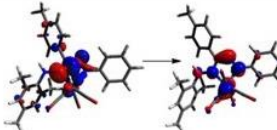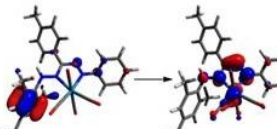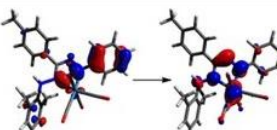
Figure S9. Comparison between experimental (blue trace) and theoretical (dash line) spectra in the isomers H5^{Br}a (upper) and H5^{Br}b. (down). The numbers refer to the corresponding excited state.

Table S5. Natural transition orbitals (isovalue = 0.05) for the main electronic transitions in H5^{Br}a.

Excited state	Electronic transitions	λ_{theo}(nm)/ Energy (eV)	λ_{exp} (nm)	Oscillator strength	Hole → Electron	Occupation number
		TD-DFT			NTO	
1	H-9→L H-2→ H-1→L H→L	608.08/2.0389		0.0014		0.99761
2	H-7→L H-5→L H-3→L H-2→ L H-1→ L H→L	542.51/2.2854	520	0.0480		0.99508
3	H-2→L H → L	504.19/2.4591		0.0695		0.99011
4	H-5→L H-3→ L H-2→ L H -1→ L H→L	443.98/2.7925		0.2957		0.98790
5	H-13→L H-12→L H-5→L H-3→L	404.68/3.0638		0.0503		0.98907
7	H-10 → L H-9 → L H-8 → L H-7 → L H-6 → L H-5 → L	344.44/3.5996	≈350	0.0525		0.98683
9	H-13 →L H-12→L H-10 →L H-9 →L H-6→ L	330.43/3.7522		0.0925		0.97532

Table S6. Natural transition orbitals (isovalue = 0.05) for the main electronic transitions in H5^{Br}b.

		TD-DFT			NTO	
Excited state	Electronic transitions	λ_{theo}(nm)/ Energy (eV)	λ_{exp}(nm)	Oscillator strength	Hole → Electron	Occupation Number
1	H-1→L H→ L	631.38/ 1.9637		0.0229		0.99873
2	H-4→L H-3→ L H-2→ L H-1 → L H → L	525.81/2.6393	452	0.0633		0.99201
3	H-6→ L H-5 → L H-4 → L H-3→L H-1 → L H → L	513.70/2.4136		0.0583		0.99712
4	H-3 → L H-2 → L H-1 → L H → L	488.84/2.5363		0.3254		0.98823
7	H-13 →L H-10 →L H-9 →L H-6 → L H-4 →L H-3 →L	343.37/3.6108		0.0591		0.98084
8	H-13 → L H-6 → L H-5 → L H-4 → L H-3 → L	339.90/3.6477	≈350	0.0605		0.98627
9	H-13 → L H-10 → L H-9 → L H-8 →L H-6 → L H-4 → L H-3 → L	329.64/3.7612		0.1694		0.97723
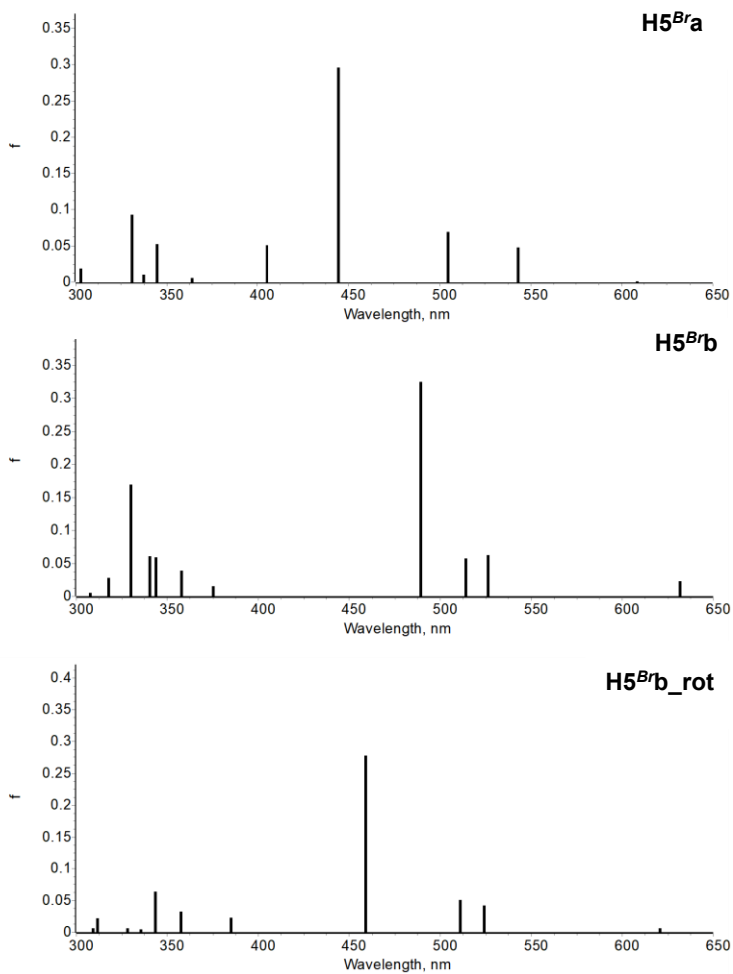
Figure S10. Comparison between TDDFT-calculated transitions in H5^{Br}a, H5^{Br}b and H5^{Br}b_rot in the range 300 to 650 nm. Structure H5^{Br}b_rot has the N-Ph group rotated to match the orientation found in H5^{Br}a.
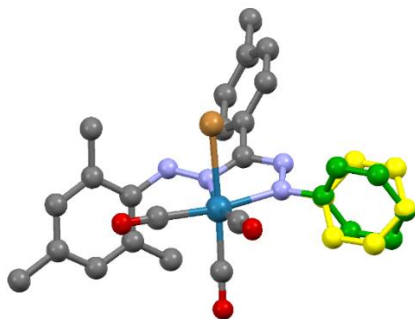
Figure S11. Overlayed structure of H5*Br*b (yellow)and H5*Br*b_rot (green).

5.3.2 Fragment-based NBO analysis

Using Gaussian16, a CAM-B3LYP/def2-TZVP calculation was performed, followed by an NBO analysis [A.E. Reed, F. Weinhold, Natural bond orbital analysis of near-Hartree-Fock water dimer, *J. Chem. Phys*. 78, 4066-4073 (1983)]. The NBOs were subsequently divided in NBOs localized on the azo-bound Ph ring, the connecting bond between the Ph ring and the rest of the complex. The Fock matrix elements between NBOs localized on different fragments were set to 0.0, and was diagonalized to find the orbitals of the complex with no interaction between the Ph-ring and the rest of the molecule. The original Fock matrix was then transformed to the basis of the non-interacting MOs, and was diagonalized to obtain the MOs of the complex in the basis of the fragment MOs.

Table S7. Orbital mixing (percentage contributions) between the azo-bound Ph ring and the rest of the complex in the geometries H5*Br*b and H5*Br*b_rot (only the orbitals involved in the excited state 4 are shown).

	H5*Br*b				H5*Br*b_rot		
MO	**C=N**	**Re**	**phenyl**	**MO**	**C=N**	**Re**	**phenyl**
H-3	0.3	98.9	0.8	H-3	0.3	91.2	8.5
H-2	0	92.9	7.1	H-2	0	98.5	1.5
H-1	0	99.4	0.6	H-1	0	99.8	0.2
H	0	95.3	4.7	H	0	99.7	0.3
L	0	89.5	10.5	L	0	98	1.9
L+1	0	87.9	12.1	L+1	0	95.5	4.5

5.4 Luminescence studies of complex H4*Br*

Luminescence spectroscopy was performed with a *Fluorolog®*-3 spectrometer from *HORIBA Jobin Yvon*. A four-window cuvette from *Hellma® Analytics* (d = 1 cm) was used. A *TBX Picosecond Photon Detection Module* from *HORIBA Jobin Yvon* served as detector. In time-dependent luminescence spectroscopy a *Nano-LED pulsed diode light source* (**λ**max = 370 nm) from *HORIBA Scientific* combined with a *Single Photon counting*

controller FluoroHub from *HORIBA Jobin Yvon* as a pulse control unit were used. Luminescence decay data were corrected for scattered light by a separate measurement of a non-emissive silica suspension at equal excitation and detection wavelength (λ = 370 nm). Lifetimes were obtained from mono exponential fits of the luminescence decay using fit options implemented in *originPro®* from *OriginLab®*. Excitation in steady state luminescence spectroscopy was performed using a *Xenon Short Arc Lamp from Ushio Inc.* light source.
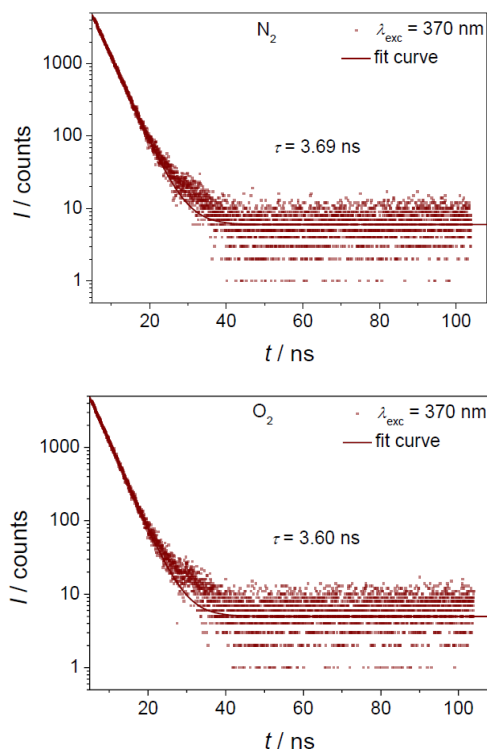
Figure S12. Lifetime decay for H4^{Br} under N_2 (upper) and under O_2 (down).

References

(1)   Maslakova, T. I.; Lipunov, I. N.; Pervova, I. G.; Maslakov, P. A. Formazan-Containing Solid-Phase Reagent Indicator Systems for Environmental Analysis. *Russ. J. Gen. Chem.* **2018**, *88* (12), 2717–2731. https://doi.org/10.1134/S1070363218120423.

(2)   Ciapetti, G.; Cenni, E.; Pratelli, L.; Pizzoferrato, A. In Vitro Evaluation of Cell/Biomaterial Interaction by MTT Assay. *Biomaterials* **1993**, *14* (5), 359–364.

(3)   Szymczyk, M.; El-shafei, A.; Freeman, H. S. Design , Synthesis , and Characterization of New Iron-Complexed Azo Dyes. *Dye. Pigment.* **2007**, *72*, 8–15. https://doi.org/10.1016/j.dyepig.2005.07.009.

(4)   Gilroy, J. B.; McKinnon, S. D. J.; Koivisto, B. D.; Hicks, R. G. Electrochemical Studies of Verdazyl Radicals. *Org. Lett.* **2007**, *9* (23), 4837–4840. https://doi.org/10.1021/ol702163a.

(5)   Hunter, L.; Roberts, C. B. The Azo-Group as a Chelating Group. Part V. Metallic Derivatives of Arylazo-Oximes and of Formazyl Compounds. *J. Chem. Soc.* **1941**, 823–826.

(6)   Barbon, S. M.; Price, J. T.; Reinkeluers, P. A.; Gilroy, J. B. Substituent-Dependent Optical and Electrochemical Properties of Triarylformazanate Boron Difluoride Complexes. *Inorg. Chem.* **2014**, *53* (19), 10585–10593. https://doi.org/10.1021/ic5016912.

(7)   Gilroy, J. B.; Otten, E. Formazanate Coordination Compounds: Synthesis, Reactivity, and Applications. *Chem. Soc. Rev.* **2020**, *49* (1), 85–113. https://doi.org/10.1039/c9cs00676a.

(8)   de Vries, F.; Otten, E. Reversible On/Off Switching of Lactide Cyclopolymerization with a Redox-Active Formazanate Ligand. *ACS Catal.* **2022**, *12* (7), 4125–4130. https://doi.org/10.1021/acscatal.1c05689.

(9)   Chang, M. C.; Roewen, P.; Travieso-Puente, R.; Lutz, M.; Otten, E. Formazanate Ligands as Structurally Versatile, Redox-Active Analogues of β-Diketiminates in Zinc Chemistry. *Inorg. Chem.* **2015**, *54* (1), 379–388. https://doi.org/10.1021/ic5025873.

(10)   Zhao, B.; Han, Z.; Ding, K. The N-H Functional Group in Organometallic Catalysis. *Angew. Chem. Int. Ed.* **2013**, *52* (18), 4744–4788. https://doi.org/10.1002/anie.201204921.

(11)   Wu, H. L.; Li, X. B.; Tung, C. H.; Wu, L. Z. Bioinspired Metal Complexes for Energy-Related Photocatalytic Small Molecule Transformation. *Chem. Commun.* **2020**, *56* (99), 15496–15512. https://doi.org/10.1039/d0cc05870j.

(12)   Drosou, M.; Kamatsos, F.; Mitsopoulou, C. A. Recent Advances in the Mechanisms of the Hydrogen Evolution Reaction by Non-Innocent Sulfur-Coordinating Metal Complexes. *Inorg. Chem. Front.* **2019**, *7* (1), 37–71. https://doi.org/10.1039/c9qi01113g.

(13)   Siewert, I. Electrochemical CO_2 Reduction Catalyzed by Binuclear $LRe_2(CO)_6Cl_2$ and $LMn_2(CO)_6Br_2$ Complexes with an Internal Proton Source. *Acc. Chem. Res.* **2022**, *55* (4), 473–483. https://doi.org/10.1021/acs.accounts.1c00609.

(14)   Fujita, E.; Grills, D. C.; Manbeck, G. F.; Polyansky, D. E. Understanding the Role of Inter- and Intramolecular Promoters in Electro- and Photochemical CO_2 Reduction Using Mn, Re, and Ru Catalysts. *Acc. Chem. Res.* **2022**, *55* (5), 616–628. https://doi.org/10.1021/acs.accounts.1c00616.

(15)   Drover, M. W. A Guide to Secondary Coordination Sphere Editing. *Chem. Soc. Rev.* **2022**, *51* (6), 1861–1880. https://doi.org/10.1039/d2cs00022a.

(16)   Gallardo-Villagrán, M.; Rivada-Wheelaghan, O.; Rahaman, S. M. W.; Fayzullin, R. R.; Khusnutdinova, J. R. Proton-Responsive Naphthyridinone-Based RuIIcomplexes and Their Reactivity with Water and Alcohols. *Dalton. Trans.* **2020**, *49* (36), 12756–12766. https://doi.org/10.1039/d0dt02505d.

(17)   Zhou, C.; Hu, J.; Wang, Y.; Yao, C.; Chakraborty, P.; Li, H.; Guan, C.; Huang, M. H.; Huang, K. W. Selective Carbonylation of Benzene to Benzaldehyde Using a Phosphorus-Nitrogen PN^3P-Rhodium(I) Complex. *Org. Chem. Front.* **2019**, *6* (6), 721–724. https://doi.org/10.1039/c8qo00892b.

(18)   Mukherjee, J.; Siewert, I. Manganese and Rhenium Tricarbonyl Complexes Equipped with Proton Relays in the Electrochemical CO_2 Reduction Reaction. *Eur. J. Inorg. Chem.* **2020**, *2020* (46), 4319–4333. https://doi.org/10.1002/ejic.202000738.

(19)   Darshani, T.; Thushara, N.; Weerasuriya, P.; Fronczek, F. R.; Perera, I. C.; Perera, T. Fluorescent Di-(2-Picolyl)Amine Based Drug-like Ligands and Their Re(CO)₃ Complexes towards

Biological Applications. *Polyhedron* **2020**, *185*, 114592. https://doi.org/10.1016/j.poly.2020.114592.

(20)   Gaire, S.; Schrage, B. R.; Ziegler, C. J. An Organometallic Isostere of an Amino Acid. *Inorg. Chem.* **2021**, *60* (14), 10105–10108. https://doi.org/10.1021/acs.inorgchem.1c01444.

(21)   Auvray, T.; Pal, A. K.; Hanan, G. S. Electronic Properties of Rhenium(I) Carbonyl Complexes Bearing Strongly Donating Hexahydro-Pyrimidopyrimidine Based Ligands. *Eur. J. Inorg. Chem.* **2021**, *2021* (26), 2570–2577. https://doi.org/10.1002/ejic.202100028.

(22)   Gonçalves, M. R.; Benvenho, A. R. V.; Frin, K. P. M. Electrical and Optical Properties of Organic Light-Emitting Diodes with Rhenium(I) Complexes Using DC and AC Methods. *Opt. Mater.* **2019**, *94* (May), 206–212. https://doi.org/10.1016/j.optmat.2019.05.042.

(23)   Deeba, R.; Molton, F.; Chardon-Noblat, S.; Costentin, C. Effective Homogeneous Catalysis of Electrochemical Reduction of Nitrous Oxide to Dinitrogen at Rhenium Carbonyl Catalysts. *ACS Catal.* **2021**, *11*, 6099–6103. https://doi.org/10.1021/acscatal.1c01197.

(24)   Hellman, A. N.; Haiges, R.; Marinescu, S. C. Rhenium Bipyridine Catalysts with Hydrogen Bonding Pendant Amines for CO_2 Reduction. *Dalton. Trans.* **2019**, *48* (38), 14251–14255. https://doi.org/10.1039/c9dt02689d.

(25)   Riplinger, C.; Carter, E. A. Influence of Weak Bronsted Acids on Electrocatalytic CO_2 Reduction by Manganese and Rhenium Bipyridine Catalysts. *ACS Catal.* **2015**, *5* (2), 900–908. https://doi.org/10.1021/cs501687n.

(26)   Wong, K. Y.; Chung, W. H.; Lau, C. P. The Effect of Weak Brönsted Acids on the Electrocatalytic Reduction of Carbon Dioxide by a Rhenium Tricarbonyl Bipyridyl Complex. *J. Electroanal. Chem.* **1998**, *453* (1–2), 161–170. https://doi.org/10.1016/S0022-0728(98)00116-8.

(27)   Sinha, S.; Berdichevsky, E. K.; Warren, J. J. Electrocatalytic CO_2 Reduction Using Rhenium(I) Complexes with Modified 2-(2′-Pyridyl)Imidazole Ligands. *Inorganica Chim. Acta* **2017**, *460*, 63–68. https://doi.org/10.1016/j.ica.2016.09.019.

(28)   Sung, S.; Kumar, D.; Gil-Sepulcre, M.; Nippe, M. Electrocatalytic CO_2 Reduction by Imidazolium-Functionalized Molecular Catalysts. *J. Am. Chem. Soc.* **2017**, *139* (40), 13993–13996. https://doi.org/10.1021/jacs.7b07709.

(29)   Manbeck, G. F.; Muckerman, J. T.; Szalda, D. J.; Himeda, Y.; Fujita, E. Push or Pull? Proton Responsive Ligand Effects in Rhenium Tricarbonyl CO_2 Reduction Catalysts. *J. Phys. Chem. B* **2015**, *119* (24), 7457–7466. https://doi.org/10.1021/jp511131x.

(30)   Rotundo, L.; Polyansky, D. E.; Gobetto, R.; Grills, D. C.; Fujita, E.; Nervi, C.; Manbeck, G. F. Molecular Catalysts with Intramolecular Re − O Bond for Electrochemical Reduction of Carbon Dioxide. *Inorg. Chem.* **2020**, *59*, 12187–12199. https://doi.org/10.1021/acs.inorgchem.0c01181.

(31)   Jia-Pei, D.; Wilting, A.; Siewert, I. Are Two Metal Ions Better than One? Mono and Binuclear Alfa-Diimine-Re(CO)$_3$ Complexes with Proton-Responsive Ligands in CO_2 Reduction Catalysis. *Chem. A Eur. J.* **2019**, *25*, 5555–5564. https://doi.org/10.1002/chem.201806398.

(32)   Vollmer, M. V.; Machan, C. W.; Clark, M. L.; Antholine, W. E.; Agarwal, J.; Schaefer, H. F.; Kubiak, C. P.; Walensky, J. R. Synthesis, Spectroscopy, and Electrochemistry of (α-Diimine)M(CO)$_3$Br, M = Mn, Re, Complexes: Ligands Isoelectronic to Bipyridyl Show Differences in CO_2 Reduction. *Organometallics* **2015**, *34* (1), 3–12. https://doi.org/10.1021/om500838z.

(33)   Mckinnon, M.; Ngo, K. T.; Sobottka, S.; Sarkar, B.; Ertem, M. Z.; Grills, D. C.; Rochford, J. Synergistic Metal–Ligand Redox Cooperativity for Electrocatalytic CO_2 Reduction Promoted by a Ligand-Based Redox Couple in Mn and Re Tricarbonyl Complexes. *Organometallics* **2019**, *38*, 1317–1329. https://doi.org/10.1021/acs.organomet.8b00584.

(34)   Benson, E. E.; Sampson, M. D.; Grice, K. A.; Smieja, J. M.; Froehlich, J. D.; Friebel, D.; Keith, J. A.; Carter, E. A.; Nilsson, A.; Kubiak, C. P. The Electronic States of Rhenium Bipyridyl Electrocatalysts for CO_2 Reduction as Revealed by X-Ray Absorption Spectroscopy and Computational Quantum Chemistry. *Angew. Chem. Int. Ed.* **2013**, *52*, 4841–4844. https://doi.org/10.1002/anie.201209911.

(35)   Matson, B. D.; McLoughlin, E. A.; Armstrong, K. C.; Waymouth, R. M.; Sarangi, R. Effect of Redox Active Ligands on the Electrochemical Properties of Manganese Tricarbonyl Complexes. *Inorg. Chem.* **2019**, *58*, 7453–7465. https://doi.org/10.1021/acs.inorgchem.9b00652.

(36)   Queyriaux, N. Redox-Active Ligands in Electro-assisted Catalytic H⁺ and CO₂ Reductions: Benefits and Risks. *ACS Catal.* **2021**, 4024–4035. https://doi.org/10.1021/acscatal.1c00237.

(37)   Travieso-Puente, R.; Chang, M. C.; Otten, E. Alkali Metal Salts of Formazanate Ligands: Diverse Coordination Modes as a Result of the Nitrogen-Rich [NNCNN] Ligand Backbone. *Dalton. Trans.* **2014**, *43* (48), 18035–18041. https://doi.org/10.1039/c4dt02578d.

(38)   Baumgardner, D. F.; Parks, W. E.; Gilbertson, J. D. Harnessing the Active Site Triad: Merging Hemilability, Proton Responsivity, and Ligand-Based Redox-Activity. *Dalton. Trans.* **2020**, *49* (4), 960–965. https://doi.org/10.1039/c9dt04470a.

(39)   V. d., G.; Steven Plovan, T.; Searless, S. Proton Nuclear Resonance Spectroscopy. Rapid Tautomerization of Formazans. *J. Org. Chem.* **1960**, *25* (2), 285–286.

(40)   Sigeikin, G. I.; Lipunova, G. N.; Pervova, I. G. Formazans and Their Metal Complexes. *Russ. Chem. Rev.* **2006**, *75* (10), 885–900. https://doi.org/10.1070/rc2006v075n10abeh003612.

(41)   Allen, F. H.; Watson, D. G.; Bramer, L.; Orpen, A. G.; Taylor, R. International Tables for Crystallography (2006). In *International Tables fo Crystallography*; 2006; Vol. C, pp 790–811.

(42)   Chakraborty, I.; Carrington, S. J.; Mascharak, P. K. Photodelivery of CO by Designed PhotoCORMs: Correlation between Absorption in the Visible Region and Metal-CO Bond Labilization in Carbonyl Complexes. *ChemMedChem* **2014**, *9* (6), 1266–1274. https://doi.org/10.1002/cmdc.201402007.

(43)   Kottelat, E.; Lucarini, F.; Crochet, A.; Ruggi, A.; Zobi, F. Correlation of MLCTs of Group 7 fac-[M(CO)₃]⁺ Complexes (M = Mn, Re) with Bipyridine, Pyridinylpyrazine, Azopyridine, and Pyridin-2-Ylmethanimine Type Ligands for Rational PhotoCORM Design. *Eur. J. Inorg. Chem.* **2019**, 3758–3768. https://doi.org/10.1002/ejic.201900568.

(44)   Samanta, S.; Ghosh, P.; Goswami, S. Recent Advances on the Chemistry of Transition Metal Complexes of 2-(Arylazo)Pyridines and Its Derivatives. *Dalton. Trans.* **2012**, *41*, 2213–2226. https://doi.org/10.1039/c2dt10986g.

(45)   Roy, S.; Sieger, M.; Sarkar, B.; Schwerdeski, B.; Lissner, F.; Schleid, T.; Fiedler, J.; Kaim, W. Establishing the Chelating Alfa-Azocarbonyl Function in Pi-Acceptor Ligands. *Angew. Chem. Int. Ed.* **2008**, *47*, 6192–6194.

(46)   Carrington, S. J.; Chakraborty, I.; Alvarado, J. R.; Mascharak, P. K. Differences in the CO Photolability of cis- and trans-[RuCl₂(Azpy)(CO)₂] Complexes: Effect of Metal-to-Ligand Back-Bonding. *Inorganica Chim. Acta* **2013**, *407*, 121–125. https://doi.org/10.1016/j.ica.2013.07.047.

(47)   Wei, L.; Babich, J. W.; Ouellette, W.; Zubieta, J. Developing the {M(CO)₃}⁺ Core for Fluorescence Applications: Rhenium Tricarbonyl Core Complexes with Benzimidazole, Quinoline, and Tryptophan Derivatives. *Inorg. Chem.* **2006**, *45*, 3057–3066. https://doi.org/10.1021/ic0517319.

(48)   Morimoto, T.; Ito, M.; Koike, K.; Kojima, T.; Ozeki, T.; Ishitani, O. Dual Emission from Rhenium(I) Complexes Induced by an Interligand Aromatic Interaction. *Chem. A Eur. J.* **2012**, *18* (11), 3292–3304. https://doi.org/10.1002/chem.201102698.

(49)   Milocco, F.; De Vries, F.; Bartels, I. M. A.; Havenith, R. W. A.; Cirera, J.; Demeshko, S.; Meyer, F.; Otten, E. Electronic Control of Spin-Crossover Properties in Four-Coordinate Bis(Formazanate) Iron(II) Complexes. *J. Am. Chem. Soc.* **2020**, *142* (47), 20170–20181. https://doi.org/10.1021/jacs.0c10010.

(50)   Chang, M. C.; Otten, E. Synthesis and Ligand-Based Reduction Chemistry of Boron Difluoride Complexes with Redox-Active Formazanate Ligands. *Chem. Commun.* **2014**, *50* (56), 7431–7433. https://doi.org/10.1039/c4cc03244f.

(51)   Yu, H. S.; He, X.; Truhlar, D. G. MN15-L: A New Local Exchange-Correlation Functional for Kohn-Sham Density Functional Theory with Broad Accuracy for Atoms, Molecules, and Solids. *J. Chem. Theory Comput.* **2016**, *12* (3), 1280–1293. https://doi.org/10.1021/acs.jctc.5b01082.

(52)   Weigend, F.; Ahlrichs, R. Balanced Basis Sets of Split Valence, Triple Zeta Valence and Quadruple Zeta Valence Quality for H to Rn: Design and Assessment of Accuracy. *Phys. Chem. Chem. Phys.* **2005**, *7* (18), 3297–3305. https://doi.org/10.1039/b508541a.

(53)   Leirer, M.; Knör, G.; Vogler, A. Synthesis and Spectroscopic Properties of 1,2-Diiminetricarbonylrhenium(I)Chloride Complexes with Aliphatic Diimines (or 1,4-Diaza-1,3-

Butadienes) as Ligands. *Z. Naturforschung B* **1999**, *54*, 341–344. https://doi.org/10.1515/znb-1999-0308.

(54)   Klemens, T.; Świtlicka, A.; Szlapa-Kula, A.; Łapok, Ł.; Obłoza, M.; Siwy, M.; Szalkowski, M.; MaćKowski, S.; Libera, M.; Schab-Balcerzak, E.; MacHura, B. Tuning Optical Properties of Re(I) Carbonyl Complexes by Modifying Push-Pull Ligands Structure. *Organometallics* **2019**, *38* (21), 4206–4223. https://doi.org/10.1021/acs.organomet.9b00517.

(55)   Stout, M. J.; Skelton, B. W.; Sobolev, A. N.; Raiteri, P.; Massi, M.; Simpson, P. V. Synthesis and Photochemical Properties of Re(I) Tricarbonyl Complexes Bound to Thione and Thiazol-2-Ylidene Ligands. *Organometallics* **2020**, *39* (17), 3202–3211. https://doi.org/10.1021/acs.organomet.0c00381.

(56)   Kumar, A.; Sun, S.-S.; Lees, A. J. Photophysics and Photochemistry of Organometallic Rhenium Diimine Complexes. In *Photophysics of Organometallics*; Lees, A. J., Ed.; Springer Berlin, Heidelberg: Binghamton, NY, 2010; p 240.

(57)   Worl, L. A.; Duesing, R.; Chen, P.; Ciana, L. Della; Meyer, T. J. Photophysical Properties of Polypyridyl Carbonyl Complexes of Rhenium(I). *J. Chem. Soc. Dalt. Trans.* **1991**, No. S, 849–858. https://doi.org/10.1039/DT9910000849.

(58)   Chang, M. C.; Chantzis, A.; Jacquemin, D.; Otten, E. Boron Difluorides with Formazanate Ligands: Redox-Switchable Fluorescent Dyes with Large Stokes Shifts. *Dalton. Trans.* **2016**, *45* (23), 9477–9484. https://doi.org/10.1039/c6dt01226d.

(59)   Maar, R. R.; Zhang, R.; Stephens, D. G.; Ding, Z.; Gilroy, J. B. Near-Infrared Photoluminescence and Electrochemicaluminescence from a Remarkably Simple Boro Difluoride Formazanate Dye. *Angew. Chem. Int. Ed.* **2019**, *58*, 1052–1056. https://doi.org/10.1002/anie.201811144.

(60)   Maar, R. R.; Barbon, S. M.; Sharma, N.; Groom, H.; Luyt, L. G.; Gilroy, J. B. Evaluation of Anisole-Substituted Born Difluoride Formazanate Complexes for Fluorescence Cell Imaging. *Chem. Eur. J.* **2015**, *21*, 15589–15599. https://doi.org/10.1002/chem.201502821.

(61)   S. P. Schmidt, W. C. Trogler, F. B. Pentacarbonylrhenium Halides. In *Inorganic syntheses*; Angelici, R. J., Ed.; Wiley, 1991; Vol. 28. https://doi.org/10.1016/0022-328x(91)83257-5.

(62)   Sheldrick, G. M. Crystal Structure Refinement with SHELXL. *Acta Crystallogr. Sect. C* **2015**, *71*, 3–8. https://doi.org/10.1107/S2053229614024218.

(63)   M. J. Frisch, G. W. Trucks, H. B. Schlegel, G. E. S.; M. A. Robb, J. R. Cheeseman, G. Scalmani, V. B.; G. A. Petersson, H. Nakatsuji, X. Li, M. Caricato, A. V. M.; J. Bloino, B. G. Janesko, R. Gomperts, B. Mennucci, H. P. H.; J. V. Ortiz, A. F. Izmaylov, J. L. Sonnenberg, D. W.-Y.; F. Ding, F. Lipparini, F. Egidi, J. Goings, B. Peng, A. P.; T. Henderson, D. Ranasinghe, V. G. Zakrzewski, J. Gao, N. R.; G. Zheng, W. Liang, M. Hada, M. Ehara, K. Toyota, R. F.; J. Hasegawa, M. Ishida, T. Nakajima, Y. Honda, O. Kitao, H. N.; T. Vreven, K. Throssell, J. A. Montgomery, Jr., J. E. P.; F. Ogliaro, M. J. Bearpark, J. J. Heyd, E. N. Brothers, K. N. K.; V. N. Staroverov, T. A. Keith, R. Kobayashi, J. N.; K. Raghavachari, A. P. Rendell, J. C. Burant, S. S. I.; J. Tomasi, M. Cossi, J. M. Millam, M. Klene, C. Adamo, R. C.; J. W. Ochterski, R. L. Martin, K. Morokuma, O. F.; J. B. Foresman, and D. J. F. Gaussian 16, Revision C.02. Wallingford CT 2019.

(64)   Dennington, Roy; Keith, Todd A.; Millam, J. M. GaussView, Version 6. Semichem Inc., Shawnee Mission: KS 2016.

(65)   Hanwell, M. D.; Curtis, D. E.; Lonie, D. C.; Vandermeersch, T.; Zurek, E.; Hutchinson, G. R. Avogadro: An Advanced Semantic Chemical Editor, Visualization, and Analysis Platform. *J. Cheminform.* **2012**, *4*, 1–17. https://doi.org/10.1186/1758-2946-4-17.

(66)   Sae-Heng, P.; Tantirungrotechai, J.; Tantirungrotechai, Y. Scale Factors for Carbonyl Vibrational Frequencies: A Study of Partial Hessian Approximation. *Chiang Mai J. Sci.* **2018**, *45* (7), 2797–2808.

(67)   Miertuš, S.; Scrocco, E.; Tomasi, J. Electrostatic Interaction of a Solute with a Continuum. A Direct Utilization of AB Initio Molecular Potentials for the Prevision of Solvent Effects. *Chem. Phys.* **1981**, *55*, 117–129. https://doi.org/10.1016/0301-0104(81)85090-2.

Chapter 3

Formazanate Re(I) complexes: Synthesis, characterization, and computational studies

Herein, we describe the synthesis and characterization of Re(I) carbonyl complexes $[ReX(CO)_3(L,L)]^n$ (n=-1 X = Br; n = 0 X = MeCN) bearing the anionic formazanate ligand $[R^1-N^1-N^2=C(R^3)-N^4=N^5-R^5]^-$. These compounds were prepared by deprotonating their Re(I) neutral *open*-formazan conjugated acids. Spectroscopic (NMR, IR) and structural characterization of these species indicate that *open* coordination is retained in the formazanate anions. Methylation of the N1-position was shown to be useful to block the proton-responsive nature of the ligand, which allows establishing a comparison between the electrochemical properties of complexes containing the neutral formazan fragment *vs* the anionic formazanate species in the following chapter. DFT calculations showed the LUMO orbital in formazanate species is purely ligand-based, unlike formazan complexes, wherein the LUMO possesses metal-ligand character. Although formazanate complexes exhibit different electronic properties to those observed in their formazan analogs —derived from their greater extent of π-delocalization— both compounds display low emissive features in the visible range.

1. Introduction

Redox-active ligands represent an emerging field in Coordination Chemistry. Gray and coworkers' first report on the redox non-innocent nature of the dithiolene ligand in the 60s,[1,2] inaugurated a new area for ligand design. Besides controlling metal reactivity by electronic and steric effects –as innocent ligands do– redox-active fragments could confer other attributes to the metal complexes. To mention a few, reversible switching of ligand redox states can influence the Lewis acidity/basicity of the metal center and create new venues for substrate activation/redox catalysis, either solely on the ligand or in a bifunctional manner *via* metal-ligand cooperativity.[3-6]

The highly conjugated, 1,2-di-thiolates, -phenolates, -aminophenolates, and -diimines motifs are commonly found in redox-active fragments, where charge delocalization within the ligand backbone allows stabilization of different redox states on the complex. Other combinations also involve merging one of these features with other functional groups. For instance, in the anionic formazanate ligand $[R^1-N^1-N^2=C(R^3)-N^4=N^5-R^5]^-$, an azo and imine fragment are combined. In metal complexes, this scaffold has shown to give access to reversible redox properties, a feature recently harnessed in catalysis.[7,8]

Our group described the reactivity of the two-electron reduced boron formazanate complex $[LBPh_2]^{2-}$ [L= PhNNC(*p*-tol)NNPh]$^-$ with H_2O and BnBr, as electrophiles. By S_N2 reaction, a boratoleucoverdazyl compound with an N-E bond (E = H, Bn) is afforded, and by homolytic N-E cleavage with TEMPO, the stable formazanate radical and the corresponding TEMPO-E product were obtained (Chapter 1, Scheme 9). This example demonstrates the capabilities of the formazanate ligand in these species to behave as a two-electron/one-electrophile storage.[9] Recently, we reported that the neutral formazan $R^1-N^1H-N^2=C(R^3)-N^4=N^5-R^5$ could also serve as a bidentate ligand and chelates metals in an *open* fashion. We prepared a series of formazan-type Re(I) complexes containing an NH pendant arm.[10] We hypothesized that these ligands could also operate as two-electron/one-proton reservoirs, and we, therefore, explore the reactivity of the NH fragment (deprotonation, alkylation) in this chapter, as well as its electrochemical properties later in the thesis (*Chapter 4*). Here, we discuss the synthetic studies and characterization (NMR, UV-vis, FT-IR, XRD, DFT) of formazanate and methylformazan Re(I) complexes (**Figure 1**).
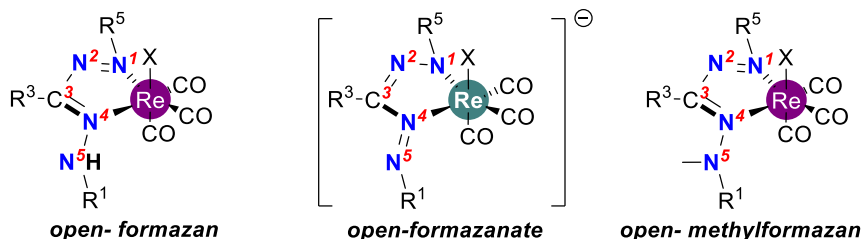
Figure 1. *Open* formazan and formazanate Re(I) complexes, herein studied R^3 = H, Ar, R^1, R^5 = Ar.

2. Results & Discussion

2.1 Synthesis of formazanate Re(I) complexes

Triethylammonium rhenium formazanate complexes [**1**^{Br}]⁻-[**4**^{Br}]⁻ were synthesized by deprotonation of the corresponding neutral precursors **H1**^{Br}-**H4**^{Br} using NEt₃ as base (Scheme 1). When the reaction is carried out in low-polarity solvents such as toluene, the formazanate complexes gradually are re-protonated by adventitious water, affording their neutral rhenium formazan precursors. Formazanate Re(I) species are less prone to protonation in polar solvents such as THF, acetonitrile, and acetone, presumably due to the stabilization of the charge species in polar media (Figure S8).[11] Indeed, we took advantage of the influence of solvent polarity on the stability of the formazanate complexes to isolate the ionic species in good yields.

Rhenium formazanate complexes exhibit a quite characteristic dark green color that can easily distinguish them from their dark purple conjugated acids. Although complexes [**1**^{Br}]⁻-[**4**^{Br}]⁻ differ in the *para*-substituent attached to the central ring (R = H, Me, MeO, F), their spectroscopic characterization by FT-IR, NMR and UV-vis indicates that they present similar electronic environments (*see* Figure S1 and S10). Therefore, we focused our subsequent studies on the reactivity of the F-containing derivative [**4**^{Br}]⁻ since tracking changes by ^{19}F NMR is more convenient.

In-situ addition of one equivalent of either bis(triphenylphosphine)iminium chloride [PPN][Cl] or tetraphenylphosphonium bromide [PPh₄][Br] to a solution of the triethylammonium formazanate [NHEt₃][**4**^{Br}] resulted in cation exchange to provide the corresponding ionic compounds [PPh₄][**4**^{Br}] and [PPN][**4**^{Br}] as solid microcrystalline materials, respectively. These species are less prone to protonation than their analog triethylammonium derivatives. Additionally, bromide substitution was achieved *via* ligand exchange. The reaction of the neutral formazan **H4**^{Br} with AgPF₆ in acetonitrile and subsequent deprotonation with DABCO afforded the neutral acetonitrile complex **4**^{MeCN} (Scheme 1).
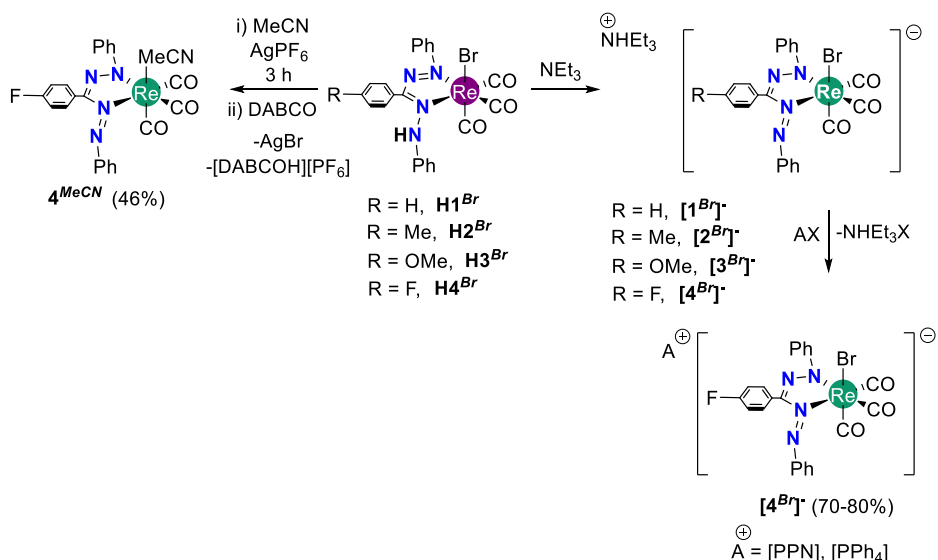
Scheme 1. Syntheses of formazanate Re(I) complexes.

As formazan/ate Re(I) species possess acid-base properties, we prepared an *N*-alkyl formazan Re(I) complex aiming to suppress the proton responsivity of the hydrazo/azo N^5 atom (Scheme 1). Unfortunately, attempts to prepare the *N*-methyl-triphenyl formazan ligand were unsuccessful since it rapidly cyclizes to generate the corresponding leucoverdazyl compound,[12,13] which oxidizes in air to a stable verdazyl radical. We also tried direct methylation on complex **H4Br** with an excess of CH₃I in the presence of Na₂CO₃. Even though the expected product was identified, the reaction was difficult to reproduce. Finally, we opted to synthesize a derivative with a small substituent (H) at the R^3 position, which is less prone to cyclization. *N*-methyl-1,5-diphenyl formazan (**L6Me**) was prepared following the procedure that Neugebauer and coworkers reported *via* methylation of 1,5-diphenyl formazan (**L6H**) in basic conditions.[12] Subsequent treatment of ligand **L6Me** with one equivalent of ReBr(CO)₅ afforded complex **Me6Br** in good isolated yield (Scheme 2).
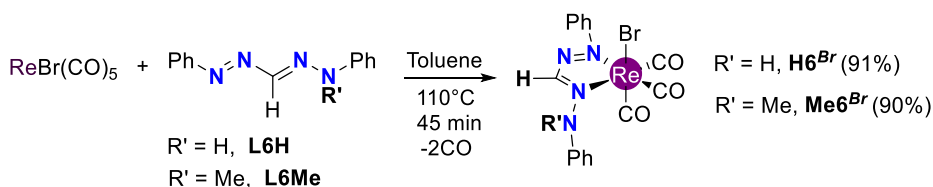
Scheme 2. Synthesis of 1,5-diphenyl formazan Re(I) complexes.

2.2   Characterization

Full deprotonation of the neutral formazan species **H1^{Br}**-**H4^{Br}** to give the formazanate complexes **[1^{Br}]**-**[4^{Br}]** upon treatment with NEt$_3$ was confirmed by ^{1}H-NMR spectroscopy. The absence of the diagnostic resonance of the NH group at *ca*. 8.5 ppm indicated the reaction proceeded to completion (Figure S1). The IR spectra (in THF solution) of anions **[1^{Br}]**-**[4^{Br}]** are essentially identical regardless of the countercation ([NHEt$_3$]$^+$, [PPN]$^+$ or [PPh$_4$]$^+$ (Figure S11), or the ligand substituent (Figure S9), and exhibit three ν(CO)bands around 2010, 1911, and 1891 cm^{-1} as expected for tricarbonyl complexes of *C1* symmetry.
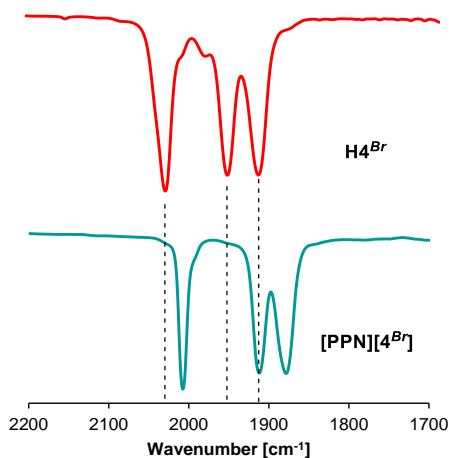
Figure 2. Comparative FT-IR spectra in THF solution between the formazan H4Br and formazanate [PPN][4Br] complexes.

Deprotonation shifts the carbonyl bands of the product formazanate tricarbonyl anions to lower frequencies due to the increased donor ability of the formazanate ligand (*e. g* **H4^{Br} =** 2031, 1955, 1918 cm^{-1}; **[PPN][*4^{Br}*]** = 2007, 1912, and 1880 cm^{-1}, *see* Figure 2). For **4^{MeCN}** (2024, 1992(br) cm^{-1}), the carbonyl bands are shifted to higher energies compared to **[4^{Br}]**$^-$ as substitution of the anionic bromide for the neutral acetonitrile ligand decreases the electron density at the metal center.

To study the influence of the methyl group on the *N*-methyl formazan complex **Me6^{Br}** we also prepared its non-alkylated version **H6^{Br}** (Scheme 2). Surprisingly, methylation of the NH function does not significantly alter the carbonyl stretching vibrations in the infrared spectra (**H6^{Br}** = 2031, 1953, 1919 cm^{-1} *vs* **Me6^{Br}** = 2031, 1952, 1915 cm^{-1}), making **Me6^{Br}** a useful reference for comparison of reactivity studies (*vide infra*).

Analysis of the ^{1}H-NMR spectra showed that the formazanate ligand coordinates asymmetrically in [**4**^{Br}]$^-$ and **4**^{MeCN}, as different sets of signals were identified for the aromatic protons in *ortho*-, *meta,* and *para*- positions (Figure S1-S3). Previous reports have established the preference for the asymmetric (*open*, five-membered chelate) over the symmetric (*closed*, six-membered chelate) coordination mode in formazanate ligands in sterically demanding environments.[14,15] To investigate the dynamics of the five-membered formazanate species in solution, we measured the [1]H-EXSY spectrum of [**PPN**][**4**^{Br}] at 80°C in toluene-d_8. The asymmetry of the ligand is retained at elevated temperature, and the lack of cross-peaks between the two distinct sets of *N*-Ar resonances indicates that exchange *via* a symmetrical six-membered formazanate chelate does not occur at an appreciable rate under such conditions (Figure S9). In the ^{13}C-NMR spectra of the anionic Re complexes, three resonances due to the CO ligands appear in the region 190-198 ppm, which are downfield shifted compared to their neutral precursors (185-193 ppm). Particularly, variations of the electronic distribution of the metallacycle upon ligand deprotonation are reflected in the chemical shift of the CO group *trans* to the deprotonated (-C=N^2-N^1-) imine-amide group (198 ppm), the most shifted downfield compared to the same CO ligand in the neutral formazan complex **H4**^{Br} (193 ppm).

The increased charge delocalization of the anionic fragment was also manifest in the chemical shift of the imine carbon, which is substantially shifted upfield (155 ppm) relative to the imine carbon in the protonated formazan complexes (164 ppm) (Figure S4). The NMR spectroscopic features of the formazanate ligand in the neutral acetonitrile complex **4**^{MeCN} are very similar to those of the anionic Re complexes (Figure S5). Finally, also the complexes with ligands **L6H** and **L6Me** have very similar NMR spectroscopic features, indicating that all compounds in this series are obtained with the Re center in a similar environment, i.e., a five-membered formazan(ate) chelate (Figure S6-S7).

2.3   Electronic spectroscopy

The electronic absorption spectrum of complex [**PPN**][**4**^{Br}] was measured in THF at 25°C ($c \approx 10^{-5}$M). It exhibits a broad and intense absorption band at 605 nm with a molar absorptivity of 54 800 M^{-1} cm^{-1} (Figure 3a), which is red-shifted compared to the neutral precursor (**H4**^{Br}: 515 nm). This feature is typical for metal complexes containing the formazanate ligand,[16] and is assigned to the π-π* electronic transitions centered on the formazanate backbone. The low-energy absorption of [**4**^{Br}]$^-$ undergoes negative solvatochromism and shifts to the red when the spectrum is recorded in toluene (620 nm). Exchanging the axial bromide ligand by acetonitrile in **4**^{MeCN} does not perturb the energy of these absorptions. However, within minutes after dissolution in THF, the main absorption band of **4**^{MeCN} undergoes a subtle shift to lower energy ($\Delta\lambda \approx 13$ nm), suggesting the displacement of MeCN by THF (Figure S12). In addition to the intense low-energy absorption, a less intense band is observed in the visible range at 440-460 nm arising from excitations of MLCT character ((Re(dπ) → formazanate (π*) based on

TDDFT calculations) (see Table S1). In comparison to complex **H4**^{Br}, which contains a triarylformazan ligand, the low-energy absorption maxima of the diphenylformazan complex **H6**^{Br} (470 nm) or the *N*-methyl derivative **Me6**^{Br} (450 nm) are blue-shifted (Figure 3b).
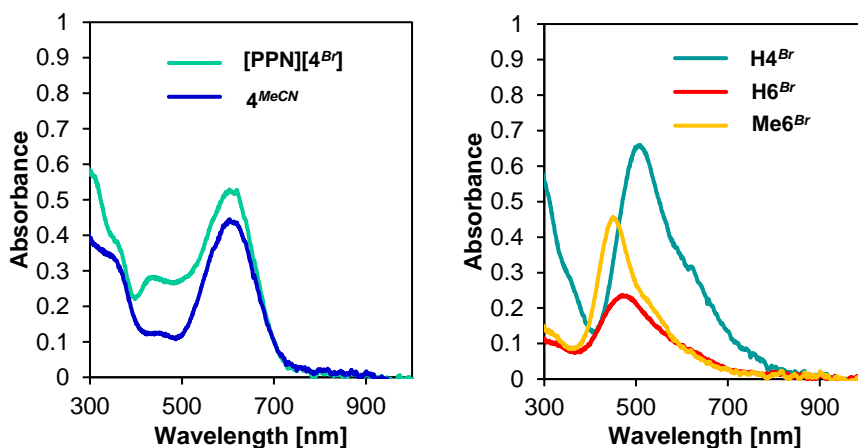
Figure 3. Absorption spectra of a) formazanate complexes [PPN][4^{Br}] and 4^{MeCN} and b) formazan complexes H4^{Br}, H6^{Br} and Me6^{Br} in THF.

Table 1. UV-vis spectrochemical data in THF

Compound	λ_{max}(nm)	ε[M^{-1}·cm^{-1}]	λ_{max}(nm)	ε[M^{-1}·cm^{-1}]	λ_{max}(nm)	ε[M^{-1}·cm^{-1}]
[PPN][4^{Br}]	603	54 800	441	28 400	350	39 200
[NHEt$_3$][4^{Br}]^a	615	26 300	462	13 600	350	26 600
4^{MeCN}	603	39 500	440	11 454	350	29 900
4$^{MeCN\,a}$	611	22 000	466	8 400	350	18 200
4^{THF}	627	40 100	470	14 300	342	37 700
H4^{Br}	515	59 400	-----	-----	353	29 200
H6^{Br}	470	22 600	-----	-----	328	9 500
Me6^{Br}	449	40 700	-----	-----	317	12 200

a = Measured in toluene

2.4 Structural characterization

Repeated attempts to obtain crystals of the anionic formazanate complex [**4**^{Br}]⁻ were unsuccessful, regardless of the countercation used. Ultimately, we were able to crystallize the compound as the decamethylcobaltocenium salt, **[Co(Cp*₂)][4**^{Br}**]**, by slow evaporation of a THF solution. An X-ray structure determination confirmed [**4**^{Br}]⁻ to consist of a *pseudo*-octahedral Re(I) center with a formazanate ligand bound in the 'open' fashion, rendering a five-membered rhenacycle, whereas the carbonyl ligands are placed in a facial arrangement. The refinement showed substitutional disorder in the Br/CO fragments *trans* to each other, but the rest of the molecule is well-defined. The metrical parameters within the metallacycle indicate that the Re1-N1 bond length (2.112(4) Å) is similar to that in the neutral precursor **H4**^{Br} (2.099(6) Å); however, it is shorter than Re-N(azo) bond lengths (2.156(3) Å [17]) in related species. The Re1-N3 bond length (2.192(4) Å) is typical for Re-N(imine) bonds.[18] Overall, the metrical parameters within the deprotonated formazanate backbone in [**4**^{Br}]⁻ are quite similar to that of the precursor, albeit a larger degree of delocalization is indicated by the equivalence of the N-N and C-N bonds, and the rhenium center is less displaced from the ligand plane (0.18 Å in [**4**^{Br}]⁻ vs. 0.46 Å in **H4**^{Br}). The complexes with the diphenylformazan ligand (**H6**^{Br} and **Me6**^{Br}) also display similar structures (Figure 4, Table 2).

[4^{Br}]$^-$
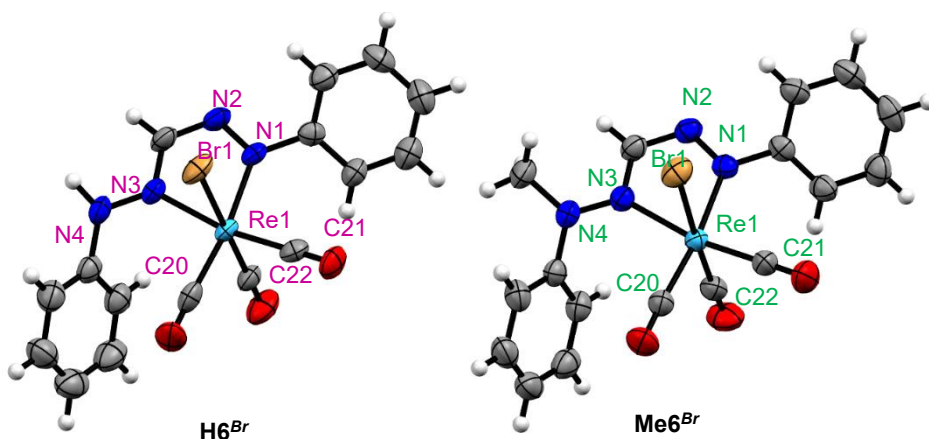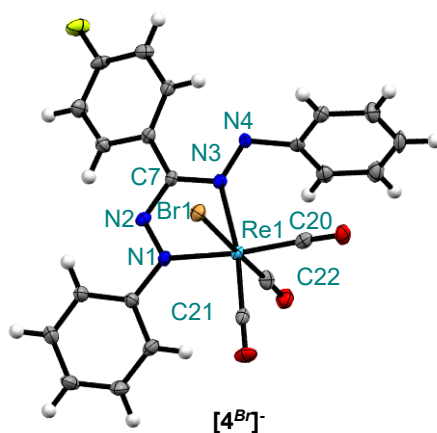
Figure 4. ORTEP representation of the molecular structure of a) H6^{Br}, b) Me6^{Br} and c) [Co(Cp*)$_2$][4^{Br}] (the counterion is omitted for clarity).

Table 2. Selected metrical parameters for [Co(Cp*)$_2$][4^{Br}]. H4^{Br}, H6^{Br} and Me6^{Br} (bond lengths in Å, angles in °).

Bond	Formazanate	Formazan		Alkylformazan
	[4^{Br}]$^-$	**H4^{BA}**	**H6^{Br}**	**Me6^{Br}**
Re1-Br1	2.6000(14)^b	2.6236(7)	2.6278(8)	2.6191(3)
Re1-N1	2.112(4)	2.099(6)	2.116(5)	2.124(2)
Re1-N3	2.192(4)	2.185(5)	2.161(4)	2.186(2)
Re1-C20	1.939(5)	1.955(6)	1.961(7)	1.941(3)
Re1-C21	1.912(5)	1.919(5)	1.936(6)	1.915(3)
Re1-C22	1.887(13)^b	1.918(6)	1.917(6)	1.913(3)
N1-N2	1.300(6)	1.291(7)	1.293(6)	1.292(3)
C7-N2	1.341(7)	1.382(7)	1.347(8)	1.369(4)
C7-N3	1.370(6)	1.319(8)	1.315(8)	1.309(4)
N3-N4	1.301(7)	1.324(8)	1.347(7)	1.354(3)

[1]Values taken from: *Inorg, Chem.*, **2022**, *61*, 13532–13542.

^{b} these bond lengths were restrained in the refinement, values shown are for the major disorder component; the large standard uncertainty in these numbers means that a comparison with the other compounds is not meaningful.

2.5   Computational studies

To gain more information about the electronic structure of the complexes herein described, DFT calculations were carried out. Geometry optimizations were run at MN15L[19]/def2-tzvp[20] level in the ground state, using the crystallographic coordinates of [**4**^{Br}]$^-$ as starting point. Analytical frequency calculations confirmed that the resulting geometries were minima on the potential energy surface (zero imaginary frequencies), and frequency values were scaled by a factor of 0.9578.[21] Time-dependent DFT computations were performed at CAM-B3LYP[22]/def2-tzvp level and the solvent was simulated using the continuum polarized model (CPM).[23]

Overall, bond lengths in the optimized structure of [**4**^{Br}]$^-$ were comparable to those found in the single-crystal X-ray diffraction, although Re1-Br1 and Re1-N1 bonds are slightly overestimated (0.07638 Å, 0.03786 Å, respectively). In [**4**^{Br}]$^-$, the HOMO is mainly localized on the formazanate backbone and spread out to some extent into the aryl groups; it contains only a minor contribution from the Re d$_\pi$ orbitals. The LUMO has primarily formazanate character (π*-orbitals) and it is extended to both terminal aryl rings. This contrasts to what we found for the neutral formazan **H4**^{Br}, wherein HOMO and LUMO orbitals possess a mixed metal-ligand character (Figure 5).
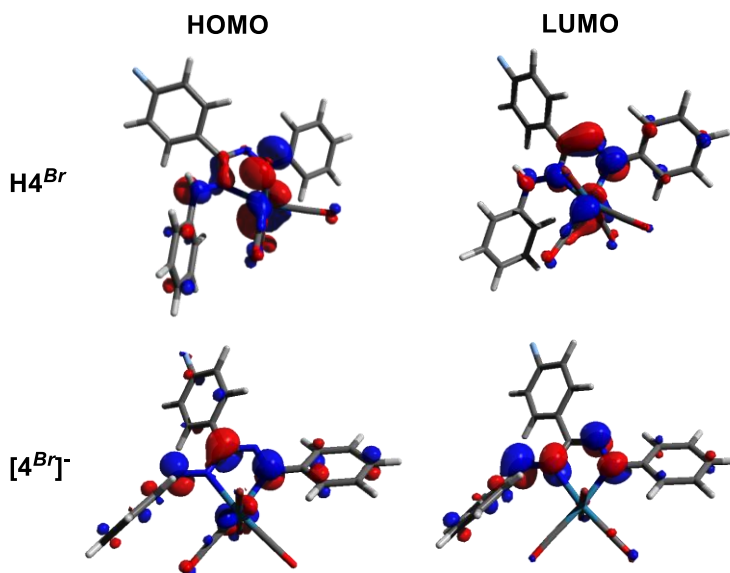
Figure 5. Comparison between H4^{Br} and [4^{Br}]$^-$ frontier orbitals (isovalue = 0.05).

Additionally, we optimized the structure of [**4**^{Br}]$^-$ with the ligand binding the metal through the terminal *N*-atoms, rendering a 6-membered chelate, since this is the most common coordination mode found in formazanate complexes.[16] The calculations showed the *open* fashion is the most thermodynamically stable configuration for formazanate Re(I) species, but only by a very small margin of 0.46 kcal/mol. Although sterics may predominantly govern the coordination mode, we cannot discard that electronic effects in carbonyl formazan/ate Re(I) species may have an influence. The 5-membered chelation could be a favorable configuration where Re→CO π-back bonding is maximized, as π-acidity of the formazanate ligand in the *open* fashion is expected to be lower compared to the *closed* coordination as a result of the lesser extent of charge delocalization.

The DFT-optimized structures for **H6**^{Br} and **Me6**^{Br} reproduce the experimental bond lengths reasonably well. In these complexes, the HOMO is composed of Re dπ orbital that interacts with the Br *p* orbital in an antibonding fashion. The contribution of the neutral formazan backbone and the N5-Ar fragment is more prominent in **H6**^{Br}. The LUMO is essentially the same in all complexes containing the neutral (alkyl)formazan ligand (Figure 6).
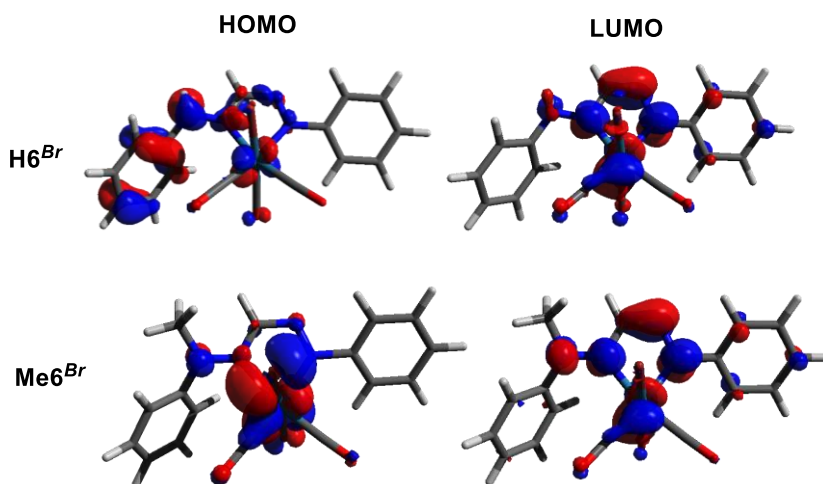
Figure 6. Comparison between frontier orbitals in H6^{Br} and Me6^{Br} (isovalue = 0.05).

Additionally, we carried out time dependent DFT calculations to determine the nature of the electronic transitions detected in the visible region by NTO analysis. The low-energy and intense absorption observed at 600 nm in [**4**^{Br}]$^-$ corresponds to the first excited state (λ_{calc} = 539 nm) that occupies a high oscillator strength. It arises primarily from HOMO → LUMO transitions of intraligand nature involving the formazanate backbone with some metal character in the donor orbital (Figure S13). The latter differs from what has been found in the formazan analogs, in which the main absorption results

from charge transfers with highly mixed character between the metal and the surrounding ligands (MLCT, LLCT, and ILCT).[10] The next four excited states (λ_{calc} = 414, 398, 379, 374 nm) build the shoulder observed at 430 nm and arise from electronic transitions from inner orbitals to the LUMO. Inspection of the NTOs showed these excitations correspond to MLCT Re(dπ) ➔ formazanate ($\pi^\star$) and LLCT Br(p) ➔formazan ($\pi^\star$) (Table S1).

We also studied the electronic spectra of **H6^{Br}** and **Me6^{Br}** by TDDFT calculations (Figure S14-S15). Essentially, both complexes display similar electronic transitions and include three excitations that account for the experimentally observed low-energy absorption band ($\lambda_{calc\ (H6Br)}$ = 557, 520, 474; $\lambda_{calc\ (Me6Br)}$ = 582, 487, 441 nm) from the HOMO/H-1/H-2/H-3 to the LUMO. Such excited states are consistent with electronic transitions of M-L (Re(dπ) ➔ formazan($\pi^\star$)), L-L (Br(p)➔ formazan($\pi^\star$)) and intra-L formazan (π➔$\pi^\star$) character. The absorption band at a lower wavelength that in related species has been assigned to a MLCT, contains several excited states at $\lambda_{calc\ (H6Br)}$ = 361, 338, 322 474 nm and λ_{calc} = 349, 319, 300 nm. These transitions result from charge transfers from orbitals of metal-ligand character (dπ + np(formazan)) to acceptor orbitals that have a high degree of metal-ligand mixing (dπ + $\pi^\star$(formazan)) (Tables S2-3).

The electronic properties of formazan/ate Re(I) contrast with the ones reported for well-studied α-diimine Re(I) species. In the latter, the MLCT band usually lies at lower energy than the intra-ligand π➔ $\pi^\star$ electronic transition.[24] This could represent a limitation in using formazanate Re(I) species as photoactive materials since, in transition-metal polypyridyl systems, the low-lying MLCT states are usually responsible for their luminescent properties.[25]

2.6   Luminescence spectroscopy

The emission spectrum of the anionic formazanate **[4^{Br}]⁻** was recorded in acetonitrile at room temperature with an excitation wavelength of 320 nm (Figure 7). It displays a structureless band at 380 nm, a feature that was also observed for the neutral analog, **H4^{Br}**. The excited state exhibits a bi-exponential decay with lifetimes τ_1 = 2.52 and τ_2 = 8.72 ns that are barely influenced by the presence of O$_2$ (τ_1 = 2.28; τ_2 = 8.71 ns), Figure S16. As discussed in *Chapter 2*, emission from ³MLCT is typical in Re(I) complexes with *N*-ligands and usually observed within a 500-600 nm range,[24] but such low-energy emission bands are absent in the complexes studied here. Since the emission band observed for **[4^{Br}]⁻** at 380 nm is not quenched in the presence of oxygen, it does not arise from a ³MLCT state. Similar observations were found in tryptophan-bisquinoline and indole-phenanthroline Re(I) derivatives. These complexes were reported to have weak emissions with short lifetimes not quenched by oxygen. It was proposed that *via* resonance-energy transfer from a fragment of the molecule (tryptophan, indole) to the chromophore, the ³MLCT emission was extinguished.[26,27] Thus, this could also explain the absence of a triplet emission.

Formazanate-containing complexes of main group elements (boron in particular) have been studied extensively for their photophysical properties, which feature highly tunable emission wavelengths and large Stokes shifts.[28,29] The lack of emissive properties of the low-energy excited states in the formazanate Re complexes studied here may originate from the difference in the coordination mode of the ligand. In the Re complexes that were studied here, the ligand is present as a 5-membered chelate ring regardless of its protonation state. The presence of a 'free', uncoordinated terminal *N*-Ph group of the ligand may introduce pathways for non-radiative decay that are less prominent in the more rigid 6-membered chelates. Vibrational-induced decay is known to be a deactivation pathway reported for complexes with O-H, N-H and C-H oscillators.[30]
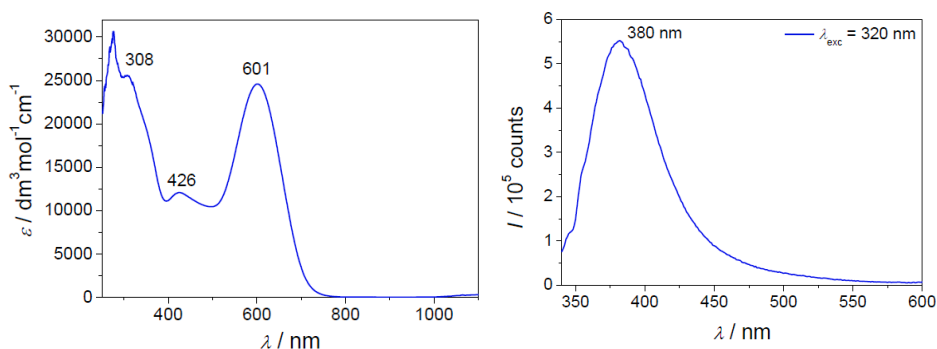
Figure 7. Emission (left) and absorption (right) spectra of [4^{Br}]⁻ recorded in acetonitrile.

3. Conclusions

In this chapter, we described synthetic studies for the preparation of formazanate Re(I) complexes through deprotonation of their neutral formazan Re(I) analogs. The formazanate core binds the metal center in an *open* fashion. Although the *open* 5-membered coordination preference over the *closed* 6-membered chelation has been observed in species with sterically demanding environments, our outcomes suggest that electronic effects may also influence ligand coordination.

Structural modifications on the formazanate backbone in R^2 or the axial ligand have little influence on the electronic properties of the resulting complexes, as shown by FT-IR and UV-vis spectroscopy. These species are stable in the solid state but are found to revert to the starting materials (NH-formazan complex) in low-polarity media due to re-protonation by water.

Compared to formazan complexes, the deprotonated formazanate analogues possess different electronic properties derived from the higher extent of π-delocalization. Computational studies indicate that the degree of covalency of the metal-ligand interaction is somewhat reduced in the anionic ligands as the LUMO orbital

was found to be purely ligand-centered. Despite this, neutral and anionic complexes display virtually identical emission spectra. Their poor luminescence properties compared to related Re(I) species and the highly emissive 6-membered boron formazanates were rationalized to be a consequence of self-quenching that could involve dissipation of the excited state energy by vibrational motion of the N-Ph pendant arm or resonance-energy transfer. Methylation of the N-terminal position was a valuable strategy to block the proton-responsivity of the formazan/ate core. The methylformazan Re(I) derivative exhibits similar properties to those observed in their formazan counterparts, although the NH acid-base equilibrium in the alkylated species is absent. N-alkylation did not result in substantial changes in the donor strength of the ligand, as demonstrated by spectroscopic and computational analysis. Full characterization by spectroscopic and DFT calculations of three different derivatives, formazanate, protonated, and methylated formazan Re(I) species, will allow to correlate the electronic structure of these species with their electrochemical behavior in *Chapter 4* and their reactivity patterns in the electrocatalysis of small molecule conversion in *Chapter 5*.

4.   Experimental section

General considerations. All manipulations were performed under N_2 atmosphere using Schlenk/vacuum line and glovebox techniques. The solvents (Aldrich, anhydrous 99.8%) were passed over columns of Al_2O_3 (Fluka) and BASF R3-11-supported Cu oxygen scavenger. **H4^{Br}** was synthesized using the methodology previously reported by our group.[95] Bis(triphenylphosphine)iminium chloride [PPN][Cl] (Aldrich, 97%) tetraphenylphosphonium bromide [PPh$_4$][Br] (Aldrich 97%), CH_3I (Merk 99%), NEt$_3$ (Aldrich 99.5%) and (1,4-diazabicyclo[2.2.2]octane) DABCO (TCI 98%), ethyl ortho-formate (Aldrich 98%), phenylhydrazine (Aldrich 97%) and HBF$_4$ (Aldrich 48 wt% in H_2O) were used without further purification. L6Me was prepared following the procedure reported by Neugebauer[80] from L6H and CH_3I.THF-d_8 was dried over Na/K and distilled *via* vacuum transfer. NMR spectra were measured on Mercury 400, Varian Inova 500, or Bruker 600 MHz spectrometers. Residual solvent signals were used as an internal reference for ^1H and 1^3C spectra and reported in ppm relative to TMS (0 ppm). Full assignments were based on two-dimensional experiments (COSY, HSQC, HMBC) using standard pulse sequences. FT-IR spectra were collected in THF solution on a JASCO 4700 series FT-IR spectrometer in transmission mode using a liquid cell with CaF$_2$ windows. UV-vis spectra were recorded in THF solution on an Avantes AvaSpec-2048 UV/Vis spectrophotometer.

Data from X-ray diffraction was measured at 100 and 295 K on a Bruker APEX2 diffractometer with Mo Kα (λ= 0.71073 Å) compound [Co(Cp*)$_2$][4^{Br}] or Cu (λ= 1.54178 Å) H/Me6^{Br}. Cell refinement and data reduction were performed with the Bruker SAINT program. Structure final refinement was carried out on SHELXTL.[96]

Table 3. Crystallographic data for [Co(Cp*)₂][4^{Br}], H6^{Br} and Me6^{Br}.

	[Co(Cp*)₂][4^{Br}]	H6^{Br}	Me6^{Br}
chemical formula	C$_{42}$H$_{44}$CoFBrN$_4$O$_3$Re	C$_{16}$H$_{12}$BrN4O$_3$Re	C$_{17}$H$_{14}$BrN$_4$O$_3$Re
M$_r$	996.86	574.41	588.43
cryst syst	Monoclinic	triclinic	orthorhombic
color, habit	Black, needle	Dark-red, block	Dark-red, needle
size (nm)	0.37×0.07×0.06	0.06×0.02×0.01	0.14×0.01×0.01
space group	P 2₁/n (No.14)	P-1 (No. 2)	P b n c (No.60)
a (Å)	15.0946(10)	7.3741(10)	30.805(3)
b (Å)	17.0051(14)	9.1941(12)	7.5141(3)
c (Å)	15.5791(12)	13.765(3)	15.9819(10)
α (deg)	90	71.633(11)	90
β (deg)	101.586(3)	86.853(10)	90
γ (deg)	90	81.765(14)	90
V (Å^3)	3917.4(5)	876.5(3)	3699.4(4)
Z	4	2	8
ρ_{calc} ($g \cdot cm^{-3}$)	1.690	2.176	2.113
radiation, λ (Å)	Mo, Kα, 0.71073	Cu, Kα, 1.54178	Cu, Kα, 1.54184
μ(Mo, Kα) (mm^{-1})	4.579	16.440	15.601
F(000)	1976	540	2224
temp (K)	100	295(2)	295(2)
θ range (deg)	2.091-26.469	3.383-69.964	2.869-72.859
data collected *(h, k, l)*	-18:18, -21:21, -19:19	-8:8, -11:11, -16:16	-38:37, -9:9, -19:19
no. of reflns collected	85,881	15,403	74,921
no. of indep reflns	8052	3267	3628
obsd reflns F$_o$ ≥2.0σ(F$_o$)	6854	2988	3530
R*(F)*[obsd reflns] (%)	3.65	2.87	1.93
R$_w$*(F²)*[all reflns] (%)	8.052	7.15	4.83
GOF	1.321	1.049	1.137
weighting *a, b*	0.0000, 22.1095	0.0000 2.2659	0.0198 3.4590
params refined	516	230	236
min, max residual densities	-1.15, 1.08	-0.97, 1.03	-0.707, 0.691

1,5-diphenylformazan, L6H. It was synthesized using a modified procedure from the one reported by von Pechmann.[45] Equimolar amounts of ethyl-orthoformate (6.7 mmol, 1.1 mL) and phenylhydrazine (13.4 mmol, 1.3 mL) under acidic conditions (30 drops of HBF$_4$ solution) were dissolved in 15 mL of acetonitrile. The reaction was refluxed overnight, turning dark red. The solvent was evaporated until 1/3, and cold water was poured into the flask till complete precipitation. The solid was filtered and purified by column chromatography in silica using as eluent DCM. The red fraction was collected, and violet crystals were formed upon solvent evaporation. (751 mg, 50%) ^{1}H NMR (CDCl$_3$, 25 °C, 400MHz) δ/ppm: 7.24 (t, ^3J = 8 Hz, 2H, Ph *p*-H), 7.43 (t, ^3J = 8 Hz, 4H, Ph *m*-H), 7.57 (d, ^3J = 8 Hz, 4H, Ph *o*-H), 7.87 (s, 1H, NNCNN, CH), 11.02 (s, 1H, NNCNN, NH).

[NHEt$_3$] [Hn^{Br}] (n = 1-4). The neutral formazan species Hn^{Br} (0.08 mmol) was dissolved in THF (5 mL) and an equimolar amount of NEt$_3$ (0.08 mmol) was added, observing an immediate color change from dark red to blue-greenish. The mixture was stirred at room temperature for 30 min. The solvent was removed under vacuo, leaving an oily dark residue. Upon trituration with 5 mL of pentane, the product precipitates as a black powder. The mixture was filtered out, and the solid was washed (2x5 mL) with pentane. Finally, the solid was dried under vacuum. **[NHEt$_3$][1^{Br}]**. ^{1}H NMR (THF-d_8, 25 °C, 400MHz) δ/ppm: 1.13 (t, ^3J = 8 Hz, 9H, NHEt$_3^+$, CH$_3$), 2.96 (q, ^3J = 8 Hz, 6H, NHEt$_3^+$, CH$_2$), 3.1 (s, 1H, NHEt$_3^+$ NH), 7.10 (m, 3H, Ph-CN m-H, Ph-CN p-H), 7.20 (m, 2H , Ph-N=N p-H, Ph-N-N p-H), 7.32 (m, 6H, Ph-N=N o-H, Ph-N-N m-H, Ph-N=N m-H), 7.85 (d, 2H, ^3J = 8 Hz, Ph-N-N o-H), 8.03 (d, 2H, ^3J = 8 Hz, Ph-NC o-H). IR(C$_7$H$_8$) ν(CO)/cm^{-1}: 2011(s), 1912(s), 1891(s). **[NHEt$_3$][2^{Br}]**. ^{1}H NMR (THF-d_8, 25 °C, 400MHz) δ/ppm: 1.10 (t, ^3J = 8 Hz, 9H, NHEt$_3^+$, CH$_3$), 2.33 (s, 3H, p-tol CH$_3$) 2.93 (q, ^3J = 8 Hz, 6H, NHEt$_3^+$, CH$_2$), 4.11 (s, 1H, NHEt$_3^+$, NH), 7.10 (t, 1H, ^3J = 8 Hz, Ph-N-N p-H), 7.15 (m, 4H, p-tol m-H, Ph-N=N o-H), 7.20 (t, 1H , ^3J = 8 Hz, Ph-N=N p-H), 7.31 (m, 4H, Ph-N=N m-H, Ph-N-N m-H), 7.86 (d, 2H, ^3J = 8 Hz, Ph-N-N o-H), 7.95 (d, 2H, ^3J = 8 Hz, p-tol o-H). ^{13}C{^{1}H} NMR (THF-d_8, 25 °C, 151 MHz) δ/ppm: 8.04 (NHEt$_3^+$ CH$_3$), 20.08 (p-tol CH$_3$), 46.19 (NHEt$_3^+$ CH$_2$), 121.64 (Ph-N-N $ipso$-C), 121.82 (Ph-N-N o-CH), 124. 14 (Ph-N-N p-CH), 125.45 (Ph-N=N p-CH), 127.25 (Ph-N-N m-CH), 127.44 (p-tol m-CH), 127.67 (Ph-N=N m-CH), 128.91 (p-tol o-CH), 131.24 (Ph-N=N $ipso$-C), 136.05 (p-tol p-C),156.82 (Ph-N-N $ipso$-C), 157.51 (imine-C), 189.97 (CO $trans$ Br C), 193.25(CO $trans$ Ph-N=N C), 197.39 (CO $trans$ Ph-N-N C). IR(C$_7$H$_8$) ν(CO)/cm^{-1}: 2011(s), 1912(s), 1891(s). **[NHEt$_3$][3^{Br}]**. ^{1}H NMR (THF-d_8, 25 °C, 400MHz) δ/ppm: 1.09 (t, ^3J = 8 Hz, 9H, NHEt$_3^+$, CH$_3$), 2.92 (q, ^3J = 8 Hz, 6H, NHEt$_3^+$, CH$_2$), 3.79 (s, 3H, p-MeO-Ph CH$_3$), 4.0 (s, 1H, NHEt$_3^+$, NH), 6.93 (d, 2H, ^3J = 8 Hz, p-MeO-Ph m-CH), 7.18 (m, 4H, Ph-N=N p-H, Ph-N-N p-H, Ph-N=N o-H), 7.35 (m, 4H, Ph-N-N m-H, Ph-N=N m-H), 7.87 (d, 2H, ^3J = 8 Hz, Ph-N-N o-H), 7.98 (d, 2H, ^3J = 8 Hz, p-MeO-Ph o-H). ^{13}C{^{1}H} NMR (THF-d_8, 25 °C, 151 MHz) δ/ppm: 9.15 (NHEt$_3^+$ CH$_3$), 47.30 (NHEt$_3^+$ CH$_2$), 55.34 (p-MeO-Ph CH$_3$), 113.73 (p-MeO-Ph m-CH), 122.42 (Ph-N=N p-CH), 123.30 (Ph-N-N o-CH), 126.52 (Ph-N=N o-CH), 128.63 (Ph-N-N m-CH), 129.02 (Ph-N=N m-CH), 131.40 (p-MeO-Ph o-CH), 158.07 (Ph-N-N $ipso$-C), 160.50 (imine-C), 190.18 (CO $trans$ Br C), 194.24 (CO $trans$ Ph-N=N C), 197.55 (CO $trans$ Ph-N-N C). IR(C$_7$H$_8$) ν(CO)/cm^{-1}: 2011(s), 1912(s), 1891(s). **[NHEt$_3$][4^{Br}]**. Similar spectroscopical data to those reported with other counterions.

[PPN][4^{Br}]. A Schlenk flask was charged with 0.0490g (0.073 mmol) of H4^{Br}and 0.0422 g (0.073 mmol) of [PPN]Cl. The solids were dissolved in 5 mL of THF, and 0.01 mL (0.073 mmol) of NEt$_3$ were added, observing an immediate color change from dark purple to green-blue. The mixture was kept under stirring for 2 h, filtered out, and evaporated to dryness. A dark precipitate was formed after the addition of 5 mL of pentane. The solid was rinsed twice with pentane (5 mL) and dried under vacuum. (41.3 mg, 84 %). **[PPh$_4$][4^{Br}]**. A similar procedure was followed. The reaction was carried out with equimolar amounts of H4^{Br} (0.05 g, 0.075 mmol), NEt$_3$ (0.01 mL, 0.075 mmol), and [PPh$_4$][Br] (0.0323 g, 0.075 mmol). (29.7 mg, 40%). **[Co(Cp*)$_2$][4^{Br}].** In a 20 mL vial, 0.0580

g (0.087 mmol) of **H4^{Br}** and 0.0286g (0.087 mmol) of Co(Cp*)$_2$ were added and mixed with 5 mL of THF. The reaction was stirred for 24 h, and gradually, the solution turned dark green-blue: the characteristic color of the formazanate species. The solution was filtered, and by slow evaporation, a crystalline material was obtained. ^{1}H NMR (THF-d_8, 25 °C, 600MHz) δ/ppm: 1.67 (s, 30H, Cp* CH$_3$), 6.95-6.99 (m, 3H, Ph-N-N p-H, p-FPh m-H), 7.13-7.17 (m, 3H, Ph-N=N o-H, Ph-N=N p-H), 7.22 (t, 2H, ^3J = 8 Hz, Ph-N-N m-H), 7.28 (t, 2H, ^3J = 8 Hz, Ph-N=N m-H), 7.83 (d, 2H, ^3J = 8 Hz, Ph-N-N o-H), 8.12 (dd, 2H, $^3J_{H-H}$ = 8 Hz, $^4J_{H-F}$ = 6 Hz, p-FPh o-H). ^{19}F NMR (THF-d_8, 25 °C, 565MHz) δ/ppm: -115.80 (m, p-FPh F). ^{13}C{^{1}H} NMR (CDCl$_3$, 25 °C, 151 MHz) δ/ppm: 6.73 (CH$_3$ Cp*), 93.73 (*ipso*-C Cp*), 112.81 (d, $^2J_{C-F}$ = 21 Hz, p-FPh m-CH), 121.94 (Ph-N=N o-CH), 122. 97 (Ph-N-N p-CH), 124.89 (Ph-N=N p-CH), 126.91 (Ph-N-N m-CH), 127.20 (Ph-N=N m-CH), 130.82 (d, $^3J_{C-F}$ = 7 Hz, p-FPh o-CH), 131.25 (d, $^4J_{C-F}$ = 3 Hz, p-FPh *ipso*-C), 155.15 (imine-C), 156.94 (Ph-N-N *ipso*-C), 157.39 (Ph-N=N *ipso*-C), 160.93 (J_{C-F} = 245 Hz, p-FPh p-C), 190.49 (CO *trans* Br C), 193.64 (CO *trans* Ph-N=N C), 197.96 (CO *trans* Ph-N-N C). FT-IR(THF) ν(CO)/cm^{-1}: 2007(s), 1912(s), 1879(s). Anal. Calcd. For (C$_{42}$H$_{44}$CoFBrN$_4$O$_3$Re): C 50.6, H 4.45, N 5.62; found C 50.38, H 4.50, N 5.58.

4^{MeCN}. In 15 mL of acetonitrile were dissolved 0.3036 g (0.45 mmol) of **H4^{Br}** with 1.2 equivalents (0.1400 g) of AgPF$_6$. The system was refluxed for 3 h in the darkness and then passed over celite. Assuming full conversion to the resulting brown solution, 0.0509 g (0.45 mmol) of DABCO were added, observing immediately a blue intense color. After stirring 30 min, the solvent was evaporated to dryness, and the mixture redissolved in ether. Then, the solution was filtered over neutral alumina, and the volatiles were removed, yielding a dark solid. (131 mg, 46 %) ^{1}H NMR (Acetonitrile-d_3, 25 °C, 600MHz) δ/ppm: 1.76 (s, 3H, NCCH$_3$ CH$_3$), 6.86 (d, 2H, $^3J_{H-H}$ = 8 Hz Ph-N=N o-H), 6.96 (t, 2H, $^3J_{H-F,}$ $^3J_{H-H}$ = 8 Hz, p-FPh m-H), 6.99 (t, 1H, $^3J_{H-H}$ = 8 Hz, Ph-N-N p-H), 7.22 (m, 5H, Ph-N-N m-H ,Ph-N=N m-H , Ph-N=N p-H), 7.53 (d, 2H, ^3J = 8 Hz, Ph-N-N o-H), 7.72 (dd, 2H, $^3J_{H-H}$ = 8 Hz, $^4J_{H-F}$ = 6 Hz, p-FPh o-H). ^{19}F NMR (Acetonitrile-d_3, 25 °C, 565MHz) δ/ppm: -116.1 (m, p-FPh F). ^{13}C{^{1}H} NMR (CDCl$_3$, 25 °C, 151 MHz) δ/ppm: 0.71 (NCCH$_3$ CH$_3$), 117.1 (NCCH$_3$ CN), 114.81 (d, $^2J_{C-F}$ = 21 Hz, p-FPh m-CH), 121.95 (Ph-N-N o-CH), 122.12 (Ph-N=N o-CH), 125.61 (Ph-N-N p-CH), 128.08 (Ph-N=N p-CH), 128.69 (Ph-N=N m-CH), 129.24 (Ph-N-N m-CH), 130.29 (d, $^4J_{C-F}$ = 5 Hz, p-FPh *ipso*-C), 132.02 (d, $^3J_{C-F}$ = 7 Hz, p-FPh o-CH), 156.63 (Ph-N-N *ipso*-C), 157.27 (Ph-N=N *ipso*-C), 157.72 (imine-C), 162.31 (J_{C-F} = 245 Hz, p-FPh p-C), 191.19 (CO *trans* Br C), 192.36 (CO *trans* Ph-N=N C), 195.04 (CO *trans* Ph-N-N C). IR(THF) ν(CO)/cm^{-1}: 2024(s), 1922(broad). HRMS (ESI+) (m/z): Calcd. for [MH]$^+$ = 631.102958. Found = 631.09616. [M]$^+$ = 630.095133. Found = 630.09281. [M-CO]$^+$ = 602.100218. Found = 602.09800. [M-3CO]$^+$ = 547.118213. Found = 546.09710. Anal. Calcd. For (C$_{24}$H$_{17}$FN$_5$O$_3$Re): C 45.86, H 2.73, N 11.14; found C 46.95, H 3.23, N 11.00.

H6^{Br}. In a 50 mL two-necked round bottom flask were added 0.1018 g (0.25 mmol) of ReBr(CO)$_5$ and 0. 05621 g (0.25 mmol) of **L5H** (1,5-diphenylformazan). The mixture was dissolved in 20 mL of toluene, rendering an orange-red solution that turned dark brown

when the reaction proceeded. The solution was heated up to reflux for 45 min, and the volatiles were evaporated under vacuum to dryness, yielding a black fine powder. The solid was rinsed with hexane (3 x 5 mL). (130 mg, 91%) (^{1}H NMR (CDCl$_3$, 25 °C, 600MHz) δ/ppm: 7.46 (d, 2 H, ^3J= 8 Hz, Ph-NH o-H), 7.49 (t, 1 H, ^3J= 8 Hz, Ph-N=N p-H), 7.54 (t, 2H, ^3J= 8 Hz, Ph-N=N m-H), 7.57 (m, 3 H, ^3J= 8 Hz, Ph-NH m-H, p-H), 7.85 (d, 2H, ^3J= 8 Hz, Ph-N=N o-H), 8.72 (s, 1 H, NH), 9.1 (s, 1H, NCN H). ^{13}C{^{1}H} NMR (CDCl$_3$, 25 °C, 150 MHz) δ/ppm: 123.89 (Ph-N=N o-CH), 125.19 (Ph-NH o-CH), 129.34 (Ph-N=N m-CH), 129.39 (Ph-N=N p-CH), 130.34 (Ph-NH m-CH), 131.89 (Ph-NH p-CH), 138.52 (Ph-NH $ipso$-C), 150.52 (imine C), 156.54 (Ph-N=N $ipso$-C), 180.82 (CO $trans$ Br C), 193.07 (CO $trans$ Ph-NH-N C), 194.33 (CO $trans$ Ph-N=N C). FT-IR (THF) ν(CO)/cm^{-1}: 2031(s), 1953(s) 1919(s). HRMS (ESI-) (m/z): Calcd. for [MH]$^-$ = 574.95461. Found = 574.95544. [M]$^-$ = 573.96001. Found = 573.96034. [M-3CO]$^-$ = 489.980297. Found = 489.95629.

Me6^{Br}. Equimolar amounts of ReBr(CO)$_5$ (0.1173 g, 0.29 mmol) and [L6Me] (0. 0688 g, 0.29 mmol) were dissolved in 20 mL of toluene. The yellow-orange solution was refluxed for 45 min. The resulting dark-brown mixture was cooled down to room temperature, and the solvent evaporated to dryness, yielding a dark crystalline material. The solid was rinsed with hexane (3 x 5 mL). Crystals were obtained by redissolving the solid in CH$_2$Cl$_2$ and subsequent slow solvent evaporation. (152.6 mg, 90%) ^{1}H NMR (CDCl$_3$, 25 °C, 600MHz) δ/ppm: 3.93 (s, 3H, NMe CH$_3$) 7.41 (d, 2 H, ^3J= 8 Hz, Ph-NMe o-H), 7.54 (m, 6 H, Ph-N=N m-H, p-H; Ph-NMe m-H, p-H), 7.84 (d, 2H, ^3J= 8 Hz, Ph-N=N o-H), 8.96 (s, 1H, NCN H). ^{13}C{^{1}H} NMR (CDCl$_3$, 25 °C, 150 MHz) δ/ppm: 45.78 (Ph-NMe CH$_3$), 123.74 (Ph-N=N o-CH), 125.43 (Ph-NMe o-CH), 129.22 (Ph-N=N m-CH), 129.56 (Ph-N=N p-CH), 129.71 (Ph-NMe m-CH), 131.26 (Ph-NMe p-CH), 146.41 (Ph-NMe $ipso$-C), 149.87 (imine C), 156.84 (Ph-N=N $ipso$-C), 184.54 (CO $trans$ Br C), 191.96 (CO $trans$ Ph-NH-N C), 193.15 (CO $trans$ Ph-N=N C). FT-IR (THF) ν(CO)/cm^{-1}: 2031(s), 1952(s) 1915(s). HRMS (ESI-) (m/z): Calcd. for [M]- = 587.98013. Found = 587.98046. [M-3CO]$^+$ = 503.99547 Found = 503.98046. Anal. Calcd. For (C$_{17}$H$_{14}$BrN$_4$O$_3$Re): C 34.70, H 2.40, N 9.52; found C 33.64, H 2.22, N 9.77.

5. Supporting information

5.1 NMR
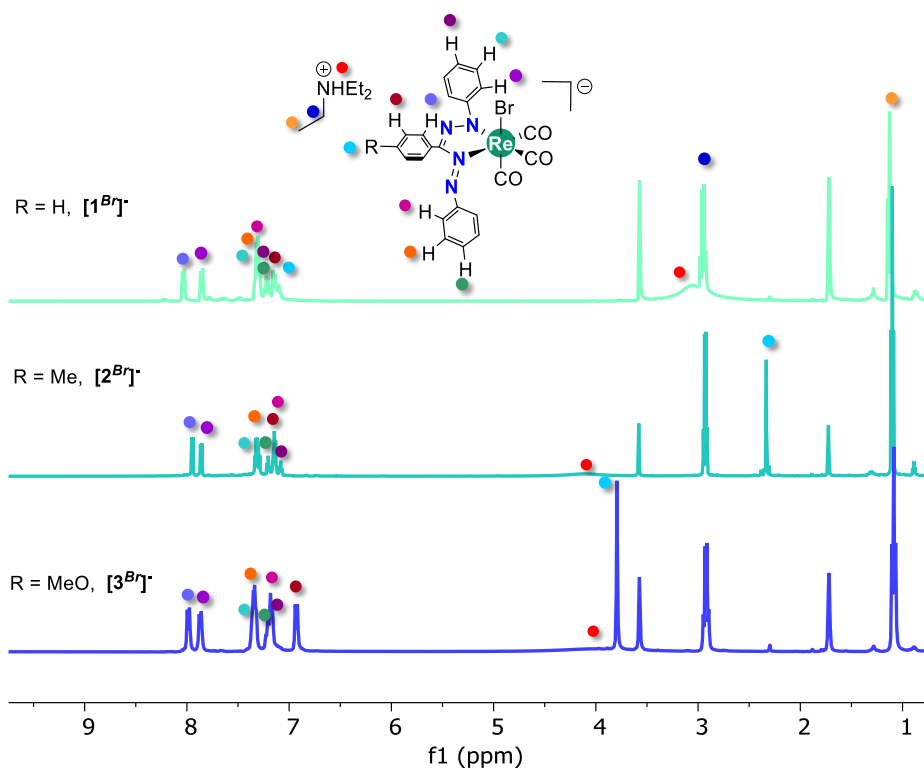
Figure S1. ^{1}H NMR spectra of complexes [1^{Br}]$^-$-[3^{Br}]$^-$ in THF-d_8.
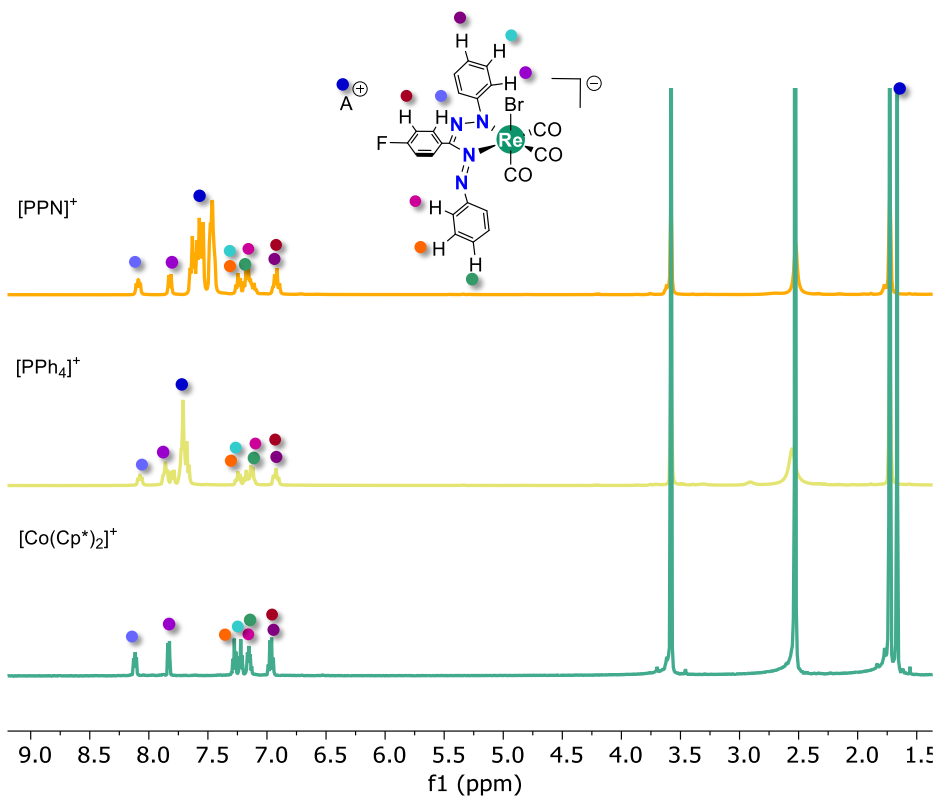
Figure S2. ^{1}H NMR spectra of [4^{Br}]$^-$ with different counterions in THF-d_8.
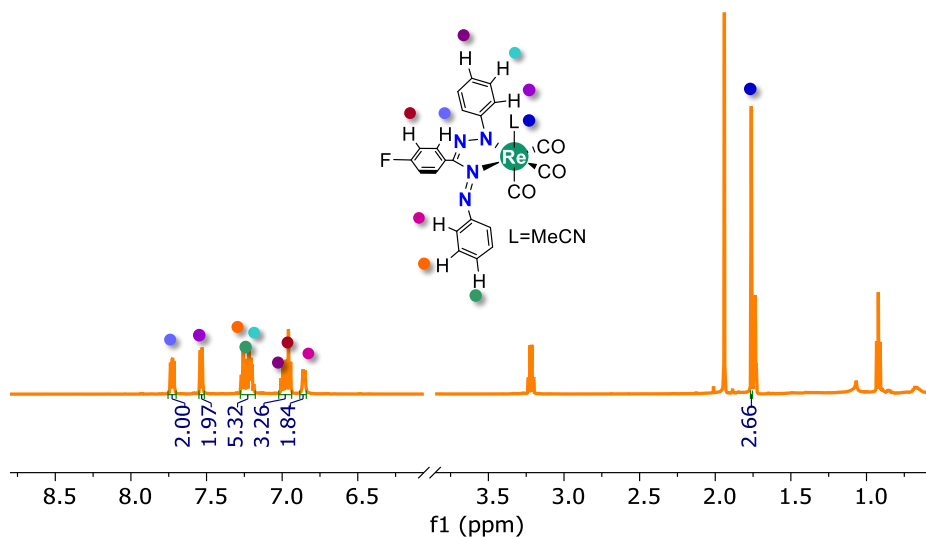
Figure S3. ^{1}H NMR spectrum of 4^{MeCN} in CD$_3$CN.
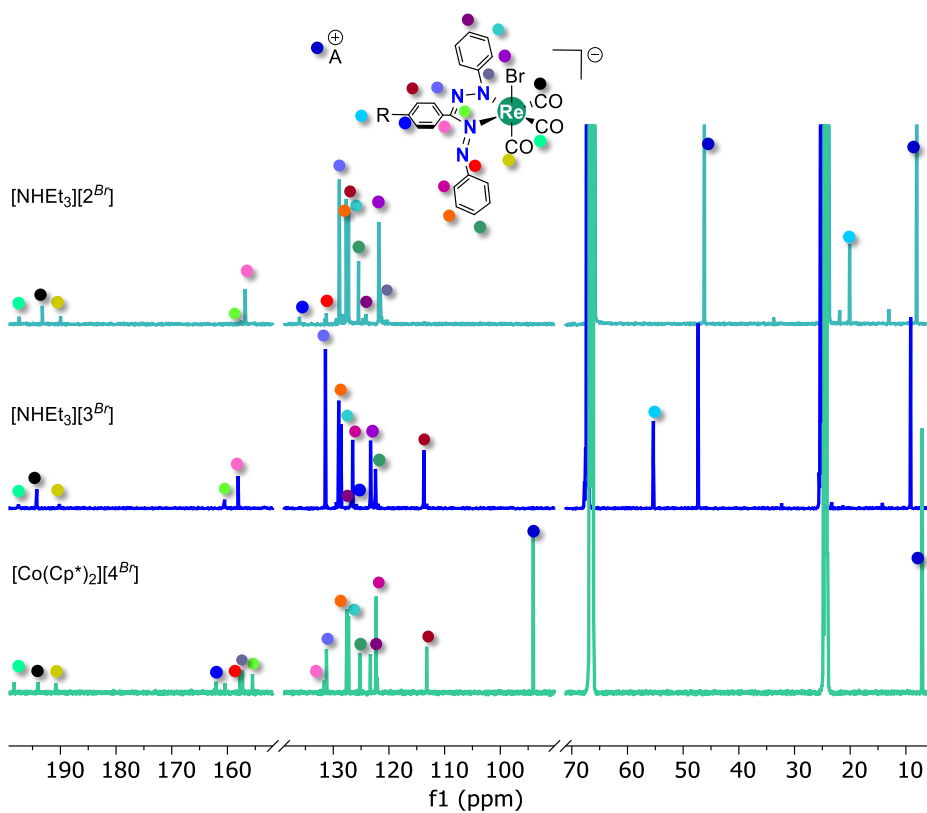
Figure S4. $^{13}C\{^1H\}$ NMR spectra for $[2^{Br}]$-$[4^{Br}]^-$ in THF-d_8.
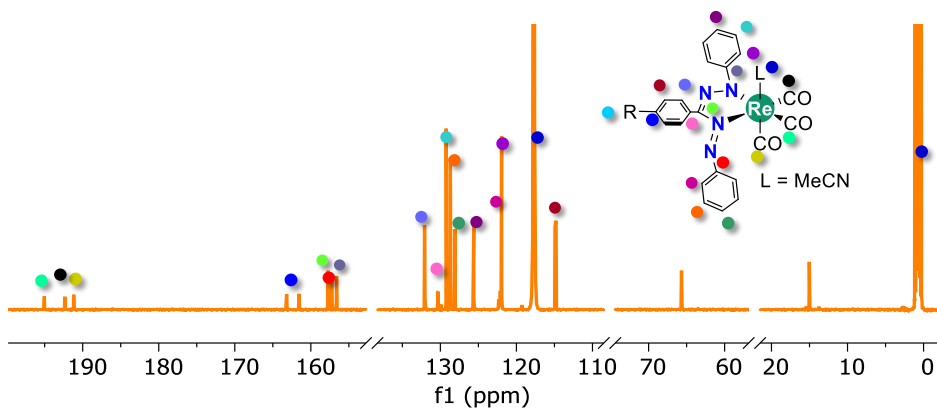
Figure S5. $^{13}C\{^1H\}$ NMR spectrum for 4^{MeCN} in CD$_3$CN.
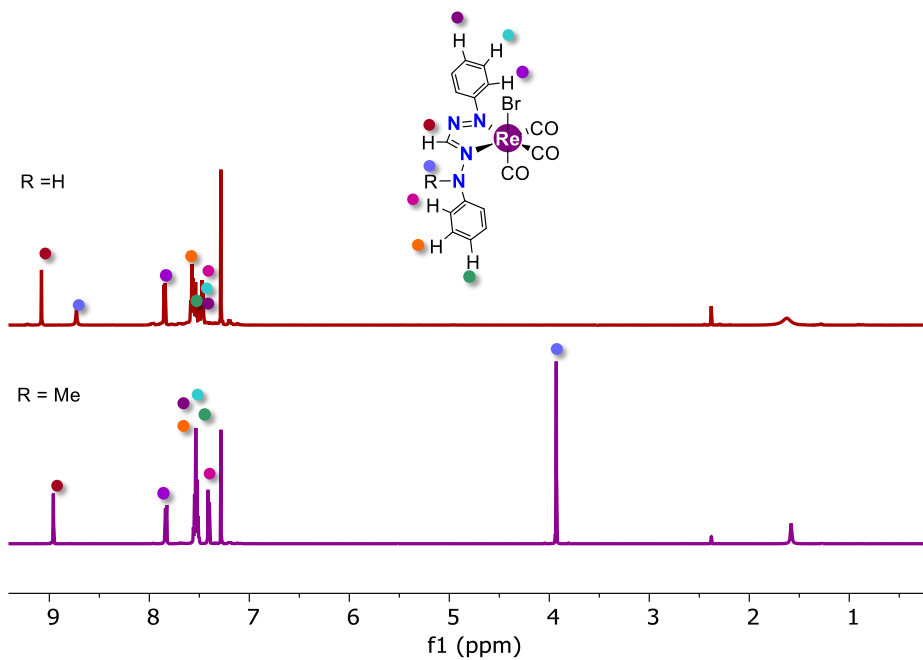
Figure S6. ^{1}H NMR spectra of H6^{Br} and Me6^{Br} in CDCl$_3$.
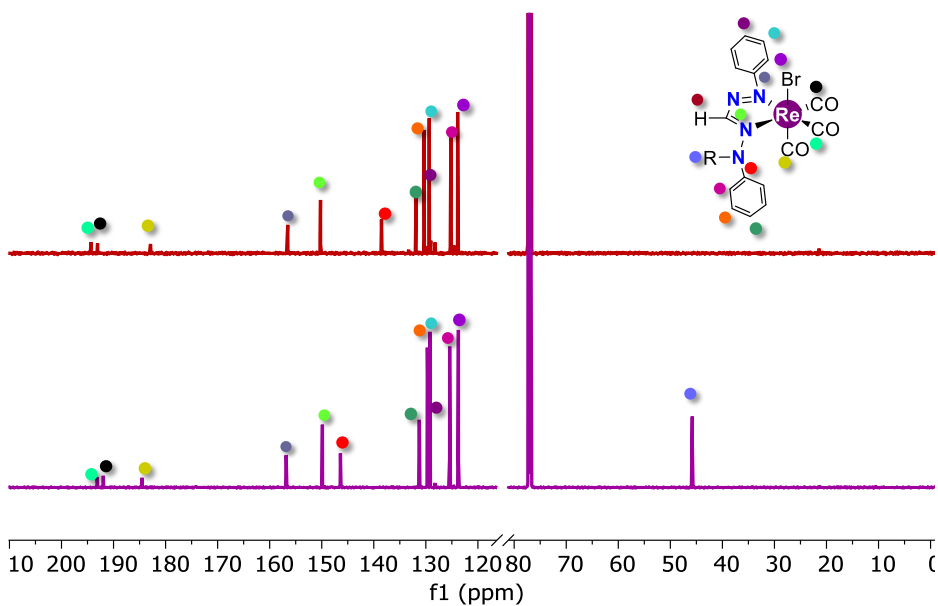
Figure S7. ^{13}C{^{1}H} NMR spectra of H6^{Br} and Me6^{Br} in CDCl$_3$.
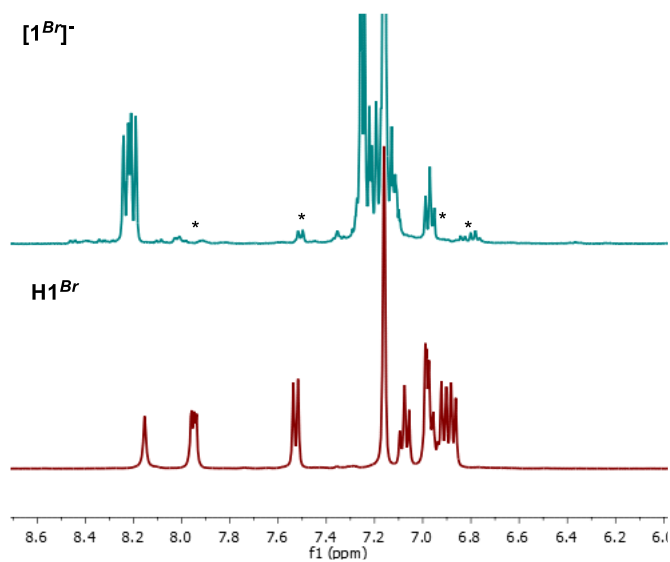
Figure S8. Protonation of [1^{Br}]$^-$ in benzene-d^6, the signals of the protonated species H1^{Br} are labelled with a star.
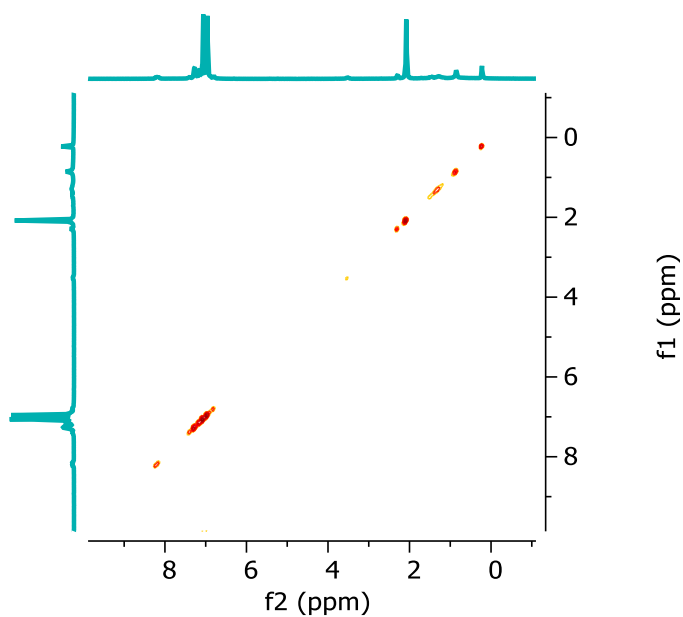
Figure S9. ^{1}H EXSY experiment at 80°C in toluene-d_8.

5.2   FT-IR
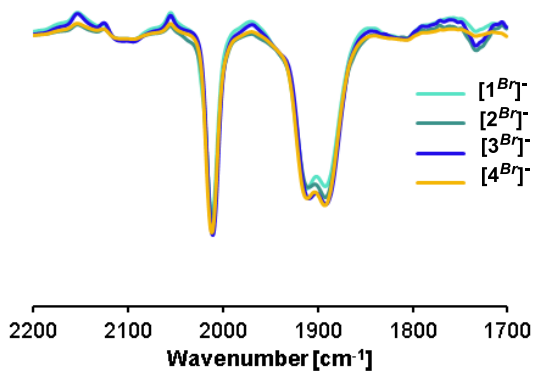
Figure S10. FT-IR spectra of triethylammonium formazanate Re(I) complexes in toluene ($c \approx 10^{-3}$ M) at rt.
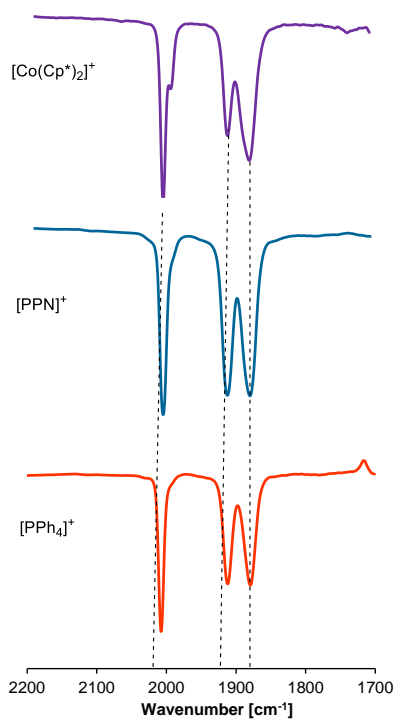
Figure S11. FT-IR spectra of [4^{Br}]$^-$ with different counterions in THF ($c \approx 10^{-3}$ M) at rt.

5.3 UV-vis
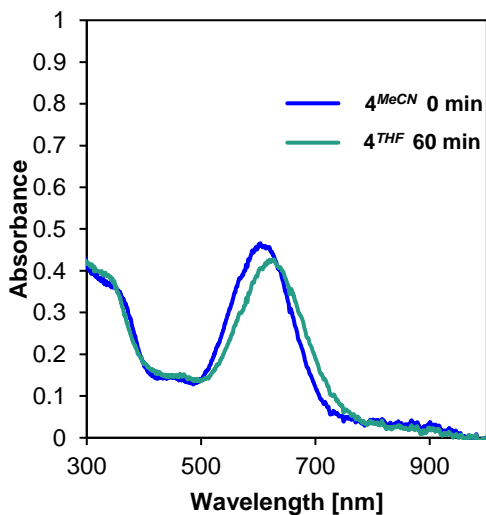
Figure S12. UV-vis spectra of 4[MeCN] taken in THF at rt.
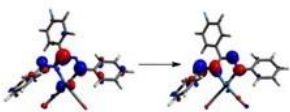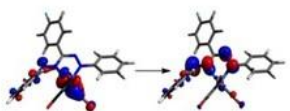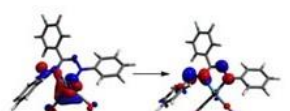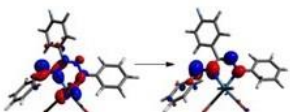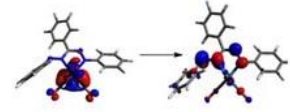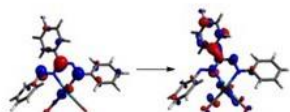
5.4 Computational details

Density functional theory (DFT) calculations were carried out in Gaussian 16 Revision C.02[34]software, and the results were visualized using Gaussview 6[35] or Avogadro.[36] Geometry optimizations in the ground state were performed in the gas phase at a MN15L[19]/def2tzvp.[20] level of theory. Theoretical carbonyl frequencies were scaled by a factor of 0.9578 [21](see Table S1). Using the optimized geometries, TDDFT calculations were performed at CAM-B3LYP[22]/def2tzvp level of theory. The solvent effect was simulated with the continuum polarized model (CPM).[23]
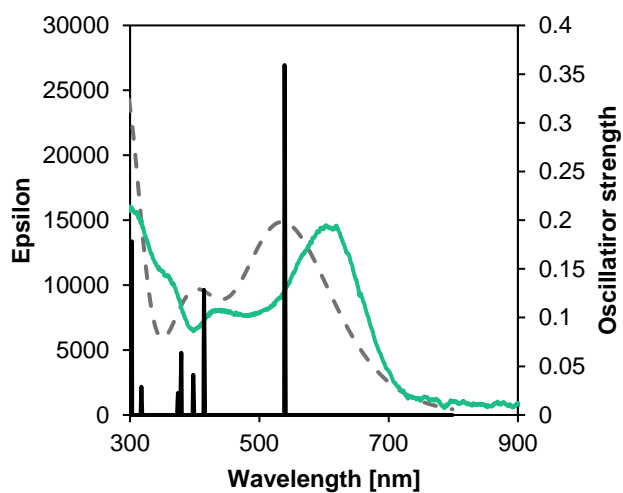
Figure S13.Comparison between experimental (turquoise trace) and theoretical (dash line) spectra in [4^{Br}]⁻.

Table S1. Natural transition orbitals (isovalue = 0.05) for the main electronic transitions in [4^{Br}]⁻

		TD-DFT			NTO	
Excited state	Electronic transitions	Energy (eV)/ λ_{theo}(nm)	λ_{exp} (nm)	Oscillator strength	Hole → Electron	Occupation number
1	H → L H-1 → L	2.3000/539.05	607	0.3593		0.99247
2	H-4 → L H-3 → L H-1 → L H → L	2.9920/414.39	440	0.1285		0.98679
3	H-4 → L H-3 → L H-2 → L	3.1171/397.76		0.0413		0.98464
4	H-13 → L H-11 → L H-4 → L H-3 → L H-2 → L H-1 → L H → L	3.2689/379.29		0.0639		0.97489
5	H-3 → L H-2 → L H-1 → L	3.3146/374.06		0.0226		0.98891
7	H-2 → L+2 H-2 → L+3 H → L+1 H → L+2 H → L+3	4.0964/302.67	350	0.1783		0.85630
9	H → L+6 H-2 → L+1 H-2 → L+3 H → L+1 H → L+2 H → L+3 H → L+4	4.2329/292.91		0.2962		0.80441
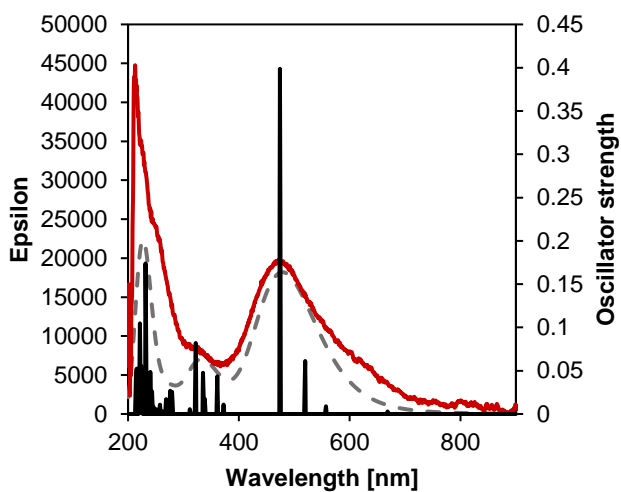
Figure S14. Comparison between experimental (red trace) and theoretical (dash line) spectra in H6*Br*.
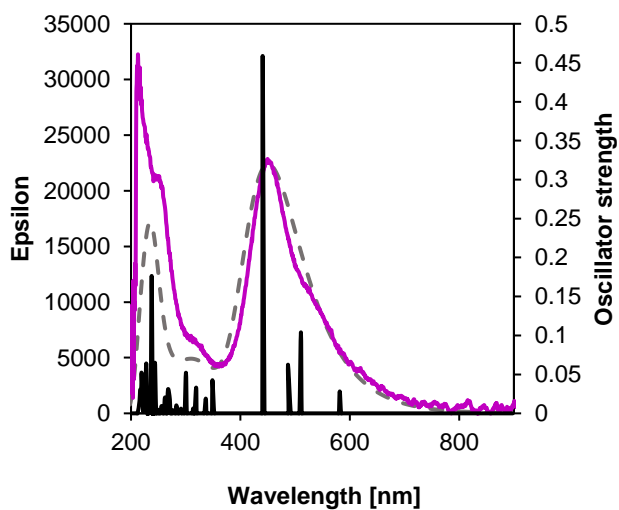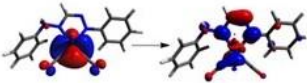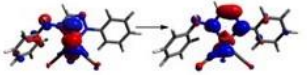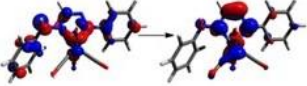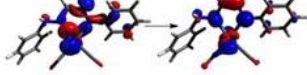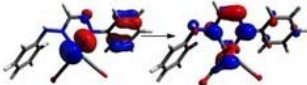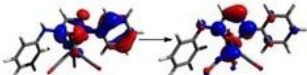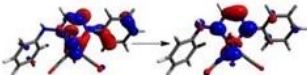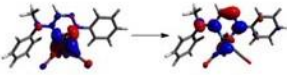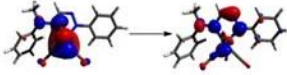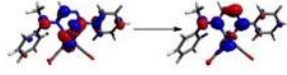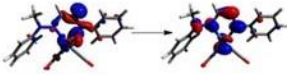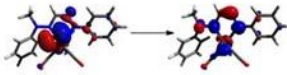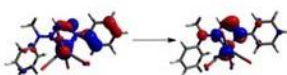
Figure S15.Comparison between experimental (purple trace) and theoretical (dash line) spectra in Me6*Br*.

Table S2. Natural transition orbitals (isovalue = 0.05) for the main electronic transitions in H6^{Br}.

Excited state	Electronic transitions	TD-DFT Energy (eV)/ λ_{theo}(nm)	λ_{exp}(nm)	Oscillator strength	NTO Hole → Electron	Occupation number
2	H-5 → L H-3 → L H-2 → L	2.2253 /557.16		0.0089		0.99869
3	H-3 → L H-2 → L H-1 → L H → L	2.3856 /519.71	470	0.0612		0.99226
4	H-3 → L H-2 → L H-1 → L H → L	2.6152 /474.09		0.3987		0.98931
6	H-11 → L H-10 → L H-7 → L H-6 → L H-5 →L H-4 →L	3.4342 /361.03		0.0435		0.98381
7	H-10 → L H-8→ L H-7 → L H -6→ L	3.6651 /338.29	328	0.0177		0.97634
8	H-11 → L H-10 → L H-8→ L H-7→ L H-6→ L H-5 → L H-4 → L	3.6984/335.23		0.0476		0.98035
9	H-11 → L H-10 → L H-8→ L H-7→ L	3.8481/322.19		0.0820		0.97433

Table S3. Natural transition orbitals (isovalue = 0.05) for the main electronic transitions in Me6^{Br}.

		TD-DFT			NTO	
Excited state	Electronic transitions	Energy (eV)/ λ_{theo}(nm)	λ_{exp} (nm)	Oscillator strength	Hole → Electron	Occupation number
1	H-1 → L H → L	2.1319/581.56		0.0282		0.99871
2	H-3 → L H-2 → L H-1 → L H → L	2.5461/486.96	456	0.1040		0.99358
4	H-3 → L H-2 → L H-1 → L H → L	2.8138/440.63		0.4587		0.98752
5	H-11 → L H-8 → L H-7 → L H-5 → L H-4 → L	3.5539/348.86		0.0426		0.98338
7	H-11 → L H-8 → L H-7 → L H-6 → L	3.8859/319.07	319	0.0331		0.97580
9	H-11 → L H-8 → L H-7 → L H-6 → L H-5 → L H-4 → L	4.1272/300.41		0.0522		0.95611

5.5   Luminescence studies

Experimental details found in supporting information *Chapter 2*.
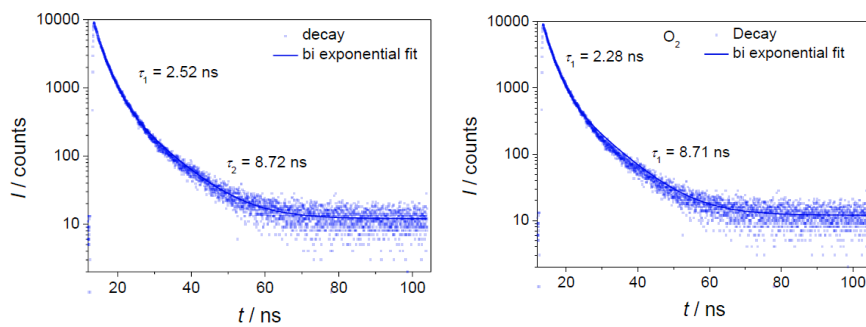
Figure S16. Lifetime decay for [4^{Br}]$^-$ under N$_2$ (left) and under O$_2$ (right).

References

(1)   Davison, B. Y. A.; Edelstein, A. T.; Holm, R. H.; Maki, A. H. The Preparation and Characterization of Four-Coordinate Complexes Related by Electron-Transfer Reactions. *Inorg. Chem.* **1963**, *2*, 1227–1231. https://doi.org/10.1021/ic50010a031.

(2)   Eisenberg, R.; Gray, H. B. Noninnocence in Metal Complexes: A Dithiolene Dawn. *Inorg, Chem.* **2011**, *50*, 9741–9751. https://doi.org/10.1021/ic2011748.

(3)   Praneeth, V. K. K.; Ringenberg, M. R.; Ward, T. R. Redox-Active Ligands in Catalysis. *Angew. Chem. Inter. Ed.* **2012**, *51*, 10228–10234. https://doi.org/10.1002/anie.201204100.

(4)   Luca, O. R.; Crabtree, R. H. Redox-Active Ligands in Catalysis. *Chem. Soc. Rev.* **2013**, *42* (4), 1440–1459. https://doi.org/10.1039/c2cs35228a.

(5)   Ivar, J.; Vlugt, V. Der. Radical-Type Reactivity and Catalysis by Single-Electron Transfer to or from Redox-Active Ligands. *Chem. Eur. J.* **2019**, 2651–2662. https://doi.org/10.1002/chem.201802606.

(6)   Khan, F. F.; Chowdhury, A. D.; Lahiri, G. K. Bond Activations Assisted by Redox Active Ligand Scaffolds. *Eur. J. Inorg. Chem.* **2020**, *2020* (13), 1138–1146. https://doi.org/10.1002/ejic.202000005.

(7)   de Vries, F.; Otten, E. Reversible On/Off Switching of Lactide Cyclopolymerization with a Redox-Active Formazanate Ligand. *ACS Catal.* **2022**, *12* (7), 4125–4130. https://doi.org/10.1021/acscatal.1c05689.

(8)   Singh, V.; Kundu, A.; Singh, K.; Adhikari, D. Redox Noninnocence of the Formazanate Ligand Applied to Catalytic Formation of α-Ketoamides. *Chem. Commun.* **2022**, *58* (46), 6630–6633. https://doi.org/10.1039/d2cc02089k.

(9)   Mondol, R.; Otten, E. Reactivity of Two-Electron-Reduced Boron Formazanate Compounds with Electrophiles: Facile N–H/N–C Bond Homolysis Due to the Formation of Stable Ligand Radicals. *Inorg. Chem.* **2018**, *57*, 9720–9727. https://doi.org/10.1021/acs.inorgchem.8b00079.

(10)   Capulín Flores, L.; Paul, L. A.; Siewert, I.; Havenith, R.; Zúñiga-Villarreal, N.; Otten, E. Neutral Formazan Ligands Bound to the *fac*-(CO)₃Re(I) Fragment: Structural, Spectroscopic and Computational Studies. *Inorg. Chem.* **2022**, *61*, 13532–13542. https://doi.org/10.1021/acs.inorgchem.2c02168.

(11)   Gutmann, V. Solvent Effects on the Reactivities Compounds of Organometallic. *Coord. Chem. Rev.* **1976**, *18*, 225–255. https://doi.org/10.1016/S0010-8545(00)82045-7.

(12)   McConnachie, G.; Neugebauer, F. A. On the Cyclization of N-Alkylformazans to Leucoverdazyls (1,2,3,4-Tetrahydro-s-Tetrazines). *Tetrahedron* **1975**, *31*, 555–560. https://doi.org/10.1016/0040-4020(75)85029-0.

(13)   Trischmann H; Kuhn Richard. Surprisingly Stable Nitrogenous Free Radicals. *Angew. Chem. Inter. Ed.* **1963**, *2* (3), 155. https://doi.org/10.1002/anie.196301552.

(14)   Kabir, E.; Mu, G.; Momtaz, D. A.; Bryce, N. A.; Teets, T. S. Formazanate Complexes of Bis-Cyclometalated Iridium. *Inorg. Chem.* **2019**, *58*, 11672–11683. https://doi.org/10.1021/acs.inorgchem.9b01657.

(15)   Chang, M. C.; Roewen, P.; Travieso-Puente, R.; Lutz, M.; Otten, E. Formazanate Ligands as Structurally Versatile, Redox-Active Analogues of β-Diketiminates in Zinc Chemistry. *Inorg. Chem.* **2015**, *54* (1), 379–388. https://doi.org/10.1021/ic5025873.

(16)   Gilroy, J. B.; Otten, E. Formazanate Coordination Compounds: Synthesis, Reactivity, and Applications. *Chem. Soc. Rev.* **2020**, *49* (1), 85–113. https://doi.org/10.1039/c9cs00676a.

(17)   Chakraborty, I.; Carrington, S. J.; Mascharak, P. K. Photodelivery of CO by Designed PhotoCORMs: Correlation between Absorption in the Visible Region and Metal-CO Bond Labilization in Carbonyl Complexes. *ChemMedChem* **2014**, *9* (6), 1266–1274. https://doi.org/10.1002/cmdc.201402007.

(18)   Kottelat, E.; Lucarini, F.; Crochet, A.; Ruggi, A.; Zobi, F. Correlation of MLCTs of Group 7 fac-[M(CO)₃]⁺ Complexes (M = Mn, Re) with Bipyridine, Pyridinylpyrazine, Azopyridine, and Pyridin-2-Ylmethanimine Type Ligands for Rational PhotoCORM Design. *Eur. J. Inorg. Chem.* **2019**, *2019* (33), 3758–3768. https://doi.org/10.1002/ejic.201900568.

(19)   Yu, H. S.; He, X.; Truhlar, D. G. MN15-L: A New Local Exchange-Correlation Functional for Kohn-Sham Density Functional Theory with Broad Accuracy for Atoms, Molecules, and Solids. *J. Chem. Theory Comput.* **2016**, *12* (3), 1280–1293. https://doi.org/10.1021/acs.jctc.5b01082.

(20)   Weigend, F.; Ahlrichs, R. Balanced Basis Sets of Split Valence, Triple Zeta Valence and Quadruple Zeta Valence Quality for H to Rn: Design and Assessment of Accuracy. *Phys. Chem. Chem. Phys.* **2005**, *7* (18), 3297–3305. https://doi.org/10.1039/b508541a.

(21)   Sae-Heng, P.; Tantirungrotechai, J.; Tantirungrotechai, Y. Scale Factors for Carbonyl Vibrational Frequencies: A Study of Partial Hessian Approximation. *Chiang Mai J. Sci.* **2018**, *45* (7), 2797–2808.

(22)   Yanai, T.; Tew, D. P.; Handy, N. C. A New Hybrid Exchange-Correlation Functional Using the Coulomb-Attenuating Method (CAM-B3LYP). *Chem. Phys. Lett.* **2004**, *393*, 51–57. https://doi.org/10.1016/j.cplett.2004.06.011.

(23)   Miertuš, S.; Scrocco, E.; Tomasi, J. Electrostatic Interaction of a Solute with a Continuum. A Direct Utilization of AB Initio Molecular Potentials for the Prevision of Solvent Effects. *Chem. Phys.* **1981**, *55*, 117–129. https://doi.org/10.1016/0301-0104(81)85090-2.

(24)   Rillema, D. P.; Sullivan, B. P.; Kirgand, R. A. Photochemistry and Photophysics of Coordination Compounds: Rhenium. In *Photochemistry and Photophysics of Coordination Compounds*; **2007**; Vol. II, pp 45–100.

(25)   Shillito, G. E.; Preston, D.; Traber, P.; Steinmetzer, J.; McAdam, C. J.; Crowley, J. D.; Wagner, P.; Kupfer, S.; Gordon, K. C. Excited-State Switching Frustrates the Tuning of Properties in Triphenylamine-Donor-Ligand Rhenium(I) and Platinum(II) Complexes. *Inorg. Chem.* **2020**, *59* (10), 6736–6746. https://doi.org/10.1021/acs.inorgchem.9b03691.

(26)   Lo, K. K. W.; Tsang, K. H. K.; Hui, W. K.; Zhu, N. Luminescent Rhenium(I) Diimine Indole Conjugates - Photophysical, Electrochemical and Protein-Binding Properties. *Chem. Commun.* **2003**, *0* (21), 2704–2705. https://doi.org/10.1039/B306914A.

(27)   Wei, L.; Babich, J. W.; Ouellette, W.; Zubieta, J. Developing the {M(CO)$_3$}$^+$ Core for Fluorescence Applications: Rhenium Tricarbonyl Core Complexes with Benzimidazole, Quinoline, and Tryptophan Derivatives. *Inorg. Chem.* **2006**, *45*, 3057–3066. https://doi.org/10.1021/ic0517319.

(28)   Barbon, S. M.; Price, J. T.; Reinkeluers, P. A.; Gilroy, J. B. Substituent-Dependent Optical and Electrochemical Properties of Triarylformazanate Boron Difluoride Complexes. *Inorg. Chem.* **2014**, *53* (19), 10585–10593. https://doi.org/10.1021/ic5016912.

(29)   Chang, M. C.; Chantzis, A.; Jacquemin, D.; Otten, E. Boron Difluorides with Formazanate Ligands: Redox-Switchable Fluorescent Dyes with Large Stokes Shifts. *Dalton Trans.* **2016**, *45* (23), 9477–9484. https://doi.org/10.1039/c6dt01226d.

(30)   Bunzli, J.-C. G.; Piguet, C. Light Conversion: Lanthanide-Containing Systems. *Encyclopedia of Materials: Science and Technology*; **2006**; pp 4465–4476.

(31)   Capulín Flores, L.; Paul, L. A.; Siewert, I.; Havenith, R.; Zúñiga-Villarreal, N.; Otten, E. Neutral Formazan Ligands Bound to the fac-(CO)$_3$Re(I) Fragment: Structural, Spectroscopic, and Computational Studies. *Inorg, Chem.* **2022**, *61* (34). https://doi.org/10.1021/acs.inorgchem.2c02168.

(32)   Sheldrick, G. M. Crystal Structure Refinement with SHELXL. *Acta Crystallographica Section C* **2015**, *71*, 3–8. https://doi.org/10.1107/S2053229614024218.

(33)   Nineham, A. W. The Chemistry of Formazans and Tetrazolium Salts. *Chem. Rev.* **1955**, *55* (2), 355–483. https://doi.org/10.1021/cr50002a004.

(34)   M. J. Frisch, G. W. Trucks, H. B. Schlegel, G. E. S.; M. A. Robb, J. R. Cheeseman, G. Scalmani, V. B.; G. A. Petersson, H. Nakatsuji, X. Li, M. Caricato, A. V. M.; J. Bloino, B. G. Janesko, R. Gomperts, B. Mennucci, H. P. H.; J. V. Ortiz, A. F. Izmaylov, J. L. Sonnenberg, D. W.-Y.; F. Ding, F. Lipparini, F. Egidi, J. Goings, B. Peng, A. P.; T. Henderson, D. Ranasinghe, V. G. Zakrzewski, J. Gao, N. R.; G. Zheng, W. Liang, M. Hada, M. Ehara, K. Toyota, R. F.; J. Hasegawa, M. Ishida, T. Nakajima, Y. Honda, O. Kitao, H. N.; T. Vreven, K. Throssell, J. A. Montgomery, Jr., J. E. P.; F. Ogliaro, M. J. Bearpark, J. J. Heyd, E. N. Brothers, K. N. K.; V. N. Staroverov, T. A. Keith, R. Kobayashi, J. N.; K. Raghavachari, A. P. Rendell, J. C. Burant, S. S. I.; J. Tomasi, M. Cossi, J. M. Millam, M. Klene, C. Adamo, R. C.; J. W. Ochterski, R. L. Martin, K. Morokuma, O. F.; J. B. Foresman, and D. J. F. Gaussian 16, Revision C.02. Wallingford CT 2019.

(35)   Dennington, Roy; Keith, Todd A.; Millam, J. M. GaussView, Version 6. Semichem Inc., Shawnee Mission: KS 2016.

(36)   Hanwell, M. D.; Curtis, D. E.; Lonie, D. C.; Vandermeersch, T.; Zurek, E.; Hutchinson, G. R. Avogadro: An Advanced Semantic Chemical Editor, Visualization, and Analysis Platform. *J. Cheminformatics* **2012**, *4*, 1–17. https://doi.org/10.1186/1758-2946-4-17.

Chapter 4

Electrochemistry of (alkyl)formazan and formazanate Re(I) complexes

In this chapter, the electrochemistry of (alkyl)formazan and formazanate Re(I) species was investigated by (spectro)electrochemical and computational methods. The results indicate that the methylformazan Re(I) derivative can be reversibly reduced and oxidized via one-electron reactions, while formazanate Re(I) complexes exhibit a less reversible behavior. Both ligands behave as two-electron reservoirs, allowing two consecutive one-electron reductions to take place on the ligand. Although halide-dissociation upon one-electron transfer was observed, the formation of ligand-based radical seems to prevent its dimerization. The redox potentials are cathodically shifted in formazanate complexes, as expected for the negatively charged ligand. Reduction of protonated formazan Re(I) complexes generates their formazanate analogues by reductive deprotonation. The potential reduction pathways that generate the mono-, double- and triple-reduced species are discussed.

1. Introduction

Azo-based compounds have been investigated as active materials since they exhibit reversible redox and photophysical properties.[1,2] Having low-lying frontier orbitals centered on the N=N fragment, these molecules show low-energy intense absorptions and accessible redox potentials. Adding one electron into the π^*-azo centered LUMO generates the azo radical anion *II* as an intermediate, and with a second-electron transfer, a hydrazido species *III* is formed (Scheme 1a).[3]

As ligands, azo-compounds are strong π-acceptors involved in π-backbonding interactions with metal centers in low oxidation states.[4,5] Being azo species redox active fragments, when coordinated to a metal, the accessible frontier orbitals enable multielectron redox events generally of ligand-based nature.[6,7] In particular, for formazan (azo-imine) compounds, their oxidation to the corresponding tetrazolium salts is quite characteristic and harnessed in clinical assays (Scheme 1b).[8] In contrast, metal formazanate complexes are more prone to be engaged in reduction processes.
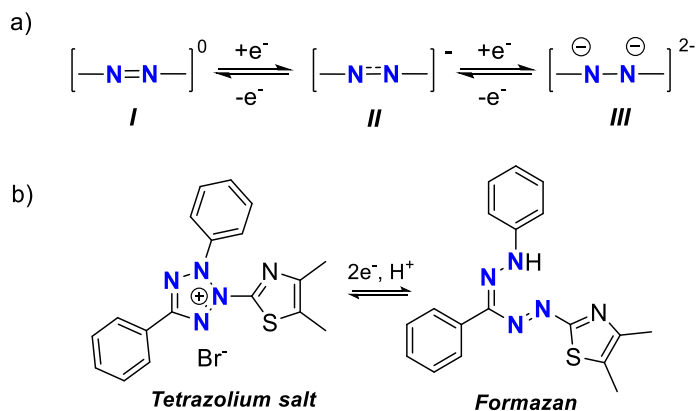
Scheme 1. Reversible two-electron reduction in azo-compounds.

Our group has extensively studied the electrochemical properties of metal formazanates with main group and transition elements and found that in most cases, the ligand can accept up to two reducing equivalents. No reports have been published on formazan/ate complexes with group 7. However, some Re(I) complexes with azo-type ligands are known, and their electrochemical properties were studied. Kaim and coworkers investigated a series of tricarbonylhalidorhenium(I) (F, Cl, Br, I) complexes bearing the azobispyridine (abpy) ligand. Such complexes exhibit two redox events, poorly influenced by the X ligand. In these species, the first reduction is a ligand-based reversible process, mainly attributed to the formation of a stable azo-type radical, also been observed in ReCl(CO)$_3$(azpy) (azpy = 2-(chloropenylazo)pyridine).[9] The second reduction is accompanied by halide dissociation yielding the double-reduced anion (Scheme 2).[10]

$$+e^-$$
$$(abpy)\mathbf{Re}(CO)_3(X) \underset{-e^-}{\overset{+e^-}{\rightleftharpoons}} [(abpy)\mathbf{Re}(CO)_3(X)]^{\bullet-} \overset{+e^-}{\underset{-X}{\longrightarrow}} [(abpy)Re(CO)_3]^-$$

X = F	$E_{1/2}$ = -0.70		X = F	E^{pc} = -1.54	
Cl	$E_{1/2}$ = -0.78	vs Fc$^{+/0}$	Cl	E^{pc} = -1.54	vs Fc$^{+/0}$
Br	$E_{1/2}$ = -0.78		Br	E^{pc} = -1.42	
I	$E_{1/2}$ = -0.79		I	E^{pc} = -1.33	
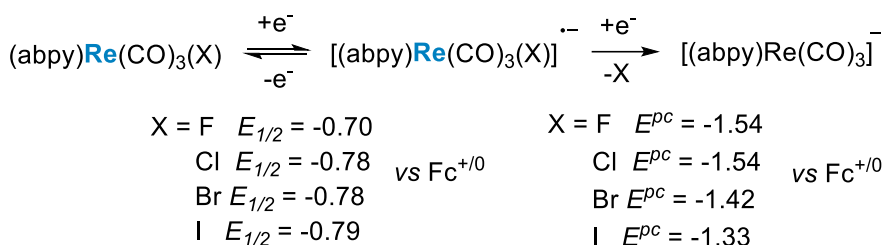
Scheme 2. Reduction of ReX(CO)$_3$(abpy) complexes.

In this chapter, we discuss the electrochemistry of heteroleptic Re(I) (alkyl)formazan and formazanate complexes. By combination of (electro)chemical and theoretical methods we identify the plausible mechanisms during the reduction of these species.

2.   Results & Discussion

2.1   Electrochemical studies

Cyclic voltammograms were recorded at 0.05 V/s in a 0.1 M [NBu$_4$][PF$_6$] acetonitrile solution containing 1 mM of the analyte. The potentials herein reported (Table 1) were referenced internally with ferrocene. We first discussed the electrochemistry of the neutral methyl formazan derivative **Me6^{Br}** since it exhibits the neatest redox behavior. On the first cycle, three reductions were identified when scanning to negative potentials at *I'* = -0.53, *II'* -0.84 and *III'* = -2.83 V. On the reverse scan, the oxidations coupled to these reductions were observed at *I"* = -0.60, *II"* = -0.89, and *III"* = -2.73 V, an additional feature was observed at *IV"* = -0.38 V (Figure 1a, turquoise trace). Starting the second cycle, the corresponding cathodic wave *IV'* was detected at -0.41 V (Figure 1a, blue trace). We carried out complementary experiments at different potential windows and found that *IV"* only appears when the potential is swept past *I'* (Figure 1b). Thus, the formation of the species at *IV"* requires the generation of the first reduced complex at *I'*. In all cases, the peak separation (58 mV<Δp<74 mV) and current indicate such events are *quasi*-reversible one-electron reductions. Such peak separation gradually increases at higher scan rates (Figure S1.)

a)

b)
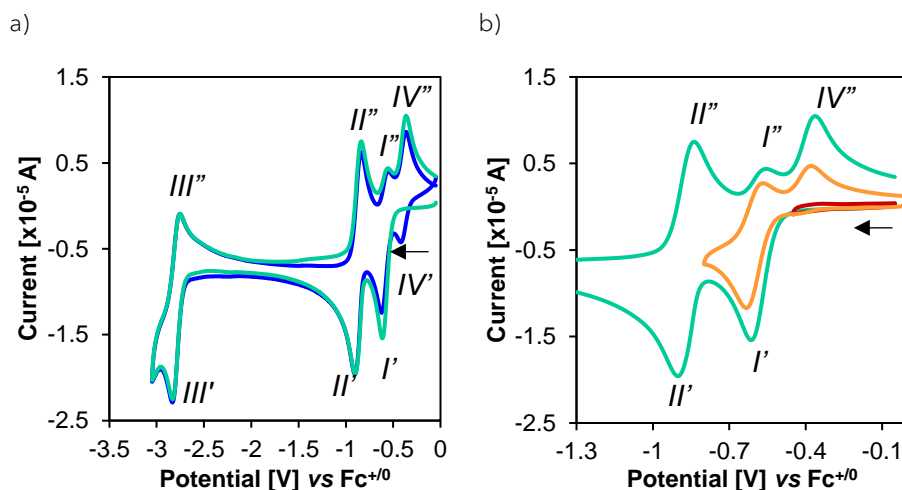
Figure 1. Voltammograms of complex Me6^{Br} in acetonitrile at 50 mV/s. a) Whole potential window, first (turquoise trace) and second cycle (blue trace). b) At different potential windows showing the first cycle.

Table 1. Electrochemical data for Me6^{Br}.

Redox Event	I"/I'	II"/II'	II$_b^{"}$/II$_b^{'}$	III"/III'	IV"/IV'
$E^{1/2}$ [V]	-0.59	-0.87	-0.97	-2.80	-0.38

The four redox events detected during the electrochemical reduction of **Me6^{Br}** are depicted in Scheme 3. They were assigned based on the collected spectroscopic data and supported by computational studies, as described in detail below. This proposal is in agreement with the electrochemical characterization of group 7 *fac*-MX(CO)$_3$(L,L) species (X = Cl, Br; L,L = α-diimines) informed in several reports.[11,12] The one-electron transfer at *I'* corresponds to the formation of the radical intermediate **[Me6^{Br}]**$^{•-}$. The current at this step decreases on the second cycle, suggesting **[Me6^{Br}]**$^{•-}$ is unstable. Based on what has been reported in analogous systems, it is very likely that bromide dissociation is occurring, rendering the neutral radical **[Me6]$^{•}$** or its solvato species **[Me6^{S}]$^{•}$** *S* = MeCN**.** The second electron transfer can take place on **[Me6]$^{•}$** generating the double-reduced species **[Me6]$^{-}$**. At *III'*, the third reduction is achieved tentatively assigned to the radical dianion **[Me6]$^{2•-}$**. This feature has also been reported in *fac*-MnBr(bpy)(CO)$_3$[13] and *fac*-ReCl(bpy((C(O)Me)$_2$)[14] although not investigated in detail. On the reverse scan, the oxidation wave *III"* corresponds to the formation of the double-reduced **[Me6]$^{-}$**. Removing an electron from **[Me6]$^{-}$** then affords **[Me6]$^{•}$** assigned to the anodic peak *II"*. This species is in equilibrium with **[Me6^{Br}]$^{•-}$** since an oxidation current is observed at *I"*. The observation of a significantly decreased current at *I"* suggests the concentration of **[Me6^{Br}]$^{•-}$** is low. Instead, direct oxidation of **[Me6]$^{•}$** occurs, yielding its

solvent-adduct [**Me6**^{S}]$^+$ at *IV"*. This was further confirmed by running the voltammogram of the solvato complex [**Me6**^{S}]$^+$[**PF$_6$**]$^-$, which was independently synthesized by treatment of **Me6**^{Br} with AgPF$_6$ (*see* Figure S2a). As expected, the CV of the cationic complex lacks the redox waves *I'* and *I"* assigned to the [**Me6**^{Br}]$^{\bullet-}$/ [**Me6**^{Br}] couple. Additional oxidation waves were not observed in the voltammogram of **Me6**^{Br} at more positive potentials, that could indicate dimerization of the radical [**Me6**]$^{\bullet}$, as reported in *fac*-MnBr(CO)$_3$(bpy)[12] nor indicia of its formation was found by FT-IR (Scheme 3, in blue).

When the cyclic voltammogram of **Me6**^{Br} is run in excess of Br$^-$ (50 equivalents of NBu$_4$Br were added), the electrochemical profile exhibits only three reversible redox events (Figure 2a, green trace). The first reduction at *I'* that regained reversibility in the presence of bromide is assigned to the species [**Me6**^{Br}]$^{\bullet-}$. The second reduction is cathodically shifted *ca.* 0.15 V at *II'$_b$*, which we assigned to a one-electron transfer on [**Me6**^{Br}]$^{\bullet-}$ yielding the double reduced species [**Me6**^{Br}]$^{2-}$, that upon halide loss will afford [**Me6**]$^-$. Then, the reduction *III'* yields [**Me6**]$^{2\bullet-}$. On the reverse scan, the oxidation *III"* corresponds to [**Me6**]$^-$. Of note, a subtle cathodic shift at *II"* indicates that in excess of bromide the complex [**Me6**^{Br}]$^{\bullet-}$ is afforded at *II"$_b$*. Then, the oxidation at *I"* regenerates **Me6**^{Br}. No prominent features were observed at more positive potentials (either on the second cycle, Figure 2b), confirming that increasing bromide concentrations effectively prevents halide dissociation. Under those conditions, the CV shows exclusively the electron transfer series indicated in green in Scheme 3.
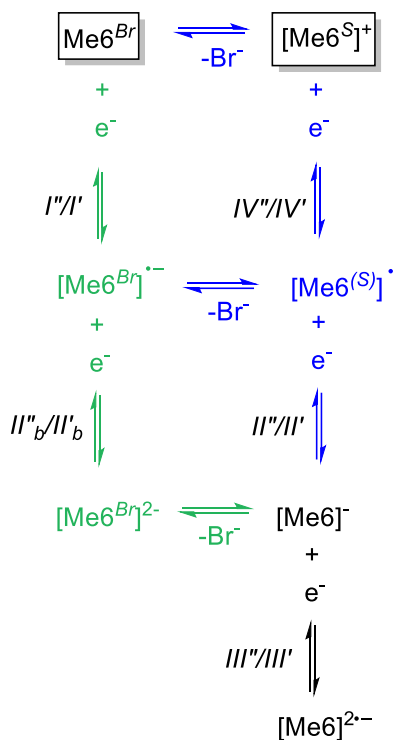
Scheme 3. Mechanistic pathway for the reduction of Me6^{Br}.

a)

b)
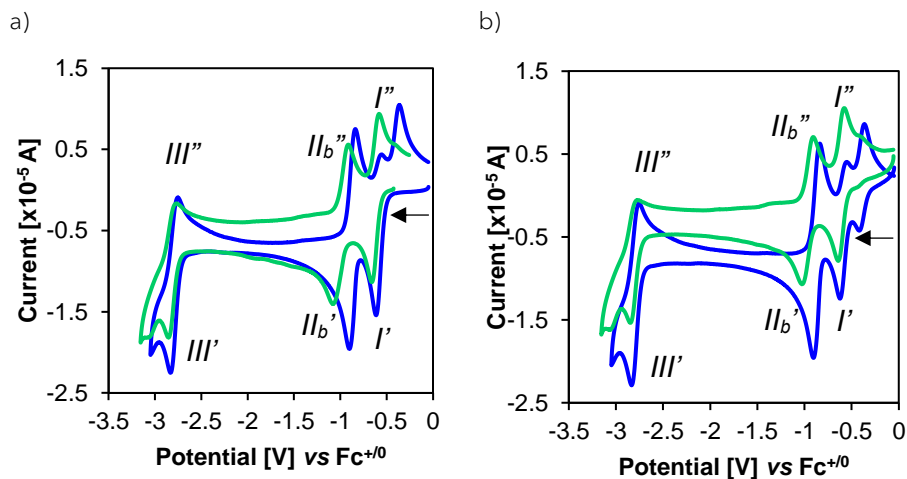
Figure 2. Voltammograms of Me6^{Br} run with (green trace) and without an excess of bromide (blue trace), depicting the a) first and b) second cycle.

The electrochemical response of the non-alkylated species **H6^{Br}** is more complex, similar to the one observed for the neutral formazan **H4^{Br}** (Figure 3a-b). In both cases, a pronounced irreversible cathodic wave, labeled as *a* in the voltammograms, is observed at -0.6 — -0.7V followed by a series of sequential redox steps of irreversible nature, as sweeping at higher scan rates showed (Figure S4). Moving toward more negative potentials, a redox wave at *III"/III'* = -2.8 V is observed, which exhibits reversibility, similar feature to the one detected for the triple reduction of **Me6^{Br}**. On the reverse scan, at least two prominent oxidations are identified at *E* = -1.5 — -1.6V and *E* = -1V. Finally, the reduction wave previously detected at -0.6 V is faded on the second cycle. Given the intricacy of the voltammograms, we decided to explore these processes separately by other means.
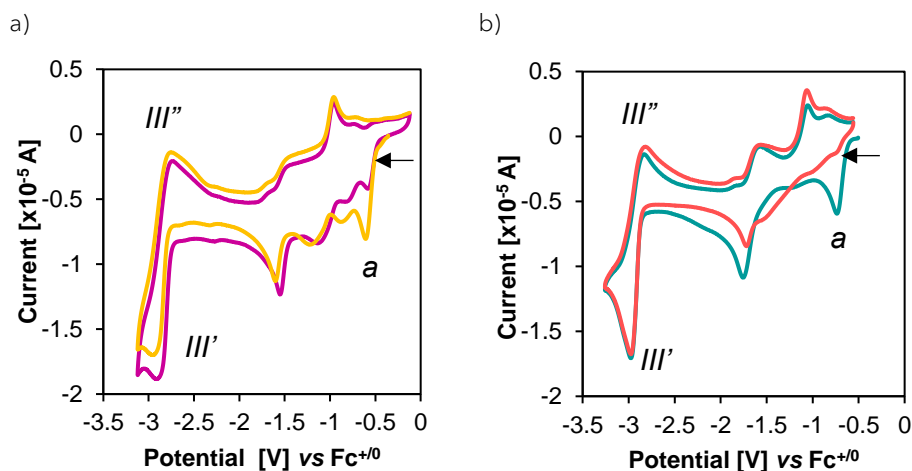
Figure 3. Voltammograms of a) H6^{Br} first (yellow) and second (purple) cycle and b) H4^{Br} first (turquoise trace) and second (red) cycle.

We studied the first reduction *a* by chemical means, using decamethylcobaltocene Co(Cp*)$_2$ as a reducing agent. Adding one equivalent of Co(Cp*)$_2$ into a solution of **H4^{Br}** in THF resulted in an immediate color change from purple to dark blue, characteristic of formazanate species. Analysis of the reaction mixture by FT-IR showed that the resulting product indeed exhibits bands in the carbonyl region at 2008, 1912, and 1880 cm^{-1}, which are in agreement with those determined in **[4^{Br}]$^-$**. Such changes are equivalent to what was observed after the chemical deprotonation of **H4^{Br}** (Figure S6). UV-vis and ^{19}F NMR spectroscopy further corroborated this, wherein a broad and intense band at 600 nm and a singlet at -115 ppm, respectively, indicates the generation of the formazanate-based product **[Co(Cp*)$_2$][4^{Br}]**. Ultimately, the isolation of crystalline material from this reaction mixture allowed its characterization by X-ray diffraction, verifying the formation of a formazanate Re(I) complex *via* reductive deprotonation of compound **H4^{Br}** (*see* Scheme 4). Similar reactivity was reported for metal complexes bearing ligands containing proton-responsive groups, such as dihydroxy-bipyridine[15,16] and imidazole

fragments.[17] The fate of the putative H$^{\bullet}$ radical generated upon reductive deprotonation is still unclear as the typical signal of H_2 was not detected in ^{1}H NMR.

Although the electrochemical response of the protonated formazan derivatives seems more complex than the behavior observed in the formazanate species, this must be a consequence of additional equilibria and not background reactivity, since FT-IR SPEC detected the same intermediates for both classes of complexes. (see below).

Having identified reductive deprotonation as the first step in the reduction of formazan complexes, we decided to focus our attention on the electrochemistry of the corresponding formazanate species. To this end, we recorded the voltammogram of the formazanates **[4^{Br}]⁻** and **4^{MeCN}** and compared their electrochemical response (Figure 4, Scheme 4 and Table 2). Overall, the four redox events detected previously for **Me6^{Br}** are present, although in this case, they are less reversible, as was also observed at higher scan rates (Figure S3). The redox potentials are cathodically shifted compared to **Me6^{Br}** as a consequence of having an anionic formazanate fragment. Starting the first cycle, the reduction at *I'* is anodically shifted (*ca*. 100 mV) for the neutral formazanate complex **4^{MeCN}** compared to the anionic analogue **[4^{Br}]⁻**, which indicates the addition of one electron yields the radicals **[4$^{(S)}$]$^{\bullet-}$** and **[4^{Br}]$^{2\bullet-}$**, respectively. Since the second reduction *II'* occurs at similar *E* in both cases regardless of whether **4^{MeCN}** or **[4^{Br}]⁻** is used as analyte, it is likely that both complexes lose bromide after the first reduction to form the radical **[4]$^{\bullet-}$**. This subsequently gets reduced at *II'* to form the double-reduced complex **[4]$^{2-}$**. Additional features (*) were identified at more negative potentials that may come from decomposition of **[4]$^{2-}$** (Figure 4). The CV of the anionic complex **[4^{Br}]⁻** shows a reduction wave at ca. -2.5 V that is absent in **4^{MeCN}**, this feature corresponds to the **[PPN]⁺** counterion, as confirmed by measuring the CV of the simple salt [PPN]⁺[Cl]⁻ (*see* Figure S1 in *Chapter 5*). In both formazanate species, we recognized a redox event at -2.80 V that was also observed in the voltammogram of **Me6^{Br}** assigned to the putative triple-reduced complex, in this case **[4]$^{3\bullet-}$**. On the reverse scan, the oxidation *III"* produces **[4]$^{2-}$**. The anodic wave at *II"* exhibits similar potentials in **4^{MeCN}** and **[4^{Br}]⁻**, accounting for species **[4]$^{\bullet-}$**. The lack of an oxidation peak at *I"* suggests that a chemical step takes place that gives rise to the anodic feature at *IV"*, that it is only observed when sweeping the potential past the first reduction *I"* in **4^{MeCN}** and **[4^{Br}]⁻**. We discard dimerization occurs since FT-IR SPEC did not show indicia of the dimer formation (*see below*). However, it indicates the presence of **[4]$^{\bullet-}$** and **[4^{S}]$^{\bullet-}$** (as calculations supported, *vide infra*) that points out the existence of an equilibrium between coordination and decoordination of the axial ligand.

a)

b)
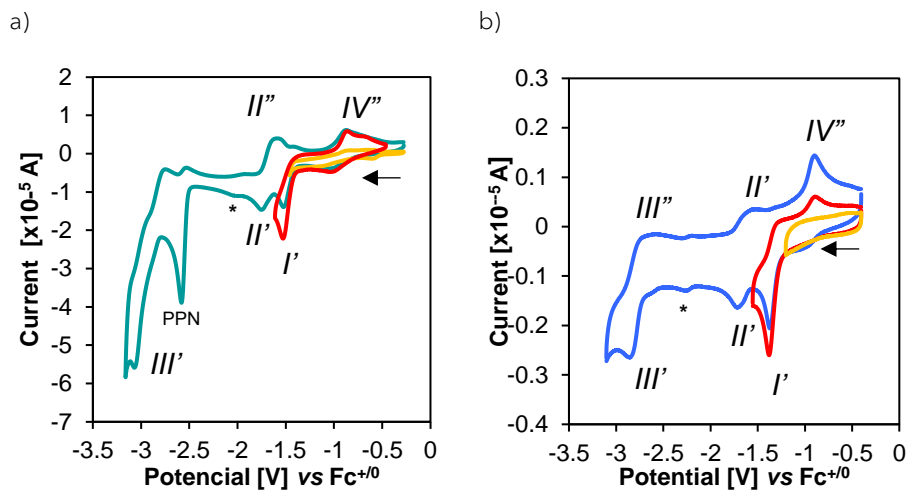
Figure 4. Voltammograms of complexes a) [4^{Br}]$^{- \text{ and}}$ b) 4^{MeCN} in acetonitrile at 50 mV/s at different potential windows showing the second cycle.

Table 2. Redox potentials for [4^{Br}]$^-$ and 4^{MeCN}.

Compound	Redox event [V] vs *Fc*$^{+/0}$			
	I'	II"/II'	III"/III'	IV"
[4^{Br}]$^-$	-1.51	-1.67	-2.90	-0.88
4^{MeCN}	-1.40	-1.65	-2.80	-0.87
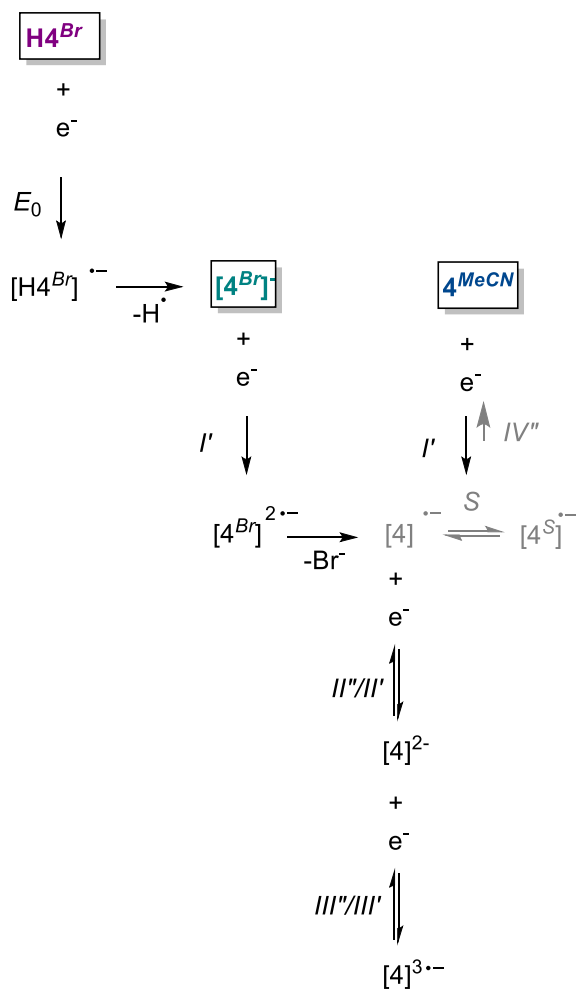
Scheme 4. Mechanistic pathway for the reduction of formazan/ate Re(I) complexes.

2.2   Spectroelectrochemistry

To gain more insight into the nature of the intermediates generated upon reduction, IR and UV-vis spectroelectrochemical measurements were performed. For FT-IR spectroscopy, the data were collected by sweeping the potential from -0.5 to -2.5 V *vs* Ag$^{+/0}$ at a scan rate of 2.5 mV/s. For UV-vis spectroscopy, the measurements were recorded at fixed potentials at the first and second reduction waves. Evolution of spectra is depicted as differential spectra considering as starting point the non-reduced species. We also performed computational studies to support the assignment (Table S1).

In acetonitrile, **Me6^{Br}** in its native form exhibits three bands at 2032, 1950, and 1919 cm^{-1}. Upon reaching the potential of the first reduction *I'*, two intense carbonyl bands rise at 2019 and 1914 cm^{-1}, along with two other bands of lower intensity at 2001 and 1876(br) cm^{-1} (Figure 5; red trace). This profile is maintained upon passing the first reduction wave. The major species is assigned to the solvato-radical **[Me6^S]**• and it was also detected *via* chemical reduction of either the neutral complex **Me6^{Br}** or the cation **[Me6^S]$^+$** (Figure S5). The carbonyl bands of the minor product (2001, 1876 cm^{-1}), are assigned to the naked-radical **[Me6]**•, as computations indicate (see below). We discard radical dimerization, as the four-band characteristic pattern ([Re(CO)$_3$(bpy)]$_2$ = 1991, 1951, 1885, 1862)[18] expected for these species was not observed.

When the potential of the second reduction is reached, three carbonyl bands of similar intensity raised at 1977, 1870, and 1857 cm^{-1}, attributed to the double-reduced complex **[Me6]$^-$** (Figure 5, blue trace). The assignment of these bands to a two-electron reduction product is further supported by the appearance of the same three IR bands in a solution of **Me6^{Br}** that was treated with two equivalents of Co(Cp*)$_2$. This species is predominant in the mixture for a while until the potential reaches values that are more negative than -2 V. At that point, two new bands at 1960 and 1830 cm^{-1} start to appear, which we tentatively assigned to the triple-reduced complex **[Me6]$^{2•-}$** (Figure 5, green trace).

The shifting of the carbonyl bands to lower wavenumbers upon two-electron reduction (**Me6^{Br}** → **[Me6]$^-$**) is in agreement with the formation of more electron-rich compounds. However, the shift in the high-energy band is rather small (55 cm^{-1}) compared to related complexes in the literature. For example, the archetypical complex *fac*-ReCl(CO)$_3$(bpy) by Lehn shows a much larger shift of the CO band at higher wavenumbers upon two-electron reduction (74 cm^{-1}).[19] We attribute this to a difference in the supporting ligands used: the low-lying π* orbitals of our formazan ligands result in ligand-based reductions, whereas reductions are more metal-centered in the case of the bipyridine. This is further supported by the work of Costentin and Chardon-Noblat, who reported that the introduction of electron-withdrawing groups onto the bpy scaffold makes reductions more ligand-centered, leading to a smaller shift in ν(CO) (37 cm^{-1}).[14]
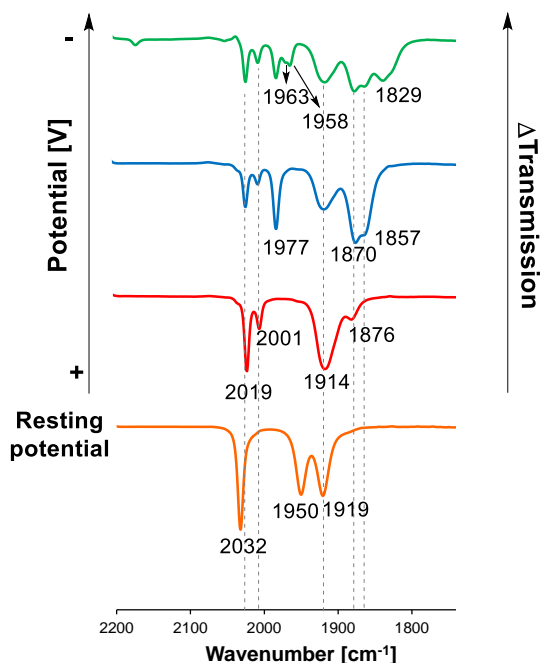
Figure 5. FT-IR-SPEC of Me6^{Br} under N$_2$ in an 0.1 M NBu$_4$PF$_6$ solution in acetonitrile.

For the UV-vis monitoring, controlled potential electrolysis was performed at *I'* = -0.6 V and *II'* = -1 V. Setting the potential at the first reduction decreases the absorption of the native complex **Me6^{Br}** at 449 nm, whereas a band at 360 nm arises. This profile is maintained during the electrolysis (red trace, Figure 6a). In the chemical reduction, two absorptions of lower intensity were detected at 530 and 700 nm (Figure 6c, red trace). The computed spectra of **[Me6]•** and **[Me6^S]•** exhibit similar absorptions, making it difficult to unambiguously assign the experimental UV-vis. When the potential is set after the second reduction, sequential changes are observed (Figure 6b). First, **Me6^{Br}** is consumed (band at 449 nm decreases). Then a decrease in absorbance at 530 nm and 700 nm, with a concomitant rise of a new band at 419 nm (blue trace) hints that the neutral radical **[Me6$^{(S)}$]•** was generated and consumed, yielding the double-reduced complex **[Me6]⁻'** (band at 419 nm). Two-electron reduction of **Me6^{Br}** and **[Me6^S]⁺** in excess of Co(Cp*)$_2$ renders the double-reduced complex **[Me6]⁻** as the only product with a broad absorption at 419 nm (Figure 6c, blue trace). We also tried to study the third reduction by spectroelectrochemical means, however, solvent decomposition was observed on the Pt mesh electrode of the SPEC setup, which prevented further analysis of the spectrum of the Re species generated at this negative potential.

a)

b)

c)
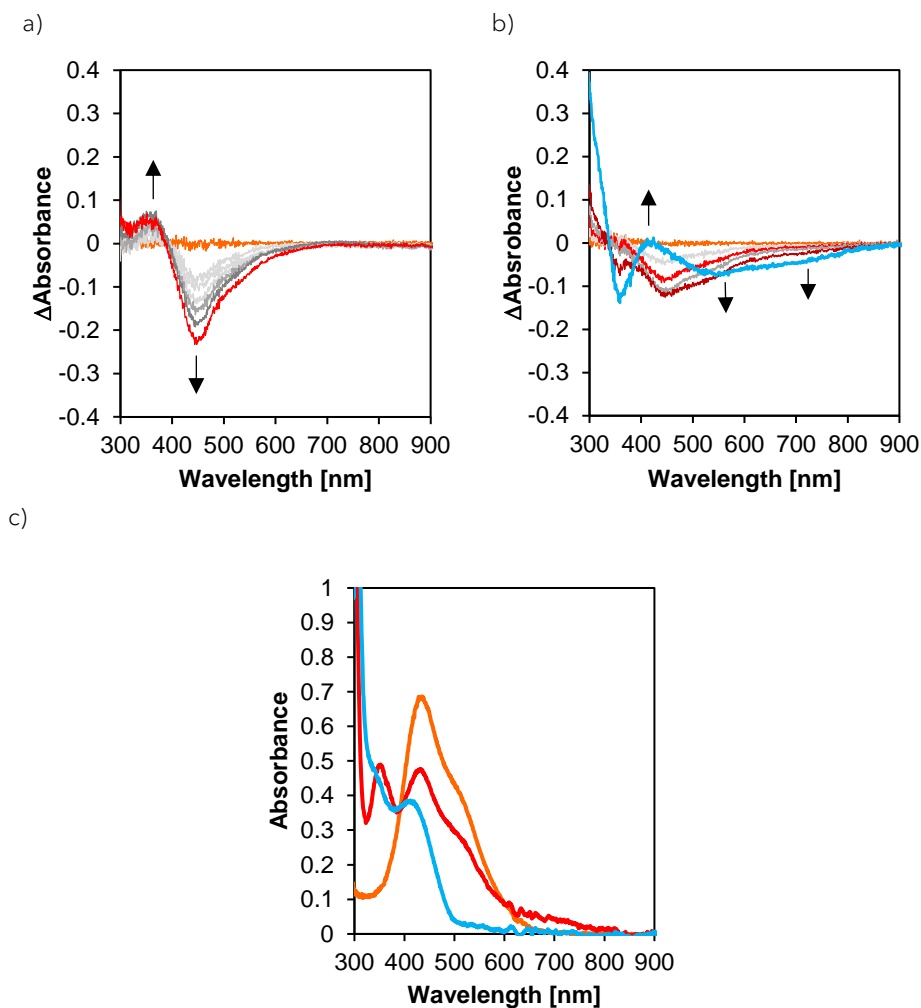
Figure 6. UV-vis SPEC ≈2.5x10^{-5}M in acetonitrile of Me6^{Br} a) at the potential of the first reduction (-0.3V) and b) after the second reduction (-1.0 V). Changes in absorption are depicted as a difference in absorbance with respect to the native species (yellow trace), meaning that traces above this line correspond to an increment in absorbance while the traces below are due to a decrease in absorbance. c) Chemical reduction of Me6^{Br} with Co(Cp⋆)$_2$ as reducing agent, depicting the UV-vis of the native species in orange, one-electron reduction in red and two-electron reduction in blue.

Table 3. Spectroscopic data of Me6^{Br}, [Me6^{Br}]$^{--}$, [Me6]$^{•}$ and [Me6]$^{-}$ in acetonitrile.

Complex	v(CO)[cm^{-1}]	Wavelength [nm]
Me6^{Br}	2032, 1950, 1919	449
[Me6^{S}]$^{•}$	2019,1914(br)	360, 432, 530, 700
[Me6]$^{•}$	2001, 1876	360, 432, 530, 700
[Me6]$^{-}$	1977,1870,1857	419

We carried out FT-IR and UV-vis SPEC for the formazanate species $[4^{Br}]^-$ and 4^{MecN} as well. Similar intermediates were detected by FT-IR, in accordance with what was observed by cyclic voltammetry (Figure 7). Upon reaching the potential of the reduction *I'*, two sets of bands rise at 1976, 1868(br) and 1858(sh) cm^{-1} and 1995,1894(sh). The former corresponds to the free-radical anion $[4]^{\bullet-}$, while the latter set of bands can be attributed to the solvated-radical $[4^S]^{\bullet-}$, as DFT calculations predict. One-electron chemical reduction of $[4^{Br}]^-$ and 4^{MecN} displayed a similar profile (Figure S7). No evidence of dimerization was detected by FT-IR. Finally, at the *E = II'*, two bands arose at 1958 and 1830(br) cm^{-1} that were assigned to the double-reduced complex $[4]^{2-}$. The carbonyl shifting of the CO high-energy band upon two-electron reduction in formazanate complexes is similar to the CO shifting found for the methylformazan species (52 cm^{-1} vs 55 cm^{-1}, respectively). Thus, the small shifting indicates these reductions are ligand-centered. Moreover, it means Re→ CO π-backdonation is similar for the neutral formazan and the anionic formazanate complexes despite the charge of the supporting ligand.
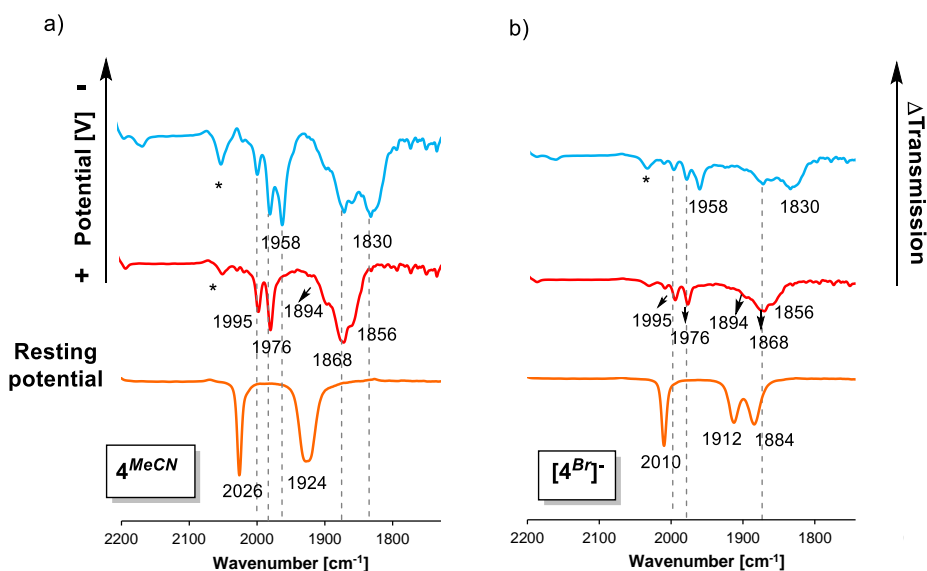
Figure 7. FT-IR-SPEC of a)4^{MeCN} and b)$[4^{Br}]^-$ under N_2 in an 0.1 M NBu_4PF_6 solution in acetonitrile

In UV-vis SPEC, passing the potential of the first reduction, an absorption at 440 nm emerges while the band of the formazanate native species at 600 nm decreases its absorbance (Figure 8a). One-electron reduction of $[4^{Br}]^-$ using a chemical agent, renders a spectrum with an intense band at 440 and another one of lower intensity at 590 nm that are assigned to the radical anion $[4^{(S)}]^{\bullet-}$ (Figure 8c, red trace) There is no evidence of dimerization since no absorptions were observed beyond 600 nm. After the potential of the second reduction, the decrease in absorbance of the band at 600 nm is more pronounced (blue trace), while the band at 440 nm remains (Figure 8b).

This profile is assigned to the double-reduced complex **[4]²⁻**, as was also confirmed by the two-electron chemical reduction of **[4^Br]⁻** (Figure 8c, blue trace). The spectroscopic signatures of reduced formazanate complexes past the potentials *I'* and *II'* are summarized in Table 4.

a)

b)

c)
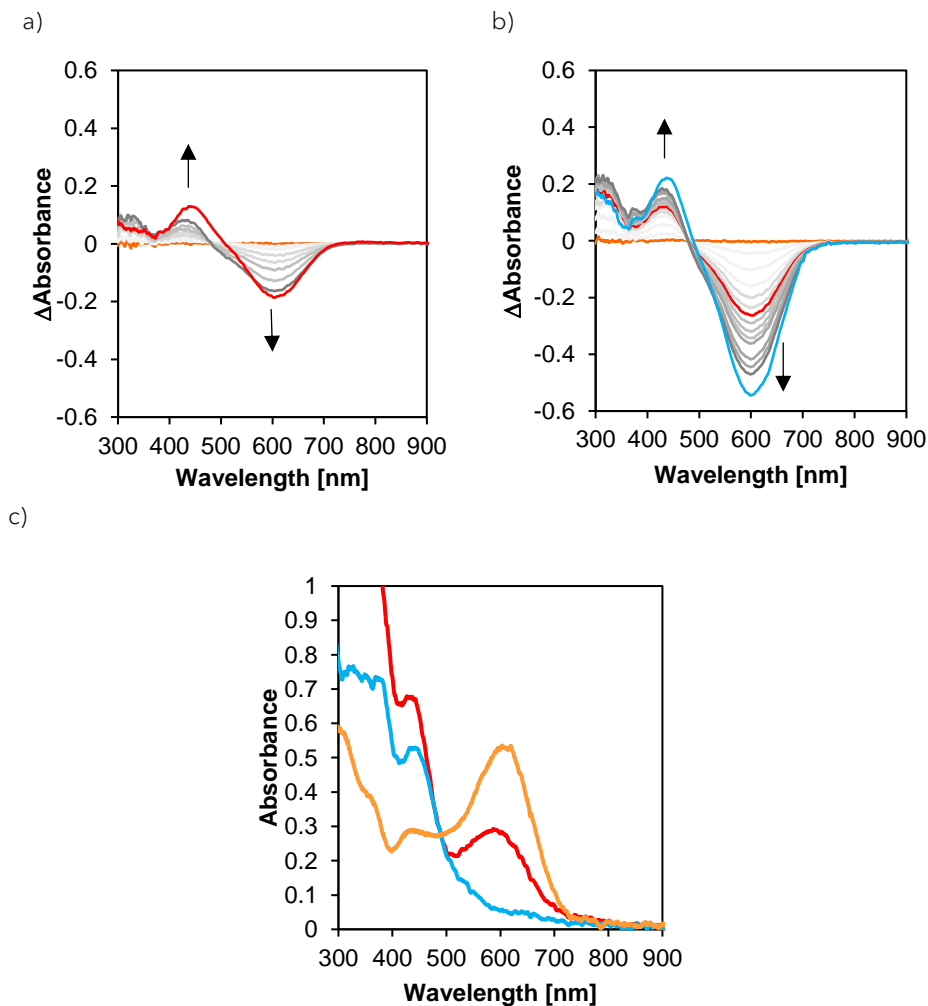
Figure 8. UV-vis SPEC ≈2.5x10⁻⁵ᴹ in acetonitrile past the a) first reduction (-1 V) and b) the second reduction (-1.4 V) in 4^MeCN. Changes in absorption are depicted as a difference in absorbance with respect to the native species (orange trace), c) UV-vis spectra ≈ 1.x10⁻⁵ M in THF for the chemical reduction of [4^Br]⁻ with [Na][C₆H₅)₂(CO)]•⁻.

Table 4. Spectroscopic data of $[4^{Br}]^-$, 4^{MeCN} $[4]^{\bullet-}$, and $[4]^{2-}$ in acetonitrile.

Complex	$v(CO)[cm^{-1}]$	Wavelength [nm]
$[4^{Br}]^-$	2010, 1912, 1884	603, 440
4^{MeCN}	2026 1924(br)	603, 440
$[4]^{\bullet-}$	1976, 1868, 1856	590, 440
$[4^S]^{\bullet-}$	1995, 1894(br)	
$[4]^{2-}$	1958, 1830(br)	440

2.3 Computational studies

We computed the structure of the first, second and third-reduced complexes of the methylformazan and formazanate derivatives to determine the nature of such reductions, using the crystallographic structure of the native species as starting point. (Scheme 5). The scaled analytical frequency calculations are comparable to those detected by FT-IR (Table S1).

Unrestricted DFT calculations were carried out on the bromide one-electron reduced radicals $[Me6^{Br}]^{\bullet-}$ and $[4^{Br}]^{2\bullet-}$. The rather elongated Re-Br bond compared to the native species accounts for its labile nature observed experimentally ($Me6^{Br}$ = 2.64078 Å, $[Me6^{Br}]^{\bullet-}$ = 2.70624 Å; $[4^{Br}]^-$ = 2.68058 Å, $[4^{Br}]^{2\bullet-}$ = 2.76518 Å). For the halide-free radicals $[Me6]^{\bullet}$ and $[4]^{\bullet-}$ the low energy conformation was found in a distorted square pyramidal geometry. The bond lengths within the five-membered metallacycle also differ from the ones observed in the non-reduced complexes. The shortening of C7-N2 bond and elongation of N1-N2 bond are consistent with a more bond-localized picture. Dissociation of bromide stretches C7-N2 and C7-N3 bonds while shortens the N1-N2 in the methylformazan derivative. In the formazanate species, halide dissociation shrinks the C7-N2 bond, whereas C7-N3 is elongated. For the solvato species $[Me6^S]^{\bullet}$ and $[4^S]^{\bullet}$, the trends in metrical parameters are similar to those observed in the non-solvated radicals. Spin density calculations on these species indicate the unpaired electron is mainly confined to the formazan fragment, being the first reduction of ligand character (Figure 9). We also studied the structure of the dimers $[Me6]_2$ and $[4]_2^{2-}$ and the somewhat elongated Re-Re bond compared to $[Re(CO)_3(bpy)]_2$ ($[Me6]_2$ = 3.2093 Å, $[4]_2^{2-}$ = 3.29279 Å vs 3.0791 Å in $[Re(CO)_3(bpy)]_2$) suggests dimerization is less favorable in formazan and formazanate species.
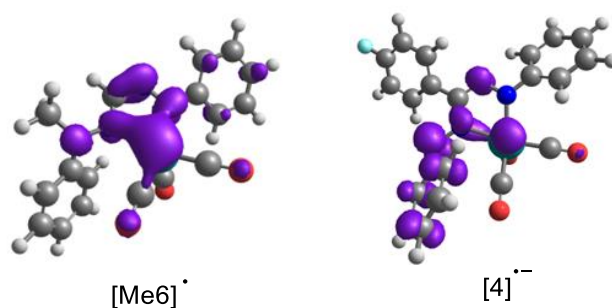
Figure 9. Spin density plots (isovalue = 0.003) for the methylformazan and formazanate Re(I) radicals [Me6]$^{\bullet}$ and [4]$^{\bullet-}$, respectively.

The broken symmetry approach was used when computing the structure of the double-reduced complexes to determine whether the most stable configuration would be an *open* or *closed*- shell singlet. The calculations for **[Me6]$^-$** and **[4]$^{2-}$** converged to a closed-shell singlet-state solution. The gradual reduction of the C7-N2 bond length (**Me6^{Br}** = 1.355 Å, **[Me6^{Br}]$^{\bullet-}$**= 1.329 Å, **[Me6]$^{\bullet}$**= 1.335 Å **[Me6]$^-$** = 1.297 Å; **[4^{Br}]$^-$** = 1.338 Å, **[4^{Br}]$^{2\bullet-}$ =** 1.329 Å, **[4]$^{\bullet-}$** =1.322, **[4]$^{2-}$** = 1.316 Å) strongly suggests the second reduction is also ligand-based. In both cases, the double-reduced complex displays a trigonal bipyramidal(TBP)-like geometry placing N1 in the apical position. We also optimized these structures in the triplet state and found the singlet is more stable by 30-40 kcal/mol. The computed metrical parameters indicate that the stability of the two-electron reduction products is due to the presence of the five-membered chelate in which the ligand has a neutral azo-imine structure (N=N-C=N) that can be reduced to a dianionic N-N=C-N fragment, analogous to the well-known redox chemistry of α-diimines.[20,21]

For the triple-reduced state, we studied the structure that results from adding one electron into the double-reduced complex. Therefore, we conducted the computational analysis on **[Me6]$^{2\bullet-}$** and **[4]$^{3\bullet-}$**. The unrestricted calculations rendered as more stable configuration a distorted TBP geometry. Bond elongation in the five-membered metallacycle compared to the double-reduced complex is observed, except for the C7-N3 bond, which is shortened. Spin density calculations place the unpaired electron into the Re *d*-orbital. Thus, the third electron transfer is metal based in nature (Figure 10).
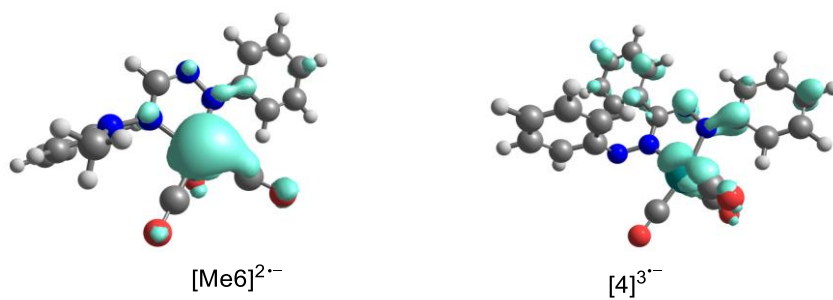
Figure 10. Spin density plots (isovalue = 0.003) for the methylformazan and formazanate Re(I) radicals [Me6]$^{2\bullet-}$ and [4]$^{3\bullet-}$, respectively.

Scheme 5. Reduction of methylformazan and formazanate Re(I) complexes
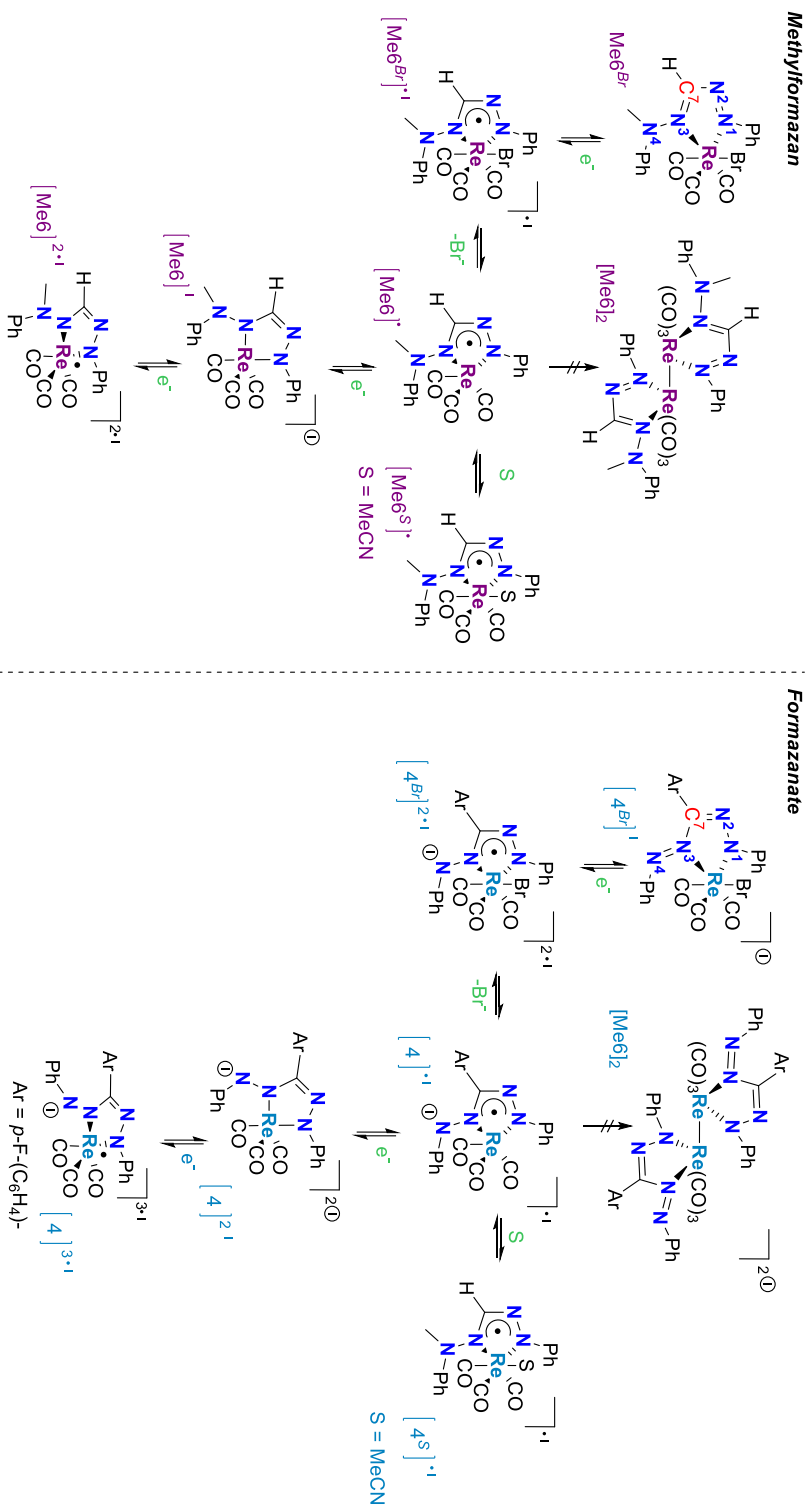
2.3.1 Time-dependent DFT calculations

TD-DFT calculations were performed to identify the characteristic electronic transitions expected for the different reduced species detected by UV-vis SPEC. PCM was used as a solvation model (acetonitrile).

The one-electron reduced species $[Me6^{Br}]^{\bullet-}$, $[Me6]^{\bullet}$ and $[Me6^S]^{\bullet}$ exhibit somewhat different electronic spectra (Figure 11b). In $[Me6^{Br}]^{\bullet-}$ the low-energy absorption corresponds to ML(Br) → ML(π^*-formazan) charge transfer (λ_{theo} = 561, 468, 448 nm), while the neutral radical $[Me6]^{\bullet}$ displays excitations with high oscillator strength at low-energy (λ_{theo} = 817 nm) and high energy (λ_{theo} = 535, 441 nm), both of highly mixed nature arising from Re(dπ)/L(formazan) → Re(dπ)/(NCNN(π^*) electronic transitions. While its solvated species $[Me6^S]^{\bullet}$ renders similar absorptions at low (λ_{theo1} = 596 nm) and high energy (with three main excitations at 360, 327, and 324 nm). We also computed the UV-vis spectrum of the dimer $[Me6]_2$ and found its predicted spectrum exhibits excitations of MLCT character (λ_{theo} = 720, 500, 427 nm) in a similar region to those observed in $[Me6]^{\bullet}$. Thus, it is not possible to distinguish these species in the experimental UV-vis during one-electron reduction since $[Me6^S]^{\bullet}$, $[Me6]^{\bullet}$ and $[Me6]_2$ depict comparable features (see Figure SX). The theoretical spectrum of the double-reduced complex $[Me6]^-$ reasonably resembles the experimental one. The less intense absorption observed experimentally at 440 nm emerges from a HOMO of Re(dπ)/NCNN(π) character to a metal (dπ) LUMO orbital (λ_{theo} = 402 nm).

The mono-reduced formazanate complexes $[4^{Br}]^{2\bullet-}$, $[4]^{\bullet-}$ and $[4^S]^{\bullet-}$ were also studied. The three species display excitations in a similar region: $[4^{Br}]^{2\bullet-}$ (λ_{theo} = 758 nm, 448 nm) of mainly ILCT character, $[4]^{\bullet-}$ (λ_{theo} = 712 nm, 530; 369 nm) LMCT, MLCT and ILCT, and $[4^S]^{\bullet-}$ (λ_{theo} = 718 nm, 448, 382 nm) ML/ILCT. For the doubly reduced species $[4]^{2-}$, the low energy absorption (λ_{theo1} = 410 nm) comprises electronic transitions of ML/IL charge character (Figure 12).

a)

b)
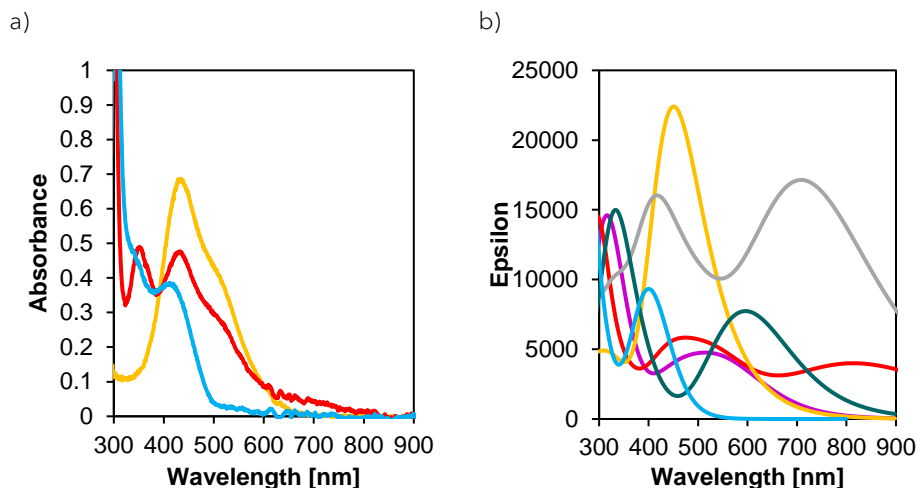
Figure 11. a) UV-vis spectra ≈ 1.4x10^{-5} M in MeCN for the chemical reduction of Me6^{Br} with Co(Cp*)$_2$. Yellow trace Me6^{Br}, red trace Me6^{Br} + 1 eq of red. agent, blue trace Me6^{Br} + 2 eq. of red. agent. b) Computed spectra, Yellow trace Me6^{Br}, purple trace [Me6^{Br}]$^{•-}$, red trace [Me6]$^{•}$, dark green trace [Me6^S]$^{•}$, gray trace [Me6]$_2$ and light blue trace [Me6]$^{-}$.

a)

b)
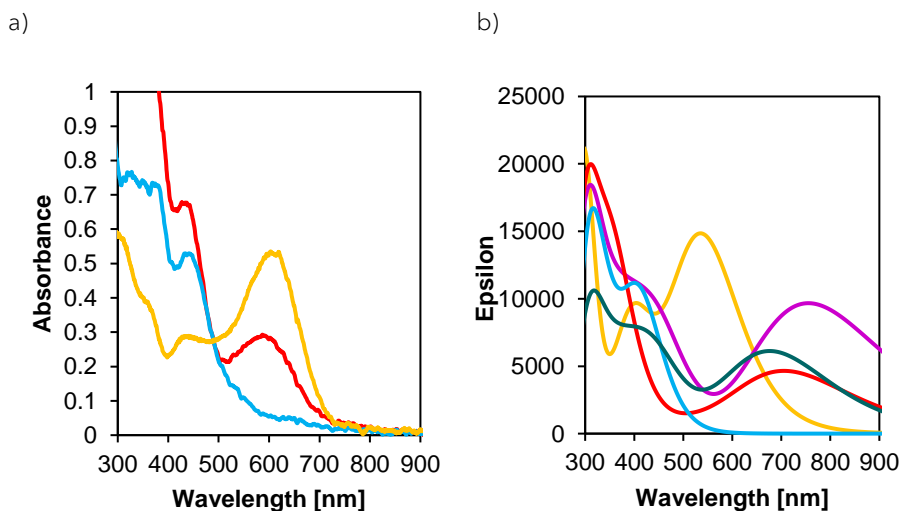
Figure 12. a) UV-vis spectra ≈ 1.x10^{-5} M in THF for the chemical reduction of [4^{Br}]$^{-}$ with [Na][C$_6$H$_5$)$_2$(CO)]$^{•-}$. Yellow trace [4^{Br}]$^{-}$, red trace [4^{Br}]$^{-}$ + 1 eq of red. agent, blue trace [4^{Br}]$^{-}$ + 2 eq. of red. agent. b) Computed spectra yellow trace [4^{Br}]$^{-}$, purple trace [4^{Br}]$^{2•-}$, red trace [4]$^{•-}$, dark green trace [4^S]$^{•-}$ and blue trace [4]$^{2-}$.

3.   Conclusions

The electrochemical properties of (methyl)formazan and formazanate Re(I) complexes were studied, and the different reduced forms were identified and their electronic structure elucidated by computational methods. Complexes with the protonated formazan showed to be unstable under reductive conditions, limiting their use as a proton-responsive ligand. In this regard, alkylation of the pendant N-H arm effectively blocks the reductive deprotonation pathway, enabling the access of one-, two- and three-electron reduced forms of the methylformazan Re(I) complex. Similarly, three different reduced species were also identified in the formazanate derivatives. Two consecutive one-electron reductions of ligand nature and a third metal-based reduction were observed. Calculations revealed that methylformazan and formazanate ligands in Re(I) species are redox-active and behave as a two-electron sink. However, the reduced forms from the methylformazan species are more stable, as manifested by its enhanced electrochemical reversibility compared to the formazanate analogues.

Radical dimerization has been reported in the bipyridine Re(I) complexes as a consequence of the poor charge stabilization of the nitrogen-donor ligand, leading to halide dissociation upon one-electron transfer. Although in formazanate and methylformazan complexes, halide decoordination takes place, the resulting highly stabilized azo-type radical prevents localization of the electron density on the metal center, thus disfavoring dimerization. Dimerization is a known deactivation pathway for the family of catalysts of group 7 for CO_2 reduction. In this matter, the incorporation of bulky substituents on the ligand framework has been shown to be a useful strategy to eliminate the deleterious reaction. Herein, we have also demonstrated that dimerization can also be prevented through electronic effects, in which case, the ability of the ligand to accept and distribute electrons within its backbone could be an important feature to be considered for catalytic design.

4.   Acknowledgements

5.   Supporting information

5.1   Synthesis

[Me6^{MeCN}][PF$_6$]. In a round-bottom flask, 0.0995 g (0.17 mmol) of **Me6^{Br}** and 1.2 equivalents of AgPF$_6$ (0.0561g, 0.22 mmol) were dissolved in 5 mL of MeCN. The reaction was performed in the darkness and heated to reflux for 2.5 h. Then, the mixture was cooled down and filtered through celite. The supernatant solution was evaporated, obtaining a crystalline dark brown powder (73.1 mg,63%). ^{1}H NMR (CDCl$_3$, 25 °C, 400MHz) δ/ppm:2.44 (s, 3H, MeCN CH$_3$), 4.07 (s, 3H, NMe, CH$_3$), 7.42 (m, 2 H, Ph-NMe o-H), 7.54 (m, 6 H, Ph-N=N m-H, p-H; Ph-NMe m-H, p-H), 7.82 (d, 2H, ^3J= 8 Hz, Ph-N=N o-H), 9.13 (s, 1H, NCN H). FT-IR (THF) ν(CO)/cm^{-1}: 2048(s), 1968(s) 1952(s).

5.2   Electrochemical studies

Cyclic voltammograms were recorded in a CHI600C potentiostat under N$_2$ atmosphere at room temperature in dry acetonitrile containing 0.1 M of NBu$_4$PF$_6$. The solutions were purged for 5 min with a stream of N$_2$ prior to the electrochemical measurements. CV was performed using a three-electrode set up comprised of a glassy carbon working electrode (3 mm^2), a silver wire as pseudoreference electrode, and a Pt wire as a counter electrode. The working electrode was polished before each measurement with an alumina slurry (0.05 μm), rinsed with distilled water, and sonicated for a few minutes, then washed with acetone. The concentration of the analyte was 1 mM in all cases. Ferrocene was added at the end of each measurement as an internal reference (1mM).
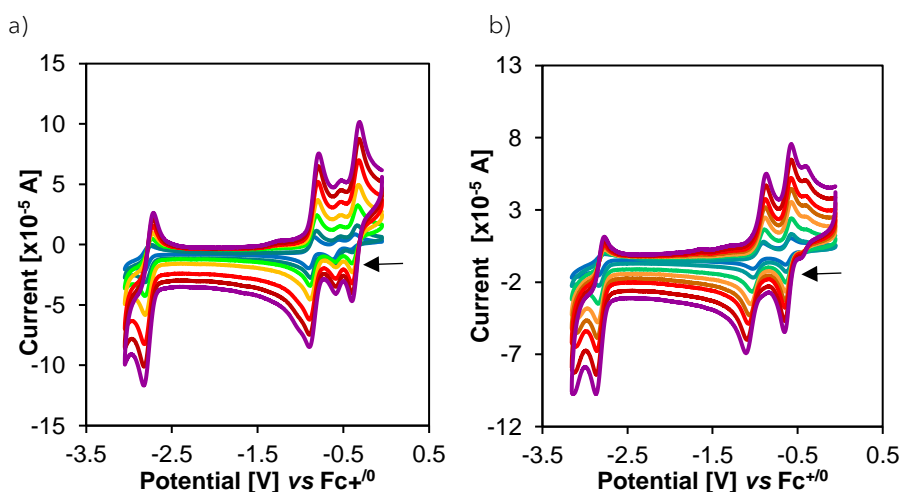
Figure S1. Cyclic voltammograms at different scan rates (0.05, 0.1, 0.25, 0.5, 1, 1.5 and 2V/s) showing the second cycle of a) Me6^{Br} and B) Me6^{Br} + 50 eq of NBu$_4$Br.

a)

b)
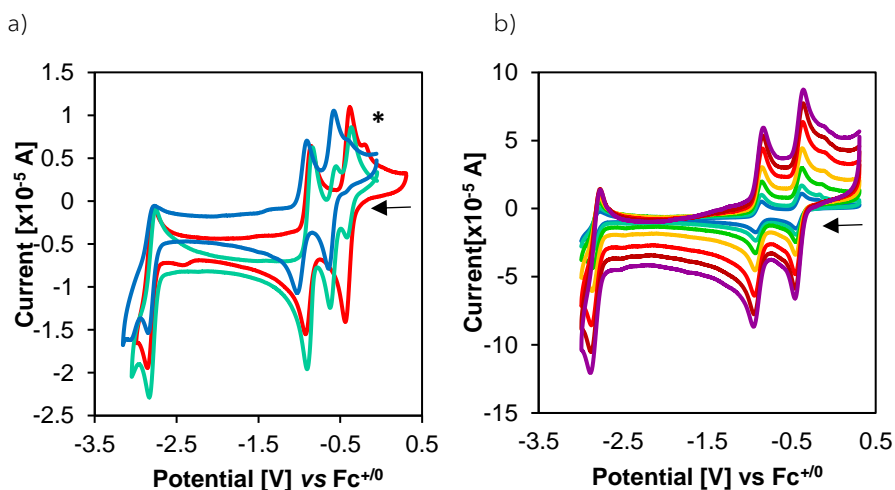
Figure S2. Cyclic voltammograms of a) [Me6^{MeCN}]$^+$[PF$_6$] (red trace), Me6^{Br} (green trace) and Me6^{Br} + 50 eq of NBu$_4$Br (blue trace). The peak * could belong to an impurity. b) [Me6^{MeCN}]$^+$[PF$_6$] at different scan rates (0.05, 0.1, 0.25, 0.5, 1, 1.5 and 2V/s) showing the second cycle.

a)

b)
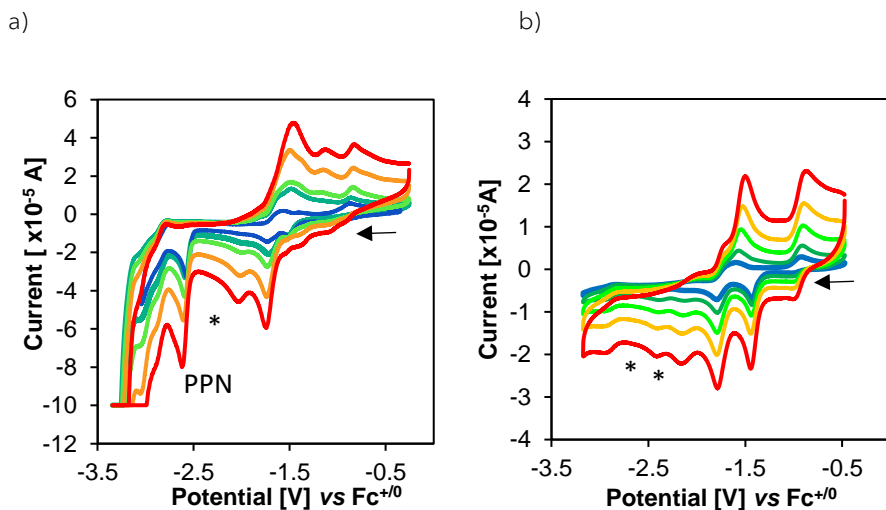
Figure S3. Cyclic voltammograms at different scan rates (0.05, 0.1, 0.2, 0.5, and 1 V/s) showing the second cycle of a) [PPN][4^{Br}] and b) 4^{MeCN} in acetonitrile, 0.1 M [NBu$_4$][PF$_6$].

a)

b)
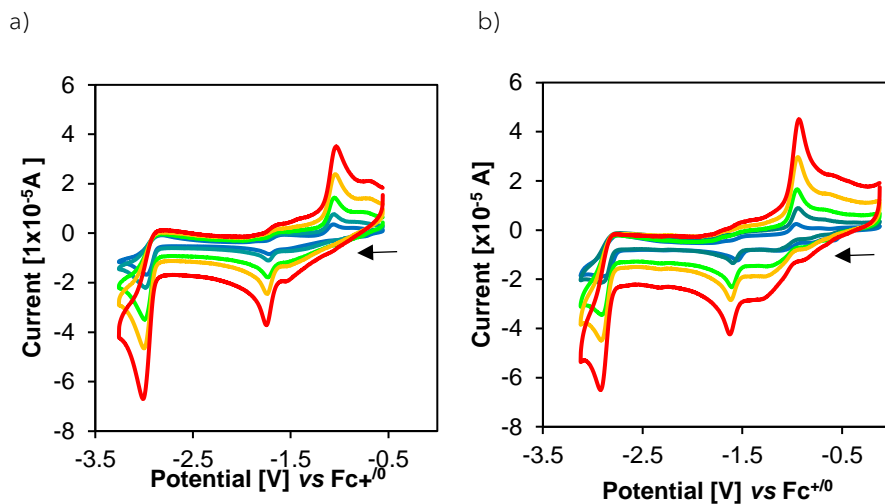
Figure S4. Cyclic voltammograms at different scan rates (0.05, 0.1, 0.2, 0.5, and 1 V/s) showing the second cycle of a) H4^{Br} and b) H6^{Bt} in acetonitrile, 0.1 M [NBu$_4$][PF$_6$].

5.3   Spectroelectrochemistry

FT-IR spectroelectrochemical measurements were performed on a Bruker Invenio-R spectrometer with a MCT-Detector using an OTTLE cell containing a platinum mesh as the working electrode, Ag wire as pseudoreference electrode, and a platinum counter electrode. The potential was applied by a GamryReference 600 potentiostat. The spectra were recorded every twelve seconds during a linear potential sweep with a scan rate of 2.5 mV/s. UV-vis SPEC was measured on a custom-made electrochemical cell assembled inside a 1 cm UV-vis cuvette, using graphite as a working electrode, a Pt wire as a counter electrode, and a Ag wire as a pseudoreference electrode. The measurements were recorded on a CHI600C potentiostat, and the spectra were measured every 1 s during a controlled potential electrolysis experiment until an end current ratio of 10%.

5.4   Chemical reductions

Chemical reductions were carried out inside the glovebox using dry and degassed solvents. Stock solutions from the reducing agent ($Co(Cp^{\star})_2$ or $[Na][C_6H_5)_2(CO)]^{\bullet-22}$) and the substrate were freshly prepared in 2.4 mM concentration in acetonitrile or THF, respectively. For UV-vis measurements, the solutions were diluted to 2.4×10^{-5}M. Inside the UV-vis cuvette, 1.5 mL of complex's solution and 1.5 mL of reducing agent solution were mixed, and immediately, the spectrum was recorded. For the two-electron reduction, a 4.8×10^{-5}M solution of the reducing agent was prepared from the same stock solution, and then 1.5 mL of this solution were poured into the UV-vis cuvette containing 1.5 mL of the substrate solution. For FT-IR, equivalent volumes of the stock solutions were mixed, and the spectrum was recorded.
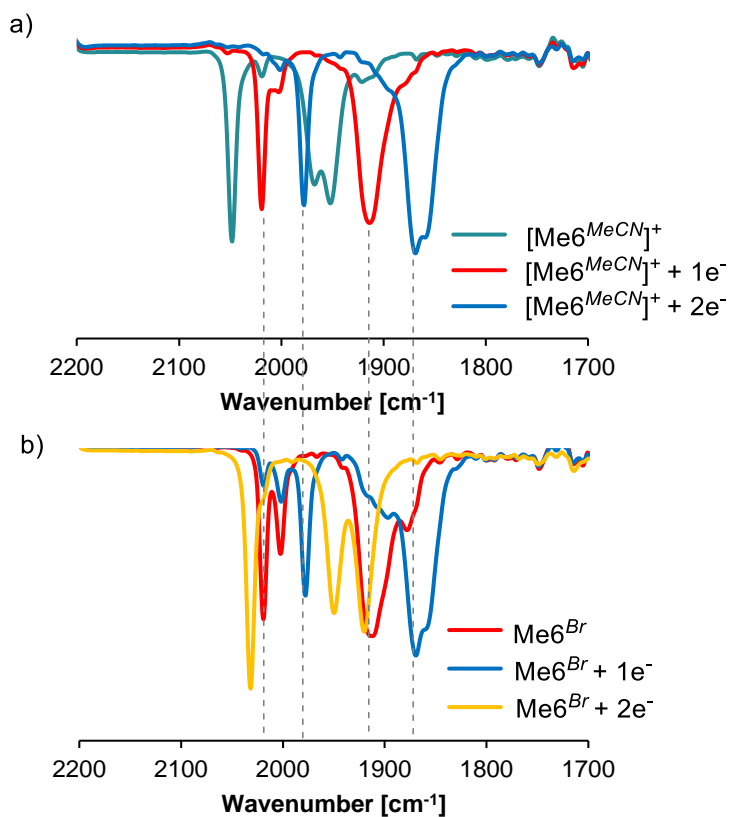
Figure S5. FT-IR upon chemical reduction of a) [Me6^{MeCN}]$^+$[PF$_6$] and b) Me6^{Br} in acetonitrile at rt.
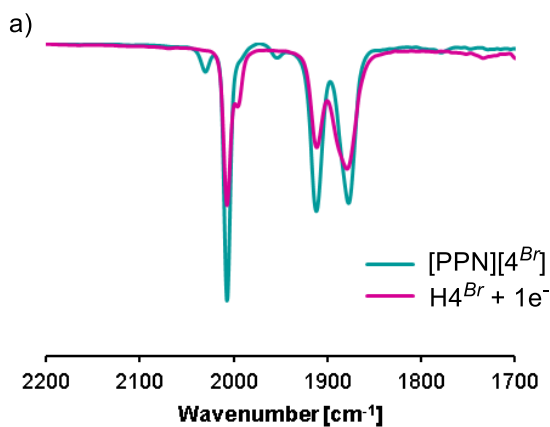
Figure S6. Comparison of FT-IR spectrum upon one-electron chemical reduction of H4^{Br} and b) [PPN][4^{Br}] in THFat rt.
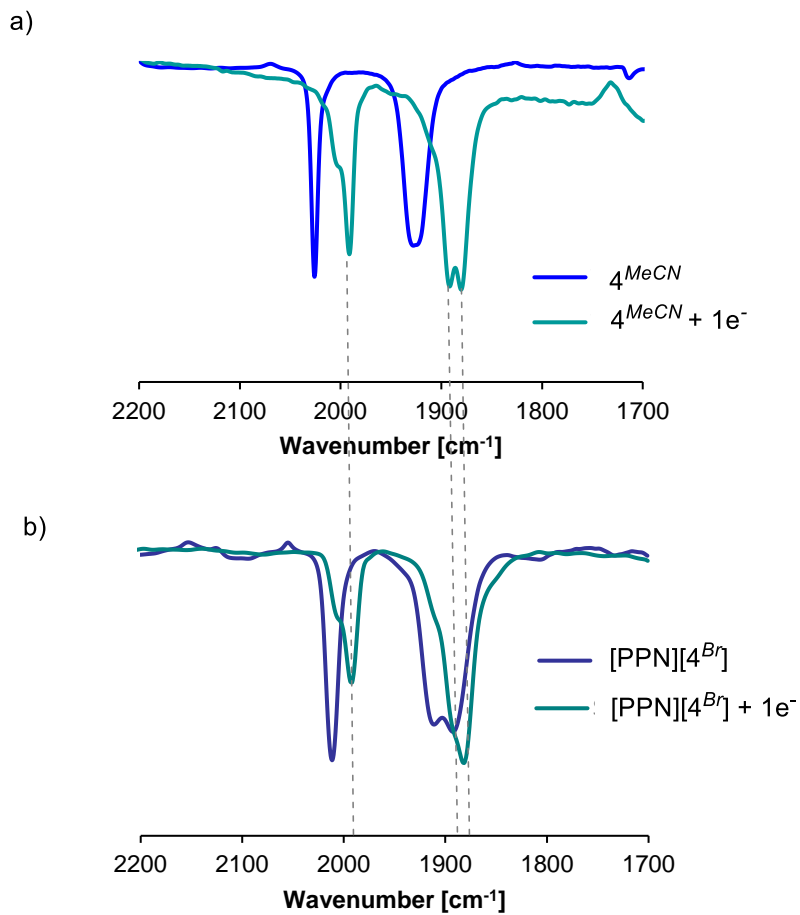
Figure S7. FT-IR spectra upon one-electron chemical reduction of a) 4^{MeCN} and b) $[PPN][4^{Br}]$ in THF at rt.

5.5   Computational details

The geometry optimizations were calculated on the gas phase and confirmed to be a minimum on the potential energy surface (no imaginary frequencies were found). The analytical frequencies were scaled by a factor of 0.9578[23] and the values are comparable to the experimental ones (Table S1). For time-dependent DFT calculations, the computations were performed using PCM as a solvation model for acetonitrile.

Table S1. Theoretical vs experimental carbonyl stretching frequencies.

Complex	Theoretical	Experimental	Complex	Theoretical	Experimental
$Me6^{Br}$	2022	2032	$[4^{Br}]^-$	1997	2010
	1960	1950		1915	1912
	1924	1919		1911	1884
$[Me6^{Br}]^{\bullet-}$	1986		$[4^{Br}]^{2\bullet-}$	1969	
	1908			1877	
	1880			1861	
$[Me6]^{\bullet}$	2009	2001	$[4]^{\bullet-}$	1977	1976
	1936	1876(br)		1892	1868(br)
	1920			1889	
$[Me6^{S}]^{\bullet}$	2011	2019	$[4^{S}]^{\bullet-}$	1991	1992
	1932	1914(br)		1912	1894
	1929			1885	1880
$[Me6]_2$	2003		$[4]_2^{2-}$	1971	
	1991			1956	
	1935			1901	
	1924			1885	
				1877	
				1865	
$[Me6]^-$	1969	1977	$[4]^{2-}$	1951	1958
	1883	1869		1860	1830
	1876	1857		1827	
$[Me6]^{2\bullet-}$	1875		$[4]^{3\bullet-}$	1882	
	1796			1772	
	1781			1773	

References

(1)   Shimizu, T.; Tanifuji, N.; Yoshikawa, H. Azo Compounds as Active Materials of Energy Storage Systems. *Angew. Chem. Inter. Ed.* **2022**, *61* (36). https://doi.org/10.1002/anie.202206093.

(2)   Crespi, S.; Simeth, N. A.; König, B. Heteroaryl Azo Dyes as Molecular Photoswitches. *Nat. Rev. Chem.* **2019**, *3* (3), 133–146. https://doi.org/10.1038/s41570-019-0074-6.

(3)   Samanta, S.; Ghosh, P.; Goswami, S. Recent Advances on the Chemistry of Transition Metal Complexes of 2-(Arylazo)Pyridines and Its Derivatives. *Dalton Trans.* **2012**, *41*, 2213–2226. https://doi.org/10.1039/c2dt10986g.

(4)   Pramanik, K.; Shivakumar, M.; Ghosh, P.; Chakravorty, A. Azo Anion Radical Complexes of Osmium and Related Nonradical Species. *Inorg. Chem.* **2000**, *39* (2), 195–199. https://doi.org/10.1021/ic9908322.

(5)   Paul, N.; Samanta, S.; Goswami, S. Redox Induced Electron Transfer in Doublet Azo-Anion Diradical Rhenium(II) Complexes. Characterization of Complete Electron Transfer Series. *Inorg. Chem.* **2010**, *49* (6), 2649–2655. https://doi.org/10.1021/ic9016195.

(6)   Kaim, W. Complexes with 2,2-Azobispyridine and Related S-Frame Bridging Ligands Containing the Azo Function. *Coord. Chem. Rev.* **2001**, *221*, 463–488. https://doi.org/10.1016/S0010-8545(01)00347-2.

(7)   Ghosh, P.; Samanta, S.; Roy, S. K.; Demeshko, S.; Meyer, F.; Goswami, S. Introducing a New Azoaromatic Pincer Ligand. Isolation and Characterization of Redox Events in Its Ferrous Complexes. *Inorg Chem* **2014**, *53* (9), 4678–4686. https://doi.org/10.1021/ic500355f.

(8)   Ishiki, K.; Nguyen, D. Q.; Morishita, A.; Shiigi, H.; Nagaoka, T. Electrochemical Detection of Viable Bacterial Cells Using a Tetrazolium Salt. *Anal. Chem.* **2018**, *90* (18), 10903–10909. https://doi.org/10.1021/acs.analchem.8b02404.

(9)   Sengupta, S.; Panda, B. K. Synthesis and Structure of the 2-(Chlorophenylazo)Pyridine Chelated Tricarbonylrhenium(I) Complex and Its Anion Radical Derivatives via Electrochemical Reduction. *Transit. Met. Chem.* **2005**, *30*, 426–432. https://doi.org/10.1007/s11243-005-0726-x.

(10)   Frantz, S.; Fiedler, J.; Hartenbach, I.; Schleid, T.; Kaim, W. A Complete Series of Tricarbonylhalidorhenium(I) Complexes (Abpy)Re(CO)₃(Hal), Hal = F, Cl, Br, I; Abpy = 2,2′-Azobispyridine: Structures, Spectroelectrochemistry and EPR of Reduced Forms. *J. Organomet. Chem.* **2004**, *689*, 3031–3039. https://doi.org/10.1016/j.jorganchem.2004.06.047.

(11)   Mukherjee, J.; Siewert, I. Manganese and Rhenium Tricarbonyl Complexes Equipped with Proton Relays in the Electrochemical CO₂ Reduction Reaction. *Eur. J. Inorg. Chem.* **2020**, *2020* (46), 4319–4333. https://doi.org/10.1002/ejic.202000738.

(12)   Sinopoli, A.; La, N. T.; Martinez, J. F.; Wasielewski, M. R.; Sohail, M. Manganese Carbonyl Complexes for CO₂ Reduction. *Coord. Chem. Rev.* **2018**, *365*, 60–74. https://doi.org/10.1016/j.ccr.2018.03.011.

(13)   Bourrez, M.; Molton, F.; Chardon-Noblat, S.; Deronzier, A. [Mn(Bipyridyl)(CO)₃Br]: An Abundant Metal Carbonyl Complex as Efficient Electrocatalyst for CO₂ Reduction. *Angew. Chem., Inter. Ed.* **2011**, *50* (42), 9903–9906. https://doi.org/10.1002/anie.201103616.

(14)   Guyot, M.; Lalloz, M. N.; Aguirre-Araque, J. S.; Rogez, G.; Costentin, C.; Chardon-Noblat, S. Rhenium Carbonyl Molecular Catalysts for CO₂ Electroreduction: Effects on Catalysis of Bipyridine Substituents Mimicking Anchorage Functions to Modify Electrodes. *Inorg. Chem.* **2022**, *61* (40), 16072–16080. https://doi.org/10.1021/acs.inorgchem.2c02473.

(15)   Duan, L.; Manbeck, G. F.; Kowalczyk, M.; Szalda, D. J.; Muckerman, J. T.; Himeda, Y.; Fujita, E. Non-innocent Proton-Responsive Ligand Facilitates Reductive Deprotonation and Hinders CO₂ Reduction Catalysis in [Ru(Tpy)(6DHBP)(NCCH₃)]²⁺ (6DHBP = 6,6′-(OH)2bpy). *Inorg. Chem.* **2016**, *55* (9), 4582–4594. https://doi.org/10.1021/acs.inorgchem.6b00398.

(16)   Manbeck, G. F.; Muckerman, J. T.; Szalda, D. J.; Himeda, Y.; Fujita, E. Push or Pull? Proton Responsive Ligand Effects in Rhenium Tricarbonyl CO₂ Reduction Catalysts. *J. Phys. Chem. B* **2015**, *119* (24), 7457–7466. https://doi.org/10.1021/jp511131x.

(17)   Zeng, Q.; Messaoudani, M.; Vlček, A.; Hartl, F. Temperature-Dependent Reduction Pathways of Complexes fac-[Re(CO)₃(N-R-Imidazole)(1,10-Phenanthroline)]+ (R = H, CH₃). *Electrochim. Acta* **2013**, *110*, 702–708. https://doi.org/10.1016/j.electacta.2013.02.018.

(18)   Benson, E. E.; Kubiak, C. P. Structural Investigations into the Deactivation Pathway of the CO_2 Reduction Electrocatalyst $Re(Bpy)(CO)_3Cl$. *Chem. Commun.* **2012**, *48*, 7374–7376. https://doi.org/10.1039/c2cc32617e.

(19)   Benson, E. E.; Sampson, M. D.; Grice, K. A.; Smieja, J. M.; Froehlich, J. D.; Friebel, D.; Keith, J. A.; Carter, E. A.; Nilsson, A.; Kubiak, C. P. The Electronic States of Rhenium Bipyridyl Electrocatalysts for CO_2 Reduction as Revealed by X-Ray Absorption Spectroscopy and Computational Quantum Chemistry. *Angew. Chem. Inter. Ed.* **2013**, *52*, 4841–4844. https://doi.org/10.1002/anie.201209911.

(20)   Vollmer, M. V.; Machan, C. W.; Clark, M. L.; Antholine, W. E.; Agarwal, J.; Schaefer, H. F.; Kubiak, C. P.; Walensky, J. R. Synthesis, Spectroscopy, and Electrochemistry of (α-Diimine)$M(CO)_3$Br, M = Mn, Re, Complexes: Ligands Isoelectronic to Bipyridyl Show Differences in CO_2 Reduction. *Organometallics* **2015**, *34* (1), 3–12. https://doi.org/10.1021/om500838z.

(21)   Mashima, K. Redox-Active α-Diimine Complexes of Early Transition Metals: From Bonding to Catalysis. *Bull. Chem. Soc. Jpn.* **2020**, *93* (6), 799–820. https://doi.org/10.1246/BCSJ.20200056.

(22)   Connelly, N. G.; Geiger, W. E. Chemical Redox Agents for Organometallic Chemistry. *Chem. Rev.* **1996**, *96* (2), 877–910. https://doi.org/10.1021/cr940053x.

(23)   Sae-Heng, P.; Tantirungrotechai, J.; Tantirungrotechai, Y. Scale Factors for Carbonyl Vibrational Frequencies: A Study of Partial Hessian Approximation. *Chiang Mai J. Sci.* **2018**, *45* (7), 2797–2808.

Chapter 5

(Alkyl)formazan and formazanate Re(I) complexes in the electrocatalytic reduction of CO$_2$

In this section, we describe the studies on the catalytic activity of formazanate and methylformazan Re(I) complexes for the electrochemical reduction of CO$_2$. Although the cyclic voltammogram of these complexes exhibit a significant current enhancement under CO$_2$ at -2.4 – -2.8 V vs Fc$^{+/0}$ without a proton source, low turnovers are observed in controlled potential electrolysis experiments, which suggests the conversion occurs at stoichiometric level. In particular, formazanate catalysts also display a current increment at more positive potentials (-1.2 – -1.5 V vs Fc$^{+/0}$) in CO$_2$ saturated electrolytic solutions, behavior that is suppressed in the presence of a Brønsted acid. Controlled potential electrolysis experiments confirmed CO formation with low faradaic efficiencies in both voltage regimes for formazanate complexes. In the methylformazan Re(I) species also CO was detected. Studies on the reactivity of formazanate species by (spectro)electrochemical techniques revealed the mono-reduced complex captures CO$_2$, but CO conversion is triggered at more negative potentials. The absence of activity at low overpotentials for the methylformazan Re(I) catalyst contrasted to what was observed in formazanate complexes, suggesting the involvement of the pendant azo-fragment in formazanate derivatives in substrate activation. These findings provide new insights into the advantages and limitations of using catalysts with redox-active ligands to activate and convert small molecules.

1.   Introduction

Energy transition from fossil-based fuels to renewable energy sources will continue to be a priority area in research as the consequences of the increased CO_2 concentration into the atmosphere are severe. For instance, the product of liquid fuels from CO_2 through the Fisher-Tropsch process ($nCO + (2n+1)H_2 \xrightarrow{cat} C_nH_{(2n+2)} + nH_2O$) could alleviate the environmental impact by reducing *ca.* 30% of the CO_2 emissions.[1,2] However, the high thermodynamic and kinetic stability of CO_2 make its conversion to value-added chemicals highly challenging. Electrocatalytic CO_2 reduction is under active investigation using both homo- and heterogeneous catalysis, but in general large overpotentials are required to achieve meaningful turnovers. Molecular catalysts offer the possibility for fine-tuning the reactivity by using ligand design strategies, both *via* the environment directly around the catalytically active metal[3,4] as well as its secondary coordination sphere.[5-8] This has led to a large variety of molecular catalysts that can drive the electrochemical CO_2 reduction through increasingly energy-efficient pathways.

Extensively explored for the electrochemical reduction of CO_2 to CO, *fac-*[(L,L)ReX(CO)₃] (L = functionalized bipyridine) catalysts have been shown to operate by two different mechanisms depending on whether the electron transfer is aided or not by protons. [4] For the more efficient proton-assisted two-electron pathway,[9] the double reduced complex **II'** captures CO_2, forming a metallocarboxylate species that releases CO and water upon protonation (Scheme 1b). In this scenario, the redox non-innocent bipyridine fragment has been proposed to play an essential role in product selectivity by delocalizing the negative charge to render the metal center a softer nucleophile that preferentially binds CO_2 over H^+.[10] Incorporation of proton-relays within the ligand framework to control local proton concentration has been shown to improve, in some cases, catalyst activity.[11]

For the proton-free pathway a bimolecular mechanism has been proposed, in which the one-electron reduced complex *I'* (active species) incorporates sequentially two equivalents of substrate forming a bridging CO_2 adduct. A subsequent reduction produces CO and CO_3^{2-} and the catalyst is regenerated (Scheme 1a).[12] One of the advantages of this pathway relies on avoiding constantly supplying protons to sustain catalysis, circumventing the parasitic hydrogen evolution reaction, hence enhancing product selectivity.[13]

Transition metal complexes are good candidates for CO_2 reductive disproportionation because they are robust reductants. [14] In 2015, Kubiak reported that $MnBr(CO)_3$(mesbpy) (mesbpy = 6,6'dimesityl-2,2'-bipyridine) promotes the reductive disproportionation reaction at low overpotentials (η = 0.3-0.45 V), wherein Mg^{2+} stabilizes the CO_2 adduct, resulting from the coordination of the substrate into the double reduced complex.

Similarly, Luca and coworkers informed that the dicarbene-pyridine complex $[MnCNC^{Bn}(CO)_3]Br$ (CNC^{Bn} = 2,6-bis(1-(alkyl)imidazole-2-ylidene)pyridine) afforded the catalytic reductive disproportionation of CO_2 with good faradaic efficiencies (93%).

One-electron pathway   Two-electron pathway
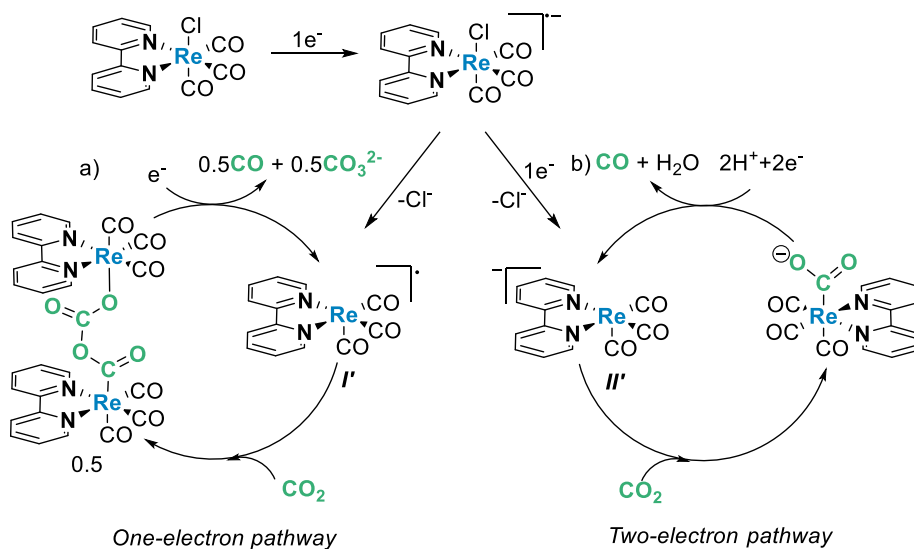
Scheme 1. General pathway for electrochemical reduction of CO_2 driven by the Lehn's catalyst, modified scheme taken from ***Chem. Soc. Rev.***, 2017,**46**, 761-796

In this chapter, we investigated the impact of a proton-responsive catalyst by comparing the activity of both formazanate and alkylformazan Re(I) complexes in the electrochemical reduction of CO_2 with and without protons. Two suspected catalytic regimes were observed at low and high overpotentials in formazanate Re(I) complexes under reductive disproportionation conditions. In contrast, the alkylformazan Re(I) derivative exhibits solely activity at high overpotentials under similar conditions. (Spectro)electrochemical studies and labeling experiments revealed the redox-active formazanate ligand promotes substrate activation at low overpotentials *via* the formation of a putative formazanate-CO_2-based adduct, while CO_2 conversion into CO and CO_3^{2-} is triggered upon applying more negative potentials. Although N-alkylation of the pendant N-Ar arm in the methylformazan Re(I) derivative enhances the electrochemical stability of the complex, it suppresses the reactivity at low overpotentials.

2.   Results & Discussion

2.1   Electrochemistry under CO_2 atmosphere

2.1.1   Cyclic voltammetry

The cyclic voltammograms of **Me6**^{Br}, **[4**^{Br}**]**$^-$, and **4**^{MeCN} were recorded upon CO_2 saturation in the absence and the presence of phenol as a weak Brønsted acid (Figure 1). We chose phenol as a proton source since it has been shown to enhance the catalytic rates more efficiently than other acids.[15] As NMR experiments demonstrated, it does not protonate the formazanate-based complexes under these conditions. The potential at which an increase in the current that could be due to an electrocatalytic reaction was observed, $E_{cat/2}$, was determined from the value of half the catalytic current $i_{cat/2}$, as reported by Helm and Appel.[16] Therefore, the overpotentials herein reported correspond to $\eta = E^{\circ}_{(CO2/CO)} - E_{cat/2}$. Considering that small amounts of water were present in the electrochemical cell for the reductive disproportionation reaction in acetonitrile, the standard reduction potential for $2CO_2 + H_2O + 2e^- \rightarrow CO_3^{2-} + CO + H_2O$, E° = -1.3 V vs $Fc^{+/0}$ was used, since CO_3^{2-} was produced under these conditions.[17,18] For the proton-coupled reduction $CO_2 + 2H^+ + 2e^- \rightarrow CO + H_2O$ in acetonitrile E° = -0.541 V vs $Fc^{+/0}$ was employed.[19]

When running a voltammogram of the formazanate complexes **[4**^{Br}**]**$^-$ and **4**^{MeCN} under CO_2, a modest current increase was observed at the onset of the reduction waves II'(-1.47 V) and I' (-1.13 V), respectively, that is at the potential at which one-electron reduction occurs and the radical anion **[4]**$^{\bullet-}$(or a solvent adduct thereof) is generated (Figure 1a-b). Such activation occurs at pretty low potentials compared to the E° of the reductive disproportionation of CO_2. The current ratio is 1.6 times higher in **[4**^{Br}**]**$^-$ compared to the current observed in **4**^{MeCN} as expected since the catalytic wave is slightly shifted to more negative potentials. However, it is only until reaching more negative values that a more prominent current is detected for **4**^{MeCN}.at -2.4 V vs $Fc^{+/0}$ (Figure 1a, Table 1), which has a peak current that is ca. 200 times higher than in the absence of CO_2. In the case of **[PPN][4**^{Br}**]**. The catalytic current overlaps with the reduction peak of [PPN]$^+$, which complicates the analysis. A control experiment using the salt [PPN][Cl] in the absence of Re also showed an increase in current (Figure S1). Although this is an interesting observation in its own right, in the context of this research, it makes assignment of activity to the bromide Re species ambiguous. Of note, the fact that a current increase is observed in the formazanate **4**^{MeCN}(without the interference of any cation) indicates the complex is active in the presence of CO_2. When the CVs were recorded in the presence of phenol (5%), the current at low overpotential decreases, and a current increase is only observed at -2.8 V vs $Fc^{+/0}$(Figure 1a). These observations suggest that two catalytic regimes are present under reductive disproportionation conditions.

A decrease in the faradaic current is observed in subsequent cycles, indicating catalyst degradation over time. Polishing the electrode allowed recovering some of the initial activity, suggesting that precipitation and electrode fouling may occur.

The voltammogram under CO_2 of the alkylated derivative **Me6^{Br}** (Figure 1c) displays a subtle anodic shift (40-50 mV) of the reduction waves *I'(-0.84 V)* and *II'(-0.57V)* accompanied by the formation of a new reduction peak *b* at -1.52 V; however, no current increase was observed at such potentials. An increased current was identified at –2.6 V, close to the reduction *III'* detected under N_2 assigned to the triple-reduced species [**Me6**]$^{2•-}$ with a current ratio of 8.6. Upon addition of phenol (5%), the reduction peak *II'*, (at -0.77 V, corresponding to the double-reduced species) is anodically shifted *ca.* 80 mV compared to the same reduction under CO_2, while the reduction **b** at -1.52 V observed under CO_2 is faded with added protons. Finally, the current detected at the onset of *III'* (-2.80 V, the potential at which the triple-reduced species, [Me6]$^{2•-}$ is formed) is 4-fold and anodically shifted in the presence of phenol by 250 mV (E_{cat}= -2.6 V). Although no current enhancement was observed at more positive potentials, changes on the voltammogram upon CO_2 saturation in **Me6^{Br}** suggest CO_2 interacts with the two-electron reduced species [**Me6**]$^-$, but CO_2 reduction is triggered by adding more electrons.

The divergence in the electrochemical response of the formazanate and methylformazan Re(I) complexes in the presence of CO_2 at low overpotentials manifests they react differently towards the substrate. The appearance of the reduction peak *b* in the methylformazan complex, passing the second reduction wave, advocates the double reduced complex [**Me6**]$^-$ might interact with CO_2, while changes on the first reduction wave in formazanate species point out the one-electron radical [**4**]$^{•-}$ is active. The lack of reactivity at low overpotentials upon adding protons in the formazanate complex hints that the pendant free N-atom in the ligand could be involved in CO_2 activation. This behavior differs from what was reported for Lehn's catalyst. In this case, the cyclic voltammogram of [ReCl(bpy)(CO)$_3$] measured in our set-up under the same conditions exhibits a catalytic current only after reaching the potential of the double reduced complex [Re(bpy)(CO)$_3$]$^-$ (-2.1V), that improves by adding phenol (5-fold current increase). Johnson and coworkers explored in detail the reactivity of Lehn's catalyst. They reported that catalysis at the potential of the first reduction wave under reductive disproportionation conditions only takes place when the experiment is measured in poor coordinating solvents such as THF and DMF, allowing the formation of the naked radical [Re(bpy)(CO)$_3$]$^•$.[20] Therefore, in formazanate species, the resulting azo-type radical [**4**]$^{•-}$ is stable enough to be formed in MeCN (as shown by FT-IR SPEC in *Chapter 4*) and react with the substrate.

Since both formazanate and methylformazan Re(I) complexes exhibit current enhancements *ca* -2.4 – -2.8 V, these compounds might follow analogous pathways at more negative potentials, which likely involve binding of CO_2 at the metal center. In Lehn's catalyst, a current increase is not observed at the third reduction wave, suggesting the putative triple-reduced complex is inactive, behavior that contrasts with the analogous Mn catalyst, in which case a catalytic current is observed at the third reduction wave.[21]
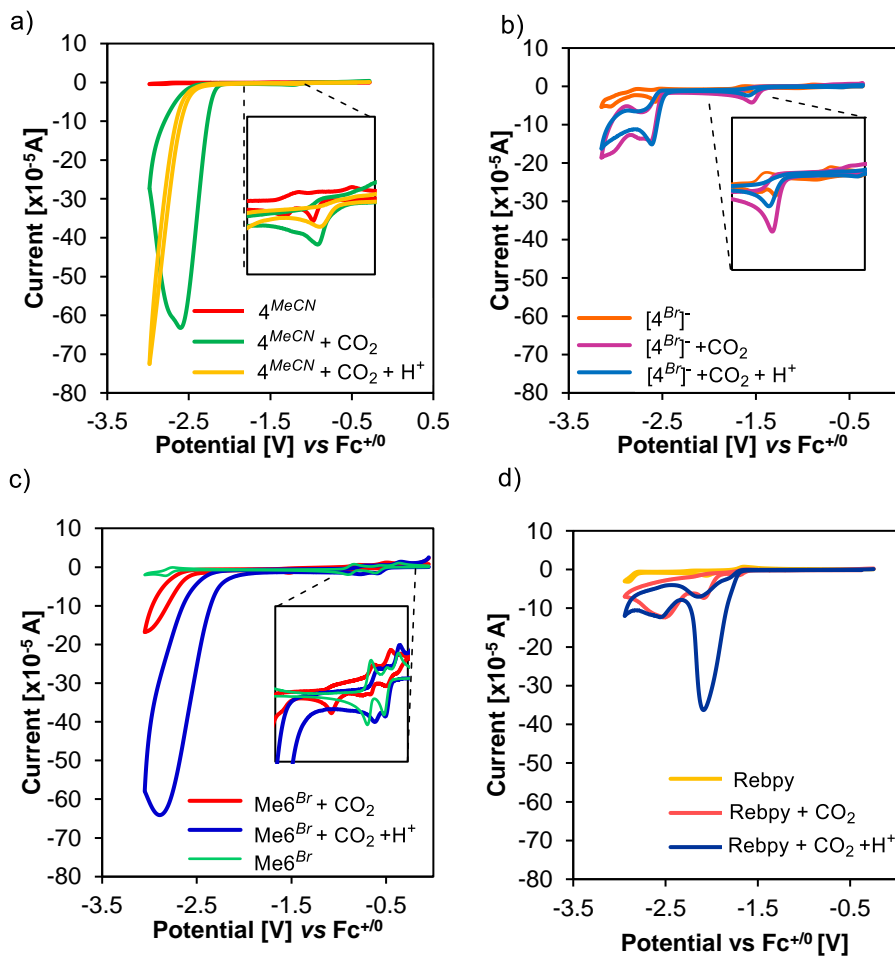
Figure 1. Cyclic voltammograms under CO_2 with and without 5% phenol at 50 mV/s for a) 4^{MeCN}, b)[PPN][4^{Br}], c) Me6^{Br} and d)Rebpy, Lehn's catalyst.

Table 1. Electrochemical parameters under CO_2 atmosphere for formazanate species.

Catalyst	CO₂				
	Low Overpotential		High overpotential		
	$E^1_{cat/2}$ [V]	i_{cat}/i_p	$E^2_{cat/2}$ [V]	i_{cat}/i_p	η_2
4^{MeCN}	-1.1	1.8	-2.4	173.6	1.1
$[4^{Br}]^-$	-1.5	2.8	--	--	--
$Me6^{Br}$			-2.8	8.6	1.5

Table 2. Electrochemical parameters under CO_2 atmosphere with 5% phenol for formazanate species.

Catalyst	CO₂ +5% Phenol				
	Low overpotential		High overpotential		
	$E^1_{cat/2}$ [V]	i_{cat}/i_p	$E^2_{cat/2}$ [V]	i_{cat}/i_p	η_2
4^{MeCN}	-1.06	1.1	-2.8	201.7	2.2
$[4^{Br}]^-$	-1.47	1.5	---	---	---
$Me6^{Br}$			-2.6	32.7	2.0

2.1.2   Controlled potential electrolysis

The current enhancements detected by cyclic voltammetry experiments suggest formazanate and methylformazanate Re(I) complexes exhibit catalytic behavior. Therefore, a bulk electrolysis technique was carried out to corroborate the current increased is due to catalysis. In controlled potential electrolysis experiments, the solution was exhaustively electrolyzed at the potential of *suspected* catalysis. At the end of the experiment, the headspace was analyzed by gas chromatography to identify and quantify the products. Then, one can conclude if the conversion is catalytically in nature based on the amount of product(s) generated.

For the formazanate species, two different potentials where *suspected* catalysis was observed in the cyclic voltammograms under a CO_2 atmosphere were studied using CPE. At low overpotentials (past the wave *I'* at ca. -1.5 V), the current decayed over 35 min, accompanied by a color change of the solution from dark blue to yellow-green (Figure 2). Similar changes were observed regardless of whether **$[4^{Br}]^-$** or **4^{MeCN}** was used (Figure S5). In both cases, CO was identified by GC. We discarded the possibility it could be generated due to catalyst decomposition, as performing a CPE in similar conditions under N_2 did not produce detectable quantities of CO by GC (Figure S6). Moreover, the yellow solution obtained during electrolysis with CO_2 compared to the red solution under electrolysis without substrate indicates the Re complex reacts with CO_2.
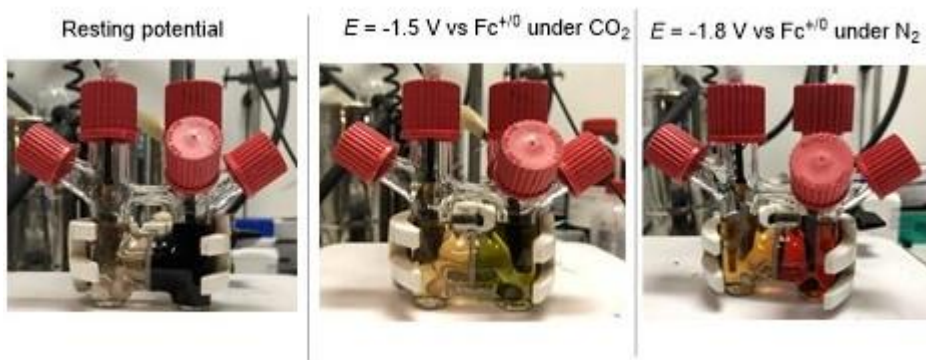
Figure 2. Bulk electrolysis solutions in an H-cell of 4^{MeCN}. The cathode on the right compartment: before electrolysis (left), after electrolysis under CO_2, (middle) and under N_2 (right).

Although the current enhancements observed for **4^{MeCN}** and **[4^{Br}]⁻** by cyclic voltammetry suggest catalysis may occur, the TON < 1 indicates the process observed at low overpotentials is not catalytic (Table 3), but (sub)stoichiometric instead. For instance, it might be possible conversion does not proceed due to the formation of a stabilized adduct, and it will be triggered only upon applying negative potentials, as proposed for $[MnX(CO)_3(mesbpy)]^n$ (X = Br, n= 0; X = M(eCN, n =1+)[17]. We did not explore this path in the presence of phenol since the cyclic voltammograms did not show an enhanced current under these conditions.

For the second wave at high overpotentials (-2.8 V), CPE experiments were conducted under CO_2 for 2 h (Figure S4), wherein CO gas was identified by GC, albeit with poor faradaic efficiencies and low TON (Table 3). The poor catalytic performance could be caused by the inherent instability of the catalyst at rather quite negative potentials or the consequence of solvent decomposition that could lead to unwanted background reactivity. Moreover, we cannot discard the possibility that in **[PPN][4^{Br}]** the counterion could have an influence. Traces of formic acid, besides $^{13}CO_3^{2-}$ (164.4 ppm), H-$^{13}CO_3^-$ (160.2 ppm), $^{13}CO_2$, (125 ppm) and an unidentified *C*-product (170.7 ppm), were detected by ^1H and $^{13}C\{^1H\}$ NMR when the CPE was conducted at -2.4 V vs $Fc^{+/0}$ with $^{13}CO_2$ and **[4^{Br}]⁻** (Figure S7)**.**[22] The unexpected generation of formic acid under 'anhydrous' conditions suggests that adventitious water is present in the electrolysis cell, either from the solvent or absorbed on the surface of the glass or electrode. The addition of phenol did not improve catalyst performance (Table 4, Figure S5), which we rationalize is due to the deactivation of the proton-responsive formazanate complex, as similarly reported for $[ReCl(CO)_3(6DHBP)]$ (6DHBP = 6,6′-dihydroxy-2,2′-bipyridine).[23] Table 5 shows that hydrogen evolution reaction accounts for only 1-2% of the observed current in the experiments when phenol is added.

Table 3. Data from controlled potential electrolysis for formazanate complexes 4^{MeCN} and $[4^{Br}]^-$ under CO_2.

Catalyst	CO₂				
	Low Overpotential		High Overpotential		
	FE$_{CO}$ %	TON	FE$_{CO}$ %	FE$_{HCOOH}$ %	TON
4^{MeCN}	25	0.63	48	---	4.97
$[4^{Br}]^-$	19	0.45	9	<1	0.67

Table 4. Data from controlled potential electrolysis for formazanate complexes 4^{MeCN} and $[4^{Br}]^-$ under CO_2 and 5% phenol.

Catalyst	CO₂ + 5% Phenol		
	High Overpotential		
	FE$_{CO}$%	TON	FE$_{H2}$%
4^{MeCN}	19	0.66	1
$[4^{Br}]^-$	21	1.62	2
Me6^{Br}	16	0.93	7

Therefore, we expected that by blocking the proton-responsive group, the catalytic activity may be improved. However, CPE experiments carried out on the alkylated formazan **Me6^{Br}** with 5% phenol also showed only stoichiometric amounts of CO, with faradaic efficiencies of 16% for CO and 7% for H₂. Overall, these outcomes indicate that the current increase observed in cyclic voltammetry under CO_2 atmosphere are not due to efficient electrocatalytic CO_2 reduction by the Re complexes studied here.

2.2 CO_2 activation at low overpotentials

The poor catalytic performance at quite negative potentials for formazan/ate Re(I) catalysts discouraged us from studying this pathway further. Instead, we focused on understanding what causes the changes that occur in the cyclic voltammetry at low overpotentials for the formazanate Re(I) complexes.

2.2.1   Spectroelectrochemistry

FT-IR SPEC of 4^{MeCN} was carried out by dissolving the complex in a solution partially saturated with CO_2 (≈0.14 M), that was prepared by diluting to 1:1 ratio a saturated solution of CO_2 in acetonitrile. We use 4^{MeCN} in the discussion below as a representative example as similar outcomes were found for $[4^{Br}]^-$, which is consistent with the notion that both compounds generate the same bromide-free species upon reduction (see *Chapter 4*). Under N₂, at the potential of the first reduction (*ca* -1.4 V), the species in solution are the radicals $[4]^{\bullet-}$ and $[4^S]^{\bullet-}$, but in the presence of CO_2, three IR bands in the metal-carbonyl region appeared at 1976, 1867 and 1854 cm^{-1} –which coincidentally, are similar to those detected for $[4]^{\bullet-}$ – and an additional band is observed at 1714 cm^{-1}

(Figure 3, red trace). These bands become more intense when sweeping to more negative potentials (-2.0 V *vs* Fc$^{+/0}$, Figure 3a, green trace), unlike what was observed under N$_2$, in which case CO bands at 1958 and 1830(br) were identified at similar potentials assigned to the double-reduced complex **[4]$^{2-}$** (Figure 3b, green trace). Therefore, the CO bands at 1976, 1867, 1857 and 1714 cm^{-1} may correspond to a different metal carbonyl species, that we tentatively assigned to the CO_2-adduct ***A***. The bands of ***A*** continue growing until reaching quite negative potentials (-2.7 V *vs* Fc$^{+/0}$, Figure 3a, blue trace) From then on, new CO absorptions, not well-resolved, were observed at 1999 and 1894 cm^{-1} while the bands of the adduct ***A*** started to disappear. The new CO bands detected at 1999 and 1894 cm^{-1} lie in a similar region to those reported for metallocarboxylate or metallocarbonate species in related complexes under reductive disproportionation conditions (for [(bpy)-Mn-CO_2-Mg]$^+$ ν_{CO} = 2006 1907 cm^{-1},[17]; for [Re(DAB)(CO)$_3$(OCO$_2$)]$^-$ DAB: 1,4-diazabutadiene, ν_{CO} = 2003 1870 cm^{-1},[24]). Moreover, a simultaneous decrease of the band at 2332 cm^{-1} assigned to CO_2 was observed at such negative potentials, indicating substrate conversion was occurring. At lower frequencies, three intense bands at 1683, 1648, and 1616 cm^{-1} were identified (Figure S7). The vibrations at 1683 and 1648 cm^{-1} are consistent with HCO_3^-/CO_3^{2-},[25] formation, while CO was detected from CPE experiments by off-line analysis of the headspace by GC, expected products for CO_2 reduction *via* disproportionation. The identity of the band at 1616 cm^{-1} is still unknown.
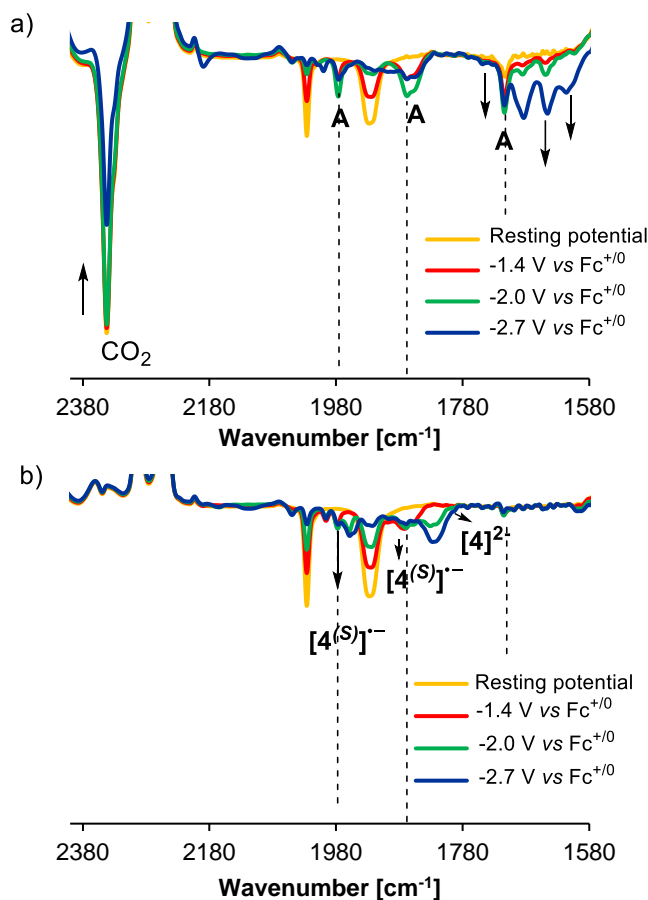
Figure 3. FT-IR SPEC of 1.5 mM of 4^{MeCN} with 0.1 M of NBu_4PF_6 under a) a solution partially saturated with CO_2 and b) N_2 by linear potential sweep.

2.2.2 Chemical reductions in the presence of $^{13}CO_2$

Cyclic voltammetry results under an atmosphere of CO_2 pointed out the radical $[4]^{•-}$ could be involved in substrate activation, as differences in the voltammogram under CO_2 were observed at the onset of the first reduction wave. Thus, to collect more evidence about the activation at low overpotentials, we carried out NMR experiments with $^{13}CO_2$. We prepared samples of the mono- and double-reduced complexes $[4^{(S)}]^{•-}$ and $[4]^{2-}$ by dissolving complex 4^{MeCN} with one and two equivalents of $Co(Cp^*)_2$ in CD_3CN saturated with $^{13}CO_2$. The samples were analyzed by $^{13}C\{^1H\}$ NMR, and the spectra is depicted in Figure 4. Upon one-electron reduction, the spectrum exhibits two signals at 159.4 and 161.3 pm, and at 125.72 ppm the peak corresponding to $^{13}CO_2$ is observed. This indicates that the one-electron reduction product of 4^{MeCN} already reacts with CO_2. The new signals lie in the region of amide-type derivatives, consistent with the formation of metal carbamate-like species[26]. These spectroscopic features are also

similar to those reported by the Roesky group for the formazanate magnesium complex that reversibly incorporates CO_2. The resulting magnesium formazanate-carbamate species exhibits in carbon-NMR a chemical shift of 155 ppm and an IR band at 1702 cm[-1,] assigned to the carbamate group. [27]

When two equivalents of reducing agent are added, a new intense peak at 160.5 ppm is observed along with traces of the signals at 159.3 and 161.3 ppm. We discard the peak corresponds to a CO_2-adduct because ^{19}F NMR showed the double-reduced complex **[4]²⁻** is the major species. Thus, we suggest the signal at 160.2 be consistent with a product derived from [13]CO_2 activation that, based on the chemical shift, we tentatively assigned to bicarbonate [H-O-[13]C(=O)O]⁻.[22] With this in mind, we studied the nature of the putative CO_2 adduct by computational means.
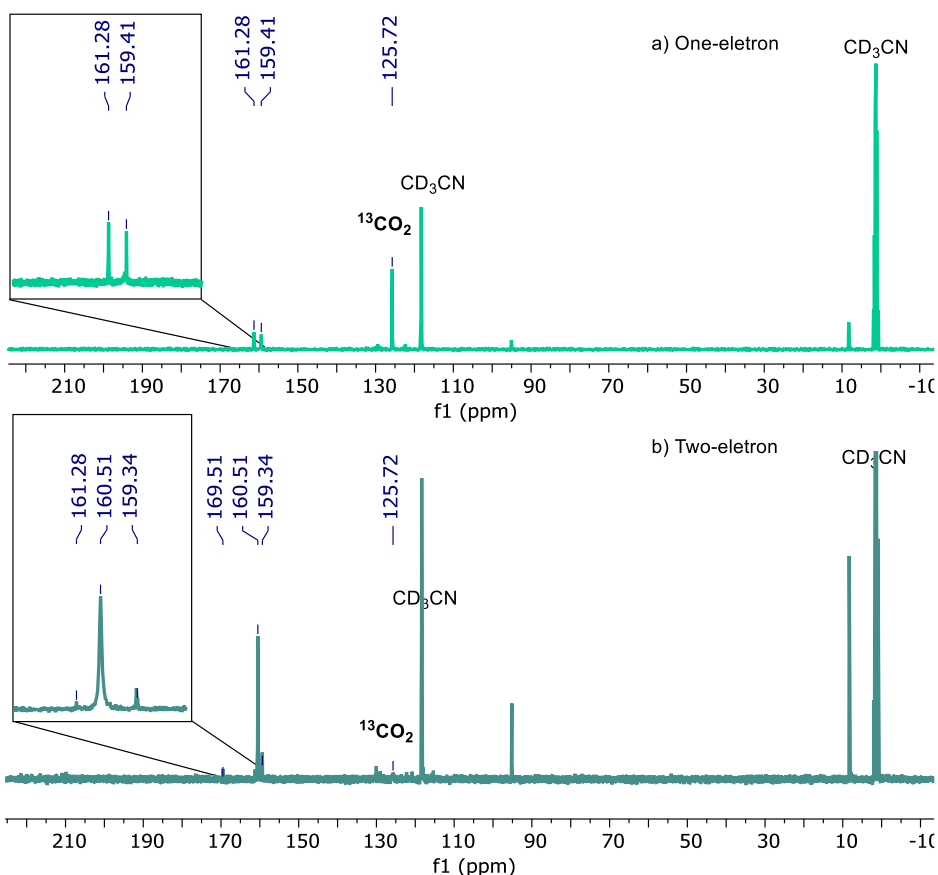
Figure 4. ^{13}C{^{1}H} NMR upon [13]CO_2 saturation of a solution of a) mono and b) double reduced species in acetonitrile.

2.3 Nature of the CO₂ adduct

The spectroscopic evidence suggests the one-electron reduced formazanate Re(I) radical [4]•⁻ reacts with the substrate in the absence of protons. In related one-electron reduced species under reductive disproportionation conditions –for instance, [Re(CO)₃(bpy)]•– it has been proposed the metal center is the site where CO_2 is bound and activated for further transformation. (Spectro)electrochemical experiments along with DFT calculations support the reduction is of ligand-based nature making the ligand a better nucleophile upon reduction compared to Re. Analysis of the charge distribution in [4]•⁻ evidences that part of the electron density is located on the terminal nitrogen in the formazanate ligand (*see* Mulliken charge distribution in Figure S11). Furthermore, the detection of signals in the carbamate region in the labeling experiment and by FT-IR (spectro)electrochemistry, supports the hypothesis that the activation proceeds by nucleophilic attack of the terminal nitrogen on the electrophilic carbon in CO_2. Assumption that agrees with the absence of activity in the presence of protons, as H⁺ is a stronger electrophile. In such case, ligand protonation would be favored over carbamate formation. This could also explain the poor reactivity of the one-electron reduced methylformazan radical [Me6]•, since the terminal nitrogen is less nucleophilic in this species (*see* Mulliken charge distribution Figure S11).

The nucleophilic nature of the N-atoms in reduced formazanate species was also manifested in other complexes. For instance, in the 5-membered mono-formazanate Zn(II) radical (obtained from the one-electron reduction of a dinuclear formazanate Zn(II) species), the nucleophilic character of the pendant terminal nitrogen has been harnessed to initiate ring opening polymerization *via* nucleophilic attack of the N-Ar fragment to the carbonyl group in the *O*-coordinated lactide.[28] In the case of the 6-membered boron monoformazanate doubly-reduced species, the addition of electrophiles takes place at the internal nitrogen, manifesting the nucleophilic nature of the internal N-atoms, reactivity that was rationalized in terms of the stability of the 6-membered chelate over the 5-membered boratacycle (Figure 5.).[29]
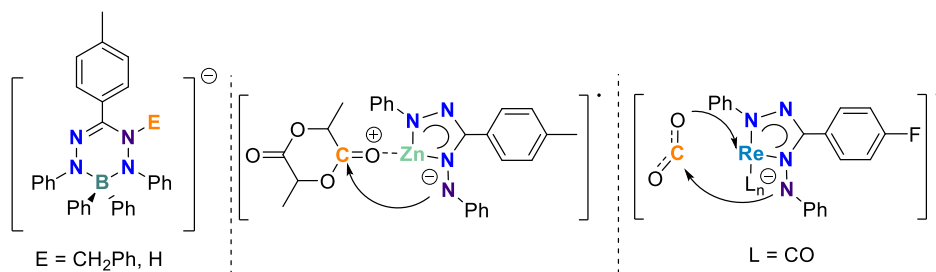
Figure 5. Nucleophilic character of reduced formazanate complexes.

Taking inspiration from the magnesium formazanate CO_2 complex reported by Roesky, we investigated the structure *mer*-[4^{N-CO2}]$^{•-}$ that results from the nucleophilic addition of the terminal N-atom to CO_2 and subsequent coordination of the pendant-oxo fragment to the metal center that generates a formazanate-carbamoyl pincer-like moiety with two 5-membered rings fused. In this structure, the CO ligands are arranged in a meridional conformation. Geometry optimization and analytical frequency calculations indicate *mer*-[4^{N-CO2}]$^{•-}$ is a minimum on the potential energy surface (no imaginary frequencies) with scaled-theoretical frequencies at 2000, 1907, 1879, and 1730 cm^{-1}, which deviate from the experimental ones by 40-16 cm^{-1}. Spin density calculations placed the unpaired electron on the formazanate fragment, a stabilized azo-radical (Figure S12). We computed, as well, the structure of the *facial* isomer *fac*-[4^{N-CO2}]$^{•}$; however, the optimized geometry rendered a carbamate species that is formed with the internal nitrogen atom instead of the terminal one (Scheme 2). Thus, we discarded it as a potential configuration since the internal nitrogen is not expected to be nucleophilic enough to lead to the activation of CO_2.
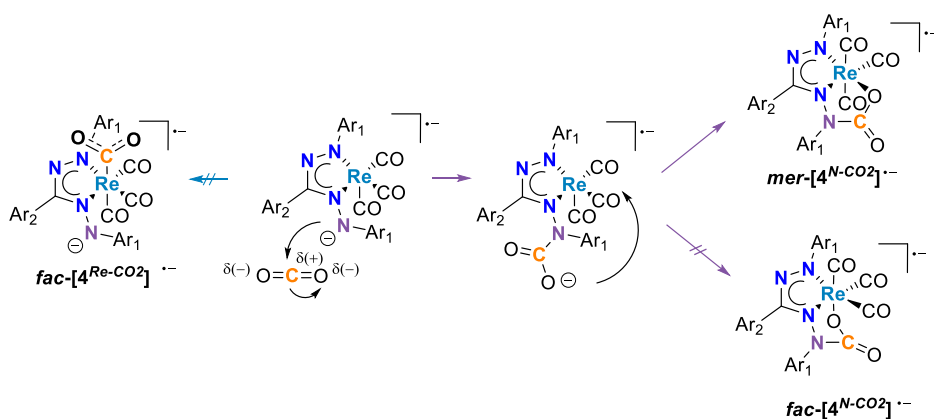
Scheme 2. Structures studied by DFT-calculations.

To confirm the resulting adduct did not correspond to the typical metal-CO_2 species, we also investigated the structure [4^{Re-CO2}]$^{•-}$ that arises from substrate coordination to the metal and found no interaction between CO_2 and the complex upon convergence. We neither observed metal-CO_2 binding in the double reduced species [4^{Re-CO2}]$^{2-}$ and only obtained a stable Re-CO_2 structure for the triple reduced adduct [4^{Re-CO2}]$^{3•-}$ (Table S1). Such outcome is in accordance with the electronic structure predicted for the triple reduced complex [4]$^{3•-}$ by DFT calculations, a metal-based radical –formally Re(0) species– that can be engaged in CO_2 activation.

Taking together the experimental and theoretical studies, we can conclude the presence of redox-active fragments in the structure of Re(I) catalyst has a detrimental effect on the catalytic activity because these ligands prevent metal-based reductions, therefore metal-CO_2 binding affinity. A particular case are redox-active ligands with

negatively charged groups, as the formazanate ligand in its *open*-form. Molybdenum carbonyl complexes supporting a pyridine monoimine ligand in their reduced forms also displayed similar ligand-based reactivity in the presence of CO_2.[30] In these cases, the ligands play the role of nucleophiles instead. It is likely that the formation of strong E-C bonds (E = C, N) may prevent catalysis from taking place.

3.   Conclusions

In this chapter, we assessed Re(I) tricarbonyl complexes with the formazanate and methylformazan ligands as catalysts for the electrochemical reduction of CO_2. It was found that both complexes convert CO_2 at the potential of the third reduction wave with CO identified as the main product, with and without a proton source present in solution. Although cyclic voltammetry experiments suggest the behavior was catalytic in nature, the low FE and TON determined by bulk electrolysis experiments failed to confirm catalytic turnover, presumably due to decomposition reactions that could take place at such negative potentials (possibly involving the solvent). This contrasts with the behavior reported for the Lehn's catalyst, in which case catalysis is observed at the potential of the double-reduced species with high FE for CO production. Since CO_2 binding to the metal center is the first requirement for substrate activation, we rationalized the lack of catalytic activity of the double reduced formazan/ate Re(I) complexes as the consequence of having a redox-active fragment that decreases metal nucleophilicity; thereby, reactivity is only observed when reduction is metal-centered, which is only the case for three-electron reduction to form a Re(0) species.

For the formazanate species, the observation of current enhancement at low overpotentials in the absence of protons suggests the redox-active fragment can be involved in substrate activation, demonstrating the versatility of redox-active ligands to serve not only as an electron reservoir but also as a center of reactivity. Labeling experiments confirmed CO_2 activation took place at low overpotentials. Perhaps the incorporation of strong electron-donating groups on the ligand scaffold or the substitution of one of the ancillary CO groups by a strong donor ligand in the structure of the catalyst might enhance the nucleophilicity of the Re center, albeit likely at the expense of a cathodic shift in redox potentials.

Although our initial interest was to replace the redox non-innocent bipyridine ligand in the structure of Lehn's catalyst by the redox-active formazanate ligand to suppress catalyst degradation pathways (*e.g.,* dimerization), our findings highlight the crucial role of the non-innocent motif in the catalysis of the electrochemical reduction of CO_2. Herein, the distinction between redox-non-innocent and redox-active character in the ligand becomes relevant for an efficient and selective electrocatalytic reduction of CO_2.

While catalysts with redox-active fragments are barely reactive at the metal center, redox-non innocent ligands allow a suitable control of metal nucleophilicity that increases their selectivity towards CO_2 reduction over protons, avoiding compromising catalytic performance.[31]

Despite redox processes where a metal-based nucleophile drives the activation step are not facilitated by complexes with redox-active ligands[32], this does not restrict the use of these motifs in other redox reactions. For instance, in radical catalysis *via* single-electron transfer from a redox-active moiety to a substrate[33] or in ligand-centered coupling reactions circumventing the use of precious metals[34,35] Overall, a better understanding of the role that the redox-active ligand plays in multielectron reactions (e.g. as electron reservoir, center of reactivity) is key for a rational catalytic design and thereby could expand the applicability of these fragments in novel chemical transformations.

4.   Acknowledgements

5.   Supplementary information
5.1   Electrochemical studies under CO_2

All measurements were recorded in 0.1 M solution of NBu_4PF_6 in dry acetonitrile at a scan rate of 50 mV/s, unless otherwise is stated. For CV, the voltammograms were recorded in a custom-made cell with a three-electrode set up using a glassy carbon (3 mm^2) working electrode, a Pt wire counter electrode and a Ag/AgCl wire pseudoreference electrode. The experiments were measured on CHI600C potentiostat. The solution was purged with a stream of N_2 prior to starting the experiments. Upon recording the voltammogram of the complex, the electrolytic solution was saturated with CO_2 for 5 min (0.28 M), then the CV was measured. In experiments with added proton source, phenol was added (0.500 g, 0.53 M) into the CO_2 saturated solution and the voltammogram collected. The electrode was polished between each measurement.

For controlled potential electrolysis (CPE), the experiments were carried in an air-tight two-port cell, where the Pt spiral counter electrode was separated from the bulk solution by a immersing the electrode in a capillary with a porous glass frit containing the supporting electrolyte solution (0.1 M of NBu_4PF_6). A glassy carbon rod (3 mm) was used as a working electrode and a Ag/AgNO₃ as a reference electrode. The cell was charged with 3 mL of supporting electrolyte solution with a 1mM concentration of the catalyst.

The solution was purged for 10 min with CO_2, then 500 μL of methane were injected as an internal standard. After electrolysis, samples from the headspace were taken and analyzed by gas chromatography. Gas quantification was carried out on a a Shimadzu GC-2014 equipped with a TCD detector and on a ShinCarbon column. The number of moles of H_2 and CO were determined in independent experiments, where helium and argon were used as carrier gas, respectively. Calibration curves were built by injecting know quantities of the respective gas (CO or H_2) into the bulk electrolysis cell and mixed with a constant amount of CH_4. Faradaic efficiencies were determined by multiplying the number of moles of CO by $2F/Q$, where 2 corresponds to the number of electrons needed for the reduction of CO_2 to CO, F stands for the Faraday constant equals to 96485 C/mol, and Q the charge passed during the bulk electrolysis experiment.

For the controlled potential electrolysis experiments at lower overpotential, another custom-made cell was used, where the cathode and the anode were separated by a porous glass frit. A reticulated vitreous carbon (Duocel 45 ppi) working electrode and a Ag/AgCl wire pseudo reference electrode were placed in the cathode chamber with 6 mL of the supporting electrolyte solution and the catalyst added in a 1mM concentration. On the anode chamber 6 mL of supporting electrolyte were added and a Pt mesh was used as a counter electrode. Both sides were purged for 5 min with N_2 and 10 min each with a stream of CO_2. Upon electrolysis 1 mL of the headspace was injected into a HP 5890 series II instrument with a TCD detector. The sample was passed through a Varian CP-PoraBOND Q (50 m x 0.53 m x 10 μm) and an Agilent Technologies HP-Molsieve (30 m x 0.53 mm x 50 μm) column. The amount of CO was determined by comparing the area against a calibration mixture of known concentrations.
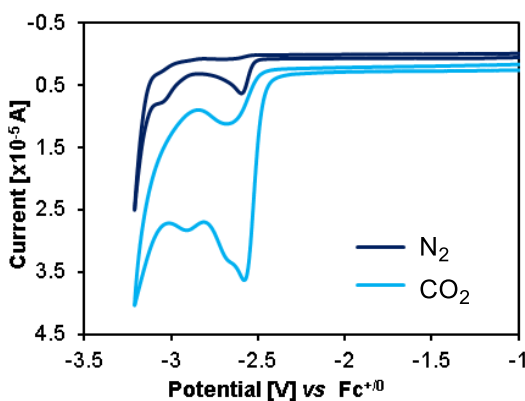
Figure S1. CV of 1 mM of [PPN]Cl in 0.1 M NBu_4PF_6 in acetonitrile under CO_2 and N_2.
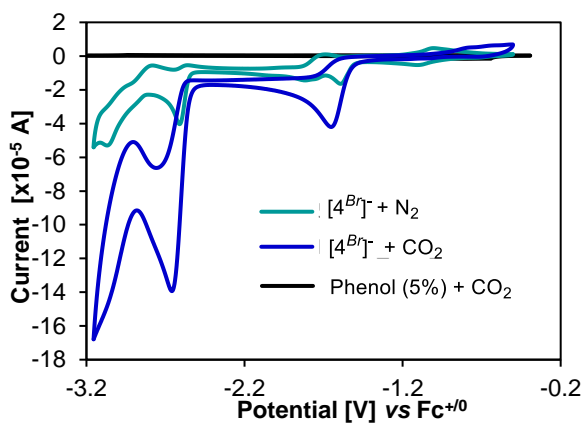
Figure S2. CV control experiment ran at 50 mV/s in acetonitrile in the absence of catalyst (black trace) no CO_2 reduction was observed within the potential window.
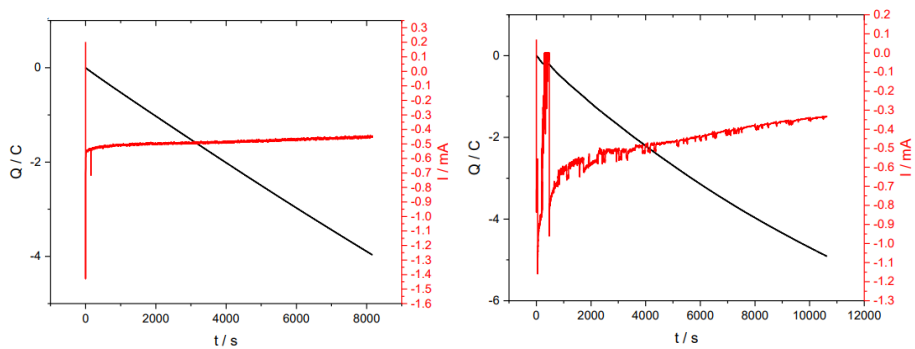
Figure S3. CPE of [PPN][4^{Br}] at -2.6 V vs Ag$^{+/0}$ under CO_2 (left) and under CO_2 + 5% phenol.
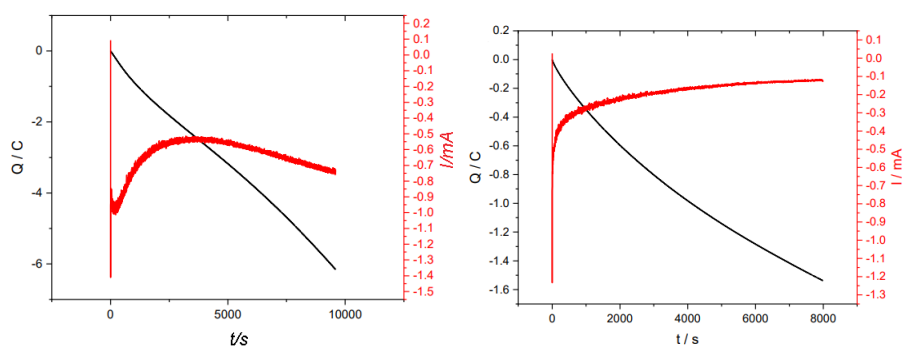
Figure S4. CPE of 4^{MeCN} -2.9 V vs Ag$^{+/0}$ under CO_2 (left) and under CO_2 + 5% phenol.
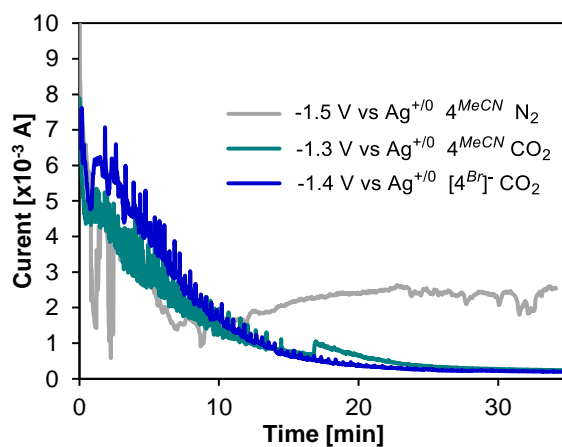
Figure S5. CPE at low overpotentials for 4^{MeCN} and [4^{Br}]$^-$ under CO$_2$ and N$_2$.
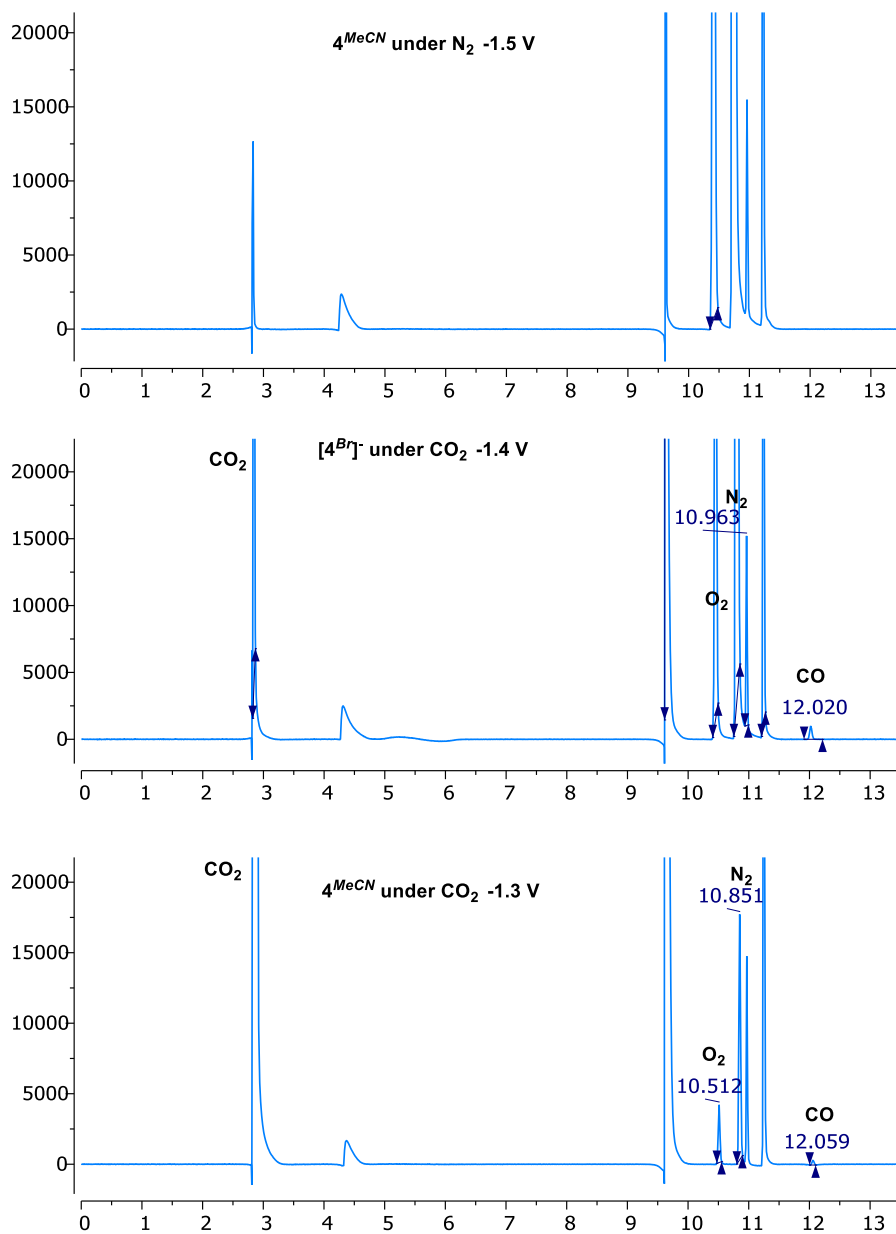
Figure S6. Chromatograms of the analysis of the headspace of electrolysis at low overpotentials. CO was only detected in samples sparged with CO_2.

5.2   Spectroelectrochemical measurements

FT-IR-SPEC experiments were performed in an OTTLE cell, that was equipped with a platinum working electrode, an Ag wire pseudoreference electrode and a platinum counter electrode and the spectra were recorded with a Bruker Vertex 70 IR spectrometer. The cell was filled with an electrolytic solution partially saturated with CO_2 containing the analyte in 1 mM concentration. The spectra were recorded every 12 s during a linear swept voltammetry.
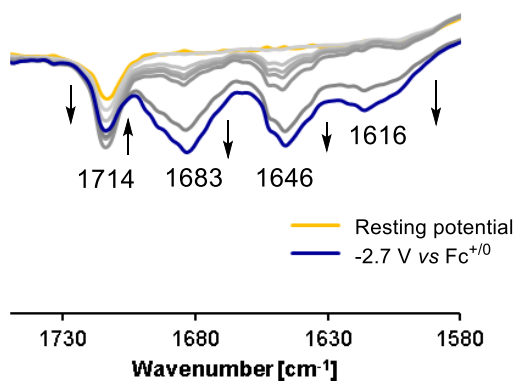
Figure S7. Evolution of the FT-IR spectra during linear swept voltammetry of 4^{MeCN} spanning the 1750-1580 cm^{-1} region.

5.3   Experiments with $^{13}CO_2$

Bulk electrolysis was conducted at -2.15 V vs $Ag^{+/0}$ (-2.4 V vs $Fc^{+/0}$) with **[4^{Br}]**⁻ in CD_3CN sparged with $^{13}CO_2$. Upon 2 h of electrolysis, a sample from the cathode was taken and analyzed by ^1H and $^{13}C\{^1H\}$ NMR. A doublet at 8.7 ppm with a coupling constant of 174 Hz (typical for C-H bonds) and a broad signal at 10.3 ppm in proton NMR were assigned to formic acid. In 13-carbon NMR, a peak at 166.7 ppm confirmed its presence. Besides the identification of carbonate (164.4 ppm), bicarbonate (160.2 ppm), and CO_2 (125 ppm), a peak at 170.4 ppm was detected (Figure S8-9).
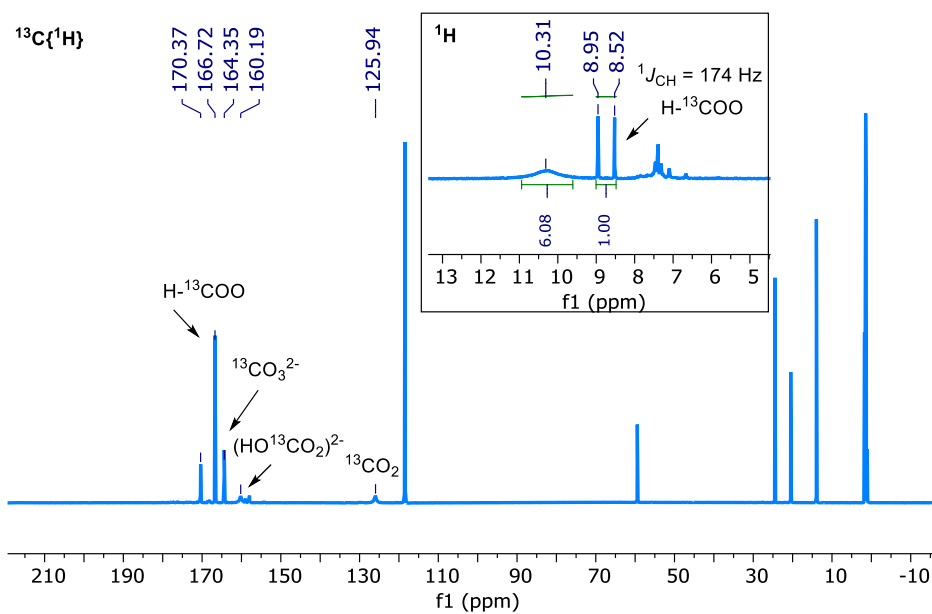
Figure S8. NMR spectra after electrolysis of [**4**^{Br}]$^-$ under 'dry' CO_2 at -2.15V *vs* Ag$^{+/0}$.
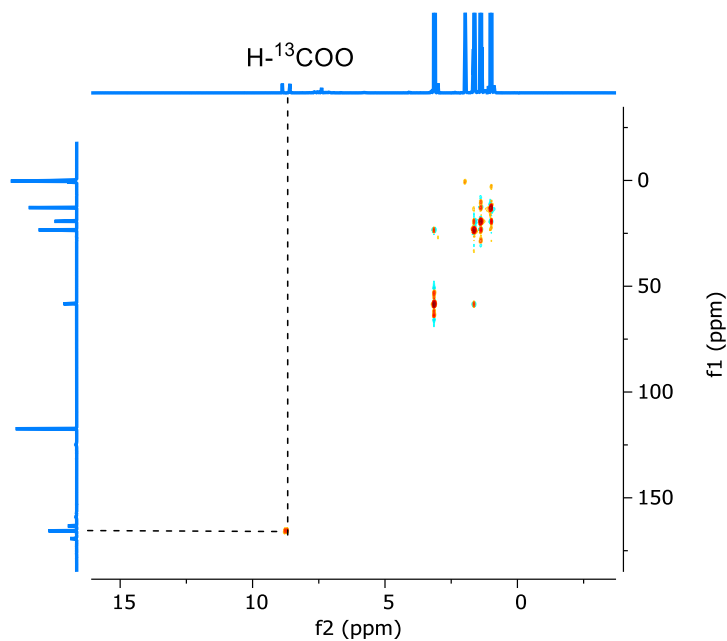
Figure S9. HSQC experiment of the cathode solution upon CPE under $^{13}CO_2$ at -2.15V *vs* Ag$^{+/0}$.

5.4   Chemical reductions

The samples were prepared inside the glovebox by adding 1.3 (6.8 mg, 0.021 mmol) or 2.3 (13 mg, 0.037 mmol) equivalents of the reducing agent Co(Cp*)$_2$ with one equivalent of the catalyst **4**^{MeCN} (10 mg, 0.016 mmol) into an NMR Young-tube. Then, 0.5 mL of CD$_3$CN previously saturated with $^{13}CO_2$ were poured into the tube. The solutions were mixed at room temperature and after 2 h the NMR recorded. Samples of the one and two-electron reductions without the substrate were also prepared in the same manner for comparison.
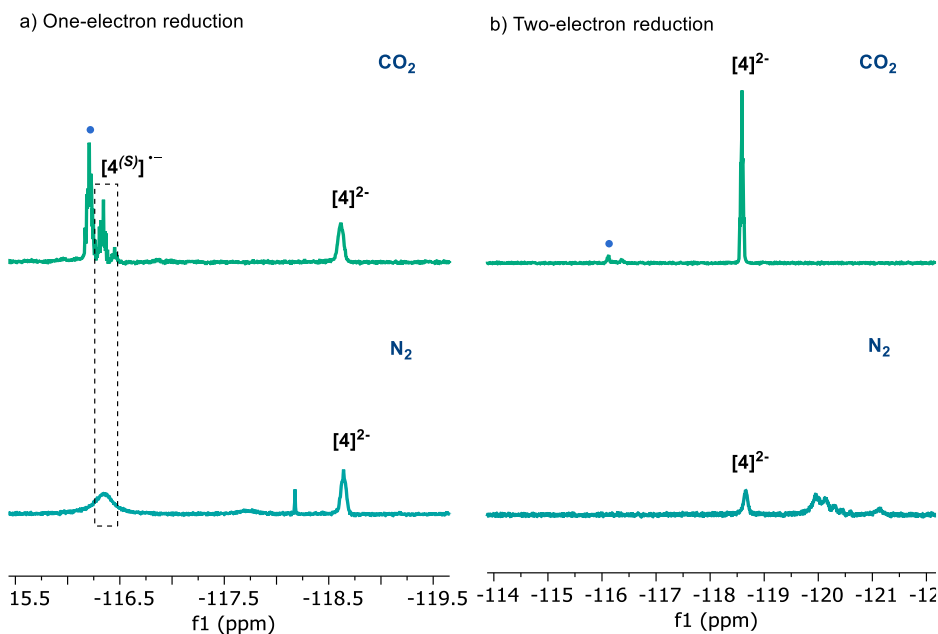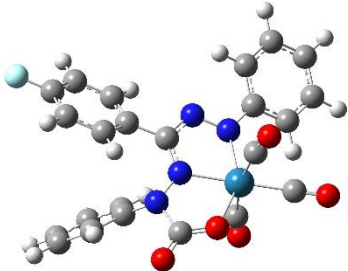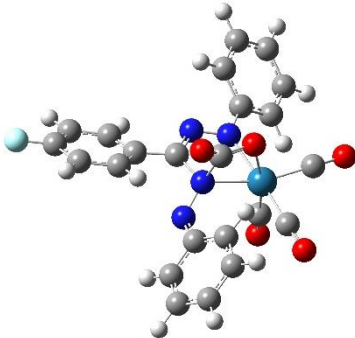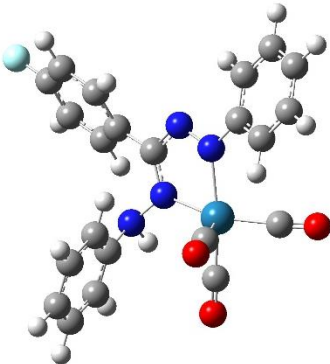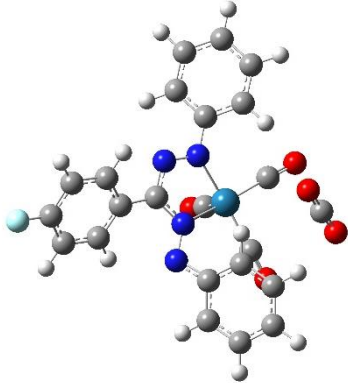
Figure S10. ^{19}F spectra of the solutions for a) one and b) two electron reduction of 4^{MeCN} with and without substrate.

5.5   Computational studies

Geometry optimizations were calculated at MN15L/ def2tsvp level of theory on the gas phase and confirmed to be a minimum on the potential energy surface (no imaginary frequencies were found). The analytical frequencies presented were scaled by a factor of 0.9578[36.]

Table S1. Optimized structures of the potential CO_2-adduct and their ν(CO) theoretical frequencies.

mer-[4^{N-CO2}]$^{\bullet-}$	*fac*-[4^{N-CO2}]$^{\bullet-}$
2000	1995
1907	1907
1879	1896
1730	1816

fac-[4^{H-CO2}]$^{\bullet-}$	*fac*-[4^{Re-CO2}]$^{\bullet-}$
2005	No interaction between the substrate
1932	and catalyst was found.
1928	
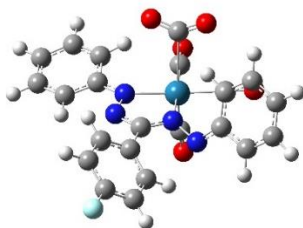
fac-[4^{Re-CO2}]$^{3•-}$
1932
1837
1803
1794
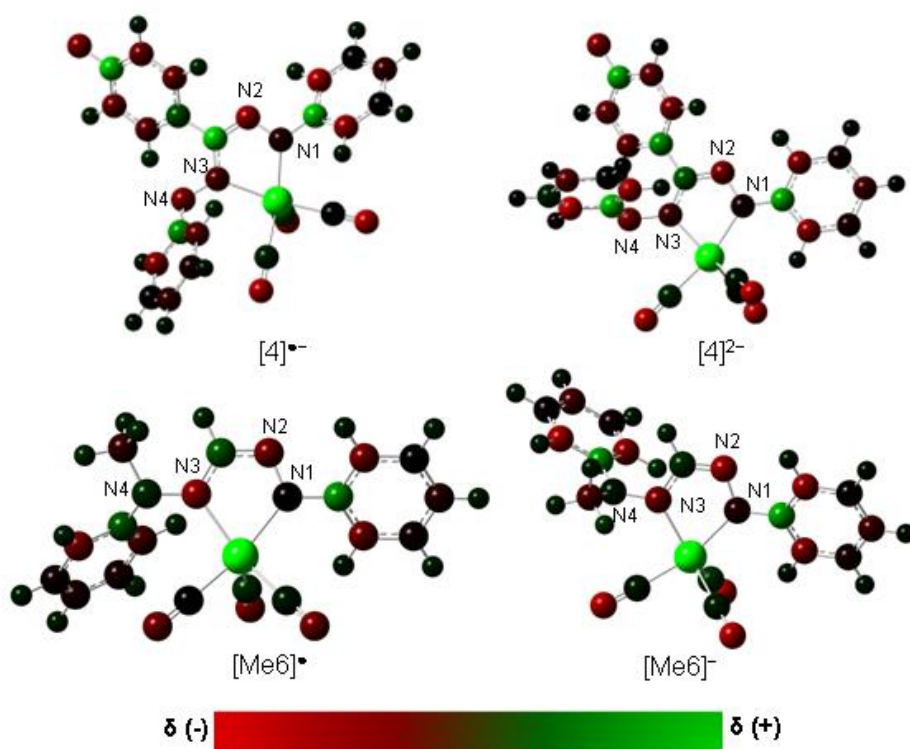
Figure S11. Mulliken charge distribution of the optimized structure of the formazanate [4]•− and [4]2- and methylformazan [Me6]• and [Me6]2- reduced species.
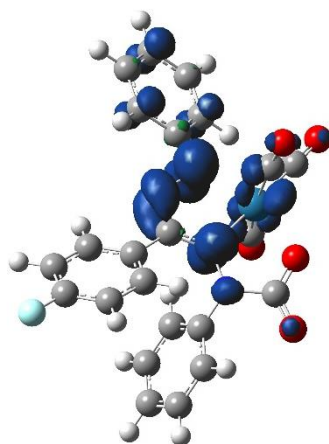
Figure S12. Spin density plot of *mer*-[4$^{N\text{-}CO2}$]$^{\bullet-}$ (isovalue = 0.003).

References

(1)   Modak, A.; Bhanja, P.; Dutta, S.; Chowdhury, B.; Bhaumik, A. Catalytic Reduction of CO_2 into Fuels and Fine Chemicals. *Green Chem.* **2020**, *22* (13), 4002–4033. https://doi.org/10.1039/d0gc01092h.

(2)   Kaiser, P.; Unde, R. B.; Kern, C.; Jess, A. Production of Liquid Hydrocarbons with CO_2 as Carbon Source Based on Reverse Water-Gas Shift and Fischer-Tropsch Synthesis. *Chemie Ingenieur Technik* **2013**, *85* (4), 489–499. https://doi.org/10.1002/cite.201200179.

(3)   Zhang, B.; Sun, L. Artificial Photosynthesis: Opportunities and Challenges of Molecular Catalysts. *Chem. Soc. Rev.* **2019**, *48* (7), 2216–2264. https://doi.org/10.1039/c8cs00897c.

(4)   Barlow, J. M.; Yang, J. Y. Thermodynamic Considerations for Optimizing Selective CO_2 Reduction by Molecular Catalysts. *ACS Cent. Sci.* **2019**, *5* (4), 580–588. https://doi.org/10.1021/acscentsci.9b00095.

(5)   Loewen, N. D.; Berben, L. A. Secondary Coordination Sphere Design to Modify Transport of Protons and CO_2. *Inorg. Chem.* **2019**, *58* (24), 16849–16857. https://doi.org/10.1021/acs.inorgchem.9b03102.

(6)   Nichols, A. W.; Machan, C. W. Secondary-Sphere Effects in Molecular Electrocatalytic CO_2 Reduction. *Front. Chem.* **2019**, *7* (397), 1–19. https://doi.org/10.3389/fchem.2019.00397.

(7)   Zee, D. Z.; Nippe, M.; King, A. E.; Chang, C. J.; Long, J. R. Tuning Second Coordination Sphere Interactions in Polypyridyl-Iron Complexes to Achieve Selective Electrocatalytic Reduction of Carbon Dioxide to Carbon Monoxide. *Inorg. Chem.* **2020**, *59* (7), 5206–5217. https://doi.org/10.1021/acs.inorgchem.0c00455.

(8)   Drover, M. W. A Guide to Secondary Coordination Sphere Editing. *Chem. Soc. Rev.* **2022**, *51* (6), 1861–1880. https://doi.org/10.1039/d2cs00022a.

(9)   Sánchez, P.; Hernández-Juárez, M.; Rendón, N.; López-Serrano, J.; Álvarez, E.; Paneque, M.; Suárez, A. Selective, Base-Free Hydrogenation of Aldehydes Catalyzed by IR Complexes Based on Proton-Responsive Lutidine-Derived CNP Ligands. *Organometallics* **2021**, *40* (9), 1314–1327. https://doi.org/10.1021/acs.organomet.1c00109.

(10)   Benson, E. E.; Sampson, M. D.; Grice, K. A.; Smieja, J. M.; Froehlich, J. D.; Friebel, D.; Keith, J. A.; Carter, E. A.; Nilsson, A.; Kubiak, C. P. The Electronic States of Rhenium Bipyridyl Electrocatalysts for CO_2 Reduction as Revealed by X-Ray Absorption Spectroscopy and Computational Quantum Chemistry. *Angew. Chem. Inter. Ed.* **2013**, *52*, 4841–4844. https://doi.org/10.1002/anie.201209911.

(11)   Mukherjee, J.; Siewert, I. Manganese and Rhenium Tricarbonyl Complexes Equipped with Proton Relays in the Electrochemical CO_2 Reduction Reaction. *Eur. J. Inorg. Chem.* **2020**, *2020* (46), 4319–4333. https://doi.org/10.1002/ejic.202000738.

(12)   Machan, C. W.; Chabolla, S. A.; Yin, J.; Gilson, M. K.; Tezcan, F. A.; Kubiak, C. P. Supramolecular Assembly Promotes the Electrocatalytic Reduction of Carbon Dioxide by Re(I) Bipyridine Catalysts at a Lower Overpotential. *J. Am. Chem. Soc.* **2014**, *136* (41), 14598–14607. https://doi.org/10.1021/ja5085282.

(13)   Myren, T. H. T.; Alherz, A.; Thurston, J. R.; Stinson, T. A.; Huntzinger, C. G.; Musgrave, C. B.; Luca, O. R. Mn-Based Molecular Catalysts for the Electrocatalytic Disproportionation of CO_2 into CO and CO_3^{2-}. *ACS Catal* **2020**, *10* (3), 1961–1968. https://doi.org/10.1021/acscatal.9b04773.

(14)   Lee, G. R.; Maher, J. M.; Cooper, N. J. Reductive Disproportionation of Carbon Dioxide by Dianionic Carbonylmetalates of the Transition Metals. *J. Am. Chem. Soc.* **1987**, *109* (10), 2956–2962. https://doi.org/10.1021/ja00244a017.

(15)   Wong, K. Y.; Chung, W. H.; Lau, C. P. The Effect of Weak Brönsted Acids on the Electrocatalytic Reduction of Carbon Dioxide by a Rhenium Tricarbonyl Bipyridyl Complex. *J. Electroanal. Chem.* **1998**, *453* (1–2), 161–170. https://doi.org/10.1016/S0022-0728(98)00116-8.

(16)   Appel, A. M.; Helm, M. L. Determining the Overpotential for a Molecular Electrocatalyst. *ACS Catal.* **2014**, *4*, 630–633.

(17)   Sampson, M. D.; Kubiak, C. P. Manganese Electrocatalysts with Bulky Bipyridine Ligands: Utilizing Lewis Acids to Promote Carbon Dioxide Reduction at Low Overpotentials. *J. Am. Chem. Soc.* **2016**, *138* (4), 1386–1393. https://doi.org/10.1021/jacs.5b12215.

(18)   Costentin, C.; Drouet, S.; Robert, M.; Savéant, J.-M. A Local Proton Source Enhances CO^2 Electroreduction to CO by a Molecular Fe Catalyst. *Science (1979)* **2012**, *338*, 90–93. https://doi.org/10.1126/science.1224581.

(19)   Clark, M. L.; Cheung, P. L.; Lessio, M.; Carter, E. A.; Kubiak, C. P. Kinetic and Mechanistic Effects of Bipyridine (Bpy) Substituent, Labile Ligand, and Brønsted Acid on Electrocatalytic CO_2 Reduction by Re(Bpy) Complexes. *ACS Catal.* **2018**, *8* (3), 2021–2029. https://doi.org/10.1021/acscatal.7b03971.

(20)   Johnson, F. P. A.; George, M. W.; Hartl, F.; Turner, J. J. Electrocatalytic Reduction of CO_2 using the Complexes [Re(Bpy)(CO)$_3$L]^n(n = +1, L = P(OEt)$_3$, CH_3CN; n = 0, L = Cl$^-$, Otf$^-$; Bpy = 2,2'-Bipyridine; Otf$^-$ = CF_3SO_3) as Catalyst Precursors: Infrared Spectroelectrochemical Investigation. *Organometallics* **1996**, *15*, 3374–3387. https://doi.org/10.1021/om960044+.

(21)   Bourrez, M.; Molton, F.; Chardon-Noblat, S.; Deronzier, A. [Mn(Bipyridyl)(CO)$_3$Br]: An Abundant Metal Carbonyl Complex as Efficient Electrocatalyst for CO_2 Reduction. *Angew. Chem., Inter. Ed.* **2011**, *50* (42), 9903–9906. https://doi.org/10.1002/anie.201103616.

(22)   Duan, L.; Manbeck, G. F.; Kowalczyk, M.; Szalda, D. J.; Muckerman, J. T.; Himeda, Y.; Fujita, E. Non-innocent Proton-Responsive Ligand Facilitates Reductive Deprotonation and Hinders CO_2 Reduction Catalysis in [Ru(Tpy)(6DHBP)(NCCH$_3$)]$^{2+}$ (6DHBP = 6,6'-(OH)$_2$bpy). *Inorg. Chem.* **2016**, *55* (9), 4582–4594. https://doi.org/10.1021/acs.inorgchem.6b00398.

(23)   Manbeck, G. F.; Muckerman, J. T.; Szalda, D. J.; Himeda, Y.; Fujita, E. Push or Pull? Proton Responsive Ligand Effects in Rhenium Tricarbonyl CO_2 Reduction Catalysts. *J. Phys. Chem. B* **2015**, *119* (24), 7457–7466. https://doi.org/10.1021/jp511131x.

(24)   Vollmer, M. V.; Machan, C. W.; Clark, M. L.; Antholine, W. E.; Agarwal, J.; Schaefer, H. F.; Kubiak, C. P.; Walensky, J. R. Synthesis, Spectroscopy, and Electrochemistry of (α-Diimine)M(CO)$_3$Br, M = Mn, Re, Complexes: Ligands Isoelectronic to Bipyridyl Show Differences in CO_2 Reduction. *Organometallics* **2015**, *34* (1), 3–12. https://doi.org/10.1021/om500838z.

(25)   Lieske, L. E.; Freeman, L. A.; Wang, G.; Dickie, D. A.; Gilliard, R. J.; Machan, C. W. Metal-Free Electrochemical Reduction of Carbon Dioxide Mediated by Cyclic(Alkyl)(Amino) Carbenes. *Chem. Eur. J.* **2019**, *25* (24), 6098–6101. https://doi.org/10.1002/chem.201900316.

(26)   Bresciani, G.; Biancalana, L.; Pampaloni, G.; Marchetti, F. Recent Advances in the Chemistry of Metal Carbamates. *Molecules*, **2020**, *25*, 3603. https://doi.org/10.3390/molecules25163603.

(27)   Jin, D.; Sun, X.; Hinz, A.; Roesky, P. W. Reversible Insertion of CO_2 into a Bis(Formazanate) Magnesium Complex. *CCS Chemistry* **2023**, 1–8. https://doi.org/10.31635/ccschem.023.202202614.

(28)   de Vries, F.; Otten, E. Reversible On/Off Switching of Lactide Cyclopolymerization with a Redox-Active Formazanate Ligand. *ACS Catal.* **2022**, *12* (7), 4125–4130. https://doi.org/10.1021/acscatal.1c05689.

(29)   Mondol, R.; Otten, E. Reactivity of Two-Electron-Reduced Boron Formazanate Compounds with Electrophiles: Facile N–H/N–C Bond Homolysis Due to the Formation of Stable Ligand Radicals. *Inorg. Chem.* **2018**, *57*, 9720–9727. https://doi.org/10.1021/acs.inorgchem.8b00079.

(30)   Sieh, D.; Lacy, D. C.; Peters, J. C.; Kubiak, C. P. Reduction of CO_2 by Pyridine Monoimine Molybdenum Carbonyl Complexes: Cooperative Metal-Ligand Binding of CO2. *Chem.Eur. J.* **2015**, *21* (23), 8497–8503. https://doi.org/10.1002/chem.201500463.

(31)   Luca, O. R.; Crabtree, R. H. Redox-Active Ligands in Catalysis. *Chem. Soc. Rev.* **2013**, *42* (4), 1440–1459. https://doi.org/10.1039/c2cs35228a.

(32)   Queyriaux, N. Redox-Active Ligands in Electro-assisted Catalytic H^+ and CO_2 Reductions: Benefits and Risks. *ACS Catal.* **2021**, 4024–4035. https://doi.org/10.1021/acscatal.1c00237.

(33)   Ivar, J.; Vlugt, V. Der. Radical-Type Reactivity and Catalysis by Single-Electron Transfer to or from Redox-Active Ligands. *Chem. Eur. J.* **2019**, 2651–2662. https://doi.org/10.1002/chem.201802606.

(34)   Smith, A. L.; Hardcastle, K. I.; Soper, J. D. Redox-Active Ligand-Mediated Oxidative Addition and Reductive Elimination at Square Planar Cobalt(III): Multielectron Reactions for Cross-Coupling. *J. Am. Chem. Soc.* **2010**, *132* (41), 14358–14360. https://doi.org/10.1021/ja106212w.

(35)   Chirik, P. J.; Wieghardt, K. Radical Ligands Confer Nobility on Base-Metal Catalysts. *Science,* **2010**, *327* (5967), 794–795. https://doi.org/10.1126/science.1183281.

(36)   Sae-Heng, P.; Tantirungrotechai, J.; Tantirungrotechai, Y. Scale Factors for Carbonyl Vibrational Frequencies: A Study of Partial Hessian Approximation. *Chiang Mai J. Sci.* **2018**, *45* (7), 2797.

Summary

Energy transition from fossil fuels to renewable sources will continue to be a priority area in the global agenda, as the energetic demand is gradually growing while fossil feedstocks are limited. With the perceptible havoc of global warming, the pursuit of carbon neutrality represents one of the major challenges of the new century. Carbon dioxide capture and utilization, therefore, signifies a viable alternative to the current energy and climate crisis. Herein, the challenge resides in transforming the inert carbon dioxide molecule into a carbon source that can be used to produce fine chemicals, either fuels or other *C*-valuable products. However, thermodynamic, and kinetic constraints impede the direct reduction of CO_2. In this case, transition metal complexes have been investigated as catalysts that can function as electron carriers by successfully delivering electrons to the substrate.

Transition metal complexes are robust catalysts that can successfully drive small molecule activation and their catalytic conversion. Indeed, their versatility relies on the metal-ligand interaction that governs complex's reactivity, making possible to tailor an *ad-hoc* metal-ligand combination for a particular process. For redox transformations, such as reducing small molecules, catalysts able to reversibly accept and deliver multiple electrons whenever needed are required. Redox-active metals can play the role of electronic reservoirs; however, its capacity sometimes is limited to one electron, leading to reaction pathways that involve unwanted radical intermediates. Herein, the presence of redox-active ligands could harness, in cooperativity with the metal center, multielectron processes and, thereby, provide new vias for substrate transformation.

In this thesis, we explored the coordination chemistry of the redox active formazan and formazanate ligands towards rhenium, and we studied in depth the metal-ligand interaction in these species by spectroscopic and computational methods. This allowed us to correlate the electronic properties of Re(I) formazan and formazanate complexes with their reactivity in the presence of CO_2. The work presented here provides new insights into the role of redox-active ligands in the activation of small molecules, and thereby could serve as guidance in the development of more efficient catalysts for CO_2 reduction.

Chapter 1 addresses the fundamental aspects of CO_2 reduction and the difficulties regarding its activation. Moreover, a general view of the electrochemical CO_2 reduction is presented, where the pioneering work on CO_2 activation and its catalytic reduction by transition metal complexes is settled down. A section is devoted to the benchmark Re(I) bipyridine catalysts and the challenges to be tackled to afford more efficient catalytic conversions. The formazanate redox-active ligand is introduced, and key examples of their electrochemical properties and the reactivity of their reduced metal complexes are described. A particular section is given to briefly present the reactivity of metal formazanate complexes towards CO_2. This section closes with the motivation of this

thesis, which aimed to establish a fundamental study on the electrochemical properties of formazan and formazanate Re(I) complexes for CO_2 reduction.

Chapter 2 describes the preparation of formazan metal-based derivatives that incorporate the protonated formazan scaffold. A series of Re(I) formazan complexes were prepared and characterized by spectroscopic and computational methods. Analysis of their electronic properties by DFT calculations revealed the high extent of covalency of the metal-ligand interaction. This work provides the first example of fully characterized protonated formazan complexes with a metal of group 7.

In *Chapter 3*, we explored the reactivity of the protonated formazan Re(I) species and successfully isolated Re(I) complexes that contain the anionic formazanate ligand via direct deprotonation of their respective conjugated acids. The new formazanate Re(I) species were fully characterized in solution and solid state, providing evidence of the stability of formazanate Re(I) towards ligand protonation in polar media. Comparison of the electronic properties of both formazan and formazanate species by DFT calculations led to conclude that the higher extent of π-delocalization in formazanate complexes decreases the degree of covalency of the metal-ligand bond. Herein, we also studied the coordination chemistry of the alkylformazan ligands and the preparation and characterization of a new alkylformazan Re(I) compound is described, aiming to block the proton-responsivity of the formazan/ate scaffold.

Chapter 4 is devoted to an extensive study of the electrochemical behavior of formazan, alkylformazan, and formazanate Re(I) complexes through (spectro)electrochemical and computational means Protonated formazan species showed to be unstable under reductive conditions, and their one-electron reduction afforded their corresponding formazanate Re(I) analogous via a reductive deprotonation mechanism. Alkylation of the proton-responsive group in alkylformazan Re(I) complexes effectively blocked this pathway. Alkylformazan and formazanate Re(I) complexes exhibit three consecutive one-electron reductions that are cathodically shifted in the formazanate derivatives due to its anionic nature. Analysis of the electronic structure of the resulting reduced species by DFT calculations indicated the first two reductions are of ligand-based nature, while the reduction at most negative potentials is of metal character. Thus, alkylformazan and formazanate ligands behave as a two-electron reservoir. Labilization of the axial ligand takes place upon one-electron reduction in alkylformazan and formazanate Re(I) species, affording a stabilized azo-type radical that does not dimerize. This observation contrasts with what was reported for the archetypical Re(I) bipyridine catalysts, in which case, dimerization of the one-electron reduced species is a known deactivation pathway.

Finally, *Chapter 5* presents the evaluation of the catalytic properties of alkylformazan and formazanate Re(I) complexes toward the electrochemical reduction of CO_2. A correlation between the electronic structure of these species and their reactivity in the electrochemical reduction of CO_2 is established. Our findings reveal that redox-active

ligands may negatively impact catalytic performance by decreasing metal nucleophilicity, thus CO_2 activation by the metal center. However, a new activation pathway was found in complexes with the formazanate ligand, wherein the ligand fixates CO_2. The nature of the putative formazanate-CO_2 adduct was studied by DFT calculations. The conclusions derived from our work provide new insights into the use of redox-active ligands in catalytic transformations.

Sammenvatting

De overgang van fossiele brandstoffen naar hernieuwbare energiebronnen heeft een hoge prioriteit op de wereldwijde agenda, aangezien de energievraag nog steeds toeneemt terwijl fossiele grondstoffen beperkt voorradig zijn. Door de opwarming van de aarde vertegenwoordigt het streven naar koolstofneutraliteit een van de belangrijkste uitdagingen van deze eeuw. Koolstofdioxideopvang en -gebruik zijn een mogelijke weg uit de huidige energie- en klimaatcrisis. Wellicht de grootste uitdaging hierbij is het omzetten van het inerte koolstofdioxide molecuul in een koolstofbron die kan worden gebruikt voor het maken van producten zoals brandstoffen of andere waardevolle, op koolstof gebaseerde chemische verbindingen. Thermodynamische en kinetische beperkingen belemmeren echter de directe reductie van CO_2. Overgangsmetaal-complexen die fungeren als elektronendragers zijn onderzocht als katalysatoren om elektronen succesvol aan het substraat (CO_2) over te kunnen dragen.

Overgangsmetaalcomplexen zijn robuuste katalysatoren die in staat zijn om kleine, simpele moleculen te 'activeren' en vervolgens succesvol om te zetten in waardevolle producten. Hun veelzijdigheid berust op metaal-ligand interacties die de reactieve eigenschappen van het complex bepalen, waardoor het mogelijk is om een op maat gemaakte metaal-ligand combinatie te creëren voor een specifieke chemische omzetting. Voor redox-transformaties, zoals de reductie van koolstofdioxide, zijn katalysatoren nodig die in staat zijn om meerdere elektronen op een reversibele manier op te nemen en weer af te staan wanneer dat nodig is. Redox-actieve metalen kunnen de rol van elektronenreservoir spelen; hun capaciteit is echter veelal beperkt tot een enkel elektron, wat leidt tot reactiepaden met ongewenste radicaal intermediaren. In dit type reacties kan de aanwezigheid van redox-actieve liganden in samenwerking met het metaalcentrum multielectron-processen in gang zetten en zo nieuwe wegen openen voor de transformatie van substraten zoals CO_2.

In dit proefschrift hebben we de coördinatiechemie van de redox-actieve formazan- en formazanaat-liganden met het metaal rhenium verkend, en we hebben de interactie tussen metaal en ligand diepgaand bestudeerd met behulp van spectroscopische en computationele methoden. Dit stelde ons in staat om de elektronische eigenschappen van Re(I) formazan- en formazanaatcomplexen te correleren met hun reactieve eigenschappen in aanwezigheid van CO_2. Het hierin beschreven werk biedt nieuwe inzichten in de rol van redox-actieve liganden bij de activering van kleine moleculen zoals CO_2, en kan dienen als leidraad bij de ontwikkeling van efficiëntere katalysatoren voor de elektrochemische omzetting van koolstofdioxide.

Hoofdstuk 1 behandelt de fundamentele aspecten van CO_2-reductie en de uitdagingen met betrekking tot de activering van dit inerte molecuul. Bovendien wordt een algemeen beeld geschetst van elektrochemische CO_2-reductie, en voorgaand werk op het gebied van CO_2-activering en katalytische reductie door

overgangsmetaalcomplexen wordt besproken. Een sectie is gewijd aan de benchmark Re(I) bipyridine katalysatoren en de uitdagingen die er nog liggen om meer efficiënte katalytische omzettingen mogelijk te maken. Het redox-actieve formazanaat-ligand wordt geïntroduceerd, en enkele relevante voorbeelden van de elektrochemische eigenschappen en reactiviteit van (gereduceerde) metaal-formazanaat complexen worden beschreven. Een specifieke sectie geeft een beknopt overzicht van de in de literatuur beschreven reacties van metaal-formazanaat complexen met CO_2. Dit hoofdstuk sluit af met de motivatie van dit proefschrift, dat tot doel had een fundamentele studie te verrichten naar de elektrochemische eigenschappen van formazan- en formazanaat Re(I)-complexen voor CO_2-reductie.

Hoofdstuk 2 beschrijft de synthese van metaal complexen met geprotoneerde formazan liganden. Een reeks Re(I) formazan-complexen werd gekarakteriseerd met spectroscopische en computationele methoden. Analyse van hun elektronische eigenschappen door DFT-berekeningen liet een hoge mate van covalentie van de metaal-ligand interactie zien. Dit werk biedt de eerste voorbeelden van formazan-complexen met een metaal uit groep 7 van het periodiek systeem, en geeft inzicht in de (elektronische) structuur en spectroscopische eigenschappen.

In hoofdstuk 3 onderzochten we de reactiviteit van de geprotoneerde formazan Re(I)-verbindingen en isoleerden we de overeenkomstige complexen met anionische formazanaat-liganden via directe deprotonering van de geconjugeerde zuren. De nieuwe formazanaat Re(I) complexen werden volledig gekarakteriseerd in oplossing en in de vaste stof, en deze studies lieten de stabiliteit van deze complexen zien ten aanzien van protonering van het ligand. Een vergelijking van de elektronische eigenschappen van zowel formazan- als formazanaat-complexen met behulp van DFT-berekeningen leidde tot de conclusie dat de hogere mate van π-delokalisatie in formazanaatcomplexen het covalente karakter van de metaal-ligandbinding vermindert. In dit hoofdstuk hebben we ook de coördinatiechemie van gealkyleerde formazan-liganden bestudeerd en de synthese/karakterisering van een nieuwe alkylformazan Re(I)-verbinding beschreven, met als doel de proton-responsiviteit van de formazan/ate-scaffold te blokkeren.

Hoofdstuk 4 is gewijd aan een uitgebreide studie van het elektrochemische gedrag van formazan-, alkylformazan- en formazanaat Re(I)-complexen door middel van (spectro)elektrochemische en computationele technieken. Geprotoneerde formazan complexen bleken instabiel te zijn onder reductieve condities, want hun één-elektron reductie leidde tot de overeenkomstige formazanaat Re(I)-analogen via een reductief deprotonatie mechanisme. Alkylering van de proton-responsieve groep in alkylformazan Re(I)-complexen blokkeerde dit reactiepad. Alkylformazan- en formazanaat Re(I)-complexen vertonen drie opeenvolgende één-elektronreducties die verschoven zijn naar meer negatieve potentialen in de formazanaat-derivaten vanwege hun negatieve lading. Analyse van de elektronische structuur van de resulterende gereduceerde producten door DFT-berekeningen gaf aan dat de eerste twee reducties

ligand-gebaseerd zijn, terwijl de reductie bij de meest negatieve potentiaal op het metaalcentrum plaatsvindt. Hiermee is aangetoond dat alkylformazan- en formazanaat-liganden zich gedragen als een twee-elektronenreservoir in dit type verbindingen. Het axiale ligand (Br) laat los na één-elektronreductie in alkylformazan- en formazanaat Re(I)-complexen, waarbij een gestabiliseerd azo-type radicaal wordt gevormd dat voorkomt dat het product verder reageert tot een dimeer. Deze observatie contrasteert met wat is beschreven voor de klassieke Re(I) bipyridine katalysatoren, waarbij dimerisatie van de één-elektron gereduceerde intermediaren een bekende deactiverings-reactie is.

Tot slot beschrijft hoofdstuk 5 de evaluatie van de katalytische eigenschappen van alkylformazan- en formazanaat Re(I)-complexen voor de elektrochemische reductie van CO_2. Er wordt een correlatie gelegd tussen de elektronische structuur van dit type complexen en hun reactiviteit in elektrochemische reductie van CO_2. Onze bevindingen laten zien dat redox-actieve liganden de katalytische prestaties negatief kunnen beïnvloeden door de nucleofiliciteit van het metaal-centrum te verminderen, waardoor de binding van CO_2 aan het metaal minder makkelijk optreedt. Daar staat tegenover dat er een nieuw activeringspad werd gevonden, waarbij het gereduceerde ligand in staat is om CO_2 te binden. De structuur van het veronderstelde formazanaat-CO_2 adduct werd bestudeerd met behulp van DFT-berekeningen. Deze studie biedt nieuwe inzichten in het gebruik van redox-actieve liganden bij katalytische processen.

Resumen

La transición energética de combustibles fósiles a fuentes renovables seguirá siendo un área prioritaria en la agenda global dado que la demanda energética crece gradualmente a expensas de materias primas fósiles limitadas. Con los estragos perceptibles del calentamiento global, la búsqueda de la neutralidad de carbono representa uno de los principales desafíos del nuevo siglo. En este sentido, la captura y utilización de dióxido de carbono se presenta como una alternativa viable para combatir la actual crisis energética y climática. El reto aquí, se encuentra en transformar la inerte molécula de dióxido de carbono en otros derivados orgánicos de mayor utilidad, ya sea combustibles u otros productos químicos de relevancia a nivel industrial. Sin embargo, limitaciones cinéticas y termodinámicas impiden que la reducción directa de CO_2 se lleve a cabo de manera eficiente. En este contexto, se ha explorado el uso de complejos de metales de transición como catalizadores en la reducción de CO_2. Dichos sistemas pueden funcionar como intermediarios en el proceso de reducción al entregar de manera eficaz los equivalentes reductores al sustrato.

Los complejos de metales de transición son catalizadores robustos que pueden promover la activación y conversión catalítica de moléculas pequeñas. Su versatilidad depende de la interacción metal-ligante, relación que gobierna la reactividad del complejo haciendo posible encontrar una combinación metal-ligante *ad-hoc* para un proceso en particular. Para transformaciones redox, tales como la reducción de moléculas pequeñas, se requieren catalizadores capaces de aceptar y ceder de manera reversible electrones cuando sea necesario. Metales activos redox puede fungir como reservorios de electrones, sin embargo, en algunos casos solo pueden transferir un electrón conduciendo a la formación de intermediarios radicalarios bastante reactivos. Es así que, la presencia de ligantes activos redox puede permitir, en cooperatividad con el centro metálico, reacciones multielectrónicas que, puedan promover nuevas vías de transformación del sustrato.

En esta tesis, exploramos la química de coordinación de los ligantes activos redox formazán y formazanato hacia renio y estudiamos a profundidad la interacción metal-ligante en los complejos resultantes por métodos computacionales y espectroscópicos. Este análisis nos permitió correlacionar las propiedades electrónicas de los complejos de formazán y formazanato de Re(I) con su reactividad en la presencia de CO_2. El trabajo presentado proporciona nuevas ideas sobre el papel de los ligantes activos redox en la activación de molécula pequeñas y, por tanto, podría servir como guía en el desarrollo de catalizadores más eficientes para la reducción de CO_2.

En el *Capítulo 1*, los aspectos fundamentos sobre la reducción de CO_2 y las dificultades derivadas de su activación son presentados. Asimismo, se desarrolló de manera general el proceso de reducción electroquímica de CO_2, donde se expusieron los trabajos pioneros sobre la activación de CO_2 y su reducción catalítica mediada por

metales de transición. Una sección se dedica a los catalizadores de Re(I) con bipiridina y los desafíos que deben abordarse para lograr conversiones catalíticas más eficientes. Finalmente, se presenta el ligante activo redox formazanato y se describen ejemplos clave de sus propiedades electroquímicas y la reactividad de sus complejos metálicos reducidos. Una sección es dedicada a describir brevemente la reactividad de complejos de formazanato hacia el CO_2. Este capítulo cierra con la motivación de esta tesis que tiene como objetivo establecer un estudio fundamental sobre las propiedades electroquímicas de complejos de formazán y formazanato de Re(I) para la reducción electroquímica de CO_2.

El *Capítulo 2* describe la preparación de complejos metálicos de formazán que incorporan el fragmento formazán protonado. Una serie de complejos de formazán de Re(I) fueron sintetizados y caracterizados mediante métodos espectroscópicos y computacionales. El análisis de sus propiedades electrónicas mediante teoría de funcionales de la densidad (TFD) reveló el alto grado de covalencia de la interacción metal-ligante. Este trabajo presenta la primera caracterización completa de complejos de formazán protonados con un metal del grupo 7.

En el *Capítulo 3*, exploramos la reactividad de los complejos protonados de formazán de Re(I) y aislamos los correspondientes complejos que contienen el ligante aniónico formazanato mediante la desprotonación directa de sus respectivos ácidos conjugados. Los nuevos complejos de formazanato de Re(I) fueron caracterizados en solución y en estado sólido, lo que evidencia la estabilidad de los formazanatos de Re(I) hacia la protonación del ligante. Una comparación de las propiedades electrónicas entre los complejos de formazán y formazanato mediante TFD permitió concluir que un mayor grado de deslocalización electrónica en las especies de formazanato disminuye la covalencia del enlace metal-ligante. También se estudió la química de coordinación de ligantes de formazán alquilados y se presenta la preparación y caracterización completa de un nuevo complejo de alquilformazán de Re(I), buscando bloquear la respuesta hacia protones del fragmento formazanato.

El *Capítulo 4* se dedica a un estudio extensivo del comportamiento electroquímica de los complejos de formazán, alquilformazán y formazanato de Re(I) mediante medios espectroelectroquímicos y computacionales. Los complejos de formazán protonado son inestables hacia la reducción y su reducción de un electrón produce las correspondientes especies de formazanato vía un mecanismo de desprotonación reductora. La alquilación del grupo NH en las especies de alquilformazán bloquea efectivamente este proceso. Los complejos de formazanato y alquilformazán de Re(I) exhiben tres reducciones consecutivas de un electrón que se encuentran desplazadas catódicamente en las especies de formazanato debido a su naturaleza aniónica. El análisis de la estructura electrónica de las especies reducidas mediante TFD indica que las primeras dos reducciones ocurren en el ligante, mientras que la reducción a potenciales más negativos posee carácter del metal. Ambas clases de ligante se comportan como un reservorio de dos electrones. A pesar de la presencia del ligante

redox, se observó la labilización del ligante axial tras la primera reducción generando un radical estable de tipo azo que no dimeriza. Esta observación contrasta con lo observado en los complejos con bipiridina, en cuyo caso, la dimerización de la especie monoreducida es un mecanismo conocido de desactivación del catalizador.

Finalmente, el *Capítulo 5* presenta la evaluación de las propiedades catalíticas de los complejos de formazán y formazanato de Re(I) hacia la reducción electroquímica de CO_2. Se estableció una correlación entre la estructura electrónica de estas especies y su reactividad en la reducción electroquímica de CO_2. Nuestros hallazgos revelan que los ligantes activos redox pueden impactar de forma negativa el desempeño catalítico debido a la disminución en las propiedades nucleofílicas del metal y por tanto en el proceso de activación del sustrato por el centro metálico. Sin embargo, encontramos un nuevo mecanismo de activación en los complejos con el ligante formazanato, donde el ligante fija CO_2. La naturaleza del supuesto aducto de formazanato con CO_2 se estudió mediante TFD. Las conclusiones derivadas de este proyecto proporcionan nuevos conocimientos sobre el uso de ligantes activos redox en transformaciones catalíticas.

Conferences

September, 2023	**6th EuChemS Inorganic Chemistry Conference, Vienna Austria**
	Poster: *Reductive chemistry of (alkyl)formazan(CO)$_3$Re(I) complexes: an (spectro)electrochemical study*
June, 2023	**Reunión Bienal de la Sociedad Española de Química, Zaragoza, Spain.**
	Oral communication: *Formazan/ate Re(I) complexes as electrocatalyst for CO$_2$ reduction*
November, 2022	**LatinXChem, Virtual Conference**
	Poster: *Re(I) carbonyl complexes bearing the formazan/ate ligand: synthesis and characterization*
October, 2022	**Conference for Climate Change, Mérida, México**
	Invited Lecturer**:** *CO$_2$ capture and activation: transforming greenhouse gases into useful molecules*
September, 2022	**Chemistry As Innovative Science, CHAINS, Veldhoven, The Netherlands**
	Oral communication: *CO$_2$ reduction mediated by rhenium carbonyl formazan/ate complexes*
August, 2022	**International Coordination Chemistry Conference, Rimini, Italy**
	Oral communication: *Electrochemical studies on CO$_2$ reduction mediated by rhenium carbonyl formazan/ate complexes*
May, 2022	**The Netherlands, Catalysis and Chemistry, Conference, NCCC, Noordwijkerhout, The Netherlands**
	Poster: *Five-membered formazan/ate Re(I) tricarbonyl complexes: synthesis, characterization, and electrochemical studies.*
December, 2021	**Chemistry As Innovative Science, CHAINS, Virtual Conference, The Netherlands**
	Poster: *Rhenium carbonyl complexes bearing the formazan ligand.*
December, 2020	**Simposio Virtual del Instituto de Química, México.**
	Short Communication: Síntesis de complejos carbonílicos de Re(I) con ligantes de tipo formazán.

Neutral Formazan Ligands Bound to the *fac*-(CO)₃Re(I) Fragment: Structural, Spectroscopic, and Computational Studies

Liliana Capulín Flores, Lucas A. Paul, Inke Siewert, Remco Havenith, Noé Zúñiga-Villarreal,* and Edwin Otten*

Read Online

ACCESS | Metrics & More | Article Recommendations | Supporting Information

ABSTRACT: Metal complexes with ligands that coordinate via the nitrogen atom of azo (N═N) or imino (C═N) groups are of interest due to their π-acceptor properties and redox-active nature, which leads to interesting (opto)electronic properties and reactivity. Here, we describe the synthesis and characterization of rhenium(I) tricarbonyl complexes with neutral *N,N*-bidentate formazans, which possess both N═N and C═N fragments within the ligand backbone (Ar¹-NH-N═C(R³)-N═N-Ar⁵). The compounds were synthesized by reacting equimolar amounts of $[ReBr(CO)_5]$ and the corresponding neutral formazan. X-ray crystallographic and spectroscopic (IR, NMR) characterization confirmed the generation of formazan-type species with the structure *fac*-$[ReBr(CO)_3(\kappa^2\text{-}N^2,N^4(Ar^1\text{-}N^1H\text{-}N^2═C(R^3)\text{-}N^3═N^4\text{-}Ar^5))]$. The formazan ligand coordinates the metal center in the '*open*' form, generating a five-membered chelate ring with a pendant NH arm. The electronic absorption and emission properties of these complexes are governed by the presence of low-lying π^*-orbitals on the ligand as shown by DFT calculations. The high orbital mixing between the metal and ligand results in photophysical properties that contrast to those observed in *fac*-$[ReBr(CO)_3(L,L)]$ species with α-diimine ligands.
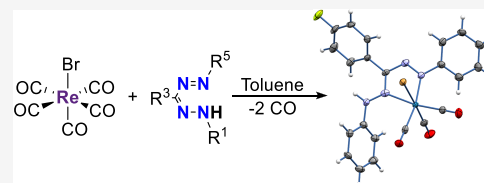
INTRODUCTION

Formazans are a large family of compounds containing the R¹-NH-N═C(R³)-N═N-R⁵ backbone, known for their use as analytical reagents for metal detection[1] and as cellular[2] and textile dyes.[3] These applications are the consequence of its well-defined redox chemistry[4] and its ability to chelate metal centers in its deprotonated form, i.e., the delocalized formazanate anion $(R^1\text{-}N═N\text{-}C(R^3)═N\text{-}N\text{-}R^5)^-$. Although formazanate coordination chemistry was first described in 1941,[5] it was not until the last decade that its study has reemerged due to its electrochemical and optical properties.[6] A wide variety of formazanate complexes with both main group and transition metal elements have been reported, wherein the (anionic) ligand usually coordinates through the terminal donor sites to form 6-membered chelates.[7] In addition to taking advantage of the unique optoelectronic properties imparted by formazanate ligands, recent reports show that their redox-active nature can also be used to obtain new catalytic reactivity.[8] In contrast to complexes with anionic formazanates, reports on coordination of the neutral formazan fragment remain scarce to date. In 2015, our group described the first example of a formazan-type complex,[9] in which the neutral ligand binds $Zn(C_6F_5)_2$ through one terminal and one internal nitrogen atoms yielding a five-membered chelate (Scheme 1), also described as the '*open*' coordination mode. It was hypothesized that the poor basicity of the Zn-C₆F₅ group in the precursor allowed the isolation of the Zn-formazan compound, as the more basic reagent ZnMe₂ does result in rapid deprotonation of the formazan NH group.[9]

Metal complexes with ligands containing the NH functionality have gained importance in catalysis since the NH arm can serve as an anchor for substrate recognition, thus enhancing catalyst selective and activity.[10] A proton source located at the proximity of the metal center has been widely investigated in the proton-coupled electron transfer reduction of small molecules relevant in energy conversion reactions such as hydrogen evolution[11,12] and CO₂ reduction.[13−15] It was proposed to modulate the redox properties, aid in the stabilization of intermediates, or impact the kinetics due to the increased local proton concentration. Furthermore, deprotonation of the NH group is known to modify the electronic and geometric structure of such complexes.[16−18]

Scheme 1. Synthesis of Zn Formazan Species

Chart 1. Representative Examples of Re Complexes Bearing an XH Functionality

Fujita, E. & Manbeck, G.F.
J. Phys. Chem. B. 2015.

Warren, J. J. *Inorg. Chim. Acta* 2017.

Nippe, M. *J. Am. Chem. Soc.* 2017.

Siewert, *Chem. Eur. J.* 2019.

Marinescu, D. *Dalton. Trans.* 2019.

Nervi, C. & Manbeck, G.F.
Inorg. Chem. 2020.

Scheme 2. Synthesis of Formazan Ligands

L1H $R^1 = R^3 = R^5 = Ph$
L2H $R^1 = R^5 = Ph$; $R^3 = p$-tol
L3H $R^1 = R^5 = Ph$; $R^3 = p$-MeOPh
L4H $R^1 = R^5 = Ph$; $R^3 = p$-FPh
L5H $R^1 = Ph$; $R^3 = p$-tol; $R^5 = Mes$

Scheme 3. General Synthesis of Compounds (a) 1−4 and (b) the Mixture of Isomers 5a and 5b

a) Toluene, 110°C, 1 h, −2 CO

1 ($R^3 = Ph$) 28%
2 ($R^3 = p$-MeC$_6$H$_4$) 46%
3 ($R^3 = p$-OMeC$_6$H$_4$) 67%
4 ($R^3 = p$-FC$_6$H$_4$) 61%

L1H - L5H

b) Toluene, 110°C, 2.5 h, −2 CO, 62%

5a   5b

Extensive research has focused on the properties and potential applications of *fac*-[L,LReX(CO)$_3$] (L = α-diimine) compounds in medicinal inorganic chemistry,[19,20] material science,[21,22] and catalysis.[23,24] Particularly, these compounds have shown to be good candidates for electrochemical CO$_2$ reduction, in which a proton source is required either for enhancing or triggering the catalytic process.[25,26] Mainly, Re-based bipyridine systems have been reported as catalysts for CO$_2$ electroreduction, wherein the presence of XH (X = O, N, C)[18,27,28] functionalizations boosts the catalytic effect or induces other reactivity patterns (Chart 1).[29−31] Key to the catalytic conversion of CO$_2$ to CO by the well-studied bipyridine Re and Mn complexes is the involvement of the supporting ('redox-active') ligand in the reduction chemistry.[28,32−34] We hypothesize that replacing the bipyridine ligand (an aromatic α-diimine) for a redox-active formazan ligand (formally an amino-substituted α-azoimine) could provide an avenue to influence the potential at which reduction of the catalyst occurs.[35,36] In addition, such ligands provide access to

flexible coordination modes (hemilability)[37] due to the presence of four nitrogen atoms in the backbone, as well as proton-responsivity via the NH moiety that is in close proximity to the metal center, features that are key to the activity/selectivity of metalloenzymes but challenging to emulate in synthetic catalysts.[38]

Herein, we report synthesis of a series of *fac*-Re-(CO)$_3$(formazan) complexes and investigate their (electronic) structures and photophysical properties.

■ RESULTS AND DISCUSSION

Ligand Synthesis. Formazan ligands **L1H−L4H** were synthesized according to the procedure reported by Hicks and coworkers, via aldehyde condensation with phenylhydrazine followed by a coupling reaction with phenyldiazonium chloride in a biphasic reaction medium (CH$_2$Cl$_2$/water) under mild basic conditions.[4] Similarly, **L5H** was prepared using the methodology previously described by our group, in which the coupling step is carried out in acetone/water with NaOH as

base (Scheme 2).[9] In all cases, the compounds were obtained in moderate yields after purification (27−54%).

Complex Synthesis. Equimolar amounts of $[ReBr(CO)_5]$ and the corresponding formazan, **L1H−L4H**, reacted in refluxing toluene for 1 h to afford complexes **1−4** in moderate to good yields (28−67%) (Scheme 3a). In all cases, complete conversion of the starting material was confirmed by ^{1}H NMR and infrared spectroscopy. The compounds are air-stable solids with dark red color and are soluble in low to medium polarity solvents. Complexes **2−4** were isolated as pure materials by either recrystallization or rinsing with pentane. A minor impurity was invariably present (^{1}H NMR spectroscopy) in the isolated material of **1**. Attempts to further purify the material by crystallization were unsuccessful. The reaction of the asymmetric formazan **L5H** with $[ReBr(CO)_5]$ in refluxing toluene gave a mixture of two complexes (**5a** and **5b**) based on ^{1}H NMR spectroscopy (Scheme 3b), which differ in the substituent at the NH position (Mes or Ph). Unsurprisingly, complexes **5a/b** present similar physical properties—dark red solids soluble in low polarity solvents—that we were unable to separate, and solution characterization data are reported below for the mixture.

FT-IR Spectroscopy. The infrared spectra of complexes **1−4** and the mixture **5a/b** feature the characteristic pattern for *fac*-tricarbonyl species: three intense bands in the $\nu(CO)$ carbonyl region arising from the IR-active 3A normal vibration modes for complexes with a C_1 symmetry (Figure 1). The CO
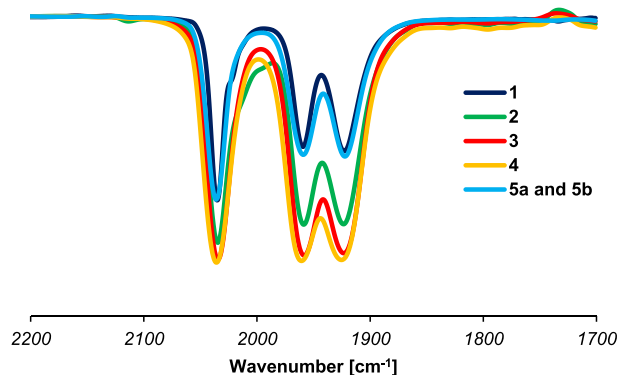
Figure 1. CO stretching bands ($\nu(CO)$) in the FT-IR spectra of complexes **1−4** and the mixture **5a** and **5b** in CH_2Cl_2 solution at rt.

stretching frequencies for compound **1** are observed at 2035, 1959, and 1923 cm^{-1} in CH_2Cl_2 solution. The effect of the *para*-substituent on the aromatic ring (R^3) is minimal, and compounds **2−5** show virtually identical IR spectra.

NMR Studies. ^{1}H NMR spectra of **1−4** show a singlet ca. 8.5 ppm assigned to the hydrazo proton, consistent with the presence of a neutral formazan ligand (see Figure S1a−S4a). In agreement with the presence of an asymmetric, protonated formazan ligand, the ^{13}C NMR spectrum shows three distinct carbonyl resonances between 185 and 192 ppm indicative of C_1 symmetry for these Re complexes. In ^{13}C NMR spectroscopy, the N-Ph *ipso*-carbon atoms attached to the formazan backbone display distinctive chemical shifts. Unequivocal assignment of these was possible based on an HSQC experiment where coupling between the hydrazo NH group and one of the Ph *ipso*-C resonances was observed. The resonance of the *ipso*-C bound to the azo group appears at 157

ppm, which is downfield from both the *ipso*-C linked to the NH function located ca. 141 ppm, and the *ipso*-C of the C-Ar group (120−125 ppm). Similarly, the N-Ph groups are inequivalent in the ^{1}H NMR spectrum also at elevated temperature (80 °C in toluene-d_8), suggesting that chemical exchange by proton transfer between the azo (C-N=N-Ph) and hydrazo (C=N-NH-Ph) fragments does not readily occur. This was further corroborated by the absence of exchange crosspeaks in the 2D EXSY spectrum (80 °C, mixing time of 0.5 s, Figure S7).

^{1}H NMR analysis of the reaction mixture of complexes **5a/b** indicates the generation of two main products in ratio of 0.7:1.0 with both compounds exhibiting the characteristic NH proton signal of the neutral formazan ligand at 8.15 and 7.60 ppm, respectively (Figure 2a). Minor signals for another species were observed (<5%) but not investigated further. For the two major products, the observation of eight unique resonances in the aliphatic region of the ^{1}H and ^{13}C NMR spectra indicates that all CH_3 groups are inequivalent: each of the two products features four signals due to the CH_3 substituents at the *p*-tolyl (1) and mesityl (3) rings. Thus, at room temperature, the rotation around the N-Mes bond is slow on the NMR timescale. In the most downfield part of the $^{13}C\{^1H\}$ NMR spectrum, i.e., between 180 and 200 ppm, there are six resonances that can be attributed to carbonyl ligands, which corroborates that both **5a** and **5b** are tricarbonyl rhenium complexes (Figure S6). Based on the spectroscopic data, we assign **5a** and **5b** as two different isomers with the composition $[(L5H)Re(CO)_3Br]$, which differ in the nature of the 'pendant' (non-coordinating) N-Ar group of the formazan (see Scheme 3b). Heating an NMR tube containing the mixture of complexes **5a/b** to 80 °C inside the NMR spectrometer did not significantly change their molar ratio. Inspection of 2D NMR experiments allowed the assignment of ^{1}H and ^{13}C spectra (see Figure S6). Identification of the *m*-CH (Mes) and the *m*- and *o*-CH (*p*-tolyl) protons allowed establishing of the connectivity in both of the isomeric compounds present in solution. The $^1H,^{13}C$ correlations in the HMBC spectrum between the NH fragment and the carbon atoms that are two and three bonds away indicate that in the major isomer (**5b**), the NH group is bound to a mesityl group, whereas in **5a** it is connected to a phenyl group. The greater shielding effect of mesityl compared to the phenyl group causes the NH proton of the former to appear at higher field (δ 7.61 ppm in **5b** and 8.22 ppm in **5a**).

To investigate the dynamics of isomers **5a/b** in solution, we collected a ^{1}H EXSY NMR spectrum at 80 °C in toluene-d_8 (Figure 2b). Crosspeaks are observed between the Mes *ortho*-CH_3 groups within each isomer due to rotation around the N-Mes bond but not between isomers **5a** and **5b**. Whereas free formazans undergo intramolecular proton exchange rapidly ('tautomerization'),[39,40] the lack of exchange between **5a/b** indicates that the Re−N bonds are non-labile and coordination to the Re center effectively blocks exchange. This is in agreement with the data for the symmetrical derivative **4**, which also does not show exchange between the azo and hydrazo fragments (*vide supra*). It should be noted however that the EXSY spectrum does evidence exchange between the NH groups in **5a/b**, which we believe to occur by an intermolecular pathway instead. This is further corroborated by the observation of exchange crosspeaks between the NH protons in **5a/b** and residual H_2O when the NMR solvent is not fully anhydrous (Figure S8).
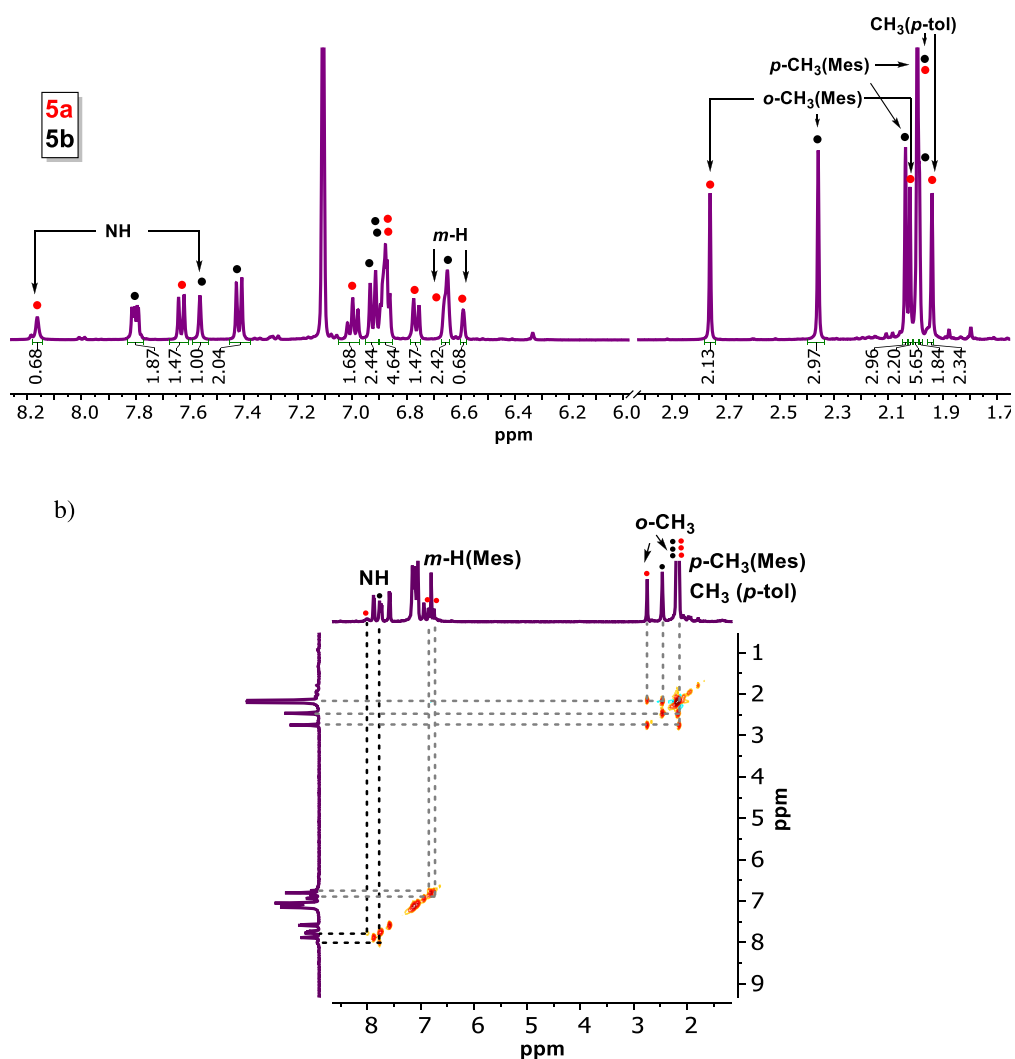
Figure 2. (a) ^{1}H NMR spectrum of the mixture **5a** and **5b** at room temperature in benzene-d_6. (b) EXSY experiment at 80 °C in toluene-d_8.
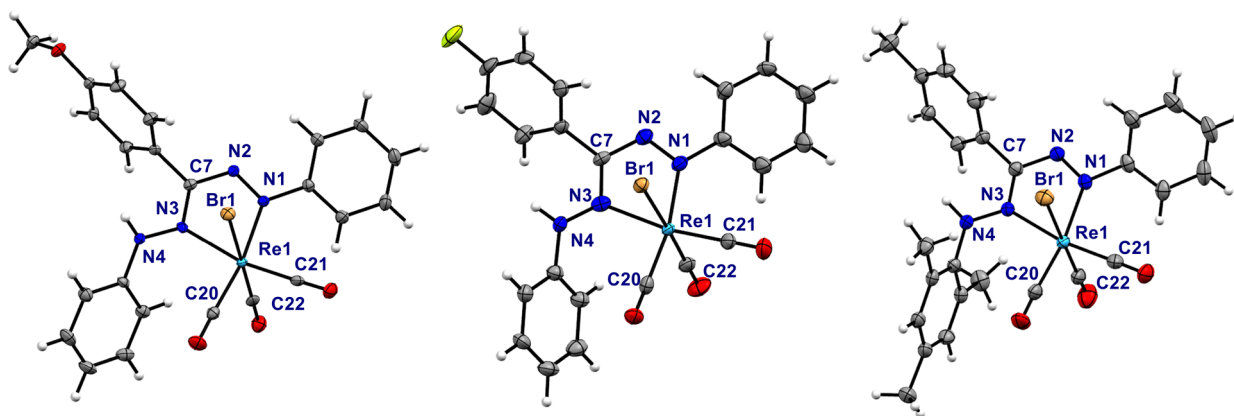
Figure 3. Molecular structures of **3** (left), **4** (middle), and **5b** (right) showing 50% of ellipsoids.

Additional experiments were conducted to determine whether intermolecular proton interchange processes also place in the complexes containing a symmetric formazan ligand. Partial H/D exchange of the NH proton in complex **4** was achieved by mixing a CDCl$_3$ solution of the aforementioned complex with D$_2$O. ^{1}H NMR analysis of the resulting mixture indicated that it was composed of 60% **4D** (deuterated product) and 40% the non-deuterated species **4**. The

remaining D$_2$O was subsequently removed by stirring over MgSO$_4$, the **4/4D** mixture was isolated and then reacted with an equivalent of **2** in C$_6$D$_6$. Monitoring the composition by ^{1}H NMR spectroscopy showed that the intensity of the NH resonance of **4** increased (to 72%) in the course of 30 min with a concomitant decrease of that in **2**, confirming that intermolecular proton exchange is taking place (see Figure S9).

Structural Studies. Crystals suitable for single-crystal X-ray diffraction were obtained from slow diffusion of pentane into a CHCl$_3$ solution of compounds **3** and **4**, respectively. The mixture of **5a/b** did not crystallize using the same method, but we were able to obtain a microcrystalline sample from hot hexane that contained some small needles that were suitable for X-ray crystallographic characterization. This was identified as isomer **5b**, in which the sterically most demanding Mes group is situated at the non-coordinated N atom of the ligand; the solid-state structure observed for this material is consistent with the major species in solution by NMR spectroscopy. Analysis of the molecular structures of **3**, **4**, and **5b** shows that the three compounds are isostructural (see Figure 3 and Table 1 for pertinent bond lengths and angles). The geometry

Table 1. Selected Metrical Parameters for 3, 4, and 5b (Bond Lengths in Å, Angles in °)

	3	4	5b
Re1−Br1	2.5977(3)	2.6236(7)	2.5946(6)
Re1−N1	2.126(2)	2.099(6)	2.122(3)
Re1−N3	2.173(3)	2.185(5)	2.174(4)
Re1−C20	1.955(3)	1.955(6)	1.957(5)
Re1−C21	1.921(3)	1.919(5)	1.916(6)
Re1−C22	1.941(2)	1.918(6)	1.964(4)
N1−N2	1.298(3)	1.291(7)	1.293(5)
C7−N2	1.363(4)	1.382(7)	1.364(8)
C7−N3	1.330(4)	1.319(8)	1.326(5)
N3−N4	1.343(4)	1.324(8)	1.343(7)
Br1−Re1−C22	178.02(9)	176.8(2)	178.6(2)
N1−Re1−C20	170.3(1)	168.7(2)	170.2(2)
N3−Re1−C21	166.5(1)	169.7(2)	170.3(2)
N1−Re1−N3	73.04(9)	73.0(2)	72.9(1)

around the metal center is pseudo-octahedral with the carbonyl ligands in a facial arrangement. The formazan fragment coordinates in a bidentate fashion through atoms N1 and N3, generating a five-membered chelate. Coordination of the neutral formazan is scarce, only observed in the complex [**L2H**]Zn(C$_6$F$_5$)$_2$ previously reported by our group.[9] The formazan bite angles are virtually identical in the three complexes (**3** = 73.04(9)°, **4** = 73.0(2)°, **5b** = 72.9(1)°) and somewhat smaller than the bite angle reported for the [**L2H**]Zn(C$_6$F$_5$)$_2$ complex (74.23(13)°). The C7−N2 and C7−N3 bond lengths are different from each other, the magnitude of the C7−N3 bond lies in between the typical values for C−N single and double bonds (−C(sp^2)−N− = 1.355 Å; −C(sp^2)=N− = 1.279 Å), while the C7−N2 bond length indicates a single bond character. The N1−N2 bond length is longer than a N=N double bond (−N=N− = 1.240 Å) and smaller than a N−N single bond (−N−N− = 1.425 Å).[41] The metallacycle is not fully planar as the Re atom is displaced out of the ligand plane (N1−N2−C7−N3) by 0.213−0.393 Å. The dihedral angle between the ligand plane and a phenyl group in the R^1 position is similar in complexes **3** (50.67°) and **4** (51.12°). Changing the R^1 substituent for the bulkier mesityl group (**5b**) causes a rotation out of the ligand plane by almost 30° resulting in a dihedral angle of 79.52° that prevents steric interactions between the Mes substituent and the equatorial CO ligand. The structure indicates that rotation around the N-Mes bond cannot occur freely due to these steric interactions, which is in agreement with the solution NMR data discussed above. The Re1−N1 bond length to the azo

moiety is virtually the same in the three complexes (2.099−2.126 Å) but it is shorter than the Re−N(azo) bond length reported for the related [ReBr(CO)$_3$(azopyridine)][42] complex (2.156(3) Å). The Re1−N3 bond lengths are in accordance with the typical Re−N(imine) bond distances (2.173−2.185 Å in compounds **3−5** *vs* 2.173(3) Å in [ReBr(CO)$_3$(6-methoxipyridine-2-yl)-*N*-(2-methylthiophenyl)methanimine)], respectively).[43] The unusually short Re−N1(azo) bond length reflects that π-backdonation from the Re center to the azo group is more pronounced in the formazan species than in azopyridine complexes.[44] The π-acceptor capabilities of the azo ligand are also reflected in the Re−carbonyl bond lengths. The Re−C20 bond length, *trans* to the azo group, is longer than the Re−C21 bond length. This is consistent with the considerable π-acidity of the azo group,[45,46] which appears to be more significant in our formazan complexes than in the corresponding azopyridine analogues.[42]

UV−vis Spectroscopy. The electronic spectra of complexes **1−4** and the mixture of complexes **5a/5b** were measured at 25 °C in toluene ($c \approx 10^{-5}$ M), Figure 4. Their
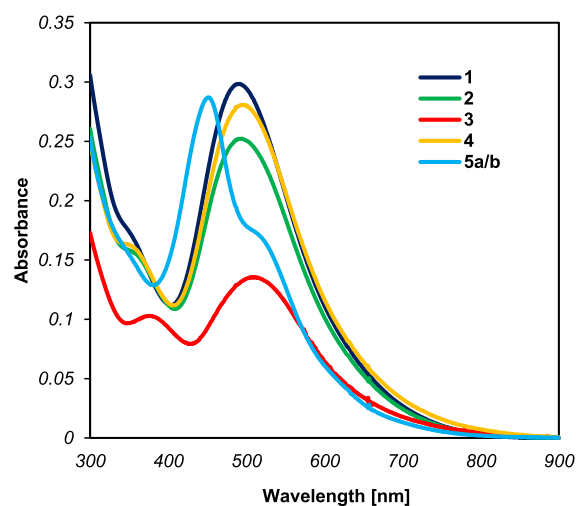
Figure 4. Absorption spectra for compounds **1−4** and **5a/b** in toluene solution.

Table 2. UV−vis Absorption Data

compound	λ_{max} (nm)	ε (M^{-1}·cm^{-1})	λ_{max} (nm)	ε (M^{-1}·cm^{-1})
1	356	16,500	490	18,100
2	353	15,300	485	19,400
3	375	10,500	509	14,100
4	353	15,300	495	27,000
5a/b			452	
			~520^a	

^{a}Approximate band position due to its appearance as a shoulder on the more intense absorption of the other isomer.

corresponding data are summarized in Table 2. Compounds **1−4** show similar features: an intense band in the range of 490−510 nm with maximum molar absorptivities from 18,000 to 28,000 M^{-1} cm^{-1}. DFT calculations and comparison to literature data allows us to assign this band to electronic excitations that are Re(d$_\pi$) → azo(π*)[42] MLCT and formazan π → π* in nature.[9] A band of lower intensity in the range of

330−400 nm (ε =15,000−16,500 M^{-1} cm^{-1}) is observed in all compounds. While bands at similar energies are typically assigned to metal-to-ligand charge transfer in related compounds,[47,48] time-dependent DFT calculations for **4** instead indicate little involvement of the Re d-orbitals in this transition (*vide infra*). Overall, the λ_{max} values of **1**, **2**, and **4** do not differ significantly, suggesting that the substituent at the *para*-position of the N-Ar rings has little influence on the energy of the electronic transitions, which is in line with the notion that the acceptor orbital in these transitions is a formazan π^*-orbital that is relatively insensitive to the *para*-substituent. In the case of complex **3**, λ_{max} is slightly red-shifted (509 nm) compared to complex **1** (490 nm), indicating that the involvement of the π-donating OMe group on the conjugated system is noticeable. When the spectrum of **4** was recorded in acetonitrile, a modest hypsochromic shift was observed (λ_{max}^{AcCN} = 483 nm (Figure 6a); $\lambda_{max}^{Toluene}$ = 495 nm), showing that these species manifest a small, negative solvatochromism. Comparing λ_{max} values to those reported for complexes with anionic formazanate ligands,[9,49,50] the absorption maxima in **1**−**4** are blue-shifted due to a smaller extent of π-conjugation within the backbone of the neutral ligands compared to the fully delocalized anions. The mixture of complexes **5a/b** features two intense bands at 520 and 452 nm derived from the MLCT and $\pi-\pi^*$ formazan electronic transitions and a shoulder at 350 nm. Overall, the influence of the substituents on the lowest energy band is more pronounced when they are located at the N=N and NH formazan positions, similar to what was observed in complexes with anionic formazanate ligands.[6] Clearly, the nature of electronic absorptions for the two isomers **5a/b** is quite distinctive, as is manifested by the significant shift in λ_{max}.

Density Functional Theory (DFT) Calculations. For representative complexes **4** and **5a/b**, geometry optimizations were carried out in the ground state using density functional theory (DFT; MN15L[51] functional and def2-TZVP[52] basis set) using the crystallographic coordinates as a starting point. The geometries were confirmed to be minima on the potential energy surface by frequency calculations (no imaginary frequencies); the resulting structures are in good agreement with the metrical parameters obtained from X-ray diffraction (complexes **4** and **5b**), albeit that the Re−Br and hydrazo N−N bonds are slightly overestimated (Tables S2 and S3). Analysis of the frontier orbitals at the optimized geometry of **4** showed that the HOMO is mainly localized on the [ReBr(CO)$_3$] core and is composed of a Re d_π orbital that is antibonding with a bromine p orbital and π-bonding with the CO ligand located *trans* to Br. The HOMO level also contains some ligand character (the hydrazo-phenyl fragment). On the other hand, the LUMO is primarily a π^*-orbital of the formazan framework, with a minor Re $5d$ character (Figure S10).

The optimized structures of **5a** and **5b** are overall similar, but the variation in the position of the Mes group (on the *azo* or *hydrazo* N-atom, respectively) leads to somewhat different frontier orbitals. While those of **5b** are similar to **4**, the HOMO of **5a** has noticeably smaller formazan contribution (Figures S12 and S14). The relative stability between the isomeric forms **5a** and **5b** was also evaluated based on these DFT calculations. Using the gas phase geometries, the Gibbs free energy difference between both compounds was computed in toluene solution using the solvation energies from SMD calculations and found to be 1.6 kcal/mol at room temper-

ature, with **5b** being the most stable isomer. Qualitatively, the trend in relative stability is consistent with our empirical data since compound **5b** is the predominant species in the reaction mixture according to the NMR integration. It should be noted that it is also possible that the **5a/5b** ratio found experimentally is kinetically controlled as no interconversion between both isomers was observed.

Time-dependent density functional theory (TDDFT) calculations were carried out on complex **4** as a representative example. Relevant excitations were analyzed in more detail using natural transition orbital calculations (NTOs) to provide insight into their nature. According to the calculations, the three lowest-energy transitions in **4** (λ_{calc} = 645, 539 and 526 nm) all have small oscillator strength and involve transitions from orbitals centered on the [ReBr(CO)$_3$] fragment (π^*(Re-Br) and (π(Re-CO)) into the formazan π^*-orbital. The fourth excited state, with the highest oscillator strength in the visible range (λ_{calc} = 487 nm; $\lambda_{max,exp}$ = 495 nm, Figure S11a-b), has a more pronounced formazan (intraligand) $\pi-\pi^*$ character, involving an occupied azo π-orbital as the donor (see Table S4 for the corresponding NTO), but also here the contribution of metal-based orbitals is still clearly noticeable. Thus, in all excitations in the visible range, there is extensive mixing between the metal and ligand orbitals in the ground and excited states, which results in electronic transitions of mixed nature: all show contributions from MLCT Re(dπ) → formazan(π^*), LLCT Br(p) → formazan(π^*), and ILCT azo(π) → formazan(π^*) excitations. The strong metal−ligand orbital mixing results in reduced charge transfer character in the MLCT bands, which is reflected in the minor influence of solvent polarity (toluene *vs* acetonitrile) on the empirical electronic absorption spectrum (*vide supra*).[53] Similar to the absorptions in the visible range, analysis of the NTOs of the higher energy transitions shows that these involve the formazan π^*-orbital as the acceptor and are also highly mixed in character.

TDDFT calculations were performed on the optimized structures of complexes **5a/b** to understand the impact of the pendant R^1/R^5 arms on the electronic transitions. The intense low-energy absorption is computed to be shifted to higher energy for **5a** (444 nm) compared to **5b** (489 nm), see Figures S13 and S14, respectively. This is in agreement with the empirical UV/vis spectrum, which shows two distinct bands at 452 and 520 nm for the **5a/b** mixture. As in **4**, the natural transition orbital pair for the main low-energy excitation in **5b** consists of a 'hole' NTO on the [ReBr(CO)$_3$] core, whereas the excited electron ('particle' NTO) consists primarily of the π^* formazan orbital. A comparison of the NTOs for **5a** and **5b** shows that the main difference between the two isomers is found in the hole NTO (Figure 5), which has a higher formazan contribution in **5a**. Based on the optimized geometries, the orientation of the azo-NAr ring changes upon swapping the aryl groups on the nitrogen atoms (Ph/Mes): the angle between the plane defined by the five-membered chelate ring and the Mes-substituent is 73.77° in **5a**, whereas the corresponding angle with the Ph-substituent in **5b** is only 39.28°. To test our hypothesis that the orientation of the azo-NAr group has a major impact on the spectral properties, we took the geometry of **5b** and rotated the N-Ph group out of the ligand plane to be in the same orientation as the N-Mes group in **5a**. This structure is labeled **5b_rot**. The main visible band in the TDDFT spectrum calculated at the **5b_rot** geometry is blue-shifted by 30 nm (1342 cm^{-1})
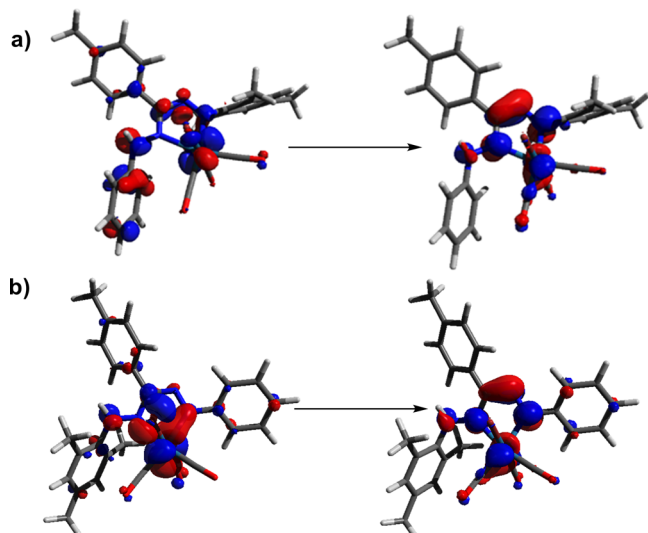
Figure 5. Natural transition orbitals for the highest-intensity excitation in the visible (isovalue = 0.05) for (a) **5a** and (b) **5b** represented as a hole → electron.

compared to **5b**, but the other transitions remain at similar energies (Figure S17). An analysis of the orbital mixing between the azo-NAr ring and the rest of the ligand π-system confirms that rotating the Ar ring out of the plane disrupts conjugation (Table S7), and thus we conclude that this is responsible for the spectral shift observed.

Luminescence Spectroscopy. The emission spectrum of **4** measured at room temperature in acetonitrile using an excitation wavelength of 320 nm shows a broad featureless emission band at 380 nm (Figure 6a). The excited state showed a monoexponential decay (λ_{ex} = 370 nm) with a lifetime (τ) of 3.69 ns under a N_2 atmosphere, which does not appreciably change under O_2 (τ = 3.60 ns) (see Figure S19). Furthermore, the excitation spectrum (λ_{em} = 380 nm) exhibits a broad band centered at 310 nm (Figure 6b). In contrast to the majority of fac-$[ReX(CO)_3(L,L)]$ complexes with bidentate N-donor ligands (e.g., α-diimines), which typically show emission at higher wavelengths (400−600 nm),[54,55] this data shows that the triplet (metal−ligand or ligand-centered)[56] excited states typical for the photoluminescence of fac-$[ReX(CO)_3(L,L)]$ compounds[57] are non-emissive in formazan Re(I) species. This also stands in contrast to complexes with anionic formazanate ligands, which show highly tunable emission with large Stokes shifts at much lower energies.[58−60]

CONCLUSIONS

We described the straightforward synthesis of the first complexes bearing the neutral formazan ligand toward a group 7 metal. The fac-$(CO)_3ReBr(formazan)$ complexes obtained contain a five-membered chelate ring, in which the ligand binds via the nitrogen atoms of the azo (N=N-Ar) and hydrazo (C=N-NHAr) groups, which leaves a pendant acidic (exchangeable) NH moiety in close proximity to the metal center. Structural and spectroscopic data demonstrate that the formazan ligand is tightly bound to the metal center, which is due to the strong π-acceptor character of the ligand. The effect of ligand substituents on the properties of the complexes is only minor, but the preparation of an asymmetric derivative with a N-Mes substituent demonstrates that changes in the sterics shift the electronic absorption spectrum due to changes
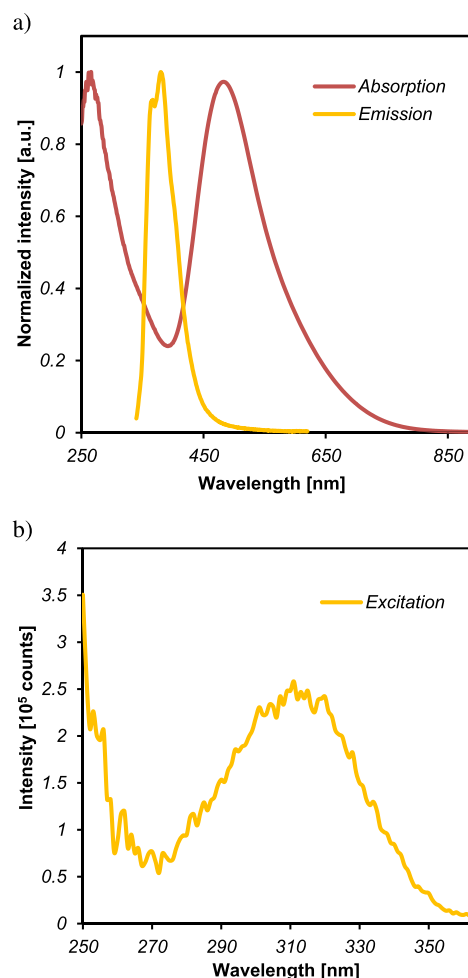
Figure 6. (a) Normalized absorption and emission spectra of **4** in MeCN recorded at λ_{exc} = 320 nm; (b) excitation spectrum of **4** in MeCN. The data were collected at room temperature.

in the conjugation within the ligand. Computational studies at the DFT level confirm a high degree of covalency in the metal-formazan interaction and highly mixed metal−ligand character of the frontier orbitals, which is sensitive to the degree of conjugation within the ligand as demonstrated by sterically switching 'off' π-interactions in the derivative with a N-Mes group (compound **5a**). Unlike many fac-$[ReX(CO)_3(L,L)]$ compounds (L,L = α-diimine ligands) reported in the literature, our formazan complexes are only weakly luminescent in the near-UV (λ_{em} = 380 nm), and emission from the lower-energy excited states is not observed. In ongoing work, we are investigating the possibility of using the proton-responsive nature of the NH group (i.e., formazan/formazanate interconversion) in 'cooperative' reactivity of this type of complexes.

EXPERIMENTAL SECTION

General Considerations. All work—except ligand synthesis—was conducted under a nitrogen atmosphere using conventional Schlenk and vacuum-line techniques. Pentane and toluene (Aldrich, anhydrous. 99.8%) were passed over columns of Al_2O_3 (Fluka) and BASF R3-11-supported Cu oxygen scavengers. $[ReBr(CO)_5]$ was prepared according to the published procedures[61] from $[Re_2(CO)_{10}]$ (Aldrich, 98%) and Br_2 (Aldrich, 98%). The ligands 1,5-diphenyl-3-p-tolylformazan (**L2H**), 1,5-diphenyl-3-p-methoxyphenylformazan (**L3H**), and 1,5-diphenyl-3-p-flourophenylformazan (**L4H**) were

Table 3. Crystallographic Data for 3, 4, and 5b

	3	4	5b
chemical formula	$C_{23}H_{18}BrN_4O_4Re$	$C_{22}H_{15}BrFN_4O_3Re$	$C_{26}H_{24}BrN_4O_3Re$
M_r	680.52	668.49	706.6
cryst syst	triclinic	monoclinic	triclinic
color, habit	purple, needle	purple, needle	purple, block
size (nm)	$0.42 \times 0.13 \times 0.04$	$0.70 \times 0.170 \times 0.060$	$0.40 \times 0.33 \times 0.20$
space group	$P\bar{1}$ (No.2)	$P2_1/n$ (No.14)	$P\bar{1}$ (No.2)
a (Å)	9.0463(6)	10.095(2)	9.9235(12)
b (Å)	11.0459(7)	18.586(6)	10.9196(13)
c (Å)	12.7033(8)	12.219(4)	13.0134(15)
α (deg)	107.379(2)	90	77.085(4)
β (deg)	94.935(3)	107.191(8)	72.218(4)
γ (deg)	103.227(2)	90	75.163(4)
V (Å³)	1162.89(13)	2190.1(11)	1281.7(3)
Z	2	4	2
ρ_{calc} (g·cm⁻³)	2.302	2.027	1.831
radiation, λ (Å)	Mo, Kα, 0.71073	Mo, Kα, 0.71073	Cu, Kα, 1.54178
μ(Mo, Kα) (mm⁻¹)	8.777	7.413	11.384
$F(000)$	750	1272	684
temp (K)	100(2)	100(2)	100(2)
θ range (deg)	3.028−27.191	3.044−27.200	3.612−70.304
data collected (h, k, l)	−11:11, −14:14, −16:16	−12:12, −23:23, −15:15	−12:12, −13:13, −15:15
no. of reflns collected	45,523	27,390	21,942
no. of indep reflns	5166	4818	4526
obsd reflns $F_o \geq 2.0\sigma(F_o)$	4966	4288	4396
$R(F)$ [obsd reflns] (%)	1.78	2.81	2.19
$R_w(F^2)$ [all reflns] (%)	5.24	6.13	5.51
GOF	1.051	1.192	1.119
weighting a, b	0.03300, 1.26140	0.0000, 12.4515	0.0000, 2.9889
params refined	303	293	324
min, max residual densities	−1.04, 1.32	−1.61, 1.82	−0.83, 0.85

synthesized using the methodology reported by Hicks and cow-orkers.[4] Particularly, 5-mesityl-1-phenyl-3-*p*-tolylformazan (**L5H**) was prepared using a modified procedure published by our group.[9] 1,3,5-Triphenylformazan (**L1H**, TCI, 92%), *p*-tolualdehyde (Aldrich 97%), 4-methoxybenzaldehyde (Aldrich, 98%), 4-fluorobenzaldehyde (Aldrich, 98%), phenylhydrazine (Aldrich, 99%), aniline (Aldrich 99%), sodium nitrite (Aldrich, 99%), sodium carbonate (Aldrich, 99.5%), and $[NBu_4]Br$ were used as received. $CHCl_3$ (Aldrich, 99%) and $CDCl_3$ (Aldrich, 99.8 atom %D) were used without further purification.

NMR spectra were measured on Mercury 400, Varian Inova 500, or Bruker 600 MHz spectrometers. Residual solvent signals were used as internal reference for ¹H and ¹³C spectra and reported in ppm relative to TMS (0 ppm). Complete assignments were based on two-dimensional experiments (COSY, HSQC, HMBC) using standard pulse sequences. FT-IR spectra were collected in DCM solution on a JASCO 4700 series FT-IR spectrometer in transmission mode using a liquid cell with CaF_2 windows. UV−vis spectra were recorded in toluene solution on an Agilent Technologies 8453 UV−vis spectrophotometer. Luminescence spectroscopy were measured on a Fluorolog-3 spectrometer from HORIBA Jobin Yvon.

X-ray diffraction data were collected at 100 K on a Bruker D8 Venture diffractometer with a Mo Kα ($\lambda = 0.71073$ Å) (compounds **3** and **4**) or Cu Kα ($\lambda = 1.54178$ Å) (compound **5b**) radiation source. Crystal structures were refined using the SHELXL[62] software (Table 3). Non-hydrogen atoms were refined anisotropically.

Computational Details. Density functional theory (DFT) calculations were carried out in Gaussian 16 Revision C.02[63] software and visualized using Gaussview 6[64] or Avogadro.[65] Geometry optimizations in the ground state were performed in the gas phase at a MN15L[51] level of theory combined with a triple ζ-basis set: def2tzvp.[52] The carbonyl frequency values were scaled using a factor

of 0.9578[66] (see Table S1). TDDFT calculations were performed on the optimized structures at the CAM-B3LYP/def2tzvp level of theory. The solvent effect was simulated using the continuum polarized model (CPM).[67]

Procedure for the Synthesis of Complexes 1−4. Equimolar amounts of $[ReBr(CO)_5]$ and the corresponding ligand were poured into a two-necked round bottom flask and dissolved in 20 mL of toluene. The reaction was heated up at reflux for 1 h observing that the mixture darkened upon completion. The solvent was evaporated to dryness. Specific details for the purification of the entitled complexes are mentioned below.

1 ($C_{22}H_{16}BrN_4O_3Re$). $[ReBr(CO)_5]$ (0.0934 g, 0.230 mmol), **L1H** (0.06938 g, 0.230 mmol). Work-up: 5 mL of pentane was added to the mixture, and the crude was stirred for 30 min allowing the formation of a dark-crimson solid material. The compound was filtered out and rinsed with pentane (3 × 5 mL). (41.8 mg, 27.9%). ¹H NMR ($CDCl_3$, 25 °C, 400 MHz) δ/ppm: 7.30 (d, 2 H, ³J = 8 Hz, Ph-NH *o*-H), 7.39 (t, 1 H, ³J = 8 Hz, Ph-NH *p*-H), 7.45−7.57 (m, 5H, Ph-NH *m*-H, Ph-N═N *m*-H, Ph-NC *p*-H), 7.64 (m, 3H, Ph-NC *m*-H, Ph-N═N *p*-H,) 7.84 (d, 2 H, ³J = 8 Hz, Ph-NC *o*-H), 7.89 (d, 2 H, ³J = 8 Hz, Ph-N═N *o*-H), 8.58 (s, 1 H, NH). ¹³C{¹H} NMR ($CDCl_3$, 25 °C, 150 MHz) δ/ppm: 123.21 (Ph-NH *o*-CH), 123.95 (Ph-N═N *o*-CH), 127.90 (Ph-NH *p*-CH), 128.48 (Ph-CN *ipso*-C), 128.93 (Ph-CN *o*-CH), 129.31 (Ph-N═N *m*-CH), 129.39 (Ph-NH *m*-CH), 130.10 (Ph-CN *m*-CH), 131.69 (Ph-N═N *p*-CH), 131.86 (Ph-CN *p*-CH), 140.83 (Ph-NH *ipso*-C), 157.20 (Ph-N═N *ipso*-C), 164.65 (NCN C), 185.33 (CO *trans* Br C), 192.35 (CO *trans* Ph-NH-N C), 192.89 (CO *trans* Ph-N═N C). IR(CH_2Cl_2) ν(CO)/cm⁻¹: 2035(s), 1959(s), 1923(s). MS (FAB+) (m/z): $[MH + 2]^+$ = 653, $[MH]^+$ = 651, $[MH-CO]^+$ = 623, $[MH-3CO]^+$ = 567. HRMS (ESI +) (m/z): Calcd. for $[MH]^+$ = 651.004167. Found = 651.00337. $[MH-3CO]^+$ = 567.01942. Found = 567.01817.

2 ($C_{23}H_{18}BrN_4O_3Re$). [ReBr(CO)$_5$] (0.1235 g, 0.304 mmol), **L2H** (0.0959 g 0.305 mmol). Work-up: similar to the procedure described above. (93.3 mg, 46.0%). ^{1}H NMR (CDCl$_3$, 25 °C, 600 MHz) δ/ppm: 2.47 (s, 1 H, CH$_3$), 7.29 (d, 2 H,^3J = 8 Hz, Ph-NH o-H), 7.38 (t, 1 H,^3J = 7 Hz, Ph-NH p-H), 7.43−7.56 (m, 7H, Ph-NH m-H, Ph-N═N m-H, p-tol m-H, Ph-N═N p-H), 7.74 (d, 2 H,^3J = 8 Hz, p-tol o-H), 7.88 (d, 2 H,^3J = 7 Hz, Ph-N═N o-H), 8.56 (s, 1 H, NH). ^{13}C{^{1}H} NMR (CDCl$_3$, 25 °C, 150 MHz) δ/ppm: 21.71 (CH$_3$), 123.11 (Ph-NH o-CH), 123.97 (Ph-N═N o-CH), 125.58 (p-tol ipso-C), 127.75 (Ph-NH p-CH), 128.85 (p-tol o-CH), 129.29 (Ph-NH m-CH), 129.40 (Ph-N═N m-CH), 130.72 (p-tol m-CH), 131.65 (Ph-N═N p-CH), 140.96 (Ph-NH ipso-C), 142.49 (p-tol p-C), 157.24 (Ph-N═N ipso-C), 165.02 (NCN C), 185.37 (CO trans Br C), 192.40 (CO trans Ph-NH-N C), 192.88 (CO trans Ph-N═N C). IR(CH$_2$Cl$_2$) ν(CO)/cm$^{−1}$: 2035(s), 1959(s), 1924(s). MS (DART+) (m/z): [MH + 2]$^+$ = 667, [MH]$^+$ = 665, [MH-CO]$^+$ = 637, [MH-2CO]$^+$ = 609, [MH-3CO]$^+$ = 581. HRMS (ESI+) (m/z): Calcd. for [MH] $^+$ = 665.01982. Found = 665.01917 [MH-3CO]$^+$ = 581.035072. Found = 581.03365.

3 ($C_{23}H_{18}BrN_4O_4Re$). [ReBr(CO)$_5$] (0.0930 g, 0.229 mmol), **L3H** (0.0758 g, 0.229 mmol). Work-up: the compound was recrystallized by slow diffusion of 15 mL of pentane into 5 mL of a DCM solution of **3**. The system was kept in the freezer for 1 day allowing the formation of crystalline material. The solid was washed with 3 × 5 mL of pentane. (105 mg, 67.07%). ^{1}H NMR (CDCl$_3$, 25 °C, 600 MHz) δ/ppm: 3.88 (s, 1 H, CH$_3$O H), 7.10 (d, 2 H,^3J = 8 Hz, p-CH$_3$OPh m-H), 7.27 (d, 2 H,^3J = 8 Hz, Ph-NH o-H), 7.35 (t, 1 H,^3J = 8 Hz, Ph-NH p-H), 7.45 (t, 2H,^3J = 8 Hz, Ph-N═N m-H), 7.49 (t, 2H,^3J = 8 Hz, Ph-NH m-H), 7.53 (t, 1H,^3J = 7 Hz, Ph-N═N p-H), 7.81 (d, 2 H,^3J = 6 Hz, p-CH$_3$OPh o-H), 7.88 (d, 2 H,^3J = 8 Hz, Ph-N═N o-H), 8.47 (s, 1 H, NH). ^{13}C{^{1}H} NMR (CDCl$_3$, 25 °C, 150 MHz) δ/ppm: 55.64 (CH$_3$O , C), 115.39 (p-CH$_3$OPh m-CH), 120.64 (p-CH$_3$OPh ipso-C), 122.80 (Ph-NH o-CH), 123.96 (Ph-N═N o-CH), 127.52 (Ph-NH p-CH), 129.29 (Ph-NH m-CH), 129.41 (Ph-N═N m-CH), 130.82 (p-CH$_3$OPh o-CH), 131.68 (Ph-N═N p-CH), 141.14 (Ph-NH ipso-C), 157.26 (Ph-N═N ipso-C), 162.17 (p-CH$_3$OPh p-C), 165.25 (NCN C), 185.38 (CO trans Br C), 192.40 (CO trans Ph-NH-N C), 192.92 (CO trans Ph-N═C C). IR(CH$_2$Cl$_2$) ν(CO)/cm$^{−1}$: 2034(s), 1958(m), 1923(s). MS (DART+) (m/z): [MH + 2]$^+$ = 683, [MH]$^+$ = 681, [MH-CO]$^+$ = 653, [MH-2CO]$^+$ = 625, [MH-3CO]$^+$ = 597. Anal. Calcd. For ($C_{23}H_{18}BrN_4O_4Re$): C 40.59, H 2.67, N 8.23; found C 39.81, H 2.59, N 7.90.

4 ($C_{22}H_{15}BrFN_4O_3Re$). [ReBr(CO)$_5$] (0.0951 g, 0.234 mmol), **L4H** (0.0745 g, 0.234 mmol). Work-up: after solvent evaporation, the crude was recrystallized by diffusion of pentane into a CHCl$_3$ solution at −30 °C. The crystalline material was filtered out and rinsed with 3 × 5 mL of pentane. (96 mg, 61.3%). ^{1}H NMR (CDCl$_3$, 25 °C, 600 MHz) δ/ppm: 7.32 (d, 2H,^3J = 8 Hz, Ph-NH o-H), 7.35 (t, 2H,$^3J_{H-H}$ = 8 Hz,$^3J_{H-F}$ = 8 Hz, p-FPh m-H), 7.41 (t, 1H,^3J = 7 Hz, Ph-NH p-H), 7.49 (t, 2H, ,^3J = 8 Hz, Ph-NH m-H), 7.54 (t, 2H,^3J = 8 Hz, Ph-N═N m-H), 7.58 (t, 1H,^3J = 7 Hz, Ph-N═N p-H), 7.90 (m, 4H, Ph-N═N o-H, p-FPh o-H), 8.42 (s, 1H, NH). ^{19}F NMR (CDCl$_3$, 25 °C, 565 MHz) δ/ppm: −105.92 (m, p-FPh F). ^{13}C{^{1}H} NMR (CDCl$_3$, 25 °C, 150 MHz) δ/ppm: 117.38 ($^2J_{C-F}$ = 22 Hz , p-FPh m-CH), 122.88 (Ph-NH o-CH), 123.94 (Ph-N═N o-CH), 124.74 ($^4J_{C-F}$ = 3 Hz, p-FPh ipso-C), 127.85 (Ph-NH p-CH), 129.36 (Ph-N═N m-CH), 129.47 (Ph-NH m-CH), 131.51 ($^3J_{C-F}$ = 9 Hz, p-FPh o-CH), 131.80 (Ph-N═N p-CH), 140.92 (Ph-NH ipso-C), 157.30 (Ph-N═N ipso-C), 164.39 (J_{C-F} = 253.5 Hz, p-FPh p-C), 164.26 (NCN C), 185.25 (CO trans Br C), 192.14 (CO trans Ph-NH-N C), 192.63 (CO trans Ph-N═C C). IR(CH$_2$Cl$_2$) ν(CO)/cm$^{−1}$: 2036(s), 1961(s), 1925(s). MS (DART +) (m/z): [MH]$^+$ = 669, [M-CO]$^+$ = 641, [M-3CO] = 585. Anal. Calcd. For ($C_{22}H_{15}BrFN_4O_3Re$): C 39.53, H 2.26, N 8.38; found C 39.12, H 2.04, N 8.29.

5a and 5b ($C_{26}H_{24}BrN_4O_3Re$). [ReBr(CO)$_5$] (0.0886 g, 0.22 mmol) and **L5H** (0.0778 g, 0.022 mmol) were dissolved in 20 mL of toluene and heated in refluxing toluene for 2.5 h. An oily material was afforded after removal of the volatiles; then, the crude was triturated with 5 mL of pentane, yielding a dark solid. (95 mg, 61.5%). ^{1}H NMR (CDCl$_3$, 25 °C, 600 MHz) δ/ppm: (**5a**) 1.99 (s, 3H, p-tol p-CH$_3$),

2.05 (s, 3H, Mes-N═N p-CH$_3$), 2.07 (s, 3H, Mes-N═N o-CH$_3$), 2.81 (s, 3H, Mes-N═N o-CH$_3$), 6.64 (s, 1H, Mes-N═N m-H), 6.71 (s, 1H, Mes-N═N m-H), 6.82 (d, 2H, ,^3J = 6 Hz, Ph-NH o-H), 6.93 (m, 3H, Ph-NH p-H, p-tol m-H), 7.05 (t, 2H,^3J = 6 Hz, Ph-NH m-H), 7.68 (d, 2H,^3J = 6 Hz, p-tol o-H), 8.22 (s, 1H, NH). (**5b**) 2.05 (s, 3H, Mes-NH p-CH$_3$), 2.05 (s, 3H, Mes-NH o-CH$_3$), 2.09 (s, 3H, p-tol p-CH$_3$), 2.41 (s, 3H, Mes-NH o-CH$_3$), 6.70 (s, 2H, Mes-NH m-H), 6.93 (m, 3H, Ph-N═N p-H, m-H), 6.99 (d, 2H,^3J = 6 Hz, p-tol m-H), 7.47 (d, 2H,^3J = 6 Hz, p-tol o-H), 7.61 (s, 1H, NH). 7.85 (m, 2H, Ph-N═N o-H). ^{13}C{^{1}H} NMR (CDCl$_3$, 25 °C, 150 MHz) δ/ppm: (**5a**) 17.80 (Mes o-CH$_3$), 20.42 (Mes o-CH$_3$), 20.80 (Mes p-CH$_3$), 21.37 (p-tol p-CH$_3$) , 121.53 (Ph o-CH), 126.68(p-tol p-C), 126.94 (Ph m-CH), 128.6 (Mes m-C), 129.24 (p-tol o-CH), 129.47 17 (Mes o-C), 130.17 (Mes m-C), 130.48 (p-tol m-CH), 131.17 (Mes o-C), 138.18 (Mes p-C), 142.20 (Ph ipso-C), 142.20 (p-tol ipso-C) , 155.20 (Mes ipso-C), 167.11 (NNCN C), 186.34 (CO trans Br C), 192.25 (CO trans Mes-N═N C), 193.04 (CO trans PhN-NH C). (**5b**) 18.61 (Mes p-CH$_3$), 19.56 (Mes o-CH$_3$), 21.14 (Mes o-CH$_3$), 21.33 (p-tol p-CH$_3$), 124.09 (Ph o-CH), 129.14 (p-tol p-C), 129.43 (p-tol o-CH), 129.49 (Mes m-C), 129.93 (Mes m-C), 130.94 (p-tol m-CH), 131.23 (Ph m-CH), 136.53 (Mes ipso-C), 137.70 (Mes o-C), 137.89 (Mes o-C), 140.68 (Mes p-C), 141.79 (p-tol ipso-C), 157.15 (Ph ipso-C), 161.04 (NNCN C), 184.77 (CO trans Br C), 192.29 (CO trans Mes-NH C), 194.16 (CO trans Ph-N=N C). IR(CH$_2$Cl$_2$) ν(CO)/cm$^{−1}$: 2036(s), 1959(s), 1922(s). MS (DART+) (m/z): [MH + 2]$^+$ = 709, [MH]$^+$ = 707, [MH-CO]$^+$ = 678, [MH-3CO]$^+$ = 623. HRMS (ESI+) (m/z): Calcd. for [MH] $^+$ = 707.06677. Found = 707.06667. [MH-2CO]$^+$ = 651.07684. Found = 651.07610. [MH-3CO]$^+$ = 623.08193. Found = 623.08092.

ASSOCIATED CONTENT

🄢 Supporting Information

The Supporting Information is available free of charge at https://pubs.acs.org/doi/10.1021/acs.inorgchem.2c02168.

> 1D (^{1}H, ^{13}C{^{1}H}) and 2D (^{1}H EXSY) NMR experiments, additional electronic spectroscopy measurements, and computational data (geometry optimizations, TDDFT calculations, and NTO analysis) (PDF)

Accession Codes

CCDC 2180752−2180754 contain the supplementary crystallographic data for this paper. These data can be obtained free of charge via www.ccdc.cam.ac.uk/data_request/cif, or by emailing data_request@ccdc.cam.ac.uk, or by contacting The Cambridge Crystallographic Data Centre, 12 Union Road, Cambridge CB2 1EZ, UK; fax: +44 1223 336033.

AUTHOR INFORMATION

Corresponding Authors

Noé Zúñiga-Villarreal − Instituto de Química, Universidad Nacional Autónoma de México, Ciudad Universitaria, 04510 México, México; Email: zuniga@unam.mx

Edwin Otten − Stratingh Institute for Chemistry, University of Groningen, 9747 AG, Groningen, The Netherlands; ⓞ orcid.org/0000-0002-5905-5108; Email: edwin.otten@rug.nl

Authors

Liliana Capulín Flores − Stratingh Institute for Chemistry, University of Groningen, 9747 AG, Groningen, The Netherlands; Instituto de Química, Universidad Nacional Autónoma de México, Ciudad Universitaria, 04510 México, México

Lucas A. Paul − Universität Göttingen, Institut für Anorganische Chemie, D-37077 Göttingen, Germany

Inke Siewert − *Universität Göttingen, Institut für Anorganische Chemie, D-37077 Göttingen, Germany;* ⊙ orcid.org/0000-0003-3121-3917

Remco Havenith − *Stratingh Institute for Chemistry, University of Groningen, 9747 AG, Groningen, The Netherlands;* ⊙ orcid.org/0000-0003-0038-6030

Complete contact information is available at:
https://pubs.acs.org/10.1021/acs.inorgchem.2c02168

Author Contributions

The manuscript was written through contributions of all authors. All authors have given approval to the final version of the manuscript.

Notes

The authors declare no competing financial interest.

■ REFERENCES

(1) Maslakova, T. I.; Lipunov, I. N.; Pervova, I. G.; Maslakov, P. A. Formazan-Containing Solid-Phase Reagent Indicator Systems for Environmental Analysis. *Russ. J. Gen. Chem.* **2018**, *88*, 2717−2731.

(2) Ciapetti, G.; Cenni, E.; Pratelli, L.; Pizzoferrato, A. In Vitro Evaluation of Cell/Biomaterial Interaction by MTT Assay. *Biomaterials* **1993**, *14*, 359−364.

(3) Szymczyk, M.; El-shafei, A.; Freeman, H. S. Design , Synthesis , and Characterization of New Iron-Complexed Azo Dyes. *Dyes Pigm.* **2007**, *72*, 8−15.

(4) Gilroy, J. B.; McKinnon, S. D. J.; Koivisto, B. D.; Hicks, R. G. Electrochemical Studies of Verdazyl Radicals. *Org. Lett.* **2007**, *9*, 4837−4840.

(5) Hunter, L.; Roberts, C. B. The Azo-Group as a Chelating Group. Part V. Metallic Derivatives of Arylazo-Oximes and of Formazyl Compounds. *J. Chem. Soc.* **1941**, 823−826.

(6) Barbon, S. M.; Price, J. T.; Reinkeluers, P. A.; Gilroy, J. B. Substituent-Dependent Optical and Electrochemical Properties of Triarylformazanate Boron Difluoride Complexes. *Inorg. Chem.* **2014**, *53*, 10585−10593.

(7) Gilroy, J. B.; Otten, E. Formazanate Coordination Compounds: Synthesis, Reactivity, and Applications. *Chem. Soc. Rev.* **2020**, *49*, 85−113.

(8) de Vries, F.; Otten, E. Reversible On/Off Switching of Lactide Cyclopolymerization with a Redox-Active Formazanate Ligand. *ACS Catal.* **2022**, *12*, 4125−4130.

(9) Chang, M. C.; Roewen, P.; Travieso-Puente, R.; Lutz, M.; Otten, E. Formazanate Ligands as Structurally Versatile, Redox-Active Analogues of β-Diketiminates in Zinc Chemistry. *Inorg. Chem.* **2015**, *54*, 379−388.

(10) Zhao, B.; Han, Z.; Ding, K. The N-H Functional Group in Organometallic Catalysis. *Angew. Chem., Int. Ed.* **2013**, *52*, 4744−4788.

(11) Wu, H. L.; Li, X. B.; Tung, C. H.; Wu, L. Z. Bioinspired Metal Complexes for Energy-Related Photocatalytic Small Molecule Transformation. *Chem. Commun.* **2020**, *56*, 15496−15512.

(12) Drosou, M.; Kamatsos, F.; Mitsopoulou, C. A. Recent Advances in the Mechanisms of the Hydrogen Evolution Reaction by Non-Innocent Sulfur-Coordinating Metal Complexes. *Inorg. Chem. Front.* **2020**, *7*, 37−71.

(13) Siewert, I. Electrochemical CO_2 Reduction Catalyzed by Binuclear $LRe_2(CO)_6Cl_2$ and $LMn_2(CO)_6Br_2$ Complexes with an Internal Proton Source. *Acc. Chem. Res.* **2022**, *55*, 473−483.

(14) Fujita, E.; Grills, D. C.; Manbeck, G. F.; Polyansky, D. E. Understanding the Role of Inter- and Intramolecular Promoters in Electro- and Photochemical CO_2 Reduction Using Mn, Re, and Ru Catalysts. *Acc. Chem. Res.* **2022**, *55*, 616−628.

(15) Drover, M. W. A Guide to Secondary Coordination Sphere Editing. *Chem. Soc. Rev.* **2022**, *51*, 1861−1880.

(16) Gallardo-Villagrán, M.; Rivada-Wheelaghan, O.; Rahaman, S. M. W.; Fayzullin, R. R.; Khusnutdinova, J. R. Proton-Responsive Naphthyridinone-Based Ru(II) Complexes and Their Reactivity with Water and Alcohols. *Dalton Trans.* **2020**, *49*, 12756−12766.

(17) Zhou, C.; Hu, J.; Wang, Y.; Yao, C.; Chakraborty, P.; Li, H.; Guan, C.; Huang, M. H.; Huang, K. W. Selective Carbonylation of Benzene to Benzaldehyde Using a Phosphorus-Nitrogen PN^3P-Rhodium(I) Complex. *Org. Chem. Front.* **2019**, *6*, 721−724.

(18) Mukherjee, J.; Siewert, I. Manganese and Rhenium Tricarbonyl Complexes Equipped with Proton Relays in the Electrochemical CO_2 Reduction Reaction. *Eur. J. Inorg. Chem.* **2020**, *2020*, 4319−4333.

(19) Darshani, T.; Thushara, N.; Weerasuriya, P.; Fronczek, F. R.; Perera, I. C.; Perera, T. Fluorescent Di-(2-Picolyl)Amine Based Drug-like Ligands and Their $Re(CO)_3$ Complexes towards Biological Applications. *Polyhedron* **2020**, *185*, No. 114592.

(20) Gaire, S.; Schrage, B. R.; Ziegler, C. J. An Organometallic Isostere of an Amino Acid. *Inorg. Chem.* **2021**, *60*, 10105−10108.

(21) Auvray, T.; Pal, A. K.; Hanan, G. S. Electronic Properties of Rhenium(I) Carbonyl Complexes Bearing Strongly Donating Hexahydro-Pyrimidopyrimidine Based Ligands. *Eur. J. Inorg. Chem.* **2021**, *2021*, 2570−2577.

(22) Gonçalves, M. R.; Benvenho, A. R. V.; Frin, K. P. M. Electrical and Optical Properties of Organic Light-Emitting Diodes with Rhenium(I) Complexes Using DC and AC Methods. *Opt. Mater.* **2019**, *94*, 206−212.

(23) Deeba, R.; Molton, F.; Chardon-Noblat, S.; Costentin, C. Effective Homogeneous Catalysis of Electrochemical Reduction of Nitrous Oxide to Dinitrogen at Rhenium Carbonyl Catalysts. *ACS Catal.* **2021**, *11*, 6099−6103.

(24) Hellman, A. N.; Haiges, R.; Marinescu, S. C. Rhenium Bipyridine Catalysts with Hydrogen Bonding Pendant Amines for CO_2 Reduction. *Dalton Trans.* **2019**, *48*, 14251−14255.

(25) Riplinger, C.; Carter, E. A. Influence of Weak Bronsted Acids on Electrocatalytic CO_2 Reduction by Manganese and Rhenium Bipyridine Catalysts. *ACS Catal.* **2015**, *5*, 900−908.

(26) Wong, K. Y.; Chung, W. H.; Lau, C. P. The Effect of Weak Brönsted Acids on the Electrocatalytic Reduction of Carbon Dioxide by a Rhenium Tricarbonyl Bipyridyl Complex. *J. Electroanal. Chem.* **1998**, *453*, 161−170.

(27) Sinha, S.; Berdichevsky, E. K.; Warren, J. J. Electrocatalytic CO_2 Reduction Using Rhenium(I) Complexes with Modified 2-(2'-Pyridyl)Imidazole Ligands. *Inorg. Chim. Acta* **2017**, *460*, 63−68.

(28) Sung, S.; Kumar, D.; Gil-Sepulcre, M.; Nippe, M. Electrocatalytic CO_2 Reduction by Imidazolium-Functionalized Molecular Catalysts. *J. Am. Chem. Soc.* **2017**, *139*, 13993−13996.

(29) Manbeck, G. F.; Muckerman, J. T.; Szalda, D. J.; Himeda, Y.; Fujita, E. Push or Pull? Proton Responsive Ligand Effects in Rhenium Tricarbonyl CO_2 Reduction Catalysts. *J. Phys. Chem. B* **2015**, *119*, 7457−7466.

(30) Rotundo, L.; Polyansky, D. E.; Gobetto, R.; Grills, D. C.; Fujita, E.; Nervi, C.; Manbeck, G. F. Molecular Catalysts with Intramolecular Re − O Bond for Electrochemical Reduction of Carbon Dioxide. *Inorg. Chem.* **2020**, *59*, 12187−12199.

(31) Jia-Pei, D.; Wilting, A.; Siewert, I. Are Two Metal Ions Better than One? Mono and Binuclear Alfa-Diimine-$Re(CO)_3$ Complexes with Proton-Responsive Ligands in CO_2 Reduction Catalysis. *Chem. − Eur. J.* **2019**, *25*, 5555−5564.

(32) Vollmer, M. V.; Machan, C. W.; Clark, M. L.; Antholine, W. E.; Agarwal, J.; Schaefer, H. F.; Kubiak, C. P.; Walensky, J. R. Synthesis, Spectroscopy, and Electrochemistry of (α-Diimine)M(CO)$_3$Br, M = Mn, Re, Complexes: Ligands Isoelectronic to Bipyridyl Show Differences in CO$_2$ Reduction. *Organometallics* **2015**, *34*, 3−12.

(33) Mckinnon, M.; Ngo, K. T.; Sobottka, S.; Sarkar, B.; Ertem, M. Z.; Grills, D. C.; Rochford, J. Synergistic Metal−Ligand Redox Cooperativity for Electrocatalytic CO$_2$ Reduction Promoted by a Ligand-Based Redox Couple in Mn and Re Tricarbonyl Complexes. *Organometallics* **2019**, *38*, 1317−1329.

(34) Benson, E. E.; Sampson, M. D.; Grice, K. A.; Smieja, J. M.; Froehlich, J. D.; Friebel, D.; Keith, J. A.; Carter, E. A.; Nilsson, A.; Kubiak, C. P. The Electronic States of Rhenium Bipyridyl Electrocatalysts for CO$_2$ Reduction as Revealed by X-Ray Absorption Spectroscopy and Computational Quantum Chemistry. *Angew. Chem., Int. Ed.* **2013**, *52*, 4841−4844.

(35) Matson, B. D.; McLoughlin, E. A.; Armstrong, K. C.; Waymouth, R. M.; Sarangi, R. Effect of Redox Active Ligands on the Electrochemical Properties of Manganese Tricarbonyl Complexes. *Inorg. Chem.* **2019**, *58*, 7453−7465.

(36) Queyriaux, N. Redox-Active Ligands in Electroassisted Catalytic H$^+$ and CO$_2$ Reductions: Benefits and Risks. *ACS Catal.* **2021**, 4024−4035.

(37) Travieso-Puente, R.; Chang, M. C.; Otten, E. Alkali Metal Salts of Formazanate Ligands: Diverse Coordination Modes as a Result of the Nitrogen-Rich [NNCNN] Ligand Backbone. *Dalton Trans.* **2014**, *43*, 18035−18041.

(38) Baumgardner, D. F.; Parks, W. E.; Gilbertson, J. D. Harnessing the Active Site Triad: Merging Hemilability, Proton Responsivity, and Ligand-Based Redox-Activity. *Dalton Trans.* **2020**, *49*, 960−965.

(39) Tiers, G.; Plovan, S.; Searles, S. Proton Nuclear Resonance Spectroscopy. Rapid Tautomerization of Formazans. *J. Org. Chem.* **1960**, *25*, 285−286.

(40) Sigeikin, G. I.; Lipunova, G. N.; Pervova, I. G. Formazans and Their Metal Complexes. *Russ. Chem. Rev.* **2006**, *75*, 885−900.

(41) Allen, F. H.; Watson, D. G.; Bramer, L.; Orpen, A. G.; Taylor, R. International Tables for Crystallography (2006). In *International Tables fo Crystallography*; 2006; Vol. *C*, pp. 790−811.

(42) Chakraborty, I.; Carrington, S. J.; Mascharak, P. K. Photodelivery of CO by Designed PhotoCORMs: Correlation between Absorption in the Visible Region and Metal-CO Bond Labilization in Carbonyl Complexes. *ChemMedChem* **2014**, *9*, 1266−1274.

(43) Kottelat, E.; Lucarini, F.; Crochet, A.; Ruggi, A.; Zobi, F. Correlation of MLCTs of Group 7 *fac*-[M(CO)$_3$]$^+$ Complexes (M = Mn, Re) with Bipyridine, Pyridinylpyrazine, Azopyridine, and Pyridin-2-Ylmethanimine Type Ligands for Rational PhotoCORM Design. *Eur. J. Inorg. Chem.* **2019**, 3758−3768.

(44) Samanta, S.; Ghosh, P.; Goswami, S. Recent Advances on the Chemistry of Transition Metal Complexes of 2-(Arylazo)Pyridines and Its Derivatives. *Dalton Trans.* **2012**, *41*, 2213−2226.

(45) Roy, S.; Sieger, M.; Sarkar, B.; Schwerdeski, B.; Lissner, F.; Schleid, T.; Fiedler, J.; Kaim, W. Establishing the Chelating Alfa-Azocarbonyl Function in Pi-Acceptor Ligands. *Angew. Chem., Int. Ed.* **2008**, *47*, 6192−6194.

(46) Carrington, S. J.; Chakraborty, I.; Alvarado, J. R.; Mascharak, P. K. Differences in the CO Photolability of *Cis*- and *Trans*-[RuCl$_2$(Azpy)(CO)$_2$] Complexes: Effect of Metal-to-Ligand Back-Bonding. *Inorg. Chim. Acta* **2013**, *407*, 121−125.

(47) Wei, L.; Babich, J. W.; Ouellette, W.; Zubieta, J. Developing the {M(CO)$_3$}$^+$ Core for Fluorescence Applications: Rhenium Tricarbonyl Core Complexes with Benzimidazole, Quinoline, and Tryptophan Derivatives. *Inorg. Chem.* **2006**, *45*, 3057−3066.

(48) Morimoto, T.; Ito, M.; Koike, K.; Kojima, T.; Ozeki, T.; Ishitani, O. Dual Emission from Rhenium(I) Complexes Induced by an Interligand Aromatic Interaction. *Chem. − Eur. J.* **2012**, *18*, 3292−3304.

(49) Milocco, F.; De Vries, F.; Bartels, I. M. A.; Havenith, R. W. A.; Cirera, J.; Demeshko, S.; Meyer, F.; Otten, E. Electronic Control of

Spin-Crossover Properties in Four-Coordinate Bis(Formazanate) Iron(II) Complexes. *J. Am. Chem. Soc.* **2020**, *142*, 20170−20181.

(50) Chang, M. C.; Otten, E. Synthesis and Ligand-Based Reduction Chemistry of Boron Difluoride Complexes with Redox-Active Formazanate Ligands. *Chem. Commun.* **2014**, *50*, 7431−7433.

(51) Yu, H. S.; He, X.; Truhlar, D. G. MN15-L: A New Local Exchange-Correlation Functional for Kohn-Sham Density Functional Theory with Broad Accuracy for Atoms, Molecules, and Solids. *J. Chem. Theory Comput.* **2016**, *12*, 1280−1293.

(52) Weigend, F.; Ahlrichs, R. Balanced Basis Sets of Split Valence, Triple Zeta Valence and Quadruple Zeta Valence Quality for H to Rn: Design and Assessment of Accuracy. *Phys. Chem. Chem. Phys.* **2005**, *7*, 3297−3305.

(53) Leirer, M.; Knör, G.; Vogler, A. Synthesis and Spectroscopic Properties of 1,2-Diiminetricarbonylrhenium(I)Chloride Complexes with Aliphatic Diimines (or 1,4-Diaza-1,3-Butadienes) as Ligands. *Zeitschrift fur Naturforschung B* **1999**, *54*, 341−344.

(54) Klemens, T.; Switlicka, A.; Szlapa-Kula, A.; Łapok, Ł.; Obłoza, M.; Siwy, M.; Szalkowski, M.; MaćKowski, S.; Libera, M.; Schab-Balcerzak, E.; MacHura, B. Tuning Optical Properties of Re(I) Carbonyl Complexes by Modifying Push-Pull Ligands Structure. *Organometallics* **2019**, *38*, 4206−4223.

(55) Stout, M. J.; Skelton, B. W.; Sobolev, A. N.; Raiteri, P.; Massi, M.; Simpson, P. V. Synthesis and Photochemical Properties of Re(I) Tricarbonyl Complexes Bound to Thione and Thiazol-2-Ylidene Ligands. *Organometallics* **2020**, *39*, 3202−3211.

(56) Kumar, A.; Sun, S.-S.; Lees, A. J. Photophysics and Photochemistry of Organometallic Rhenium Diimine Complexes. In *Photophysics of Organometallics*; Lees, A. J., Ed.; Springer Berlin, Heidelberg: Binghamton, NY, 2010; p 240.

(57) Worl, L. A.; Duesing, R.; Chen, P.; Ciana, L. Della; Meyer, T. J. Photophysical Properties of Polypyridyl Carbonyl Complexes of Rhenium(I). *J. Chem. Soc., Dalton Trans.* **1991**, 849−858.

(58) Chang, M. C.; Chantzis, A.; Jacquemin, D.; Otten, E. Boron Difluorides with Formazanate Ligands: Redox-Switchable Fluorescent Dyes with Large Stokes Shifts. *Dalton Trans.* **2016**, *45*, 9477−9484.

(59) Maar, R. R.; Zhang, R.; Stephens, D. G.; Ding, Z.; Gilroy, J. B. Near-Infrared Photoluminescence and Electrochemicalluminescence from a Remarkably Simple Boro Difluoride Formazanate Dye. *Angew. Chem., Int. Ed.* **2019**, *58*, 1052−1056.

(60) Maar, R. R.; Barbon, S. M.; Sharma, N.; Groom, H.; Luyt, L. G.; Gilroy, J. B. Evaluation of Anisole-Substituted Born Difluoride Formazanate Complexes for Fluorescence Cell Imaging. *Chem. − Eur. J.* **2015**, *21*, 15589−15599.

(61) S. P., Schmidt, W. C., Trogler, F. B. Pentacarbonylrhenium, Halides. In *Inorganic syntheses*; Angelici, R. J., Ed.; Wiley, 1991; Vol. *28*, 160−165.

(62) Sheldrick, G. M. Crystal Structure Refinement with SHELXL. *Acta Crystallogr., Sect. C: Struct. Chem.* **2015**, *71*, 3−8.

(63) Frish, M. J.; Trucks, G. W.; Schlegel, H. B.; Scuseria, G. E.; Robb, M. A.; Cheeseman, J. R.; Scalmani, G.; Barone, V.; Petersson, G. A.; Nakatsuji, H. *Gaussian 16, Revision C.02.* Wallingford CT 2019.

(64) Dennington, R.; Keith, T. A.; Millam, J. M. GaussView, Version 6. Semichem Inc., Shawnee Mission: KS 2016.

(65) Hanwell, M. D.; Curtis, D. E.; Lonie, D. C.; Vandermeersch, T.; Zurek, E.; Hutchinson, G. R. Avogadro: An Advanced Semantic Chemical Editor, Visualization, and Analysis Platform. *Aust. J. Chem.* **2012**, *4*, 1−17.

(66) Sae-Heng, P.; Tantirungrotechai, J.; Tantirungrotechai, Y. Scale Factors for Carbonyl Vibrational Frequencies: A Study of Partial Hessian Approximation. *Chiang Mai J. Sci.* **2018**, *45*, 2797−2808.

(67) Miertuš, S.; Scrocco, E.; Tomasi, J. Electrostatic Interaction of a Solute with a Continuum. A Direct Utilization of AB Initio Molecular Potentials for the Prevision of Solvent Effects. *Chem. Phys.* **1981**, *55*, 117−129.